SOLAR MAGNETIC
PHENOMENA

ARNOLD HANSLMEIER
ASTRID VERONIG
MAURO MESSEROTTI

Editors
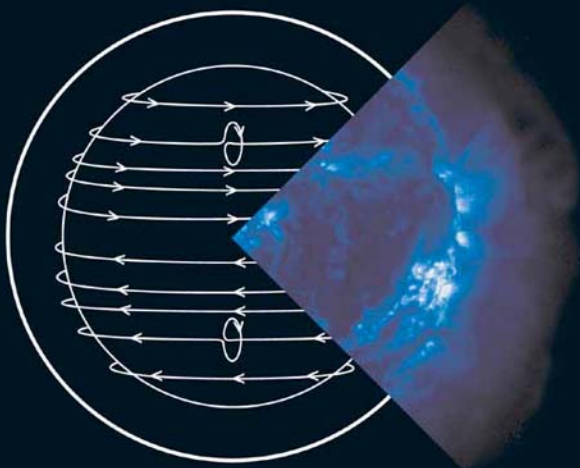
SOLAR MAGNETIC PHENOMENA

ASTROPHYSICS AND
SPACE SCIENCE LIBRARY

VOLUME 320

SOLAR MAGNETIC PHENOMENA

Proceedings of the 3rd Summerschool and
Workshop held at the Solar Observatory Kanzelhöhe,
Kärnten, Austria, August 25 - September 5, 2003

Edited by

ARNOLD HANSLMEIER
*Institute for Geophysics, Astrophysics and
Meteorology, University of Graz, Austria*

ASTRID VERONIG
*Institute for Geophysics, Astrophysics and
Meteorology, University of Graz, Austria*

and

MAURO MESSEROTTI
INAF-Trieste Astronomical Observatory, Italy

Springer

Printed in the Netherlands.

Table of Contents

Preface

The concept of summerschools and workshops at the Kanzelhöhe Solar Observatory, Kärnten, Austria, devoted to up-to-date topics in solar physics has been proven to be extremely successful, and thus in August/September 2003 the third combined summerschool and workshop was held there.

This book contains the proceedings of the Summerschool and Workshop "Solar Magnetic Phenomena" held from 25 August to 5 September 2003 at the Solar Observatory Kanzelhöhe, which belongs to the Institute for Geophysics, Astrophysics and Meteorology of the University of Graz, Austria. The book contains the contributions from six invited lecturers. They give an overview on the following topics: observations of the photosphere and chromosphere, solar flare observations and theory, coronal mass ejections and the relevance of magnetic helicity, high-energy radiation from the Sun, the physics of solar prominences and highlights from the SOHO mission. The lectures contain about 25 to 30 pages each and provide a valuable introduction to the topics mentioned above. The comprehensive lists of references at the end of each contribution enable the interested reader to go into more detail.

The second part of the book contains contributed papers. These papers were presented and discussed in the workshop sessions during the afternoons. The sessions stimulated intensive discussions between the participants and lecturers.

On behalf of the organizing committee and all the participants, we wish to thank the following organizations and companies for their financial support: the Austrian Bundesministerium für Wissenschaft und Forschung, European Space Agency (ESA), Italian Space Agency (ASI), University of Graz, INAF-Trieste Astronomical Observatory, Marktgemeinde Treffen, Land Steiermark, Raiffeisenbank Kärnten.

Graz and Trieste, July 2004

Arnold Hanslmeier, Astrid Veronig and Mauro Messerotti

OBSERVATIONS OF PHOTOSPHERE AND CHROMOSPHERE

CARSTEN DENKER

New Jersey Institute of Technology
Center for Solar-Terrestrial Research
323 Martin Luther King Blvd
Newark, New Jersey, USA

Abstract. Solar physics has seen a decade of exciting science and discoveries, which were driven by new instruments for ground- and space-based observations. Multi-wavelength observations involving many observatories now routinely cover the whole solar atmosphere from photosphere, to chromosphere, transition region, corona, and heliosphere and have become an integral part in any type of space weather forecasting. The solar photosphere and chromosphere has historically been the domain of ground-based observatories and this review will be based on observations and research projects that have been carried out at the Big Bear Solar Observatory (BBSO) to illustrate current trends and prospects for ground-based experimental solar physics.

1. Introduction

The Sun is the only star where we can observe surface structures in fine detail. Elementary magnetic flux tubes are generated by a self-excited dynamo mechanism and are embedded in convective plasma flows. A recent review of numerical simulations of solar magneto-convection has been given by Schüssler (2001) who points out that at the moment, we lack observations with adequate spatial, temporal, and spectral resolution to validate or reject theoretical models of magneto-convection. Solar observations have to cope with the earth's turbulent atmosphere, which is heated by solar radiation causing severe degradation of image quality – so-called "seeing". The advance of a next generation of solar telescopes in combination with adaptive optics (AO), post-facto image reconstruction techniques, and sophisticated post-focus instrumentation, namely two-dimensional spectro-polarimetry, have brought us closer to the goal of resolving the fundamental length and time scales of solar magneto-convection.

The present review focusses on recent observations of the solar photosphere and chromosphere to illustrate the characteristic spatial distribution of highly intermittent magnetic fields in various environments, to study

the energetics related to non-thermal heating and inhibition of convective energy transport by magnetic fields, and to link the dynamics of small-scale magnetic fields to instabilities, wave excitation and propagation, and the reconnection of magnetic field lines. Ultimately, the intrinsic temporal and spatial scales of magneto-convection are related to global aspects of solar variability and therefore to basic physical processes on the Sun that affect the Earth environment, e.g., communications technology, the power grid, civil and military assets as well as humans in space, and in the end, the terrestrial climate.

Generation and dissipation of small-scale solar magnetic features are responsible for the dynamics above the photosphere. Observations of small-scale magnetic fields, with the highest resolution possible, are crucial to the understanding of mass and energy transport throughout photosphere, chromosphere, transition region, and corona. The morphology and physics of sunspots and associated phenomena is carefully illustrated in the classical text by Bray and Loughhead (1964) and the hierarchy of solar magnetic fields has been reviewed by Zwaan (1987). The size spectrum of solar magnetic fields ranges from sunspots, pores, and magnetic knots to faculae and network clusters and finally to the theoretically predicted flux fibers with dimensions of just a few tens of kilometers. A collection of research papers relating sunspot observations and theory was assembled in the monographs by Thomas and Weiss (1992) and Schmieder, del Toro Iniesta, and Vázquez (1997).

2. Quiet sun magnetic fields

In a quiet region, magnetic fields can be generally divided into two categories: network fields and intranetwork fields (IN). The observable fields are in the form of discrete magnetic elements. Network fields are found in the boundaries and, particularly, in the vertices of supergranule cells (Simon and Leighton, 1964; Wang, 1988). The intranetwork fields are mixed-polarity magnetic elements inside the network. Two important processes for the creation and destruction of magnetic elements of the quiet sun are ephemeral regions (Harvey and Martin, 1973) and "cancellation" (Livi, Wang, and Martin, 1985; Martin, Livi, and Wang, 1985). Wang *et al.* (1995) obtained a number of sequences of quiet sun magnetograms, where they studied the distribution of IN magnetic fluxes based on some of the best BBSO magnetograms and found a peak flux distribution at 6×10^8 Wb. However, their findings cannot directly be applied to magnetic flux in other kinds of magnetic structures, i.e., their study should be extended to many regions, including quiet network, enhanced network, and coronal holes. After all, the magnetic structure is the dominant factor in producing

microflares and mini-filament eruptions. In addition, Wang *et al.* (1996) applied local correlation tracking (LCT) to long-integration magnetograms and confirmed that IN fields follow supergranular flows and are swept to the network boundary. But they do not contribute to the formation of network fields because of their bipolar nature. Furthermore, the interaction between network and IN fields, can produce at least 1.2×10^{21} J s^{-1} of energy, which is comparable to the energy required for coronal heating.

3.   Spicules, macrospicules, and surges

It is now widely accepted that magnetic fields play a fundamental role in defining the structure, mass, and energy flows in the chromosphere and corona (Withbroe and Noyes, 1977). Nevertheless, we are still some distance away from a satisfactory understanding of the detailed mechanisms of energy and mass transport in the sun, mainly because of our limited knowledge of the various kinds of small-scale dynamic structures, which are thought to be important in mass and energy transport. Spicules are common chromospheric phenomena and their appearance led to the figurative expression "burning prairie" to describe the chromosphere. They are predominantly located near the chromospheric network where the magnetic field is moderate and small-scale magnetic elements are concentrated. Spicules are less likely to occur near active regions where the magnetic field is much stronger. In polar regions and in coronal holes, spicules are more elongated and almost normal to the surface. The direction of their trajectories is preferentially along local magnetic lines of force. The upward mass flux in spicules is about 100 times that of the solar wind and has to be considered for the mass balance of the solar atmosphere. The velocities in spicules are in the order of the sound and Alfvén speed of the photosphere and chromosphere. Athay (2000) suggests that spicules are an integral part of the dynamic interaction between the chromosphere and the corona and that these dynamics are driven by the heating rates of spicules, which leads to the question: Is the chromospheric heating rate constant with height, especially in the upper layers of the chromosphere? A recent review of spicules, their observed properties and competing models is given by Sterling (2000). Figure 1 shows a typical BBSO Hα full disk image, which image has been corrected by a Kuhn-Lin style flat-field image (Kuhn, Lin, and Loranz, 1991) and a limb darkening profile was subtracted to enhance the contrast of disk and limb features (Denker *et al.*, 1998).

Johannesson and Zirin (1996) measured the height of the solar chromosphere from high resolution Hα filtergrams during the solar minimum period in 1994 and 1995. They determined the frequency of macrospicules as a function of azimuth. The chromospheric height is about 4,300 to
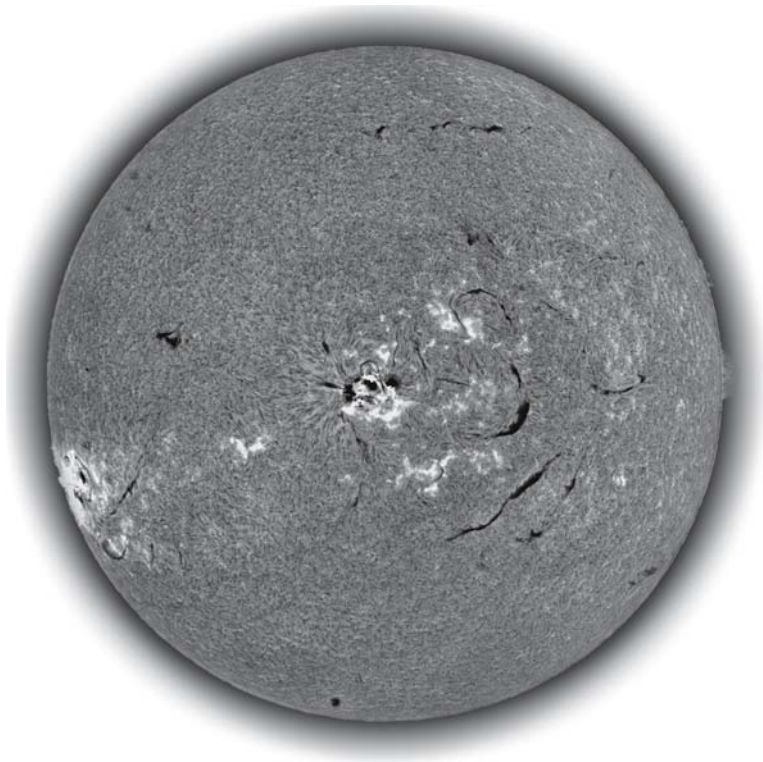
Figure 1. Hα full disk image obtained with the Singer full disk telescope at BBSO on 2003 October 23. Two of the largest active regions of Solar Cycle No. 23, the naked-eye sunspot groups NOAA 10484 and NOAA 10486, can be seen at disk center and the east limb, respectively. Both regions produced numerous X- and M-class flares including the largest flare (X28) in recorded history on 2003 November 4.

4,400 km at the equator and increases to just below 6,000 km at the poles. The height of the chromosphere increases locally above active regions. Macrospicules can be detected as elongated features extending radially outward with sizes of 7,000 km to 20,000 km above the limb. They are commonly confined to coronal holes near the solar poles. Typical numbers are about 20 macrospicules per 150″ along the limb. There is still some controversy over which disk features correspond to macrospicules. However, two-dimensional spectrometry of the Hα line in combination with accurate high-spatial polarimetry might just provide the necessary clues to clarify this question. Doppler shifts associated with macrospicules can exceed 50 pm, which makes it difficult to observe them at a single line position with Lyot-type filters. Macrospicules are therefore ideal candidates for two-dimensional spectroscopy. Due to the small size of macrospicules,

many of their properties are still uncertain, e.g., if the upward, supersonic velocity profile is ballistic or constant. Another interesting question is if macrospicules are associated with flaring X-ray bright points or if these are typical for (polar) surges only (Georgakilas, Koutchmy, and Cristopoulou, 2001).

4. Mini-filaments

Mini-filament eruptions were first described in detail by Hermans and Martin (1986). Wang *et al.* (2000b) studied them in great detail including their lifetime, morphology, and magnetic evolution. They are different from macrospicules in the sense that mini-filament eruptions have a pre-eruption phase and lack a jet-like structure. They are likely related to magnetic reconnection. Even though mini-filament eruptions appear to be different from macrospicules, there is still some similarity, since both seem to be related to magnetic reconnection. Macrospicules, long jets following polar plumes, were discovered in Skylab He II 30.4 nm overlapogram images. Moore *et al.* (1977) showed that Hα macrospicules are connected to tiny Hα limb flares in ephemeral regions, and that they are associated with ultraviolet (UV) macrospicules. Based on their observations, macrospicules and microflares may be associated. Wang (1998) compared macrospicules in He II 30.4 nm and Hα and concluded that macrospicules may appear either as jet-like ejections or as loop-like eruptions near the limb. There is strong evidence that they are the result of magnetic reconnection. The loop-like eruptions, however, might have been mini-filaments eruptions rather than macrospicules. It is still an open question whether or not mini-filaments are related to microflares and coordinated observations with the Reuven Ramaty High Energy Solar Spectroscopic Imager (RHESSI) might shed light onto this problem. Mini-filaments can be used as a stepping stone to understand the more complex physics of filaments, since mini-filaments eruptions may be the small-scale analogue of filament eruptions. Therefore, an investigation of this possibility and an assessment of the role of small-scale events in mass and energy transport to the upper atmosphere of the sun is warranted to investigate the possible existence of a scaling law from mature filaments to mini-filaments. Finding the link between the evolution of magnetic fields, microflares, and mini-filament eruptions is one of the important tasks in high resolution studies of the Sun.

5. Moustaches

Moustaches are a typical phenomenon of the active chromosphere, which are observed as excess emission in the line wings of strong chromospheric
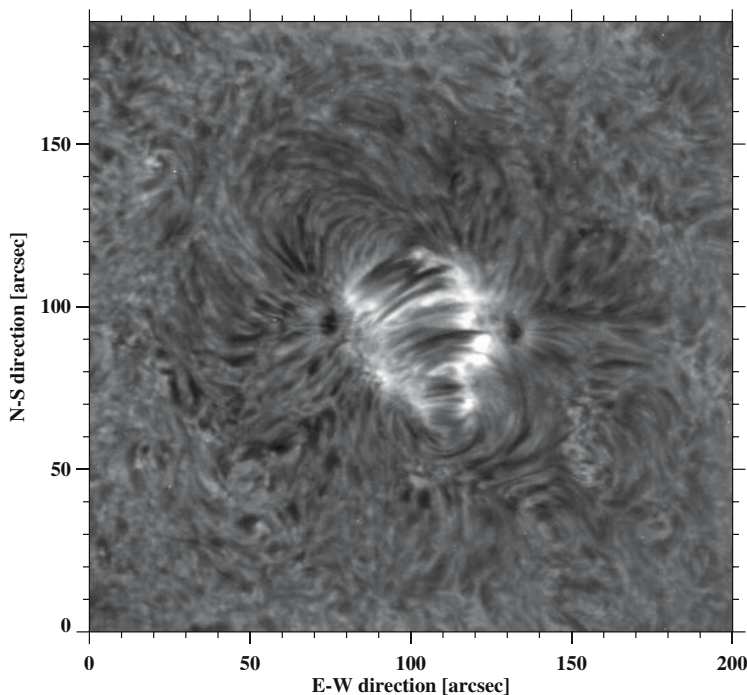
Figure 2. High resolution Hα image of an emerging flux region (NOAA 10461) with a prominent arch filament system taken with the 65 cm vacuum reflector on 2003 September 16 at 21:48 UT while a M1 flare was in progress.

absorption lines in the vicinity of sunspots, emerging flux regions, and arch filament systems. Figure 2 shows an emerging flux region and arch filament system. The moustache phenomenon was first observed by Ellerman (1917) who called these chromospheric bright points "hydrogen bombs". However, we prefer the expression "moustache" introduced by Severny (1956), which refers to their appearance in photographic negatives of the corresponding spectra (e.g., the Balmer lines up to H_{10}, Ca H and K, Na D, and Mg b, see Matres and Bruzek, 1977). In Hα, a typical moustache spectrum exhibits inconspicuous absorption at line center and a brightening in the wings with a maximum around 0.1 nm off line center. The increased line wing contrast can extend to 0.5 to 0.7 nm away from the line center. The sizes of moustaches range from 5″ down to the diffraction limit of today's solar telescopes of about 0.2″. Their typical lifetime is about 10 to 15 min and they have a tendency to reoccur.

Denker *et al.* (1995) applied the speckle masking technique to Hα line wing filtergrams and showed that the moustache contrast is as high as

1.7 times the contrast of the quiet sun background. Contrasts of small-scale features can increase up to 2 to 3 times when the seeing transfer function (STF) is properly taken into account and many flux tube models still rely on contrast values obtained without seeing correction. From these observations, they concluded that the upper limit for the size of moustaches of $5''$ is most likely due to insufficient spatial resolution in previous observations. At the highest resolution, they identified well defined intensity peaks, which are pushed around by the convective motion of granules and move along intergranular lanes with speeds of 1 to 2 km/s toward their intersections. Denker (1997) used the two-dimensional spectropolarimeter of the Universitäts-Sternwarte Göttingen (Bendlin and Volkmer, 1995) at the Teide Observatory, Tenerife, and obtained reconstructed filtergrams in the $Na D_2$ line with a bandpass of just 14 pm and demonstrated that chromospheric moustaches and photospheric filigree are co-spatial.

Nindos and Zirin (1998) studied moustaches in the neighborhood of a sunspot in a mature active region. One third of the moustaches were associated with moving magnetic features (MMFs), whereas the remainder were not associated with enhanced magnetic field elements. Moustaches associated with MMFs exhibited similar proper motions of up to 1.1 km/s, whereas the other remained stationary. Both types of moustaches were indistinguishable with regard to lifetime, shape, dimensions, contrasts, and temporal evolution. The observed moustaches were not circular in shape but had an aspect ratio of about $1\frac{1}{2}$. Qiu *et al.* (2000) found another classification where moustaches with strong chromospheric Hα emission are well correlated with ultra-violet (UV) brightenings at atmospheric heights corresponding to the temperature minimum and moustaches with weak Hα emission are uncorrelated. The majority of weak moustaches is located near magnetic inversion lines whereas strong moustaches are located at the boundary of unipolar magnetic regions or near magnetic inversion lines. Qiu *et al.* concluded that the heating mechanism of moustaches is located in very deep atmospheric layers but that this might differ for different classes of moustaches.

6. Penumbra formation and Evershed effect

Many still-open questions are related to the abrupt transition from nearly vertical fields in pores to the strongly inclined fields in sunspot penumbrae: How does the sudden topology change of the magnetic flux fibers affect the magnetic field in transition region and corona? What effect has the clustering tendency of emerging small-scale flux elements in active regions on the formation of (rudimentary) penumbrae? Is the sea-serpent-like structure attributed to penumbral filaments responsible for small-scale
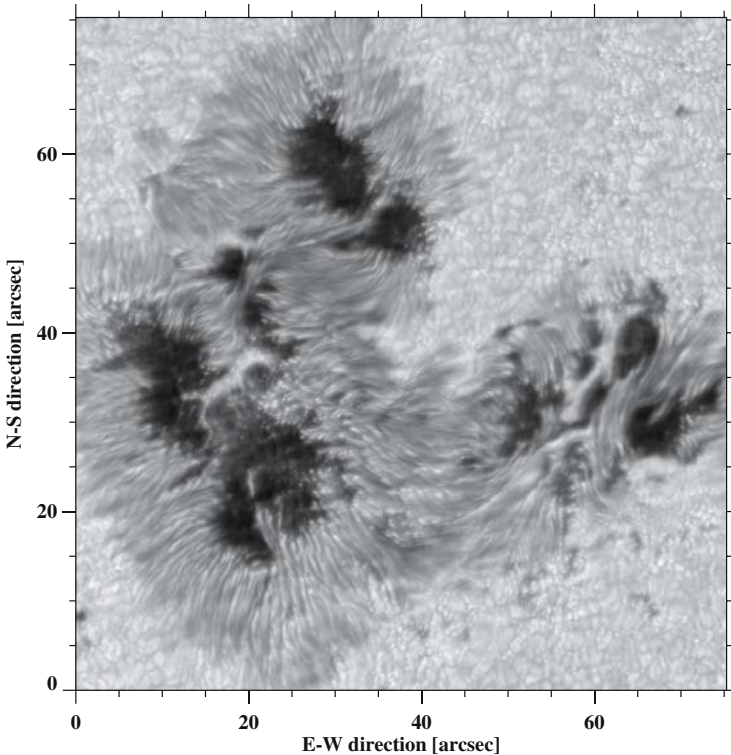
Figure 3.   Speckle reconstruction of active region NOAA 10375 on 2003 June 10 at 19:58 UT.

chromospheric heating as observed in moustaches? These questions are drivers for observations of penumbra formation with increased magnetic sensitivity, improved spectral resolving power, and appropriate temporal resolution at sub-arcsecond spatial scales. The real-time image reconstruction (RTIR) system at BBSO (Denker, Yang, and Wang, 2001) has been designed to obtain images with a spatial resolution close to the diffraction limit of the 65 cm vacuum telescope. The disk passage of solar active region NOAA 10375 is depicted in Figures 3 and 4.

What are the essential features that distinguishes a sunspot from a pore? Pores can have diameters of up to $10''$, whereas the smallest sunspots have diameters down to $5''$. Rucklidge, Schmidt, and Weiss (1995) developed a simplified model of the energy transport in sunspots and pores, which describes the transition from pores to sunspots as a function of the magnetic flux Φ and the radius R of the sunspot/pore. Sunspots and pores are located on a hysteresis curve in the Φ, R-plane, and sunspots emerge from
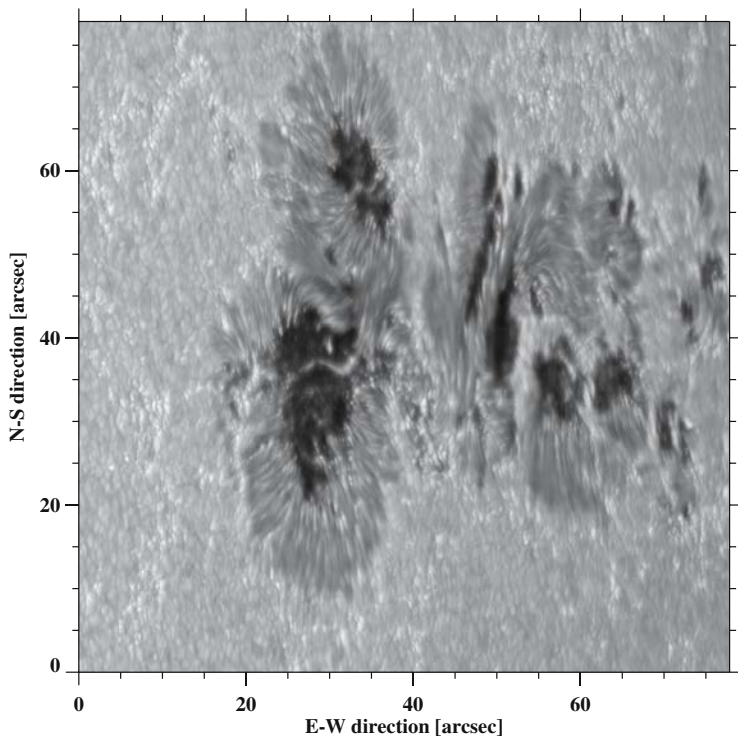
Figure 4.   Speckle reconstruction of active region NOAA 10375 near the solar East limb on 2003 June 12 at 16:52 UT.

the pore branch at a subcritical (with respect to both Φ and R) bifurcation point. At this point, lateral heat transport increases sharply and penumbral structures appear abrupt and rapidly, and become a robust feature in the evolution of the sunspot. The generation of a filamentary penumbra, the on-set of the Evershed flow, and the change of the magnetic field topology take place in less than 20 to 30 min (see Leka and Skumanich, 1998), which makes penumbra formation a challenging observational task and explains why many processes of non-linear convection involved in sunspot formation are still elusive. Penumbral grains move predominantly inwards in the inner penumbra and outwards in the outer penumbra (Denker, 1998; Sobotka, Brandt, and Simon, 1999). In addition, clouds of outflows seem to migrate outwards in Dopplergrams (Shine *et al.*, 1994; Rimmele, 1994). High resolution two-dimensional spectroscopy will enable us to resolve issues regarding the fine structure of penumbrae and its association with the Evershed effect, the size of the penumbral filaments and its correlation between continuum intensity, velocity, field strength and field inclination.

The abrupt formation of a penumbra and its effects on the surrounding environment should certainly affect the upper atmospheric layers. However, the exact mechanisms coupling photospheric flux tube dynamics with chromospheric activity and coronal heating are still elusive. Moustaches have been known to appear preferentially near young sunspots, where they are often concentrated at the outer boundary of the penumbra (Denker *et al.*, 1995), especially when the penumbral filaments penetrate deeply into the granular pattern. Denker (1997, 1998) compare the appearance of moustache near sunspot penumbrae in speckle interferometric continuum and NaD_2 filtergrams. Yang *et al.* (2003) studied two pores, which were separated by a light-bridge. A small area of penumbral filaments formed suddenly near the light-bridge indicating an abrupt change of the local magnetic field topology from almost vertical to strongly inclined magnetic fields. Subsequently cool material, which was previously suspended in a filament, stream downward. During the downward motion of the cool material, $H\alpha$ Dopplergrams revealed twisted streamlines along the filament and several well-defined $H\alpha$ brightenings. The moustaches occurred near the location of the descending filament material. These moustaches resided near a magnetic inversion line and were stationary, as opposed to moustaches associated with moving magnetic features (Nindos and Zirin, 1998).

Early observations revealed that in the Evershed effect, the amount of line shift decreases with increasing formation height, while the degree of the line asymmetry increases with formation height. Maltby (1964) noted that the dependence of the Evershed effect on the formation height presents evidence that the flow lies in the deepest photospheric layers. However, studies performed by Rimmele (1994) present evidence that the Evershed effect is confined to some elevated thin loop-like structures above the continuum height over most part of the penumbra. However, these elevated thin flow channels only exist on the center-side of the penumbra, while on the limb-side penumbra no such elevated flow channels were observed. This might be due to the line-of-sight effect. Recent observations by Hirzberger and Kneer (2001) do not confirm the results of Rimmele (1994). Their observations indicate that the Evershed flow is sharply confined to the penumbra and is mostly horizontal. Vertical flows were observed at both ends of penumbral filaments (Rimmele, 1995; Stanchfield, Thomas, and Lites, 1997; Schmidt and Schlichenmaier, 2000; del Toro Iniesta, Bellot Rubio, and Collados, 2001). Up-flows in penumbral grains may be the source of the horizontal Evershed flow. The majority of studies conclude that the Evershed flow is well correlated with dark filaments in penumbrae (Shine *et al.*, 1994; Rimmele, 1995; Stanchfield, Thomas, and Lites, 1997; Wiehr and Degenhardt, 1992; Wiehr and Degenhardt, 1994; Degenhardt and Wiehr, 1994). The correlation between the horizontal magnetic field and the dark filaments in the

penumbra is still controversial. Some authors, e.g., Degenhardt and Wiehr (1991), Schmidt *et al.* (1992), Title *et al.* (1993), Rüedi, Solanki, and Keller (1999), and Westendorp Plaza *et al.* (2001), found a correlation between horizontal fields and dark filaments, whereas Hofmann *et al.* (1994) only found correlation in the inner and Lites, Skumanich, and Scharmer (1990) only in the outer part of the penumbra. There are even more controversial observations on how the field inclination and field strength are correlated.

There are two notable models that attempt to interpret the Evershed effect. Thomas (1988) interpreted the Evershed flow as a "siphon flow" along magnetic flux tubes. If a tube forms an arch between two footpoints with different values of gas pressure (at the same geometrical level), a flow is driven from the high-pressure end to the low-pressure end. The flow velocity increases along the ascending part of the arch and reaches its sonic point at the summit. On the downstream side, it first accelerates further, but then undergoes a shock, thereby adjusting its pressure to the given end pressure. The second model, the "moving-tube model" (Schlichenmaier, Jahn, and Schmidt, 1998a, 1998b), includes time dependence and does not rely on a given pressure difference. Magnetic flux tubes emerging from the deep penumbra are able to transport heat to the penumbral photosphere. In the thin flux tube approximation, a single flux tube first rises adiabatically from the magnetopause, then, at the point where it meets the photosphere it sharply bends horizontally. At this point a high temperature is sustained by the up-flow of hot gas within the tube, which has been interpreted as the observed penumbral grains. The model also yields a horizontal pressure gradient along the tube, which drives an outward flow, as in the siphon model.

7. Sunspot umbra, umbral cores, and umbral dots

Umbral dots are easier to detect in the infrared, since the umbral contrast is diminished. Near infra-red (NIR) observations of umbral dots are rare and usually limited to continuum images (Ewell, 1992). Therefore, spectropolarimetric observations in the NIR are likely to provide deeper insight into the physics of umbral dots and the energy transfer and balance within sunspot umbrae. Theoretical models of umbral dots include non-linear oscillatory convection, non-thermal heating, and penetrative convection (García de la Rosa, 1987). However, many basic properties are still uncertain. This leads to the following questions: Do umbral dots exist throughout the umbra or are there dot free regions, i.e., umbral cores that maintain their magnetic identity, thus restricting umbral dots to their periphery? Do umbral dots play a role in the formation of light-bridges? Are peripheral umbral dots related to inward moving penumbral grains and are they distinct from

stationary central umbral dots? What is the magnetic field strength in umbral dots? Do the magnetic field strength and brightness temperatures of umbral dots depend on the sunspot geometry?

Assuming local thermal equilibrium (LTE), the continuum intensity can be converted into a brightness temperature via Planck's law. Tritschler and Schmidt (1997) find a decrease in the brightness temperature of about 30% for central umbral dots and of 20–25% for peripheral umbral dots compared to the quiet sun, which corresponds to a decrease in temperature of 1,600 K and 1,200 to 1,400 K, respectively. They do not find a significant difference between the magnetic field of umbral dots and the surrounding umbra. In both cases, the magnetic field ranges from 0.15–0.3 T. Comparing the observed spectral profiles of umbral dots with various model profiles, Tritschler and Schmidt conclude that umbral dots are a phenomenon of the deep photosphere only visible at the umbral continuum level, i.e., umbral dots are inconspicuous at the height of formation of the Fe I 630.25 nm and Fe I 864.8 nm line.

In the "cluster or spaghetti model" (Parker, 1979; Choudhuri, 1986), the magnetic field of the sunspot consists of many individual flux tubes at sub-photospheric levels. The flux tubes are embedded in nearly field-free plasma and umbral dots are the manifestation of over-stable convection, i.e., hot columns of gas rise between the flux tubes and the up-flow can be sufficiently strong to penetrate the magnetic arcs formed by the individual flux tubes. Assuming the sunspot is a "single monolithic flux tube", Knobloch and Weiss (1984) showed in a nonlinear treatment of magneto-convection that elongated convection cells of 300 km diameter and 1,500 km length contribute to the energy transport within the monolithic flux tube and umbral dots are the photospheric signature of these convection cells. Sensitive and spatially resolved magnetograms will show how uniform the magnetic field in the umbra really is and NIR continuum images allow us to identify accurately the location of umbral dots, thus providing important boundary conditions for the aforementioned models.

8. Modelling the fine structure of sunspots

Schlichenmaier (1999) demonstrated that many observed penumbral features can be reproduced by simulations. Schlichenmaier, Bruls, and Schüssler (1999) modelled the radiative cooling behavior of tubes that are substantially hotter than the surrounding photosphere and showed that the cometary tail of penumbral grains can be explained by an hot up-flow that, being channelled by a magnetic flux tube, flows essentially horizontal in the photosphere. Recent numerical results of the moving tube model reveal that a subtle balance between the centrifugal force and the magnetic

curvature force at the photospheric footpoint of the tube may be essential to understand the penumbral fine structure. For a supercritical flow speed, the centrifugal force cannot be balanced by the magnetic tension and a flow overshoots into the convectively stable photosphere. In this scenario, down-flows within the penumbra can be modelled dynamically by the moving tube model (Schlichenmaier, 2003).

Spectropolarimetric investigation, observational as well as theoretical, present strong evidence that the magnetic field of the penumbra is un-combed, such that the flow is concentrated in mostly horizontal flux tubes, while the background field is more inclined with respect to the horizontal and essentially at rest. Schlichenmaier and Collados (2002) have analyzed spectropolarimetric data, acquired in Fe I 1564.8 nm ($g = 3$) with the Tener-ife Infrared Polarimeter (TIP) at the German Vacuum Tower Telescope (VTT) in Tenerife. Investigating the Stokes-V asymmetries and comparing them to synthetic lines, Schlichenmaier and Collados find that the observa-tions are compatible with up-flow channels in the inner and horizontal flow channels in the outer penumbra, while the background is at rest. Additional support was found by comparing maps of the net circular polarization of Fe I 1564.8 nm and Fe I 630.2 nm. These maps show a different behavior for the two lines, which can be understood, if one assumes horizontal flow channels that are embedded in a background at rest (Müller *et al.*, 2002).

Steiner *et al.* (1998) simulated the magneto-hydrodynamical (MHD) interaction between non-stationary convection in the solar photosphere and small-scale magnetic flux sheets, using a numerical code for two-dimensional MHD with radiative energy transfer. Dynamical phenomena were identified such as the bending and horizontal displacement of a flux sheet and the exci-tation and propagation of shock waves and observational signatures of these phenomena (synthetic Stokes profiles) were derived. In Grossmann-Doerth, Schüssler, and Steiner (1998) the formation of concentrated magnetic flux by convective flow is simulated. Starting from an evolved state of simulated solar granulation the evolution of an initially homogeneous, vertical mag-netic field, to a field concentration with a flux density up to the thermal equipartition value is followed. Convective collapse (Parker, 1978; Spruit, 1979) with a subsequent "rebound shock" is observed of which radiation diagnostics in the continuum and in spectral lines were predicted and sub-sequently observed by Steiner (2000) and Grossmann-Doerth *et al.* (2000) investigated the problem of strongly asymmetric Stokes-V profiles and came to the conclusion that pathological Stokes profiles need not necessarily be the result of mixed polarity on very small scales but instead can be formed in the presence of a magnetic canopy. These ideas have been applied in an investigation of pores and magnetic knots by Leka and Steiner (2001). They found enhanced Stokes-V asymmetry on the periphery of pores and azimuth
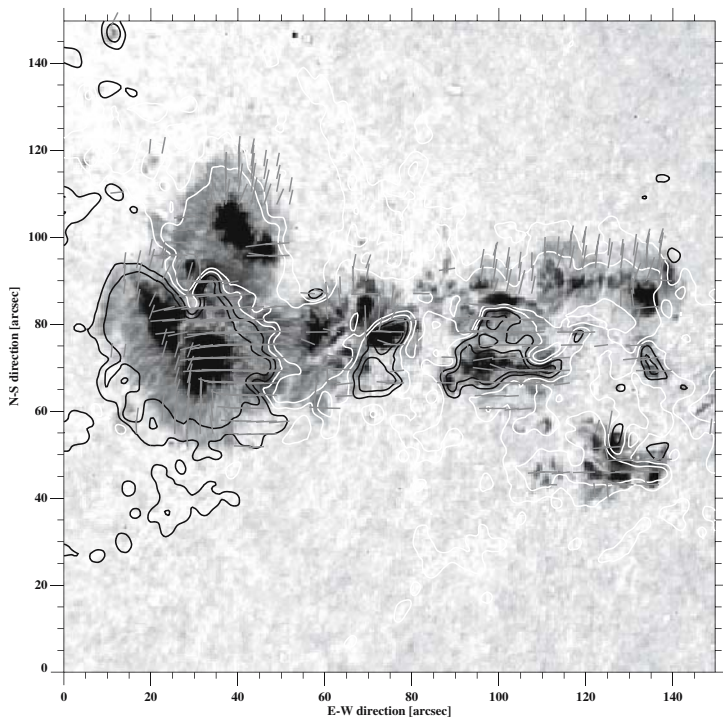
Figure 5.   Ca I 610.3 nm line wing image of active region NOAA 10375 obtained with the DVMG system at the 25 cm vacuum refractor on 2003 June 10. The longitudinal magnetic field is represented by white contour lines and the orientation of the transverse field is indicated by short gray lines. The 180° ambiguity has not been resolved.

centers, which they associate with downward drafts on the periphery of these object. Steiner, Hauschildt, and Bruls (2001) give an explanation for the high positive contrast of small-scale magnetic flux concentrations in the photosphere when observed with the G-band filter. They found that this effect is due to a reduction of the CH abundance by dissociation in the deep photospheric layers of the magnetic flux tubes, where it is hotter than in the surrounding atmosphere.

9. Active region dynamics

The size spectrum of solar magnetic fields ranges from sunspots, pores, and magnetic knots to faculae and network clusters and finally to the theoretically predicted flux fibers with dimensions of just a few tens of kilometers. In active regions, magnetic fields have small-scale structures that can be
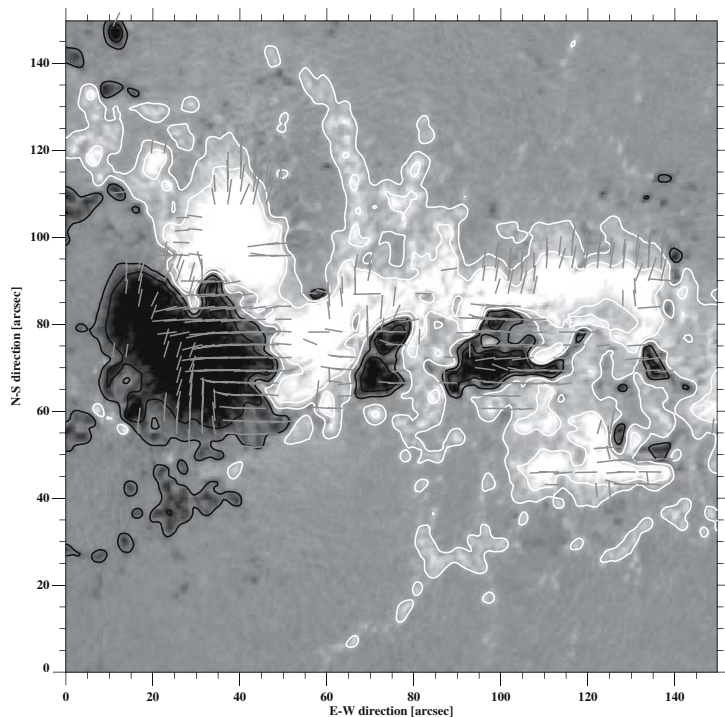
Figure 6. Ca I 610.3 nm vector magnetogram of active region NOAA 10375 obtained with the DVMG system at the 25 cm vacuum refractor on 2003 June 10.

seen only in high-resolution observations, such as umbral dots, penumbral filaments, penumbral grains, running penumbral waves, moving magnetic features, filigree, moustaches, and small-scale bipoles. Typical examples of magnetic field data obtained with the digital vector magnetograph (DVMG) are presented in Figures 5 and 6 (Spirock *et al.*, 2001).

Sunspots are the largest magnetic concentrations on the surface of the Sun. The umbra is the dark central part of a sunspot. The penumbra is a radial, filamentary structure surrounding the umbra. The magnetic field decreases gradually from about 0.3 T at the center of the umbra to about 0.08 T at the outer part of penumbra and vanishes abruptly slightly outside the penumbra in the photosphere. The magnetic field continues as magnetic canopy (Giovanelli, 1982; Solanki, Rüedi, and Livingston, 1992) in the chromosphere outside the photospheric boundaries of the penumbra. High resolution observation show that there are fine structures inside sunspots, e.g., bright and dark filaments in the penumbra, penumbral grains, light-bridges, umbral dots, and dark nuclei observed in the umbra (Sobotka,
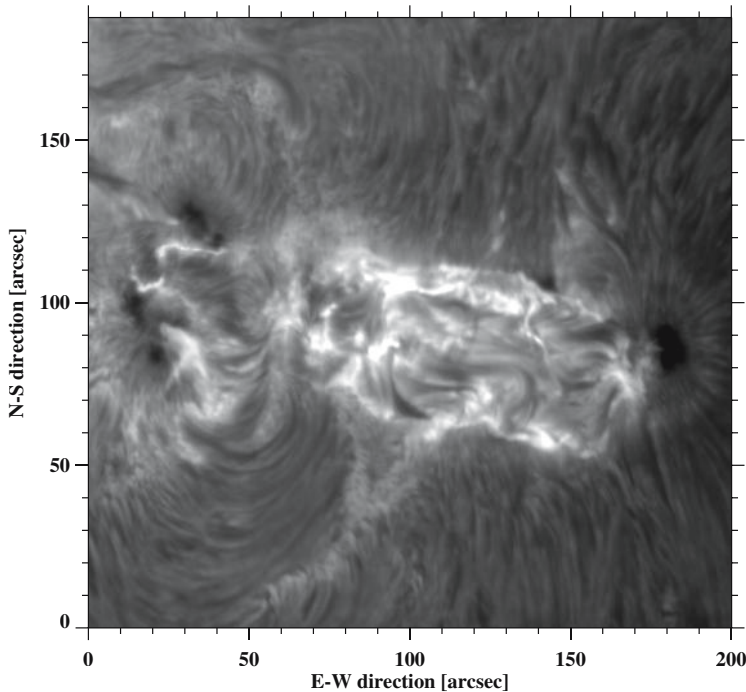
Figure 7.   High resolution Hα image of a M6 flare in solar active region NOAA 10375 taken with the 65 cm vacuum reflector on 2003 June 10 at 20:00 UT.

Bonet, and Vázquez, 1993; Sobotka, Brandt, and Simon, 1997a, 1997b, 1999; Sobotka and Sütterlin, 2001). This fine structure plays an important role in understanding the dynamics and physical nature of sunspots.

How is magnetic energy stored and released? This is a fundamental question in solar physics. Figures 7, 8, and 9 show high-resolution Hα images of flares, post-flare loops, and active sigmoidal filaments (Canfield, Hudson, and McKenzie, 1999). Solar physicists have been spending much time and effort to search for flare-related changes in the photospheric magnetic field, which would provide some clues on energy storage and release in active regions. Despite this fact, we still lack a detailed understanding on how photospheric magnetic fields evolve before, during, and after solar flares. However, new advanced instrumentation providing high-cadence and high-resolution data from ground- and space-based observatories, place is finally in a position to discover the photospheric signature of flares, in particular that of the photospheric magnetic field.

Deng *et al.* (2004) observed NOAA 9026 on 2000 June 6, where three major flares, an X1.1, M7.1, and X2.3 flare, originated within $2\frac{1}{2}$ hours
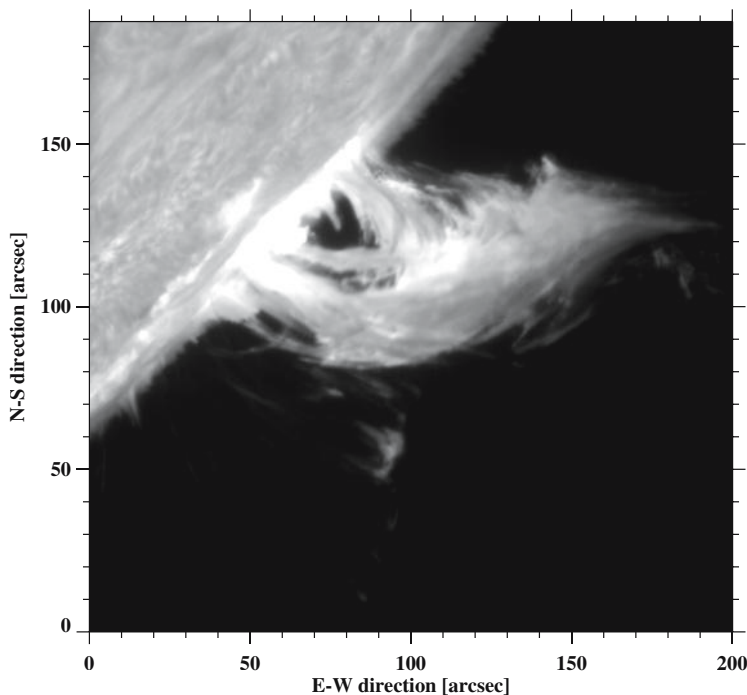
Figure 8.   High resolution Hα data taken with the 65 cm vacuum reflector on 2001 April 15 at 22:13 UT. The image shows major post-flare loops after a flare in solar active region NOAA 9415.

near the neutral line of a large δ-spot region. Subsequently, they found an increase of MMFs, flux emergence and cancellation, and in particular the disappearance of two penumbral segments located in opposite polarity regions on the north-south side of the δ-spot. In recent studies (Wang *et al.*, 2000a, 2002a, 2002b; Spirock, Yurchyshyn, and Wang, 2002), rapid and permanent changes of photospheric magnetic fields have been related to flare activity. The penumbral decay observed by Deng *et al.* (2004) is likewise interpreted as a rapid increase of the inclination angle of penumbral flux tubes, which gradually fade into the almost vertical fields of the sunspot umbrae. This sudden change of the magnetic field topology change led to an 11-degree long filament eruption and a full-halo coronal mass ejection (CME).

Some of the characteristics of the rapidly changing magnetic field topology have been related to the "magnetic breakout" model of Antiochos, Devore, and Klimchuk (1999), which can be summarized in the following statement: a magnetic breakout is the opening of initially low-lying sheared
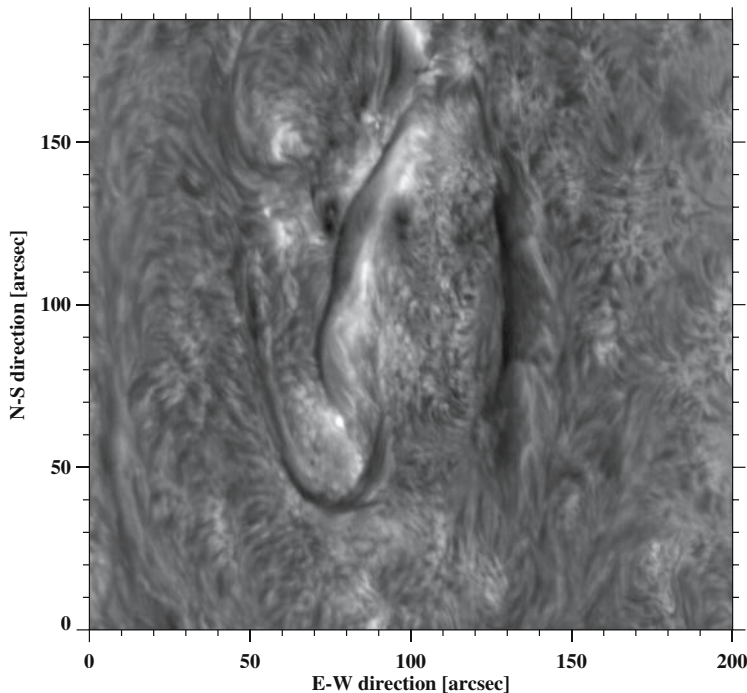
Figure 9.   High resolution Hα image of a sigmoidal filament in solar active region NOAA 10386 taken with the 65 cm vacuum reflector on 2003 June 17 at 19:54 UT.

fields, triggered by reconnection at a null point that is located high in the corona and that defines a separatrix enclosing the sheared fields. The disappearance of a penumbral segment, i.e., the change from more horizontal to almost vertical fields, might just be one of the signatures indicating the opening of magnetic field lines. Another well studied event, that fits the magnetic breakout model, was the "Bastille Day" event (Aulanier *et al.*, 2000), an M3 two-ribbon flare with subsequent CME, which occurred at 12:55 UT on 2000 July 14 in active region NOAA 8270 near disk center. In contrast to the magnetic breakout model involving multipolar magnetic field configurations, flares in bipolar regions with single neutral lines have been analyzed in terms of the classical "tether cutting" model (Sturrock, 1989).

   The aforementioned studies involving the magnetic breakout model or rapid changes in photospheric magnetic fields were focussed on highly energetic events, but there are reasons to believe that smaller events in the C- and lower M-class range will show a similar signature when observed with sufficient spatial and temporal resolution, e.g., Denker and Wang (1998)

presented a high-spatial resolution time sequence of a small δ-spot, where strong proper motions of small magnetic features, i.e., the head-on collision between a small sunspot with rudimentary penumbra and a group of small pores and magnetic knots, led to a C-class flare.

10. High-resolution two-dimensional spectropolarimetry

To advance our understanding of small-scale magnetic fields, higher light gathering capacity and spatial resolution are essential, which started several initiatives for a new generation of solar telescopes with 1-meter apertures and beyond. Major efforts are undertaken in the solar physics community to upgrade existing or build new ground-based observing facilities. These efforts include the 1-meter New Swedish Solar Telescope (NSST), which is already operational (Scharmer *et al.*, 2002); the German 1.5-meter GREGOR telescope (Volkmer *et al.*, 2003) and the 1.6-meter New Solar Telescope (NST) at BBSO (Goode *et al.*, 2003), which are currently under construction; and the 4-meter Advanced Technology Solar Telescope (ATST) under the stewardship of the National Solar Observatory (NSO), which approaches the end of its design and development phase (Keil *et al.*, 2003). All these new telescopes have one common goal, i.e., to study the solar atmosphere with high-spatial resolution and suite of post-focus instruments is currently being developed for two-dimensional spectropolarimetry. In the following paragraphs, we will use the design efforts at BBSO to illustrate some of the characteristics of these instruments.

High spatial, temporal, and spectral resolution are competing factors in precision spectro-polarimetry, which leads to the question, how to slice the multi-dimensional data set (two spatial and one spectral dimension, polarization, spectral line selection corresponding to atmospheric height, and temporal evolution)? The design goals of the visible-light imaging vector magnetograph (VIM) and the NIR imaging vector magnetograph (IRIM) at BBSO are high temporal and spatial resolution observations while maintaining moderate spectral resolution $\lambda/\delta\lambda$. Both instrument operate close to the diffraction limit $\alpha = \lambda/D$ of the 65 cm vacuum telescope and are prototypes for the post-focus instrumentation of next generation of solar telescopes. A detailed description of VIM and IRIM is presented by Denker *et al.* (2003). The imaging magnetographs use single Fabry-Pérot etalons as the passband defining elements and have a similar instrumental arrangement as the imaging magnetograph at Mees Solar Observatory, Haleakala, Maui (Mickey *et al.*, 1996). A correlation tracker and a high-order AO system with 97 actuators (Didkovsky *et al.*, 2003) provide full compensation of wave-front errors assuming fair seeing conditions with a Fried-parameter $r_0 > 6$ cm.

IRIM will be one of the first imaging spectro-polarimeters for NIR observations. Higher magnetic sensitivity (Zeeman splitting $\Delta\lambda_B \sim g\lambda^2 B$) and better seeing conditions $r_0 \sim \lambda^{6/5}$ are some of the advantages driving the development of NIR instrumentation. IRIM benefits from a larger isoplanatic angle $\theta_0 \sim \lambda^{6/5}$ and a higher Strehl ratio in the NIR, especially when operated in combination with the AO system. Diffraction limited observations over an extended field-of-view (FOV) can be achieved. Even for visible-light observations, the seeing induced cross-talk is minimized beyond the isoplanatic patch, since the tilt isoplanatic angle is substantially larger than the isoplanatic angle associated with higher order deformations.

The first Pt Si/Si NIR camera system for observations at BBSO was developed by the late Prof. Kosonocky of the New Jersey Institute of Technology (NJIT) Electrical and Computer Engineering (ECE) department. Wang *et al.* (1998) used this system to study the contrast of faculae at 1.6 μm. One of the design goals for IRIM is high light throughput without sacrificing spatial resolution. The maximum FOV of BBSO's 65 cm telescope is $240'' \times 240''$. The diffraction limit at 1,564.85 nm is $0.5''$. Therefore, a large format, 1024×1024 pixel detector is needed to exploit the capabilities of the 65 cm telescope. The next generation NIR detector will be a Complementary Metal Oxide Semiconductor (CMOS) focal plane array (FPA). IRIM is based on a 1024×1024 pixel, infrared Hg Cd Te/Cd Zn Te focal plane array developed by the Rockwell Science Center (RSC) in Thousand Oaks, California, which can provide high frame rates of up to 40 frames s^{-1}, high quantum efficiency ranging from 50% to 90% in the wavelength region from 900 to 2,500 nm, as well as a dynamic range better than 67 dB.

The study of magnetic fields on the sun is critical to the research of solar phenomena. Narrow pass band birefringent filters play a very important role in solar magnetographs, which measure the strength and direction of magnetic fields on the sun. Currently, most magnetographs operate in the wavelength range of visible light from 400 to 700 nm. IRIM will provide vector magnetograms with four times better spatial resolution and improved magnetic sensitivity, compared to the digital vector magnetograph (DVMG, Spirock *et al.*, 2001) at BBSO, due to resolved line profiles while maintaining a cadence of 1 to 4 minutes, which is necessary to follow the dynamics of small-scale magnetic fields. Usually, large sunspots possess strong magnetic fields in the order of 0.2 to 0.3 T. However, in other solar features such as plages or small bipoles in filament channels, the magnetic fields are only about 0.1 to 0.15 T. There are even weaker fields (< 0.1 T) in other structures such as the intranetwork magnetic fields. The Zeeman splitting induced by these fields is too small to be measured in the visible spectrum. For example, the DVMG system at the 25 cm vacuum refractor uses the Ca I line at $\lambda = 610.3$ nm with $g = 2$. If $B = 0.1$ T then

$\Delta\lambda = 47g\lambda^2 B = 3.5$ pm. However, for the NIR line Fe I 1,564.85 nm with $g = 3$, the Zeeman splitting $\Delta\lambda = 35$ pm is about an order of magnitude larger. Therefore, weaker magnetic field strengths can be measured more precisely using near infrared lines. The use of infrared lines as probes of solar magnetic features has been discussed in detail in Solanki, Rüedi, and Livingston (1992).

IRIM has been designed for observations in the near infrared at Fe I 1,564.85 nm and 1,565.29 nm ($g = 1.53$). The magnetograph consists of an interference prefilter, a polarization analyzer, a wavelength-tunable bire-fringent filter, a wavelength-tunable Fabry-Pérot filter, a CMOS FPA, and a real-time data processing system. IRIM is expected to achieve a clean narrow pass band of 11.3 pm. It can be tuned across a spectral line to obtain line profiles of a two-dimensional field of view. The FWHM of the interference prefilter is about 3 nm. It is followed by an innovative Lyot-filter for near infrared observations (Wang *et al.*, 2000c). The FWHM of the Lyot-filter is 0.25 nm. Finally, a Fabry-Pérot filter manufactured by IC Optical Systems (formerly Queensgate Instruments) restricts the pass band to 11.3 pm. The etalon has a clear aperture of 70 mm, the free spectral range is 0.52 nm, the finesse is about 60, and the transmission is expected to be better than 75%.

Since the imaging magnetograph system records a multi-dimensional data set (two spatial dimensions, wavelength, polarization, and time), it is an ideal case to explore parallel processing as an option to obtain real-time magnetic field measurements. Real-time data analysis will be the first step towards easy available high-level data products. On-site data processing of external data requests requires parallel processing of data. The overall goal is to provide well calibrated data products in a manner that one now routinely obtains with space-based experiments. The active region monitor (ARM, Gallagher *et al.*, 2001) at BBSO is an example of the visualization of high-level data products. A common concern related to real-time data processing is a potential distrust in processed data and an overemphasis on software development rather than scientific conquest. However, cutting-edge research can only be achieved with cutting-edge instruments while educating the next generation of solar physicists to obtain an intimate knowledge of these instruments and using them to solve scientific problems.

11. Real-time image reconstruction

In recent years, post-facto image processing algorithms have been developed to achieve diffraction limited observations of the solar surface. We are using the speckle masking imaging technique, in combination with a parallel computer built by 32 1.8 GHz AMD Athlon processors, to yield

near real-time time-series with a cadence of approximately 1 min, which is sufficient to resolve the evolution of solar surface phenomena, such as granulation, pores, sunspots and including the fine-structure of sunspot umbrae and penumbrae. The predecessor of this system has been described in Denker, Yang, and Wang (2001). The first images reconstructed by the new RTIR system are shown in Figures 3 and 4.

Since a speckle image consists of a mosaic of reconstructed isoplanatic patches, there is in principle no limitation of the FOV which is only limited by the detector size and the computational effort (Denker, 1998). This is one advantage of speckle imaging over AO which corrects only over a FOV comparable to the isoplanatic patch, even though the image quality improves over larger FOVs. On the other side, speckle imaging requires a relatively high signal-to-noise ratio for the short-exposure images which limits its application to narrow band filtergrams with pass bands of about 10 pm. The practical limits of the speckle masking method have probably been reached in a study of granular dynamics by Hirzberger *et al.* (2001) who achieved a spectral resolution of 3.5 pm and a spatial resolution of about 0.5″. Speckle masking imaging and AO are complementary with respect to spectral resolution and FOV. However, they could be combined if a solution is found for non-ergodic speckle transfer functions (STFs).

The power of parallel computing has not yet been exploited in solar physics. Supercomputers have been used for numerical calculations in astrophysics, however, they cannot be used for real-time data processing because the observational data cannot be transferred to the supercomputer centers in real-time. Usually, only a few data sets are analyzed per year, and only at the end of this process does one discover if something really interesting has been captured. The time-lag between the observation and the data analysis is far too long for any sort of rapid response, such as would be needed for space weather warnings and flare forecasting. Furthermore, the time lag renders the whole scientific enterprize less efficient than it needs to be, considering today's computer technology. Parallel processing of solar data will literally provide a new window through which we can observe the sun in exquisite detail and study the evolution of granulation, sunspots, prominences, and flares. The underlying data processing algorithms are understood, but the complexity is such that only parallel computing enables us to visualize and interpret large data sets effectively.

References

Antiochos, S. K., Devore, C. R., and Klimchuk, J. A., 1999: *Astrophys. J.* **510**, 485.

Athay, R. G., 2000: *Solar Phys.* **197**, 31.

Aulanier, G., DeLuca, E. E., Antiochos, S. K., McMullen, R. A., and Golub, L., 2000: *Astrophys. J.* **540**, 1126.

Bendlin, C. and Volkmer, R., 1995: *Astron. Astrophys. Suppl. Ser.* **112**, 371.

Bray, J. R. and Loughhead, R. E., 1964: *Sunspots*, Chapman and Hall, London.

Canfield, R. C., Hudson, H. S., and McKenzie, D. E., 1999: *Geophys. Res. Lett.* **26**, 627.

Choudhuri, A. R., 1986: *Astrophys. J.* **302**, 809.

Degenhardt, D. and Wiehr, E., 1991: *Astron. Astrophys.* **252**, 821.

Degenhardt, D. and Wiehr, E., 1994: *Astron. Astrophys.* **287**, 620.

del Toro Iniesta, J. C., Bellot Rubio, L. R., and Collados, M., 2001: *Astrophys. J. Lett.* **549**, 139.

Deng, N., Liu, C., Yang, G., Wang, H., and C. Denker, C., 2004, *Astrophys. J.*, submitted

Denker, C., 1997: *Astron. Astrophys.* **323**, 599.

Denker, C., 1998: *Solar Phys.* **180**, 81.

Denker, C. and Wang, H., 1998, *Astrophys. J.* **502**, 493.

Denker, C., de Boer, C. R., Volkmer, R., and Kneer, F., 1995: *Astron. Astrophys.* **296**, 567.

Denker, C., Johannesson, A., Goode, P. R., Marquette, W., Wang, H., and Zirin, H., 1998: *Solar Phys.* **184**, 87.

Denker, C., Yang, G., and Wang, H., 2001: *Solar Phys.* **202**, 63.

Denker, C., Ma, J., Wang, J., Didkovsky, L. V., Varsik, J. R., Wang, H., and Goode, P. R., 2003: *Proc. SPIE* **4853**, 223.

Didkovsky, L. V., Dolgushyn, A., Marquette, W. H., Nenow, J., Varsik, J., Goode, P. R., Hegwer, S. L., Ren, D., Fletcher, S., Richards, K., Rimmele, T., Denker, C., and Wang, H., 2003: *Proc. SPIE* **4853**, 630.

Ellerman, F., 1917: *Astrophys. J.* **46**, 298.

Ewell, M. W., 1992: *Solar Phys.* **137**, 215.

Gallagher, P. T., Denker, C., Yurchyshyn, V., Spirock, T., Qiu, J., Marquette, W. H., Wang, H., and Goode, P. R., 2001: *Ann. Geophys.* **20**, 1105.

García de la Rosa, J. I., 1987: *Solar Phys.* **112**, 49.

Georgakilas, A. A., Koutchmy, S., and Cristopoulou, E. B., 2001: *Astron. Astrophys.* **370**, 273.

Giovanelli, R., 1982: *Solar Phys.* **80**, 21.

Goode, P. R., Denker, C., Didkovsky, L. I., Kuhn, J. R., and Wang, H., 2003: *J. Korean Astron. Soc.* **36**, 125.

Grossmann-Doerth, U., Schüssler, M., and Steiner, O., 1998: *Astron. Astrophys.* **337**, 928.

Grossmann-Doerth, U., Schüssler, M., Sigwarth, M., and Steiner, O., 2000: *Astron. Astrophys.* **357**, 351.

Harvey, K. L. and Martin, S. F., 1973: *Solar Phys.* **28**, 61.

Hermans, L. M. and Martin, S. F., 1986: in A. Poland (ed.), *Coronal and Prominence Plasmas*, NASA Conf. Publ., Vol. 2442, p. 369.

Hirzberger, J. and Kneer, F., 2001: *Astron. Astrophys.* **378**, 1078.

Hirzberger, J., Koschinsky, M., Kneer, F., and Ritter, C., 2001: *Astron. Astrophys.* **367**, 1011.

Hofmann, J., Deubner, F. L., Fleck, B., and Schmidt, W., 1994: *Astron. Astrophys.* **284**, 269.

Johannesson, A. and Zirin, H., 1996: *Astrophys. J.* **471**, 510.

Keil, S. L., Rimmele, T., Keller, C. U., Hill, F., Radick, R. R., Oschmann, J. M., Warner, M., Dalrymple, N. E., Briggs, J., Hegwer, S. L., and Ren, D., 2003: *Proc. SPIE* **4853**, 240.

Knobloch, E. and Weiss, N. O., 1984: *Mon. Not. Roy. Astron. Soc.* **207**, 203.

Kuhn, J. R., Lin, H., and Loranz, D., 1991: *Publ. Astron. Soc. Pac.* **103**, 1097.

Leka, K. D. and Skumanich, A., 1998: *Astrophys. J.* **507**, 454.

Leka, K. D. and Steiner, O., 2001: *Astrophys. J.* **552**, 354.

Lites, B. W., Skumanich, A., and Scharmer, G. B., 1990: *Astrophys. J.* **355**, 329.

Livi, S. H. B., Wang, J., and Martin, S. F., 1985: *Austr. J. Phys.* **38**, 855.

Maltby, P., 1964: *Astrophys. Norvegica* **8**, 205.

Martin, S. F., Livi, S. H. B., and Wang, J., 1985: *Austr. J. Phys.* **38**, 929.

Matres, M. J. and Bruzek, A., 1977: in A. Bruzek and C. J. Durrant (eds.), *Illustrated Glossary for Solar and Solar Terrestrial Physics*, Reidel Publishing Company, p. 67.

Mickey, D. L., Canfield, R. C., Labonte, B. J., Leka, K. D., Waterson, M. F., and Weber, H. M., 1996: *Solar Phys.* **168**, 229.

Moore, R. L., Tang, F., Bohlin, J. D., and Golub, L., 1977: *Astrophys. J.* **218**, 286.

Müller, D. A. N., Schlichenmaier, R., Steiner, O., and Stix, M., 2002, *Astron. Astrophys.* **393**, 305.

Nindos, A. and Zirin, H., 1998: *Solar Phys.* **182**, 381.

Parker, E. N., 1978: *Astrophys. J.* **221**, 368.

Parker, E. N., 1979: *Astrophys. J.* **234**, 333.

Qiu, J., Ding, M. D., Wang, H., Denker, C., and Goode, P. R., 2000: *Astrophys. J. Lett.* **544**, 157.

Rimmele, T. R., 1994: *Astron. Astrophys.* **290**, 972.

Rimmele, T. R., 1995: *Astron. Astrophys.* **298**, 260.

Rucklidge, A. M., Schmidt, H. U., and Weiss, N. O., 1995, *Mon. Not. Roy. Astron. Soc.* **273**, 491.

Rüedi, I., Solanki, S. K., and Keller, C. U., 1999: *Astron. Astrophys.* **348**, 37.

Scharmer, G. B., Gudiksen, B. V., Kiselman, D., Löfdahl, M. G., and Rouppe van der Voort, L. H. M., 2002: *Nature* **420**, 151.

Schlichenmaier, R., 1999: in T. Rimmele, K. S. Balasubramaniam, and R. Radick (eds.), *High Resolution Solar Physics*, ASP Conf. Ser., Vol. 183, p. 91.

Schlichenmaier, R., 2003: in A. Pevtsov and H. Uitenbroek (eds.), *Current Theoretical Models and Future High Resolution Solar Observations*, ASP Conf. Ser., Vol. 286, p. 211

Schlichenmaier, R. and Collados, M., 2002: *Astron. Astrophys.* **381**, 668.

Schlichenmaier, R., Jahn, K., and Schmidt, H. U., 1998a: *Astrophys. J. Lett.* **493**, 121.

Schlichenmaier, R., Jahn, K., and Schmidt, H. U., 1998b: *Astron. Astrophys.* **337**, 897.

Schlichenmaier, R., Bruls, J., and Schüssler, M., 1999: *Astron. Astrophys.* **349**, 961.

Schmidt, W. and Schlichenmaier, R., 2000: *Astron. Astrophys.* **364**, 829.

Schmidt, W., Hofmann, A., Balthasar, H., Tarbell, T. D., and Frank, Z. A., 1992: *Astron. Astrophys.* **264**, 27.

Schmieder, B., del Toro Iniesta, J. C., and Vázquez, M., 1997: *Advances in the Physics of Sunspots*, ASP Conf. Ser., Vol. 118.

Schüssler, M., 2001: in M. Sigwarth (ed.), *Advanced Solar Polarimetry*, ASP Conf. Ser., Vol. 236, p. 343.

Severny, A. B., 1956: *Observatory* **76**, 241.

Shine, R. A., Title, A. M., Tarbell, T. D., Smith, K., Frank, Z. A., and Scharmer, G., 1994: *Astrophys. J.* **430**, 413.

Simon, G.W. and Leighton, R.B., 1964: *Astrophys. J.* **140**, 1120.

Sobotka, M. and Sütterlin, P., 2001: *Astron. Astrophys.* **380**, 714.

Sobotka, M., Bonet, J. A. and Vázquez, M., 1993: *Astrophys. J.* **415**, 832.

Sobotka, M., Brandt, P. N., and Simon, G. W., 1997a: *Astron. Astrophys.* **328**, 682.

Sobotka, M., Brandt, P. N., and Simon, G. W., 1997b: *Astron. Astrophys.* **328**, 689.

Sobotka, M., Brandt, P. N., and Simon, G. W., 1999: *Astron. Astrophys.* **348**, 621.

Solanki, S. K., Rüedi, I., and Livingston, W., 1992: *Astron. Astrophys.* **263**, 312.

Spirock, T., Denker, C., Chen, H., Chae, J., Qiu, J., Varsik, J., Wang, H., Goode, P. R., and Marquette, W., 2001: in M. Sigwarth (ed.), *Advanced Solar Polarimetry*, ASP Conf. Ser., Vol. 236, p. 65.

Spirock, T. J., Yurchyshyn, V., and Wang, H., 2002, *Astrophys. J.* **572**, 1072.

Spruit, H. C., 1979: *Solar Phys.* **61**, 363.

Stanchfield, D. C. H., Thomas, J. H., and Lites, B. W., 1997: *Astrophys. J.* **477**, 485.

Steiner, O., Grossmann-Doerth, U., Knölker, M., and Schüssler, M., 1998: *Astrophys. J. Lett.* **495**, 468.

Steiner, O., 2000: *Solar Phys.* **196**, 245.

Steiner, O., Hauschildt, P. H., and Bruls, J., 2001: *Astrophys. J. Lett.* **372**, 13.

Sterling, A. C., 2000: *Solar Phys.* **196**, 79.

Sturrock, P. A., 1989, *Solar Phys.* **121**, 387.

Thomas, J. H., 1988: *Astrophys. J.* **333**, 407.

Thomas, J. H. and Weiss, N. O., 1992: *Sunspots: Theory and Observations*, Cambridge University Press, Cambridge.

Title, A. M., Frank, Z. A., Shine, R. A., Tarbell, T. D., Topka, K. P., Scharmer, G., and Schmidt, W., 1993: *Astrophys. J.* **403**, 780.

Tritschler, A. and Schmidt, W., 1997: *Astron. Astrophys.* **321**, 643.

Volkmer, R., von der Lühe, O., Kneer, F., Staude, J., Hofmann, A., Schmidt, W., Sobotka, M., Soltau, D., Wiehr, E., Wittmann, A., and Berkefeld, T., 2003: *Proc. SPIE* **4853**, 360.

Wang, H., 1988: *Solar Phys.* **116**, 1.

Wang, H., 1998: *Astrophys. J.* **509**, 461.

Wang, H., Tang, F., Zirin, H., and Wang, J., 1996: *Solar Phys.* **165**, 223.

Wang, H., Spirock, T., Goode, P. R., Lee, C. Y., Zirin, H., and Kosonocky, W., 1998: *Astrophys. J.* **495**, 957.

Wang, H., Goode, P. R., Denker, C., Guo, Y., Yurchyshyn, V., Nitta, N., Gurman, J. B., St. Cyr, C., and Kosovichev, A. G., 2000a, *Astrophys. J.* **536**, 971.

Wang, H., Ji, H., Schmahl, E. J., Qiu, J., Liu, C., and Deng, N., 2002a, *Astrophys. J. Lett.* **580**, 177.

Wang, H., Spirock, T. J., Qiu, J., Ji, H., Yurchyshyn, V., Moon, Y.-J., Denker, C., and Goode, P. R., 2002b, *Astrophys. J.* **576**, 497.

Wang, J., Wang, H., Tang, F., Lee, J., and Zirin H., 1995: *Solar Phys.* **160**, 277.

Wang, J., Li, W., Denker, C., Lee, C. Y., Wang, H., Goode, P. R., MacAllister, A., and Martin, S., 2000b: *Astrophys. J.* **530**, 1071.

Wang, J., Wang, H., Spirock, T. J., Lee, C. Y., Ravindra, N. M., Ma, J., Goode, P. R., and Denker, C., 2000c: *Opt. Eng.* **40/6**, 1016.

Westendorp Plaza, C., del Toro Iniesta, J. C., Ruiz Cobo, B., Martínez Pillet, V., Lites, B. W., and Skumanich, A., 2001: *Astrophys. J.* **547**, 1130.

Wiehr, E. and Degenhardt, D., 1992: *Astron. Astrophys.* **259**, 313.

Wiehr, E. and Degenhardt, D., 1994: *Astron. Astrophys.* **287**, 625.

Withbroe, G. L. and Noyes, R. W., 1977: *Ann. Rev. Astron. Astrophys.* **15**, 363.

Yang, G., Xu, Y., Wang, H., and Denker, C., 2003: *Astrophys. J.* **597**, 1190.

Zwaan, C., 1987: *Ann. Rev. Astron. Astrophys.* **25**, 83.

SOLAR FLARES – OBSERVATIONS AND THEORY

B. VRŠNAK

Hvar Observatory, Faculty of Geodesy, University of Zagreb
Kačićeva 26, HR-10000 Zagreb, Croatia

Abstract. Basic properties of solar flares and associated phenomena are presented. Morphological characteristics, spectral properties of the emission output, and temporal evolution common to most flares are summarized, including basic physical processes underlying the described phenomena. Various classification schemes are presented as an introduction to the overview of the actual physical comprehension of the solar flare phenomenon. Basic theoretical concepts are described, focusing separately on the energy storage and energy release processes. The mechanism of fast magnetic reconnection is emphasized since it plays a central role in the energy release process. The non-hydrodynamical processes essential for comprehension of solar flares – the plasma instabilities and particle acceleration process – are described as an indivisible part of the reconnection process. Finally, the interacting-flux flares and two-ribbon flares are used to illustrate some details of flare modeling.

1. Introduction: general aspects

In the outer layers of the Sun the energy is transported towards the solar surface dominantly by convection, which gives rise to a differential rotation. A part of the transported energy (only about 0.1%) is stored into the magnetic field due to the coupling of the magnetic field with flows organized in differential rotation, or with large and small scale eddies. The coupling is caused by a large magnetic Reynolds number because of which the magnetic field is "frozen-in" the plasma, i.e., flows that are perpendicular to the magnetic field drag the field in the direction of the flow (e.g., Priest, 1982*)[1]. In this way field lines become kinked, which implies that $\nabla \times \mathbf{B} \neq \mathbf{0}$, i.e., electric currents $\mathbf{j} = \nabla \times \mathbf{B}/\mu_0$ are induced. This means also that free energy is being stored in the magnetic field (MHD dynamo).

---

[1] Note that in the following only some representative citations will be offered to help finding further references, rather than to give a complete list of references regarding a given issue. References of this type will be denoted by an asterisk instead of writing standard phrases like "chiefly", "e.g.", "and references therein", etc.

As the magnetic fields emerge across the solar surface the accumulated free energy is partly spent for coronal heating, whereas a part remains stored in the force-free coronal fields (Priest, 1982*). The field is further stressed by surface motions, and the resulting Poynting flux supplies the corona with additional free energy, part of which is again instantaneously released on small spatial scales to heat the corona. The rest continues to accumulate until a given magnetic structure becomes unstable, abruptly releasing stored energy in violent processes called solar flares and coronal mass ejections. This paper is focused on the solar flare phenomenon, summarizing basic observational and theoretical aspects.

2. Observational aspects

2.1. MORPHOLOGY AND EVOLUTION

Most generally, a solar flare can be defined as an abrupt release of energy accumulated in non-potential coronal magnetic fields. In flares the coronal plasma is heated up to $\approx 4 \times 10^7$ K, particles are accelerated to relativistic energies, violent mass motions and MHD blast waves are launched. Due to a flare, solar soft X-ray and radio emission can increase more than $10\,000$ times. The total energy liberated varies from, say, 10^{22} J in subflares to several 10^{25} J in the largest events. Flaring can permeate coronal volumes of a typical dimension ranging from several thousand km up to several thousand Mm, and can last from seconds to hours. Flares, especially those of long duration, are closely related to huge eruptions, called coronal mass ejections (CMEs). Such an eruption ejects a magnetic flux of 10^{23} Wb into interplanetary space, carrying along 10^{13} kg of coronal plasma at a speed in the order of 1000 $\mathrm{km\,s^{-1}}$.

Figure 1 shows a flare as seen in various spectral bands. When observed in the chromospheric spectral lines, a flare is characterized by the appearance of bright irregular patches, or sometimes more regular elongated ribbons expanding away from the magnetic inversion line[2] (Fig. 1a). The brightest elements, flare kernels, are often co-spatial and synchronized with the hard X-ray (HXR) emission (Kitahara and Kurokawa, 1990; Wang et al., 2000) that is excited by electron beams precipitating from the coronal energy release site (Brown, 1971; Li et al, 1993; Veronig et al., 2002a*). However, sometimes Hα kernels are not associated with prominent HXR emission (Kitahara and Kurokawa, 1990), indicating that some other agent transports the energy from the energy release site, most probably thermal conduction (Rust et al., 1985*; Rust, 1996*).

---

[2] Lines where the photospheric magnetic field changes sign; also called neutral lines.
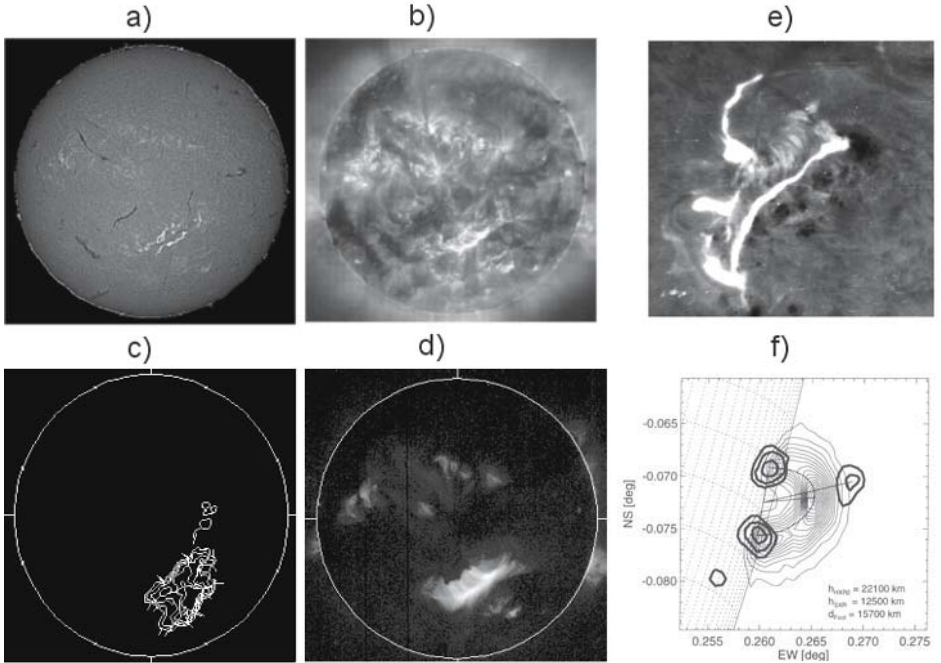
Figure 1.   Flare morphology. a)–d) Spotless two-ribbon flare of 12 September 2000 seen in: a) Hα line (Kanzelhöhe Solar Observatory, courtesy W. Otruba), b) extreme-ultraviolet (EIT-SOHO), c) radio range, type IV and moving type IV sources are indicated as IV and IVm (Nancay Radio Heliograph, 327 MHz, courtesy K.-L. Klein), d) soft X-rays (SXT-Yohkoh). e) Details of a two-ribbon flare in a sunspot group (12 July 1982, Hvar Observatory), PFL stands for cold postflare loops, parts of flare ribbons protruding over major umbrae are denoted as Z; f) "Masuda flare" of 13 January 1992 (adopted from Aschwanden et al. 1996a; thin lines depict the soft X-ray loop (SXT-Yohkoh), hard X-ray isolines (HXT-Yohkoh) revealing two foot-point sources and a loop-top source are drawn bold.

After being heated by electron beams and/or thermal conduction (Fisher, 1989; Veronig et al., 2002a*), chromospheric and transition region plasma is violently convected upwards at velocities of several hundreds of $\mathrm{km\,s^{-1}}$, which is usually called "chromospheric evaporation" or "ablation" (Antonucci et al., 1999*). The magnetic flux tubes filled with hot and dense ablated plasma become visible in extreme ultraviolet spectral lines (EUV) and soft X-rays (SXR), revealing relaxed magnetic field lines that connect flare kernels located in opposite magnetic polarities (Fig. 1b, c, and f). Sometimes HXR emission is observed (Fig. 1f) also from the loop-tops (Masuda et al., 1994; Shibata et al., 1995; Aschwanden et al., 1996a; Nitta et al., 2001; Uchida et al., 2001*).

The hot and dense plasma is rapidly cooling due to radiative losses: the
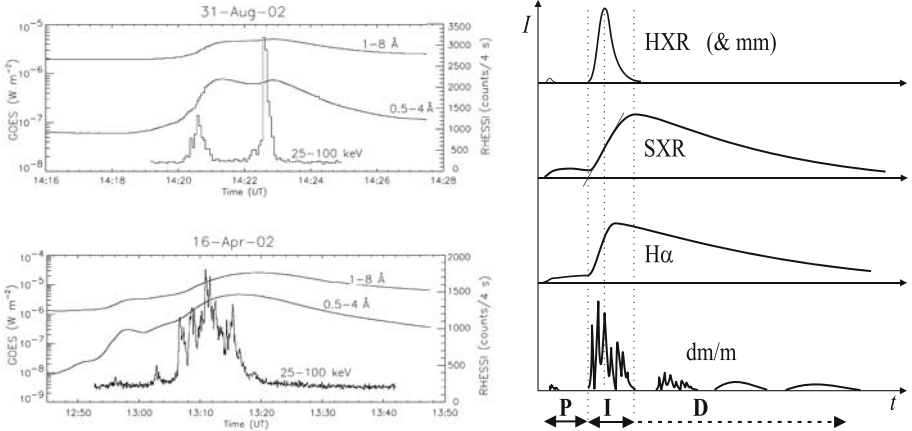
Figure 2. Temporal evolution of radiative output. *Left:* HXR (RHESSI) and SXR (GOES) light curves of an impulsive (top) and gradual (bottom) flare (courtesy A. Veronig). Note the difference in the *x*-axis scale. *Right:* Schematic presentation of light curves in various spectral channels.

emissivity is proportional to the electron density squared (n_e^2), and furthermore, at the actual temperatures it increases with decreasing temperature (Priest, 1982*). So, the radiative energy loss is "accelerated" because the decreasing temperature implies also a density increase.

2.2. TEMPORAL AND SPECTRAL CHARACTERISTICS

Flares show a large variety of duration and size, and consequently, the energy release rate and total liberated energy vary significantly from flare to flare. This can be seen most directly in a a wide palette of "light curves" recorded in spectral ranges affected by the flare emission (Kundu et al., 1994*).

In some flares the energy is released very impulsively, within seconds, whereas in others the energy release lasts for tens of minutes, sometimes even for hours (Fig. 2). However, rise times (and durations) of SXR bursts are usually longer for larger peak fluxes,[3] so a more appropriate measure of the impulsiveness is the ratio of the peak flux and the burst rise time (Pearson et al., 1989). For example, a flare with the rise time of $t = 1$ min which achieved C5 peak flux is less impulsive than a X5 flare of a rise time $t = 10$ min.

----
[3] According to the SXR-burst peak flux in the 1–8 Å channel of the GOES satellite (Donelly and Unzicker, 1974) flares are divided into SXR importance-classes A, B, C, M, and X, representing the logarithmic-scale intervals 10^{-8}–10^{-7}, 10^{-7}–10^{-6}, 10^{-6}–10^{-5}, 10^{-5}–10^{-4}, and $> 10^{-4}$ W m^{-2}, respectively. For example, C5.4 means that the associated 1–8 Å peak flux reached 5.4×10^{-6} W m^{-2}.
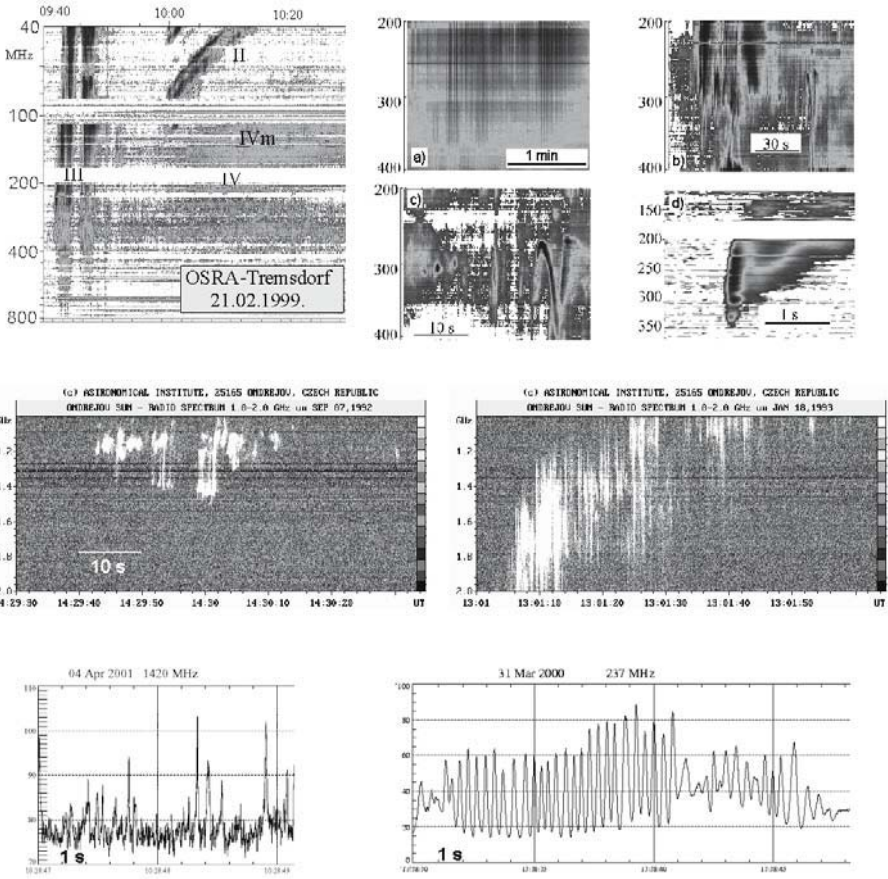
Figure 3. Radio time–spectral hierarchy. *Top-left*: Radio-burst types – a typical dynamic spectrum: type III, II, IV, and IVm radio bursts. *Top-left*: Four examples of dm-m range radio fine structures. a) broad-band pulsations; b) fast drifting bursts; c) narrow-band spiky bursts, narrow-band fast-drift bursts, and a U-burst; d) spiky burst with type III/V burst (note the difference in scales at the *x*-axes and *y*-axes (Astrophys. Inst. Potsdam, courtesy H. Aurass). *Middle*: Two examples of fine structures in a μw-burst at cm-wavelengths (Ondřejov Observatory, courtesy M. Karlický). *Bottom*: Super-fast structures and pulsations recorded at a single frequency (Trieste Observatory, courtesy J. Magdalenić and P. Zlobec).

There is a certain confusion regarding the impulsive/gradual attribute. Sometimes the term *gradual* is reserved only for flares which develop slowly and show primarily thermal characteristics, i.e., signatures of nonthermal electrons are weak or absent. In this respect a flare with an extended HXR emission, associated also with radio type III bursts and other impulsive radio features, is classified as impulsive.

The dynamic radio spectrum of an impulsive flare usually shows a large

variety of fine structures (Fig. 3), most of which can be attributed to various forms of coherent radio emission excited by electron beams or other forms of nonthermal electrons (Krüger, 1979*; McLean and Labrum, 1985*; Benz, 1993*). Such flares also show prominent HXR and microwave (μw) bursts (Fig. 3-middle), often fragmented into a number of so-called elementary flare bursts (de Jager, 1986*; Kaufmann et al., 2001*; Aschwanden, 2002*; Raulin et al., 2003*). Each elementary burst lasts around 0.1–10 s during which some 10^{35} electrons are accelerated to energies >10 keV releasing an energy of about 10^{19}–10^{20} J (de Jager, 1986*).

Radio observations reveal still finer structures, sometimes shorter than 10 ms (Fig. 3-bottom), being close to the lower limit of temporal resolution of present instruments. A typical narrow-band radio feature of this kind are so-called "spikes" (Güdel and Benz, 1990; Fleishman and Melnikov, 1998; Zlobec et al., 2003). At frequencies around $f = 1000$ MHz a typical duration (at half-power) is $\approx$10 ms and the relative spectral bandwidth is typically $\Delta f / f \approx 1\%$. In the dynamic spectrum spikes appear in "clouds", each of which corresponds to one or more HXR elementary flare bursts (Aschwanden et al., 1995; Aschwanden and Benz, 1997). There are also broader-band spectral features, which sometimes show a periodic or quasiperiodic appearance with periods down to 10 ms (Magdalenić et al., 2002).

Impulsive flares with prominent nonthermal signatures generally occur in highly stressed strong field regions associated with sunspots (Hagyard et al., 1984; Mayfield and Lawrence, 1985; Gaizauskas and Švestka, 1987; Gary et al., 1987*; Hagyard, 1988; Hofmann et al., 1992; Sakurai, 1993). Especially powerful energy release takes place when the magnetic field emanating directly from the umbra of a major sunspot becomes involved in the process, which is revealed by the appearance of bright Hα emission in the umbra (Z-flares; Vršnak et al., 2000*). Sometimes such flares can be observed also in white light and γ-rays, revealing nuclear reactions (Ramaty and Murphy, 1987*).[4] These are the most powerful solar flares. On the other hand, flares that take place in spotless active regions (G-flares) are often very gradual, showing merely thermal signatures (Ruždjak et al., 1989*).

Significant differences in flare characteristics can also appear due to the nature of field lines included in the energy release process. If only closed magnetic loops are involved, the accelerated particles stay trapped in the flaring region. Trapped electrons emit a radio continuum which is usually called type IV emission (Fig. 3), frequently superposed by narrow- and broad-band fine structures (Krüger, 1979*; McLean and Labrum, 1985*; Benz, 1993*; Karlický, 2003b*; Magdalenić et al., 2004). If field lines extend

---

[4] In fact, the first reported solar flare, observed by Carrington and Hodgson in 1859, was a white-light flare.

over large distances, electron beams can propagate to other active regions (Aurass and Klein, 1997), possibly triggering a sympathetic flare (Švestka, 1976*; Karlický, 1988). If "open" field lines are included, beams of accelerated particles can propagate to the high corona (Zlobec et al., 1990; Poqueruse and McIntosh, 1995; Vršnak et al., 2000*), or eventually escape to interplanetary (IP) space (Reiner et al., 2000*; Dröge, 2003*; Krucker, 2003*; Reiner, 2003*). Electron beams that propagate along open field lines at mildly relativistic speeds ($\approx c/3$) cause type III radio emission (McLean and Labrum, 1985*), which in the dynamic spectrum forms steep (fast-drifting) emission lanes (Fig. 3), sometimes extending to low frequencies that correspond to IP space plasma densities (see Fig. 7b in Sect. 2.5). If the beam is guided by closed magnetic loops, in the dynamic spectrum the emission takes the form of an inverted U-shaped emission lane (Fig. 3).

In spite of a large temporal/spatial diversity, many flares develop a similar overall evolutionary sequence. A typical sequence includes a precursor, an impulsive phase, and a decay phase, denoted in Fig. 2 as P, I, and D, respectively. Note that such a division is to a great deal provisional and there are different modalities employed by various authors, which brings in a certain degree of confusion. This holds especially for the impulsive phase. For example, in some cases the HXR phase shows two components – one very impulsive (like the one in left-top panel of Fig. 2) superposed onto a more extended one (like in the left-bottom panel of Fig. 2). Some authors use the term impulsive phase only for the first component, and the second component is called the gradual or main (HXR) phase. On the other hand, some authors use the term gradual, main, or thermal phase for the period after the HXR burst, during which the energy release still goes on, but has primarily thermal characteristics.

The precursor is a distinct increase of SXR emission, observed typically some 10 min before the onset of the main SXR burst. Although it shows dominantly thermal characteristics, sometimes a weak HXR and/or radio emission is observed (Tappin, 1991; Xie et al., 1994). Sometimes the precursor is simply a subflare that triggers a larger flare. Some authors also consider the so-called preflare phase as a distinct flare stage (different from the precursor), representing a gradual growth of SXR and cm/dm μw emission immediately before the steep rise of SXR emission (i.e., before the onset of the impulsive phase).

The impulsive phase is dominated by nonthermal signatures – prominent HXR and mm/cm μw emission, type III radio bursts, and fast-drifting narrow-band radio fine structures at decimeter-to-meter wavelengths (usually denoted as DCIM). The HXR burst usually shows a power-law spectrum, revealing a power-law distribution of precipitating electrons (Brown, 1971; Li et al, 1993; Veronig et al., 2002a*). In the course of time the

spectrum gradually becomes harder, i.e., the slope of the power-law spectrum becomes less steep (Brown et al., 1981*). The microwave burst at mm/cm-wavelengths (Fig. 2-right) is strongly correlated with the HXR-burst (Kundu et al., 1994*; Kosugi et al., 1988), whereas in the cm/dm range it becomes somewhat more prolonged. The Hα emission usually attains maximum between the peak and the end of the HXR burst, somewhat before the peak of SXR burst (Veronig et al., 2002b).

During the impulsive phase a coronal shock wave is sometimes launched, which is observed (Fig. 3) in the radio dynamic spectrum as type II solar burst (McLean and Labrum, 1985*). When the shock is strong enough, and is ignited by a flare that is located at the outskirts of an active region, it can cause a large-amplitude chromospheric wave-signature called flare-wave or Moreton-wave (Moreton and Ramsey, 1960; Uchida et al., 1973; Warmuth et al., 2001*; Vršnak et al., 2002*).

The decay phase is, generally speaking, the time after the SXR burst maximum. In this period the flare plasma becomes dominantly thermal, but the radio continuum emission shows one or more post-maximum increases, revealing (successively weaker) revivals of electron acceleration. The evaporation becomes weak or ceases, although in long-duration events can be going on for hours (Schmieder et al., 1990; Czaykowska et al., 2001). The SXR-emitting loops are cooling, and sometimes, especially in large flares, they become visible in the chromospheric spectral lines ("postflare loops"; see Fig. 1e).

2.3. MOSAIC OF BASIC PROCESSES

In Fig. 4 we summarize basic features of the energy release and energy transport processes, common to most flares.

Flare kernels usually appear at both sides of the magnetic inversion line. This very basic fact provides an essential information: it implies that oppositely oriented magnetic field lines are involved in the energy release process. Another important information about the nature of the energy release in flares comes from radio observations. Fast-drifting bursts observed during the impulsive phase in the 200–2000 MHz range (denoted as DCIM in Fig. 4; see examples in Fig. 3), drifting to lower as well as to higher frequencies, reveal electron beams propagating upwards and downwards. This indicates that the primary energy release takes place in the corona, at a height usually between 10^4 and 10^5 km (Bastian et al., 1998*). Such a view is supported also by the relationship between these radio features and HXR emission (Aschwanden et al., 1995; Aschwanden and Benz, 1997), as well as by relative delays of the HXR emission at successively lower energies, i.e., delays of slower electrons relative to faster ones (Aschwanden et al., 1996b; Aschwanden, 2002*).
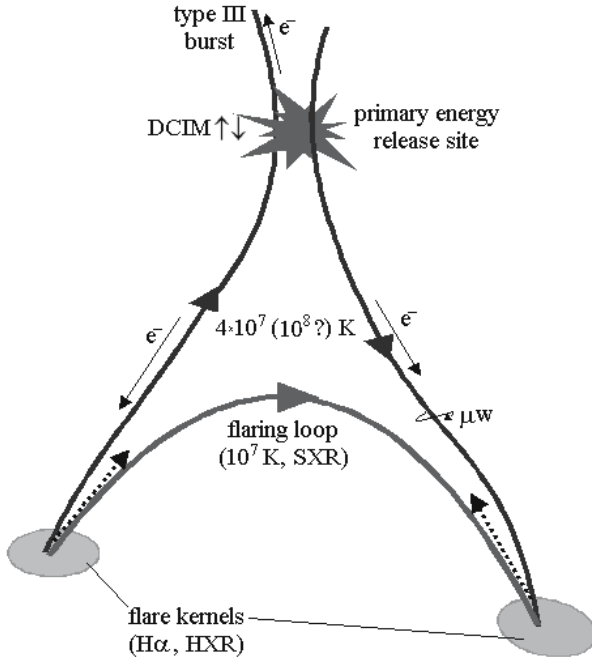
Figure 4.   Summary of basic processes common to most flares. Two interacting magnetic field lines are drawn together with the resulting flaring loop (bold arrow-lines). Electron beams are depicted by thin arrows and e$^-$. Chromospheric evaporation from the flare kernels is indicated by thick dotted arrows.

Flares in which the primary energy release site is located at low heights are usually more powerful and impulsive than those having the energy release site at large heights. This can be straightforwardly interpreted as a consequence of weakening of the magnetic field with height (see Sect. 3.1).

If electron beams produced at the primary energy release site can escape outwards, they excite type III radio bursts (Fig. 3). On the other hand, the accelerated electrons attached to the closed field lines stay trapped in the magnetic bottle between the magnetic mirrors located near the footpoints of magnetic loops, and excite type IV radio burst. In strong magnetic fields electrons with large pitch angles produce μw emission in the mm-cm range by (incoherent) gyrosynchrotron emission (Krüger, 1979*; Benz, 1993*). Electrons with small pitch angles penetrate through the magnetic mirrors and hit the dense transition region and chromosphere, exciting line emission of atoms and ions, and emitting hard X-rays by *thick target* bremsstrahlung.

The chromospheric plasma is heated and starts expanding in order to establish a new hydrostatic equilibrium ("evaporation" process). The closed loops are being filled by dense ($\approx 10^{10}$ cm^{-3}) and hot ($\approx 10^7$ K) plasma, becoming the dominant source of SXR emission. Since the evaporation,
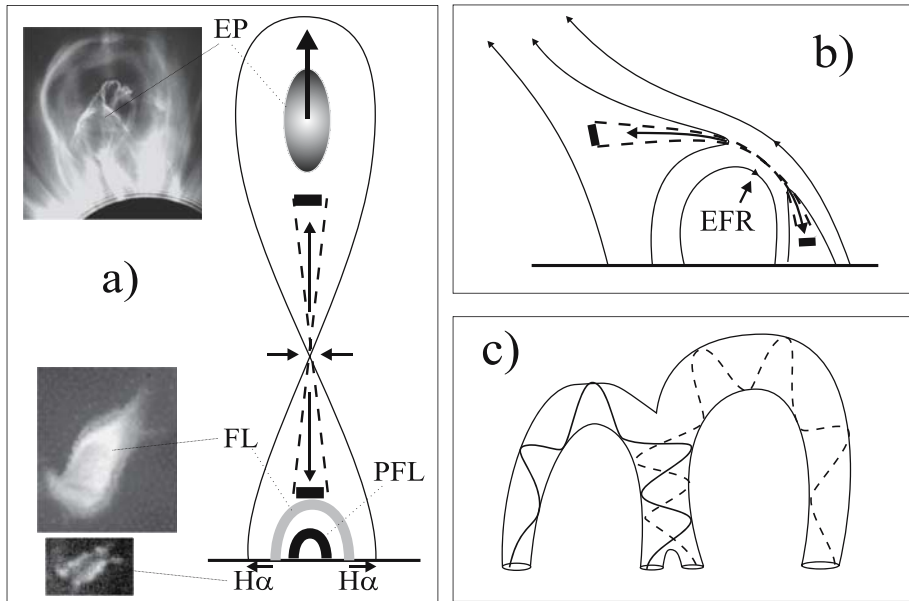
Figure 5. Flare classes: a) Two-ribbon flare (EP = erupting prominence, FL = hot flare loops, PFL = postflare loops, Hα = Hα-ribbons; fast mode standing shocks in the outflow jets are indicated by bold horizontal lines located above the PFL and below the EP). b) Emerging-flux flare (EFR = emerging flux region). c) Interacting-loop flare.

and consequently the SXR emission, is a cumulative effect of precipitating electrons (cooling is relatively slow), the SXR light curve behaves as a time integral of the HXR light curve (the HXR curve looks like the time derivative of the SXR curve; see Fig. 2), which is referred to as Neupert effect (Neupert, 1968; Dennis and Zarro, 1993*; Veronig et al., 2002a*).

Above the SXR-emitting loops filled-up by the evaporation process, a super-hot loop-top source is sometimes observed, having a temperature of some 4×10^7 K (Fig. 1f). Some authors (Tsuneta et al., 1997*; Uchida et al., 2001*) claim that the temperatures can reach 10^8 K ("hyper-hot" plasma).

2.4. CLASSIFICATIONS

Although flares expose a large variety of morphological and evolutionary characteristics, there is a clear difference between two distinct categories. The first type, the so-called confined flares, are events that take place in a magnetic structure confined within a certain coronal volume. The other type, dynamical flares, are events associated with violent disruptions of the initial magnetic field configuration and the flaring is only a part of the large

scale magnetic field restructuration (Švestka, 1976*; Forbes, 2000*; Švestka, 2001*).

According to the morphology, flares are traditionally divided into four classes: two-ribbon flares, emerging-flux flares, interacting-loop flares, and simple-loop flares. Emerging-flux flares and interacting-loop flares can be merged into a wider class representing all flares where two distinct magnetic systems interact. Therefore, we will subsume both under interacting-flux flares in the following.

Two-Ribbon Flares, being by definition dynamical, represent a majority of large, long duration events. In the standard scenario (Priest, 1982*) a sheared arcade with a twisted neutral line filament becomes unstable and erupts. The field lines overlying the magnetic rope that contains the filament are stretched and below the rope a current sheet is formed (Fig. 5a). The flare energy release starts when magnetic reconnection is turned on in the current sheet (see Sect. 3.2.1). The energy released at the current sheet is transported down the field lines by electron beams and thermal conduction. The transition region and chromospheric layers are impulsively heated and bright ribbons are formed at both sides of the neutral line (see the lowest inset in Fig. 5a). As the reconnection proceeds field lines anchored at successively larger distances from the neutral line enter into the current sheet and reconnect. The ribbons expand outwards from the inversion line and the flare/postflare loop system grows (Fig. 5a). Above the flaring loops a cusped structure (Tsuneta, 1996; Sterling et al., 2000*) is observed in soft X-rays (the middle inset in Fig. 5a).

Interacting-Flux Flares are the most frequently observed flares. The reconnection takes place between two (or more) distinct interacting magnetic systems (Fig. 5b, c), i.e., tripolar or quadrupolar configurations are involved (Aschwanden, 2002*). A frequent feature associated with flares of this class is an opposite polarity "intrusion" within the dominant photospheric field, often created by newly emerging flux. The tension of the overlying field prevents expansion of the emerging flux, leading to the formation of a current sheet, whereas the flux emergence drives reconnection (Fig. 5b). An analogous, yet distinct class of events is driven by an arcade eruption that rushes into the overlying field (Vršnak et al., 1987b). In contrast to previous examples, these are not confined flares and can be referred to as erupting-flux flares. Another specific class are flares caused by a sequence of loop interactions within an arcade (Vršnak et al., 1987a; Aurass et al., 1999*).

Simple-Loop Flares are presumably caused by an energy release confined within a single loop (Priest, 1982*; Priest, 1985*). The energy release mechanism could be: *i*) cylindrical tearing (Waddell et al., 1978; Baty and Heyvaerts, 1996); *ii*) coalescence instability of fine structure current
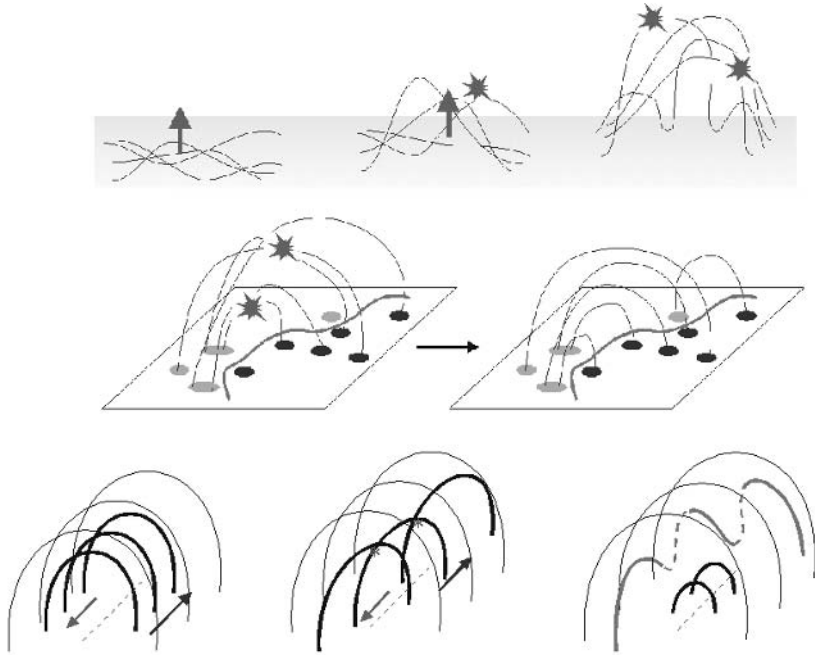
Figure 6. Flares in different phases of active region evolution. *Top*: the emerging flux phase (mainly emerging-flux flares and interacting-loop flares). *Middle*: restructuring towards the arcade formation (mainly interacting-loop flares and merging-flux flares). *Bottom*: flux rope formation (mainly interacting-loop flares).

filaments within a loop (Hoyng, 1977; Hoyng et al., 1980; Kuijpers et al., 1981); *iii*) energy release based on the double layer mechanism (Alfvén and Carlquist, 1967; Spicer and Brown, 1981*); *iv*) sudden localized resistivity enhancement (Melrose, 1992); *v*) a dynamic "current injection" (Miyagoshi et al., 2001). On the other hand, it is well possible that in the system of two interacting loops one loop is not resolved, or the upper parts of both loops are not detected so that one sees only the reconnected loops below the reconnection site (like in Fig. 4). A further option is suggested by Shibata et al. (1995) and Nitta et al. (2001) who found that soft X-ray ejecta were present in all events of the analyzed set of simple-loop flares and that the primary energy release was often above the flaring loop. This indicates that at least in some cases apparently simple-loop flares are unresolved small dynamical flares.

Finally, let us mention a complementary classification proposed by Low (1996) who divided flares according to their role in the evolution of the coronal magnetic field in an active region (Fig. 6). The smallest and most numerous are nanoflares. They are a prompt coronal response to field changes that
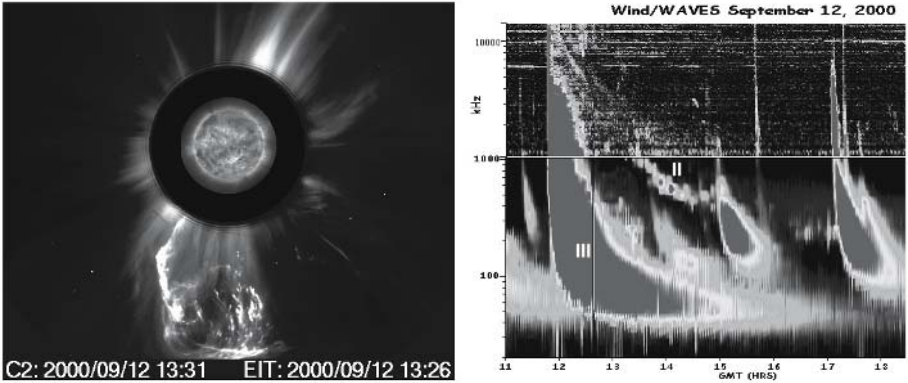
Figure 7.   Associated phenomena: a) Coronal mass ejection of 12 September 2000 (see Fig. 1a–d). Note the helical structures suggestive of a flux rope. b) Dynamic spectrum of the associated radio event: IP type III and type II bursts are indicated.

are driven by subphotospheric convection (e.g. flux emergence). Presumably, the energy released by nanoflares (Shimizu and Tsuneta, 1997*; Vlahos et al., 2002*) provides coronal heating and can be related to a gradual readjustments of coronal fields. Yet, a part of the deposited energy remains stored. It is released by various forms of confined flares, which intermittently relax the coronal fields towards simpler configurations, finally forming a large scale arcade. The next "generation" of confined flares (basically of the interacting-loop type) serves to create a flux rope within the arcade, in a process analogous to that proposed by Ballegooijen and Martens (1989). Eventually, when a sufficient fraction of the arcade field is "detached" from the photosphere, i.e. when the flux rope is sufficiently long and thick, the arcade erupts. A large scale coronal mass ejection is launched and a major two-ribbon flare occurs as a byproduct.

2.5. ASSOCIATED PHENOMENA

Flares are associated with two phenomena that affect the IP space: coronal mass ejections (CMEs) and solar energetic particles, SEPs (Kahler, 1992*; Reames, 1999*; Simnett, 2003*). Flares and CMEs are especially closely related in the case of two-ribbon flares (Švestka, 2001*). A frequent radio-feature in these events is the so-called moving type IV burst (IVm in Figs. 1c and 3). In contrast to the stationary type IV burst that is "sitting" at the flaring loop system below the CME, the type IVm burst source propagates outwards, closely associated with the motion of the CME (Klein and Mouradian, 2002*; Vršnak et al., 2003a). Consequently, the moving type IV emission drifts in the dynamic radio spectrum towards lower frequencies (McLean and Labrum, 1985*).

Two-ribbon flares are in fact a consequence of an arcade eruption, but on the other hand, it is quite likely that once started, they provide a prolonged acceleration of the parent CME (see Sect. 4.2). Indeed, large flare-related CMEs are often faster and characterized by a more impulsive acceleration (MacQueen and Fisher, 1983; Sheeley et al., 1999). Since the energy supply is prolonged, this class of CMEs is able to drive the IP shocks that are revealed by type II bursts in the deka-to-kilometric wavelength range (Gopalswamy et al., 2001*). The feed-back hypothesis is suported also by a close correlation between the SXR light-curves and the velocity time-profile of CMEs (Zhang et al., 2001; Neupert et al, 2001; Wang et al., 2003), and by a close association of the HXR phase of the flare and the acceleration stage of the eruption (Kahler et al., 1988).[5]

In the flare-CME events the growth of the loop system below the CME is lasting for hours, and coronographic observations sometimes reveal U-shaped patterns ("disconnecting events") that indicate reconnected field lines which are detached from the photosphere (Simnett et al., 1997*; Wang et al., 1998, 1999). In fact, such a behaviour can also be observed in the absence of a flare, indicating that the reconnection below the CME happens as a natural consequence of the arcade eruption (Forbes, 2000*). Just, the energy release rate/density in such events is too low to produce the "standard" flare signatures (e.g., HXR burst, or evaporation-caused SXR burst).

The story about IP particles is somewhat more complicated (Kahler, 1992*; Reames, 1999*). Usually, two basically different mechanisms are considered to explain the escaping electron beams: They might be accelerated in the CME-driven or flare-ignited shocks (so-called shock accelerated particles, or SA-events). On the other hand, they could be directly related to the energy release in the flare (Reiner et al., 2000*; Krucker, 2003*; Reiner, 2003*).

Although the mechanism of the escape of particle beams from the flare site into the IP space is still not recognized (Krucker, 2003*), one can speculate about two possibilities. The first is that the open field lines are already present in the preflare configuration, so when these field lines become included in the energy release process the particles can freely runaway from the acceleration site (Vršnak et al., 2000*). The other possibility is based on the fact that the escape is closely associated with the initiation and the lift-off of CMEs, as revealed by type III radio bursts extending to the kilometric wavelength range (Reiner et al., 2000*, 2001). This indicates that in some way the escape is enabled by the interaction of the CME with the ambient magnetoplasma. A possible mechanism includes the reconnection of the

---

[5] Yet, note that this is quite speculative: the arguments could be easily turned around, claiming that fast CMEs produce large flares.

erupting flux with the open fields of an adjacent coronal hole, providing a temporary link between the energy release site below the CME and the IP space (Vršnak et al., 2003a).

3. Theoretical concepts

3.1. WHERE DOES THE ENERGY COME FROM?

The flare occurrence rate in some region is governed by the rate at which the energy is transported through the photosphere. It is limited by the upward (z-direction) component of the Poynting flux $\mathbf{P} = \mathbf{E}\times\mathbf{B}/\mu_0$ integrated over the area of the region. The electric field is induced by the motion perpendicular to the magnetic field $\mathbf{E} = -\mathbf{v}\times\mathbf{B}$. There are two contributions to P_z: the magnetic field emergence provides $P_z^e = v_z B_x^2/\mu_0$, whereas the shearing motion contributes with $P_z^s = v_x B_z B_x/\mu_0$. Obviously, the energy is stored faster in strong magnetic field regions. Consequently, a large majority of flares takes place in sunspot groups and only occasionally in spotless regions (Dodson and Hedeman, 1960; Ruždjak et al., 1987; Ruždjak et al., 1989*).

Using order-of-magnitude values for the velocity $v = 0.1$–1 km s^{-1} and magnetic field $B = 0.01$–0.1 T, one finds $P_z \approx 10^5$–10^6 W m^{-2}. An active region (AR) covering 10^5 km $\times$ 10^5 km ($A = 10^{16}$ m^2) can store in one day 10^{25}–10^{26} J. This accounts for one large flare per day, a dozen of small-to-medium flares or hundreds of small flare-like brightenings. The largest flares can appear only in big AR complexes.

Since pressure gradients and gravity under normal coronal conditions are much smaller than the Lorentz force, the preflare field is practically force-free (Priest, 1982*). The electric current $\mathbf{j}$ is parallel to the field $\mathbf{B}$, meaning $\mu_0\mathbf{j} = \nabla\times\mathbf{B} = \alpha\mathbf{B}$, where α is a degree by which the field is sheared. For a given magnetic field, the regions that are more stressed involve stronger currents and thus contain more free energy[6]. Analogously, at a given α currents are concentrated in stronger fields (Hagyard, 1988; Hofmann et al., 1992; Sakurai, 1993).

In reality, flares occur preferably at locations where the field is strongly sheared and the energy release is more powerful when stronger fields are involved (see Sect. 2.2). Flares in highly stressed strong fields are also more impulsive and show more prominent nonthermal signatures (Aurass et al., 1999*). There are two basic reasons for such a behaviour. Since the development of an MHD process depends on the Alfvén travel time[7], the

---

[6] The energy excess above the energy of potential field ($\mathbf{j}=0$) can be expressed heuristically as LI^2 (Jackson, 1975), where L is the inductance of the current system and $I = jA$ is the current associated with the considered photospheric area A.

[7] $t_A = d/v_A$; d is the length scale involved and $v_A = B/\sqrt{\mu_0\rho}$ is the Alfvén velocity.

events employing strong fields with steep gradients (small length scales) will progress faster (Spicer, 1977*). On the other hand, since higher current densities and stronger electric fields are involved the thresholds for kinetic plasma instabilities (Spicer and Brown, 1981*; Benz, 1993*) and particle acceleration are more easily reached (see Sect. 3.2.2).

The stressed preflare magnetic field structure containing free energy, is restructured by flares into a relaxed configuration, being close to the potential state. Figure 8 illustrates such a restructuring, associated with the flare of 6 February 1992 (Sakurai, 1993; Aurass et al., 1999*). In the left-top panel, the soft X-ray preflare image shows a strongly sheared system of kinked loops. In particular the central part of the system has a sigmoidal form, such as quite frequently found in two-ribbon flares (Sterling et al., 2000*). The force-free extrapolation ($\alpha = 0.016\,\mathrm{Mm}^{-1}$) of the photospheric magnetic field (middle-top) reproduces quite well the observed SXR pattern (Aurass et al., 1999*). On the other hand, the postflare structure (left-bottom) is well depicted by potential field extrapolation ($\alpha = 0$) shown in the middle-bottom panel. The drawings on the righthand side of Fig. 8 sketch the meaning of the *topological change* of the magnetic field configuration (connectivity): In the initial (preflare) state the field lines connect point A with B and C with D, whereas aftermath (postflare state) point A is connected with C and D with B.

3.2. HOW IS THE ENERGY RELEASED?

3.2.1. *Magnetic reconnection*

Since the magnetic field lines are anchored in the inert photosphere ("line-tying condition") the topological change of magnetic field implies that the field lines must re-connect (Fig. 8, right-middle panel). The coronal plasma is characterized by a very high electric conductivity σ, i.e., very low magnetic diffusivity $\eta = 1/\mu_0\sigma$ (Priest, 1982*). Bearing in mind also large dimensions (L) of the flaring system, one finds that the magnetic Reynolds number ($R_m = Lv/\eta$) is very large (Priest, 1982*). Under such conditions the field lines can meet and interact only within extremely thin layers, where the field diffusion is still effective. In these layers, called current sheets, in the stationary state the magnetic flux inflow must be balanced by the diffusion, i.e., the magnetic Reynolds number therein becomes $R_m = 1$ (Priest, 1982*; Priest and Forbes, 2000*).

On the other hand, the mass inflow into the layer has to be balanced by the outflow along the layer ($v_{in}\lambda = v_{out}\delta$, where v_{in} and v_{out} are the inflow and outflow velocity, and λ and δ are the length and width of the region of interest, respectively). This implies that, in order to have a relatively fast inflow (high reconnection rate) providing a sufficient energy release, the layer length λ cannot be arbitrarily large. Thus, the reconnection can be
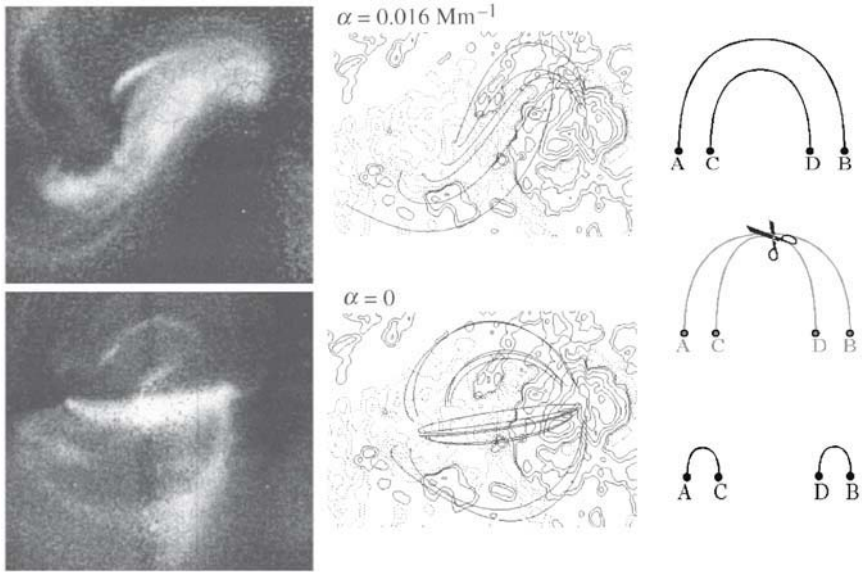
Figure 8.   Coronal magnetic field restructuring in the two-ribbon flare of 6 February 1992. Left: the preflare and postflare SXT-Yohkoh images. Middle: Kitt Peak magnetograms overlaid by force-free ($\alpha = 0.016\,\mathrm{Mm}^{-1}$) and potential ($\alpha = 0$) field extrapolation. Right: meaning of the topological change of magnetic field and the re-connection.

fast only if it occurs within an extremely small volume, called the diffusion region (DR).

Such a mechanism of *fast reconnection* (Biskamp, 2003*), sometimes also referred to as Petschek regime after Petschek (1964), including its modalities (Priest, 1985*; Priest and Forbes, 1986; Priest and Forbes, 2000*), is essential for flares (Scholer, 2003*). A simple concept of magnetic field *annihilation* in a long current sheet ($\lambda = L$ where L represents the overall dimension of the whole system), usually called Sweet-Parker regime (Sweet, 1958; Parker, 1957), is too slow to account for the energy release in flares.

Besides a small DR, the fast reconnection mechanism anticipates splitting of the current sheet into two pairs of slow-mode standing shocks (SMSSs; bold-gray lines in Fig. 9-left) extending from the DR (depicted by a small central rectangle in Fig. 9-left). The plasma inflow is almost perpendicular to the inflowing magnetic field implying that the flow is faster than the corresponding slow mode waves[8] and the SMSSs appear in the region where merging flows "collide". SMSSs are sometimes called

---

[8] MHD slow-mode waves have a very low speed when propagating almost perpendicular to the field (Priest, 1982*).
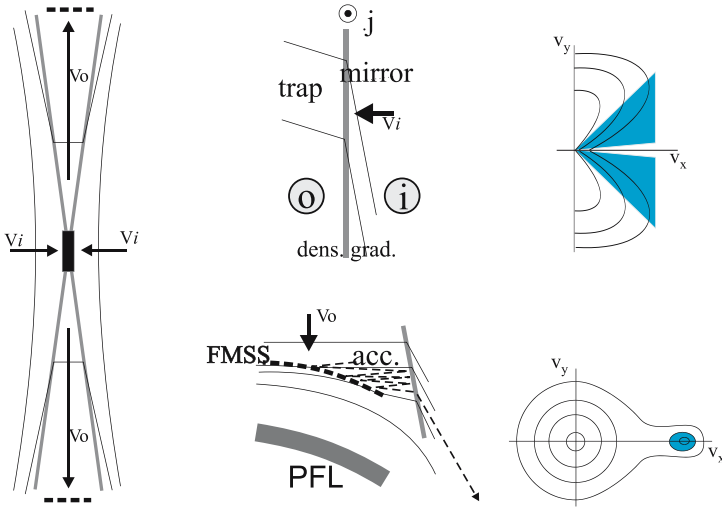
Figure 9. *Left:* Petschek's model of fast reconnection in a current sheet. *Middle:* Properties of the model – magnetic mirrors at the SMSSs form magnetic bottle between the SMSSs (top); collapsing trap configuration between the SMSS and the FMSS providing particle acceleration above postflare loops (bottom). *Right:* Unstable velocity distribution functions $f(v_x, v_y)$ – loss-cone (top); bump on tail (bottom). The velocity component in the direction of the magnetic field ("parallel velocity") is denoted as v_x, and v_y represents the perpendicular one. The unstable regions ($\partial f / \partial v_{in} > 0$) are shaded.

switch-off shocks[9] (Ugai, 1987) since the downstream magnetic field is almost perpendicular to the shock. It should be noted that the majority of the energy is released at the SMSSs (Ugai, 1987; Ugai, 1992; Ugai, 1999; Biskamp, 2003*) which after completion (Nitta et al., 2001) extend all along the contact region between the merging magnetic systems. The role of the small DR is only to turn-on the reconnection.

In the SMSSs plasma is heated, whereas the inflow is deflected and accelerated (Biskamp, 2003*) to form two fast outflow jets of hot plasma (Fig. 9). Electric fields associated with the DR and the SMSSs also accelerate particles and trigger plasma kinetic instabilities (see Sect. 3.2.2). These nonthermal processes excite radio emission in the decimeter/meter wavelength range (Krüger, 1979*; Benz, 1993*), providing the most immediate signature of the primary energy release (Bastian et al., 1998*).

The plasma density in the outflow is larger than in the inflow by factor $N = n_{out}/n_{in} \approx 2.5$, whereas the pressure and the temperature depend primarily on the plasma-to-magnetic pressure ratio $\beta_{in} = 2\mu_0 p_{in}/B_{in}^2$ in the inflowing region: $P = p_{out}/p_{in} \approx \beta_{in}^{-1}$, $T = T_{out}/T_{in} = P/N \approx N^{-1}\beta_{in}^{-1}$

---

[9] For shock-modes and the terminology see Priest (1982*).

(Aurass et al., 2002; Skender et al., 2003). Thus, one finds that typical flare temperatures can be achieved only if $\beta_{in} > 0.01$–0.1, which is a condition met primarily in the active region corona (Gary, 2001).

The flow velocity v_{out} of the outflow jet is roughly equal to the Alfvén speed in the inflow region, $v_{out} \approx v_{Ai}$ (Aurass et al., 2002; Skender et al., 2003). The magnetosonic Mach number of the jet ($M_{ms} = v_{out}/v_{ms}$, where v_{ms} is the magnetosonic speed) at the flare-appropriate β_{in} is generally $M_{ms} > 1$ (Forbes and Malherbe, 1986), having the value $M_{ms} \rightarrow \sqrt{3}$ for $\beta_{in} \rightarrow 0$ (Aurass et al., 2002; Skender et al., 2003). Since the jet is supermagnetosonic, a fast mode standing shock (FMSS) should be formed at the location where the jet encounters an obstacle and terminates (Forbes, 1986; Aurass et al., 2002). Since the flow is perpendicular to the magnetic field, the shock is quasi-perpendicular and can accelerate particles to high energies (Tsuneta and Naito, 1998; Somov and Kosugi, 1997).

The reconnection is effective only if the current sheet length is much larger than its width – only then the magnetic field strength in the outflow region is much smaller than in the inflow region (Fig. 9), i.e., only in such case the conversion of magnetic energy into thermal and kinetic energy is significant. The reconnection in a long current sheet can be either driven, or it can be caused by tearing instability (Furth et al., 1963; Spicer and Brown, 1981*). In the former case the reconnection is caused by external flows like vortices behind an erupting plasmoid (see Sect. 4.2) or by coalescence instability (see Sect. 4.1). Such type of process is usually described by posing a certain flow pattern as boundary condition (Sato and Hayashi, 1979; Priest and Forbes, 1986). If the inflow velocity is larger than allowed in the Petschek-regime (usually some 1–10% of the Alfvén velocity in the inflowing region), the magnetic field piles-up at the borders of the current sheet ("pile-up" regime), forcing the diffusion region to become thinner and longer (Priest, 1982*; Priest, 1985*).

On the other hand, long current sheets are unstable to the tearing instability (Forbes, 1986; Magara et al., 1996; Nitta et al., 2001; Ugai, 1987; Yokoyama and Shibata, 2001), which can be initiated by a localized increase of resistivity caused by some plasma instabilities (Ugai, 1987; Yokoyama and Shibata, 2001). When at a given location in the sheet two field lines reconnect, the resulting field line is strongly bent (Fig. 9) – the magnetic tension, like a slingshot, ejects the plasma out of the diffusion region and new plasma is sucked-in, carrying a "fresh field" to be reconnected. In this case, the flow pattern at the boundaries of the system is a consequence, and not the cause, of the reconnection.

When the sheet is sufficiently long, two or more diffusion regions can be formed along the sheet (Spicer and Brown, 1981*; Kliem, 1995*). In between X-type neutral points growing plasmoids are created, forming

O-type neutral points. The plasmoids are mutually attracted and merged by coalescence instability, causing an intermittent energy release, which might be an explanation for temporal fine structures in flares (Kliem, 1995*). Such a multiple tearing is presumed to be a transition towards a turbulent reconnection regime (Priest, 1982*).

So far only 2-dimensional situations were considered, meaning that the magnetic field component B_z perpendicular to the reconnection plane (the plane of Fig. 9) was neglected. The influence of this field component is usually described by employing the angle Ω defined by $\tan \Omega = B_z/B_{xy}$, where B_{xy} is the magnetic field component in the reconnection plane. In the presence of B_z, in front of the SMSSs rotational discontinuities (RD) develop (Petschek and Thorn, 1967; Soward, 1982) where plasma flow is deflected and accelerated, while the temperature, density, and magnetic field strength remain constant (Priest, 1982*). The plasma is heated and compressed at the SMSSs. In the region between the RD and the SMSS, the B_z component is larger than in the inflow, and there is a v_z component of the plasma velocity. In the outflow region between the SMSSs, B_z is also larger than in the inflowing region. The energy release rate and the outflowing plasma temperature are highest when $\Omega \to 0$ (Petschek and Thorn, 1967; Soward, 1982; Skender et al., 2003), whereas the outflow magnetosonic Mach number and the compression N attain maximum at some Ω_{in} which depends on β_{in} (Skender et al., 2003).

In the transition $\Omega \to 0$ a number of interesting phenomena should take place, including MHD turbulence (Skender et al., 2003). A turbulent reconnection could generate an energy release that might be described in terms of numerous elementary flare bursts (see Sect. 2.2) and would have to be considered in the framework of "statistical flare" models (Anastasiadis et al., 1997; Isliker et al., 2001*).

3.2.2. *Plasma instabilities and particle acceleration*

Several features of the fast-reconnection geometry (Fig. 9) provide a further step in understanding of the energy release and energy transport in flares. However, most of these phenomena, mainly associated with plasma instabilities and particle acceleration, cannot be described in the scope of MHD. For a comprehension of such processes it is necessary to consider the non-Maxwellian velocity distributions of particles, $f(v_x, v_y, v_z)$ since plasma instabilities generally occur if the distribution is characterized by $\partial f/\partial v_{in} > 0$ (Benz, 1993*).[10] Situations of this kind usually take place in presence of high density/temperature or magnetic field gradients, strong

---

[10] First recognized, and most exploited is the Buneman two-stream instability (Buneman, 1959), resulting in a Langmuir turbulence (electron plasma waves) that excites spiky coherent radio emission at the plasma frequency or its harmonic (Krüger, 1979*).

electric fields (i.e., high current densities), particle beams, etc. (Kaplan and Tsytovich, 1973; Kuperus, 1976; Spicer and Brown, 1981*; Duijveman et al., 1981; Dum, 1985*; Somov, 1992*; Benz, 1993*; Schlickeiser, 2003*). So, the plasma instabilities are usually classified to gradient instabilities, (perpendicular/longitudinal) current-driven instabilities, beam instabilities, etc. (Spicer and Brown, 1981*; Somov, 1992*).

The fast-reconnection geometry is an environment naturally providing generation of all of the mentioned features. The most important property is that the magnetic field in the inflowing region is 10–100 times stronger than in the outflowing jet (Skender et al., 2003). First of all, this means that in the DR and SMSSs the current density is very high since the width of these structures is very small. In other words, the electron drift velocity can be higher than the threshold for (perpendicular) current-driven instabilities, e.g., the thermal speed of protons or electrons (Spicer and Brown, 1981*). Thus, the DR and the SMSSs are in a turbulent state (Vršnak, 1989; Somov, 1992*; Karlický, 2003a), emitting coherent radio emission at some of the characteristic plasma frequencies (Benz, 1993*).

Secondly, in the region between the SMSSs particles are trapped, since $B_{out}/B_{in} \ll 1$ implies that the SMSSs act as strong magnetic mirrors. Only particles with pitch angle smaller than θ_m, defined by $\sin^2\theta_m = B_{out}/B_{in}$, can escape into the inflow region. Furthermore, this means that the electron distribution function in the outflow jet has a lost-cone form (Benz, 1993*), as shown in the top-right panel of Fig. 9. Such a distribution is unstable since it is characterized by $\partial f/\partial v_y > 0$, resulting in electron-cyclotron maser emission (Benz, 1993*).

The escaping electrons form beams in the inflow region, and the resulting distribution ("bump-on-tail distribution", shown in the bottom-right panel of Fig. 9) is unstable as there is a part of the velocity space characterized by $\partial f/\partial v_x > 0$. The resulting radio emission is emitted at the plasma frequency. Consequently, the beams produce fast-drifting radio bursts (see Sect. 2.2) as they excite the plasma of lower/higher densities in propagating upwards/downwards along the inflowing region field lines.

Note that plasma instabilities result in various forms of ("microscopic") plasma turbulence (Dum, 1985*; Spicer and Brown, 1981*; Benz, 1993*; Melrose, 1994*). This alters the transport coefficients of the plasma (thermal and electric conductivity) because of electron scattering on the electrostatic wave field associated with the plasma turbulence (Kaplan and Tsytovich, 1973; Dum, 1985*). For example, in the presence of ion-accoustic turbulence (Spicer and Brown, 1981*), the resistivity can increase by six orders of magnitude (Kaplan and Tsytovich, 1973). If going back to the MHD description, one should take this phenomenon into account by replacing the classical conductivity (Spitzer, 1962) by the anomalus one (Sato

and Hayashi, 1979; Ugai, 1987; Yokoyama and Shibata, 2001). On the other hand, most high-frequency turbulences (electron oscillations) excite coherent radio emission (Krüger, 1979*; Benz, 1993*; Melrose, 1994*) which thus could be used as a diagnostic tool for the processes in the primary energy release.

Another aspect of the fast reconnection is that it provides a number of features suitable for the acceleration of nonthermal particles, being one of the main ingredients of the energy release process in flares. Generally, particles can be accelerated: *i*) directly by DC-electric field; *ii*) at shocks by shock-drift acceleration at quasiperpendicular fast-mode shocks; *iii*) stochastically by resonant particle interaction with the wave field in regions of plasma turbulence (Schlickeiser, 2003*).

The first mechanism should be effective in the diffusion region and along the slow-mode shocks (Hoyng, 1977; Blackman, 1997; Somov, 1992*; Litvinenko, 2003*). In these regions the stochastic acceleration could also be efficient (Vlahos, 1989*), since the diffusion region and shocks are sites of high current densities which probably drive plasma instabilities generating plasma turbulence.

On the other hand, the reconnection outflows are supermagnetosonic (Skender et al., 2003), which means that a fast-mode standing shock should appear at locations where the flow encounters an obstacle. Especially interesting is the one above the reconnected loops (Fig. 5a,b) since it corresponds to super-hot HXR loop-top sources (see Sects. 2.3 and 4.2). There, particles could be efficiently accelerated in the so-called collapsing trap geometry (Tsuneta and Naito, 1998; Somov and Kosugi, 1997).

4. Flare models

The phenomena and processes described in Sect. 3 can be used as basic elements that can be incorporated in different magnetic field configurations to construct a variety of flare modalities. Let us now consider the basic features of two main flare models – the model of flares in interacting magnetic systems and the model of a two-ribbon flare.

4.1. INTERACTING-FLUX FLARES

Reconnection between interacting magnetic systems (Fig. 5b,c) can be caused by emerging/merging motions, or can be driven by coalescence instability (Finn and Kaw, 1977; Kliem, 1995*; Tajima et al., 1987).

A distinct type of flares, directly associated with emerging flux regions, is usually referred to as emerging-flux flare. In these flares the emerging flux pushes into the preexisting field of opposite polarity. Due to the tension of

the overlying field, a current sheet is formed in between the two systems (Fig. 5b). When the sheet becomes long enough, tearing instability sets-in and fast reconnection starts. A frequent feature of such flares is a hot jet, which can be interpreted as the upward-directed reconnection outflow (Yokoyama and Shibata, 1996*).

Another distinct type are interacting-loop flares. Aligned loops can interact in two different manners (Linton et al., 2001). The one involving coalescence instability is caused by the attraction of longitudinal currents driving reconnection of azimuthal fields (Fig. 5a). Another possibility is the reconnection of longitudinal fields (Fig. 5b).

The first option requires highly twisted loops (large pitch angles of field lines). Since the pitch angle decreases towards the loop axis (Priest, 1982*) the energy release can last only until the magnetic field component perpendicular to the plane of reconnection becomes too large slowing down the reconnection (Forbes and Malherbe, 1986; Soward, 1982; Skender et al., 2003). The second possibility requires anti-parallel axial magnetic fields in the contact region and small field line pitch angles.

It can be presumed that coronal loops have small pitch angles. Otherwise they would be unstable and erupt (Vršnak, 1990; Vršnak et al., 1991). A further drawback of the coalescence mechanism is that in the final state the loops should stay "glued" in the contact region (Linton et al., 2001), which is not clearly demonstrated by observations.

The most favorable situation for the interaction is when two loops have anti-parallel axial fields and opposite helicities (sign of α) since then the azimuthal fields are also anti-parallel. Such configurations can be found in ARs substructures (Pevtsov et al., 1994), but they are probably rare at larger scales due to a helicity segregation rule (Rust, 1996*; Rust and Kumar, 1996).

In the opposite situation, when the loops have opposite helicities and parallel axial fields, reconnection is not possible.

4.2. TWO-RIBBON FLARES

The standard two-ribbon flare scenario begins with an arcade/filament eruption. It is presumed that the preflare structure slowly evolves through a series of equilibrium states during which the filament slowly rises.[11] When the filament/arcade structure comes to the state where the equilibrium is lost, the entire structure erupts (Ballegooijen and Martens, 1989; Priest, 1982*; Priest and Forbes, 1986; Vršnak, 1990; Vršnak et al., 1991). The flare starts with the onset of fast reconnection below the rising filament.

---

[11] The slow rise can be caused by emerging flux, flux cancellation, twisting of filament footpoints, mass-loss from the filament, etc.

In Fig. 5a an idealized magnetic configuration presumably correspond-
ing to the main phase of two-ribbon flares is shown. The sheared arcade field
lines are stretched by the eruption and electric currents are redistributed,
forming a current sheet below the arcade core (Martens and Kuin, 1989; Lin
and Forbes, 2000). In front of the erupting structure plasma is compressed,
creating flows towards the trailing edge of the eruption (Cargill et al., 1996).
The vortices formed behind the arcade core (Cargill et al., 1996) drive the
plasma towards the current sheet. The resulting increase of the current den-
sity excites kinetic plasma instabilities (see Sect. 3.2.2) causing a localized
anomalous resistivity enhancement[12]. The increased magnetic diffusivity
provides the initiation of reconnection and subsequent triggering of tearing
instability when the sheet becomes long enough (Forbes, 1986; Magara et
al., 1996; Nitta et al., 2001; Ugai, 1987; Ugai, 1992; Yokoyama and Shibata,
2001).

Since the formation of vortices is governed by the eruption kinematics,
the onset of reconnection should be expected during its acceleration phase.
Indeed, the flare onset is often closely associated with the acceleration phase
of the filament eruption (Kahler et al., 1988; Zhang et al., 2001; Wang et al.,
2003). Note also the feedback: the reconnection "supplies" the erupting ar-
cade core with a "fresh" azimuthal field, enhancing the upward component
of the Lorentz force and increasing/prolonging the acceleration (Vršnak,
1990; Lin and Forbes, 2000). A prolonged acceleration and enhanced vortex
motion can in turn prolong the reconnection (and consequently the energy
release), driving the reconnection after the tearing-instability-phase would
normally cease.

The fast reconnection regime cannot set-in if the current sheet is not
long enough (Furth et al., 1963; Ugai, 1987), i.e. the flare cannot start until
the eruption attains some critical height. In the simple two ribbon spotless
flare of September 12, 2000 (Fig. 1a–d) the erupting Hα filament was still
visible at the time of flare onset (Vršnak et al., 2003a, 2003b; Wang et
al., 2003). Measuring the height of the lower edge of the filament and the
initial separation of the flare ribbons, it is possible to estimate the current
sheet width to length ratio as $\delta/\lambda \approx 1/10$–$1/20$ (Vršnak et al., 2003b).
Such a value is in agreement with the value $1/15$ anticipated by numerical
simulations (Ugai, 1987), and is fairly close to the analytical-model value
$1/2\pi$ (Furth et al., 1963).

The situation is simplest when reconnection occurs at only one X-line
(Fig. 5a), corresponding to the 2-D reconnection model shown in Fig. 9.
However, by definition, there is a non-zero horizontal magnetic field present

---

[12] The necessary merging velocity for a transition to the anomalous resistivity regime
is in the order of only 10 - 100 m s^{-1}. However, to get a significant level of resistivity it
must be in the order of 10 km s^{-1} (Vršnak, 1989).

in the current sheet formed out of the sheared arcade. Reconnection takes place between pairs of field lines whose footpoints are located on a line perpendicular to the inversion line. In $2\frac{1}{2}$-D and 3-D situations these footpoints are not magnetically connected before reconnection. After the reconnection, loops below the X-line are lying in planes perpendicular to the inversion line, whereas the upper "loops" form helical field lines (Démoulin and Priest, 1989; Démoulin and Raadu, 1992; Gosling, 1993; Vršnak et al., 2003a).

If too strong, the horizontal field component prevents the reconnection process (Soward, 1982; Forbes and Malherbe, 1986; Skender et al., 2003). This is another reason why reconnection cannot start before the eruption attains a sufficient height – the field lines have to stretch enough in order to decrease the horizontal-to-vertical field ratio sufficiently.

Besides the expansion of the chromospheric ribbons, growth of the flare/ postflare loop system, the cusped structure above the hot loops, and the eruption/flare relative timing (see Sects. 2.4 and 2.5), there are also some other observations that could be considered as a supporting evidence for the presented two-ribbon flare model. Among these are downward directed flows observed in soft X-rays above hot loops (McKenzie and Hudson, 1999; McKenzie, 2000) and streams which can be interpreted as reconnection inflows (Yokoyama et al., 2001). Finally, there is a good correlation between the energy release rate and the values of $(v \times B)_{ch}$ measured in the chromosphere, where v is the velocity of the ribbon expansion and B is the photospheric magnetic field (Wang et al., 2003). Bearing in mind the magnetic flux conservation, the quantity $(v \times B)_{ch}$ presumably corresponds to the reconnection rate, expressed as the electric field in the current sheet, $(v \times B)_{cs} \approx (v \times B)_{ch}$.

5. Conclusions

The solar flare phenomenon includes a wide palette of physical processes, involving different physical aspects from (magneto)hydrodynamics to nuclear and elementary-particles physics. In this respect flares are an excellent laboratory for plasma physics where our knowledge on plasma and MHD instabilities, particle acceleration processes, emission mechanisms, etc., can be advanced and our ideas and theories tested.

Various magnetic field configurations and amounts of stored energy can be involved in the preflare state. Consequently a broad variety of physical processes becomes feasible, yielding a potpourri of evolutionary scenarios and modes of energy release. As a consequence, flares show a large diversity of appearances, from small and compact events up to a large, CME-associated exciting spectacle that severely affects the interplanetary space, up to the Earth and beyond.

References

Alfvén, H. and Carlquist, P.: 1967, *Solar Phys.* **1**, 220.

Anastasiadis, A., Vlahos, L., and Georgoulis, M.K.: 1997, *Astrophys. J.* **489**, 367.

Antonucci, E, Alexander, D., Culhane, J.L., et al.: 1999, in K.T. Strong, J.L.R. Saba, B.M. Haish, J.T. and Schmelz (eds.), *The Many Faces of the Sun*, Springer, p. 331.

Aschwanden, M.J.: 2002, *Space Sci. Rev.* **101**, 1.

Aschwanden, M.J. and Benz, A.O.: 1997, *Astrophys. J.* **480**, 825.

Aschwanden, M.J., Benz, A.O., Dennis, B.R., and Schwartz, R.A.: 1995, *Astrophys. J.* **455**, 347.

Aschwanden, M.J., Hudson, H.S., Kosugi, T., and Schwartz, R.A.: 1996a, *Astrophys. J.* **464**, 985.

Aschwanden, M.J., Kosugi, T., Hudson, H.S., Wills, M.J., and Schwartz, R.A.: 1996b, *Astrophys. J.* **470**, 1198.

Aurass, H. and Klein, K.-L.: 1997, *Astron. Astrophys. Suppl.* **123**, 279.

Aurass, H., Vršnak, B., Hofmann, A., and Ruždjak, V.: 1999, *Solar Phys.* **190**, 267.

Aurass, H., Vršnak, B., and Mann, G.: 2002, *Astron. Astrophys.* **384**, 273.

Ballegooijen, A.A. and Martens P.C.H.: 1989, *Astrophys. J.* **343**, 971.

Bastian, T.S., Benz, A.O. and Gary, D.E.: 1998, *Ann. Rev. Astron. Astrophys.* **36**, 131.

Baty, H. and Heyvaerts, J.: 1996, *Astron. Astrophys.* **308**, 935.

Benz, A.O.: 1993, *Plasma Astrophysics*, Kluwer, Dordrecht.

Biskamp, D.: 2003, in K.-L. Klein (ed.), *Energy Conversion and Particle Acceleration in the Solar Corona*, Lect. Notes Phys. 612, Springer, Heidelberg, p. 109.

Blackman, E.G.: 1997, *Astrophys. J.* **484**, L79.

Brown, J.C.: 1971, *Solar Phys.* **18**, 489.

Brown, J.C., Smith, D.F., and Spicer, D.S.: 1981, in S. Jordan, *The Sun as a Star*, NASA SP-450, Washington, p. 181.

Buneman, O.: 1959, *Phys. Rev.* **115**, 503.

Cargill, P.J., Chen, J., Spicer, D.S., and Zalesak, S.T.: 1996, *J. Geophys. Res.* **101**, 4855.

Czaykowska, A., Alexander, D., and De Pontieu, B.: 2001, *Astrophys. J.* **552**, 849.

de Jager, C.: 1986, *Space Sci. Rev.* **44**, 43.

Démoulin, P. and Priest, E.R.: 1989, *Astron. Astrophys.* **214**, 360.

Démoulin, P. and Raadu, M.A.: 1992, *Solar Phys.* **142**, 291.

Dennis, B.R. and Zarro, D.M.: 1993, *Solar Phys.* **146**, 177.

Dodson, H.W., Hedeman, E.R.: 1960, *Astron. J.* **65**, 51.

Donelly, B.R., and Unzicker, A.: 1974, *NOAA Tech. Memo.* ELR SEL-72.

Dröge, W.: 2003, in K.-L. Klein (ed.), *Energy Conversion and Particle Acceleration in the Solar Corona*, Lect. Notes Phys. 612, Springer, Heidelberg, p. 193.

Duijveman, A., Hoyng, P., and Ionson, J.A.: 1981, *Astrophys. J.* **245**, 721.

Dum, C.T.: 1985, *Space Sci. Rev.* **42**, 467.

Finn, J.M. and Kaw, P.K.: 1977, *Phys. Fluids* **20**, 72.

Fisher, G.H.: 1989, *Astrophys. J.* **346**, 1019.

Fleishman, G.D. and Melnikov, V.F.: 1998, *Physics Uspekhi* **41**, 1157.

Forbes, T.G.: 1986, *Astrophys. J.* **305**, 553.

Forbes, T.G.: 2000, *J. Geophys. Res.* **105**, 23153.

Forbes, T.G. and Malherbe, J.M.: 1986, *Astrophys. J.* **302**, L67.

Furth, H.P., Kileen, J., and Rosenbluth, M.N.: 1963, *Phys. Fluids* **6**, 459.

Gaizauskas, V. and Švestka, Z.: 1987, *Solar Phys.* **114**, 389.

Gary, G.A.: 2001, *Solar Phys.* **203**, 71.

Gary, G.A., Moore, R.L., Hagyard, M.J., Haisch, B.M.: 1987, *Astrophys. J.* **314**, 782.

Gopalswamy, N., Yashiro, S., Kaiser, M.L., Howard, R.A., and Bougeret, J.-L.: 2001, *J. Geophys. Res.*, **106**, 29219.

Gosling, J.T.: 1993, *J. Geophys. Res.* **98**, 18937.

Güdel, M. and Benz, A.O.: 1990, *Astron. Astrophys.* **213**, 202.

Hagyard, M.J.: 1988, *Solar Phys. 115*, 107.

Hagyard, M.J., Teuber, D., West, E.A., and Smith, J.B.: 1984, *Solar Phys. 91*, 115.

Hofmann, A. Ruždjak, V., and Vršnak, B.: 1992 *Hvar Obs. Bull.* **16**, 29.

Hoyng, P.: 1977, *Astron. Astrophys. 55*, 23.

Hoyng, P., Duijveman, A., van Grunsven, T.F.J., and Nicholson, D.R.: 1980, *Astron. Astrophys. 91*, 17.

Isliker, H., Anastasiadis, A., and Vlahos, L.: 2001, *Astron. Astrophys.* **377**, 1068.

Jackson, W.D.: 1975, *Classical Electrodynamics*, Wiley & Sons, New York.

Kahler, S.W.: 1992, *Ann. Rev. Astron. Astrophys.* **30**, 113.

Kahler, S.W., Moore, R.L., Kane, S.R., and Zirin, H.: 1988, *Astrophys. J.* **328**, 824.

Kaplan, S.A. and Tsytovich, V.N.: 1973, *Plasma Astrophysics*, Pergamon, Oxford.

Karlický, M.: 1988, *Bull. Astron. Inst. Czech.* **39**, 13.

Karlický, M.: 2003a, *Solar Phys.* **212**, 389.

Karlický, M.: 2003b, *Space Sci. Rev.* **107**, 81.

Kaufmann, P., Raulin, J.-P., Correia, E., et al.: 2001, *Astrophys. J.* **548**, L95.

Kitahara, T. and Kurokawa, H.: 1990, *Solar Phys.* **125**, 321.

Klein, K.-L. and Mouradian, Z.: 2002, *Astron. Astrophys.*, **381**, 683.

Kliem, B.: 1995 *Lect. Notes Phys.* **444**, 93.

Kosugi, T., Dennis, B.R., and Kai, K.: 1988, *Astrophys. J.* **324**, 1118.

Krucker, S.: 2003, in K.-L. Klein (ed.), *Energy Conversion and Particle Acceleration in the Solar Corona*, Lect. Notes Phys. 612, Springer, Heidelberg, p. 179.

Krüger, A.: 1979, *Introduction to Solar Radio Astronomy and Radio Physics*, Reidel, Dordrecht.

Kuijpers, J., van der Post, P., and Slottje, C.: 1981, *Astron. Astrophys.* **103**, 331.

Kundu, M.R., White, S.M., Gopalswamy, N., and Lim, J.: 1994, *Astrophys. J. Suppl. Ser.* **90**, 599.

Kuperus, M.: 1976, *Solar Phys.* **47**, 79.

Li, P., Emslie, A.G., and Mariska, J.T.: 1993, *Astrophys. J.* **417**, 313.

Lin, J. and Forbes, T.G.: 2000, *J. Geophys. Res.* **105**, 2375.

Linton, M.G., Dahlburg, R.B., and Antiochos, S.K.: 2001, *Astrophys. J.* **553**, 905.

Litvinenko, Y.E.: 2003, in K.-L. Klein (ed.), *Energy Conversion and Particle Acceleration in the Solar Corona*, Lect. Notes Phys. 612, Springer, Heidelberg, p. 211.

Low, B.C.: 1996, *Solar Phys.* **167**, 217.

MacQueen, R.M. and Fisher, R.R.: 1983, *Solar Phys.* **89**, 89.

Magara, T., Mineshige, S., Yokoyama, T., and Shibata, K.: 1996, *Astrophys. J.* **466**, 1054.

Magdalenić J., Zlobec P., Messerotti M., Vršnak B.: 2002, in A. Wilson (ed.), *Proc. 10th European Solar Physics Meeting: Solar Variability – From Core to Outer Frontiers*, ESA SP-506, 331.

Magdalenić, J., Zlobec, P., Messerotti, M., and Vršnak, B.: 2004, this issue

Martens, P.C.H. and Kuin, N.P.M.: 1989, *Solar Phys.* **122**, 263.

Masuda, S., Kosugi, T., Hara, H., Tsuneta, S., and Ogawa, Y.: 1994, *Nature* **371**, 495.

Mayfield, E.B., and Lawrence, J.: 1985, *Solar Phys.* **96**, 293.

McKenzie, D.E.: 2000, *Solar Phys.* **195**, 381.

McKenzie, D.E. and Hudson, H.S.: 1999, *Astrophys. J.* **519**, L93.

McLean, D.J. and Labrum, N.R.: 1985, *Solar Radiophysics*, Cambridge Univ. Press, Cambridge.

Melrose, D.B.: 1992, *Astrophys. J.* **387**, 403.

Melrose, D.B.: 1994, in A.O. Benz and T.J.-L. Courvoisier (eds.), *Plasma Astrophysics*, Springer, Berlin, p. 113

Miyagoshi, T., Uchida, Y., Yabiku, T., Hirose, S., and Cable, S.: 2001, *Publ. Astron. Soc. Japan* **53**, 341.

Moreton, G.E. and Ramsey, H.E.: 1960, *Publ. Astron. Soc. Pacific*, **72**, 357.

Neupert, W.M.: 1968, *Astrophys. J.* **153**, L59.

Neupert, W.M., Thompson, B.J., Gurman, J.B., and Plunkett, S.P.: 2001, *J. Geophys. Res.* **106**, 25215.

Nitta, N.V., Sato, J., and Hudson H.S.: 2001, *Astrophys. J.* **552**, 821.

Nitta, S., Tanuma, S., Shibata, K., and Maezawa, K.: 2001, *Astrophys. J.* **550**, 1119.

Parker E.N.: 1957, *J. Geophys. Res.* **62**, 509.

Pearson, D.H., Nelson, R., Kojoian, G., and Seal, J.: 1989, *Astrophys. J.* **336**, 1050.

Petschek, H.E.: 1964, in W.N. Hess (ed.), *AAS-NASA Symposion on the Physsics of Solar Flares*, NASA SP-50, p. 425.

Petschek, H.E. and Thorne, R.M.: 1967, *Astrophys. J.* **147**, 1157.

Pevtsov, A.A., Canfield, R.C., and Metcalf, T.R.: 1994, *Astrophys. J.* **425**, L117.

Poqueruse, M. and McIntosh, P.S.: 1995, *Solar Phys.* **159**, 301.

Priest, E.R.: 1982, *Solar Magneto-hydrodynamics*, Reidel, Dordrecht.

Priest, E.R.: 1985, *Rep. Prog. Phys.* **48**, 955.

Priest, E.R. and Forbes, T.G.: 1986, *J. Geophys. Res.* **91**, 5579.

Priest, E.R. and Forbes, T.G.: 2000, *Magnetic Reconnection*, Cambridge Univ. Press, Cambridge.

Ramaty, R. and Murphy, R.J.: 1987, *Space Sci. Rev.* **45**, 213.

Raulin, J.-P., Kaufmann, P., Gimenez, C.G., et al.: 2003, *Astrophys. J.* **592**, 580.

Reames, D.V.: 1999, *Space Sci. Rev.* **90**, 413.

Reiner, M.J.: 2003, in Proc. ISCS 2003 Symposium 'Solar Variability as an input to the Earth's Environment', ed. A. Wilson, ESA SP-**535**, 517

Reiner, M.J., Karlický, M., Jiřička, K., Aurass, H., Mann, G., and Kaiser, M.L.: 2000, *Astrophys. J.*, **530**, 1049.

Reiner, M.J., Kaiser, M.L., and Bougeret, J.-L.: 2001, *J. Geophys. Res.*, **106**, 29989.

Rust, D.M.: 1996, in R.D. Bentley and J.T. Mariska (eds.), *Magnetic Reconnection in the Solar Atmosphere*, ASP Conf. Series 111, Astron. Soc. Pacific, San Francisco, p. 353.

Rust, D.M. and Kumar, A.: 1996, *Astrophys. J.* **464**, L199.

Rust, D.M., Simnett, G.M., and Smith, D.F.: 1985, *Astrophys. J.* **288**, 401.

Ruždjak, V., Vršnak, B., Zlobec, P., and Schroll, A.: 1986, *Solar Phys.* **104**, 169.

Ruždjak, V., Messerotti, M., Nonino, M., Schroll, A., Vršnak, B., and Zlobec, P.: 1987, *Solar Phys.* **111**, 103.

Ruždjak, V., Vršnak, B., Schroll, A., and Brajša, R.: 1989, *Solar Phys.* **123**, 309.

Sakurai, T.: 1993, *Adv. Space. Res.* **13**, 109.

Sato, T. and Hayashi, T.: 1979, *Phys. Fluids* **22**, 1189.

Schlickeiser, R.: 2003, in K.-L. Klein (ed.), *Energy Conversion and Particle Acceleration in the Solar Corona*, Lect. Notes Phys. 612, Springer, Heidelberg, p. 230.

Schmieder, B., Malherbe, J.M., Simnett, G.M., Forbes, T.G., and Tandberg Hanssen, E.: 1990, *Astrophys. J.* **356**, 720.

Scholer, M.: 2003, in K.-L. Klein (ed.), *Energy Conversion and Particle Acceleration in the Solar Corona*, Lect. Notes Phys. 612, Springer, Heidelberg, p. 9.

Sheeley, N.R. Jr., Walters, J.H., Wang, Y.-M., and Howard, R.A.: 1999, *J. Geophys. Res.*, **104**, 24739.

Shibata, K., Masuda , S., Shimojo, M., *et al.*: 1995, *Astrophys. J.* **451**, L83.

Shimizu, T. and Tsuneta, S.: 1997, *Astrophys. J.* **486**, 1045.

Simnett, G.M.: 2003, *Solar Phys.* **213**, 387.

Simnett, G.M., Tappin, S.J., Plunkett, S.P., et al.: 1997, *Solar Phys.* **175**, 685.

Skender, M., Vršnak, B., and Martinis, M.: 2003, *Phys. Rev. E* **68**, 046405.

Somov, B.V.: 1992, *Physical Processes in Solar Flares*, Kluwer, Dordrecht.

Somov, B.V. and Kosugi, T.: 1997, *Astrophys. J.* **485**, 859.

Soward, A.M.: 1982, *J. Plasma Phys.* **28**, 415.

Spicer, D.S.: 1977, *Solar Phys.* **53**, 305.

Spicer, D.S. and Brown, J.C.: 1981, in S. Jordan (ed.), *The Sun as a Star*, NASA SP-450, Washington, p. 413.

Spitzer, L.: 1962, *Physics of Fully Ionized Gasses*, Intersciece, New york.

Sterling, A.C., Hudson, H.S., Thompson, B.J., and Zarro, D.M.: 2000 *Astrophys. J.* **532**, 628.

Sweet, P.A.: 1958, in Lehnert, B. (ed.), *Electromagnetic Phenomena in Cosmical Physics*, IAU Symp. **6**, Cambridge University Press, p. 123.

Švestka, Z.: 1976, *Solar Flares*, Reidel, Dordrecht.

Švestka, Z.: 2001, *Space Sci. Rev.*, **95**, 135.

Tajima, T., Sakai, J., Nakajima, H., Kosugi, T., Brunel, F., and Kundu, M.R.: 1987, *Astrophys. J.* **321**, 1031.

Tappin, S.J.: 1991, *Astron. Astrophys. Suppl. Ser.* **87**, 277.

Tsuneta, S.: 1996, *Astrophys. J.* **456**, 840.

Tsuneta, S., and Naito, T.: 1998, *Astrophys. J.* **495**, L67.

Tsuneta, S., Masuda, S., Kosugi, T., and Sato, J.: 1997, *Astrophys. J.* **478**, 787.

Uchida, Y., Altschuler, M.D., and Newkirk, G. Jr.: 1973, *Solar Phys.* 28, 495.

Uchida, Y., Wheatland, M.S., Haga, R., Yoshitake, I., and Melrose, D.: 2001, *Solar Phys.* **202**, 117.

Ugai, M.: 1987, *Geophys. Res. Lett.* **14**, 103.

Ugai, M.: 1992, *Phys. Fluids* **4**, 2953.

Ugai, M.: 1999, *J. Geophys. Res.* **104**, 6929.

Veronig, A., Vršnak, B., Dennis, B.R., Temmer, M., Hanslmeier, A., and Magdalenić, J.: 2002a, *Astron. Astrophys.* **392**, 699.

Veronig, A., Vršnak, B., Temmer, M., and Hanslmeier, A.: 2002b, *Solar Phys.* **208**, 295.

Vlahos, L.: 1989, *Solar Phys.* **121**, 431.

Vlahos, L., Fragos, T., Isliker, H., and Georgoulis, M.: 2002, *Astrophys. J.* **575**, L87.

Vršnak, B.: 1989, *Solar Phys.* **120**, 79.

Vršnak, B.: 1990, *Solar Phys.* **129**, 295.

Vršnak, B., Ruždjak, V., Messerotti, M., and Zlobec, P.: 1987a, *Solar Phys.* **111**, 23.

Vršnak, B., Ruždjak, V., Messerotti, M., Mouradian, Z., Urbarz, H., and Zlobec, P.: 1987b, *Solar Phys.* **114**, 289.

Vršnak, B., Ruždjak, V., and Rompolt, B.: 1991, *Solar Phys.* **136**, 151.

Vršnak, B., Ruždjak, V., Brajša, R., et al.: 2000, *Solar Phys.* **194**, 285.

Vršnak, B., Warmuth, A., Brajša, R., and Hanslmeier, A.: 2002, *Astron. Astrophys.* **394**, 299.

Vršnak, B., Warmuth, A., Maričić, D., Otruba, W., Ruždjak, V.: 2003a, *Solar Phys.* **217**, 187.

Vršnak, B., Klein, K.-L., Warmuth, A., Otruba, W., and Skender, M.: 2003b, *Solar Phys.*, **214**, 325.

Waddell, B.V., Carreras, B., Hicks, H.R., Holmes, J.A., and Lee, D.K.: 1978, *Phys. Rev. Lett.* **41**, 1386.

Wang, H., Qiu, J., Denker, C., Spirock, T., Chen, H., and Goode, P.R.: 2000, *Astrophys. J.* **542**, 1080.

Wang, H., Qiu, J., Ju, J., and Zhang, H.: 2003, *Astrophys. J.* **593**, 564.

Wang, Y.-M., Sheeley, N.R., Walters, J.H., et al.: 1998, *Astrophys. J.* **498**, L165.

Wang, Y.-M., Sheeley, N.R., Howard, R.A., St.Cyr, O.C., and Simnett, G.M.: 1999, *Geophys. Res. Lett.* **26**, 1203.

Warmuth, A., Vršnak, B., Aurass, H., and Hanslmeier, A.: 2001, *Astrophys. J.* **560**, L105.

Xie, R.X., Song, Q., Wang, M., and Chen, G.Q.: 1994, *Solar Phys.* **155**, 113.

Yokoyama, T. and Shibata, K.: 1996, *Publ. Astron. Soc. Japan*, **48**, 353.

Yokoyama, T. and Shibata, K.: 2001 *Astrophys. J.* **549**, 1160.

Yokoyama, T., Akita, K., Morimoto, T., Inoue, K., and Newmark, J.: 2001, *Astrophys. J.* **546**, L69.

Zhang, J., Dere, K.P., Howard, R.A., Kundu, M.R., and White, S.M.: 2001, *Astrophys. J.* **559**, 452.

Zlobec, P., Ruždjak, V., Vršnak, B., Karlický, M., and Messerotti, M.: 1990, *Solar Phys.* **130**, 31.

Zlobec, P., Mészárosova, H., Veronig, A., Karlický, M., and Magdalenić, J.: 2003, *Hvar Obs. Bull.* **27**, 115.

CORONAL MASS EJECTIONS AND MAGNETIC HELICITY

L. VAN DRIEL-GESZTELYI

Mullard Space Science Laboratory, Univ. College London, UK

Observatoire de Paris, LESIA
FRE 2461 (CNRS), Meudon Cedex, France

Konkoly Observatory of the Hungarian Academy of Sciences
Budapest, Hungary

Abstract. Coronal mass ejections (CMEs) are the most energetic events in the solar system, expelling up to 10^{16} g of coronal material at speeds of several hundreds or thousands of km s^{-1} from the Sun. As CMEs are the primary cause of space weather disturbances, we need to understand their underlying cause(s) in order to be able to predict them. After an overview of their basic properties based on multi-wavelength and multi-instrument data, including optical, EUV, X-ray and radio observations from microwaves to kilometric wavelengths, we follow CMEs from the low solar atmosphere through the interplanetary medium to the Earth. A discussion on CME source regions is presented, followed by a discussion on theoretical CME models, comparing them to observations. Evidence is emerging that magnetic helicity is the key to understand CMEs: they go off when too much helicity has built up in the corona. Therefore, in the second part an overview of this young and dynamic field of solar physics is presented. During the last four years, attempts were made to estimate/measure magnetic helicity from solar and interplanetary observations. As magnetic helicity (unlike current helicity) is one of the few global quantities that is conserved even in resistive MHD on a timescale less than the global diffusion timescale, magnetic helicity studies make it possible to trace helicity as it emerges from the sub-photospheric layers into the corona, then being ejected via CMEs into the interplanetary space, and reaching the Earth in a magnetic cloud. Observational studies on the relative importance of different sources of magnetic helicity investigate whether the dominant helicity source is photospheric plasma motions (photospheric differential rotation and localized shearing motions) or the twist of the emerging flux tubes created under the photosphere (presumably by the radial shear in the differential rotation in the tachocline).

1. Introduction

Hundhausen (1997) wrote that a coronal mass ejection (CME) is "a massive expulsion of plasma from an atmosphere, that is, in the main, gravitation-

ally and magnetically bound" – expressing that the existence of CMEs is not a trivial matter. Nevertheless, mass and magnetic field do leave the Sun in these eruptions, and we still do not understand exactly why.

Coronal mass ejections are the most energetic events in the solar system, expelling up to 10^{16} g of coronal material at speeds of several hundreds or thousands of km s^{-1}. CMEs are the primary cause of space weather disturbances, like permanent failure of satellites, degradation or disruption of communication, navigation and power systems and even the exposure of astronauts and polar-route airline crews to harmful doses of radiation. Due to our exponentially evolving dependence on such facilities and services, there is an ever-increasing need to understand the underlying cause(s) of CMEs in order to be able to predict them.

CME-like structures have been seen in historical eclipse drawings (e.g. on 18 July 1860, see Eddy, 1974), but the idea that they are large-scale structures expelled from the Sun, arose in the early 70s, based on space-born coronograph observations like OSO-7 and Skylab (Tousey, 1973; MacQueen *et al.*, 1974). At first, they were called coronal transients, and only in 1976 articles were published in which the 'coronal mass ejection' term appeared (Gosling *et al.*, 1976). During the last three decades a broad wavelength range (UV, EUV, X-rays, radio) was added to the traditional white-light observations, enabling us to follow CMEs from the low solar atmosphere through the interplanetary medium to the Earth and beyond. There have been significant efforts to understand the origin, nature and effects of CMEs (e.g. Schwenn, 1995; Hundhausen, 1999; Gosling, 2000; Webb *et al.*, 2000; Gopalswamy, 2003; and references therein).

In the first part of this review, I make an attempt to sketch an up-to-date picture of these intriguing solar and interplanetary phenomena. First, the main characteristics and signatures of CMEs are described as observed with different instruments covering a broad wavelength range. Then, after a discussion on CME source regions, an overview on CME models is presented. Since evidence is emerging that magnetic twist and shear (i.e. magnetic helicity) is the key to understand CMEs, in the second part I present an overview of this young and dynamic field of solar physics. After a brief discussion on the theoretical foundations, I describe very recent attempts to estimate/measure magnetic helicity from solar and interplanetary observations.

2. Characteristics of CMEs

Figure 1 shows a typical CME displaying the three-part structure: (1) the bright frontal part, (2) the darker cavity or void and (3) the core, which is frequently the brightest feature and thought to contain an erupting promi-
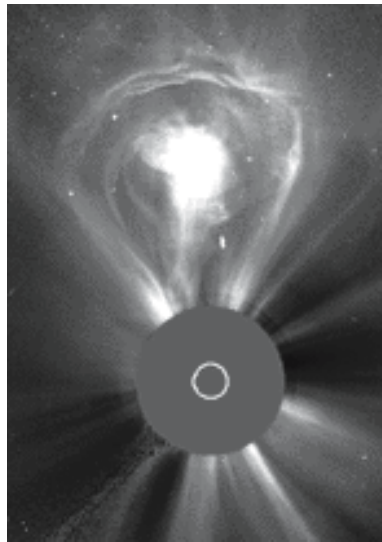
Figure 1. The so-called 'lightbulb' CME on 27 February 2000 at 7:42 UT (LASCO/C3) shows clearly the classical three-part structure: (1) a bright curved leading edge followed by (2) a darker region called the void and (3) a bright interior structure, which is normally an erupting prominence. The white circle in the middle of the occulting disc indicates the size of the Sun. Courtesy of SOHO (ESA & NASA).

nence. This structuring is best observed in CMEs which erupt close to the limb and are seen from the side, while Earth- (or oppositely) directed CMEs mainly show an outflow and expanding coronal brightness around the Sun – these are called halo CMEs (Howard *et al.*, 1982). A recent halo event is shown in Figure 2.

CMEs are principally observed in white-light blocking out the photospheric light, which is 10^6 times brighter than the corona, by an occulting disc (or the Moon during solar eclipses). Since in white-light coronograph images we see photospheric light scattered on coronal free electrons (Thomson scattering) the images sample mass irrespective of temperature.

Other wavelengths reveal near-surface (Hα, He 10830 Å, EUV, X-rays, from microwaves to metric radio) and interplanetary (white-light, long-wavelength radio, interplanetary scintillation – IPS) and *in situ* signatures of CMEs, which, besides electron density (n_e) carry temperature and magnetic field information as well.

CMEs are quite common features of solar activity: during activity minimum SOHO observed a CME frequency of $\nu_{CME} \approx 0.5$ day^{-1}, while around the maximum of the cycle $\nu_{CME} \approx 4.5$ day^{-1}, though during the latter period sometimes it is difficult to distinguish between consecutive CMEs, the corona appears to have an almost continuous outflow. The SOHO LASCO
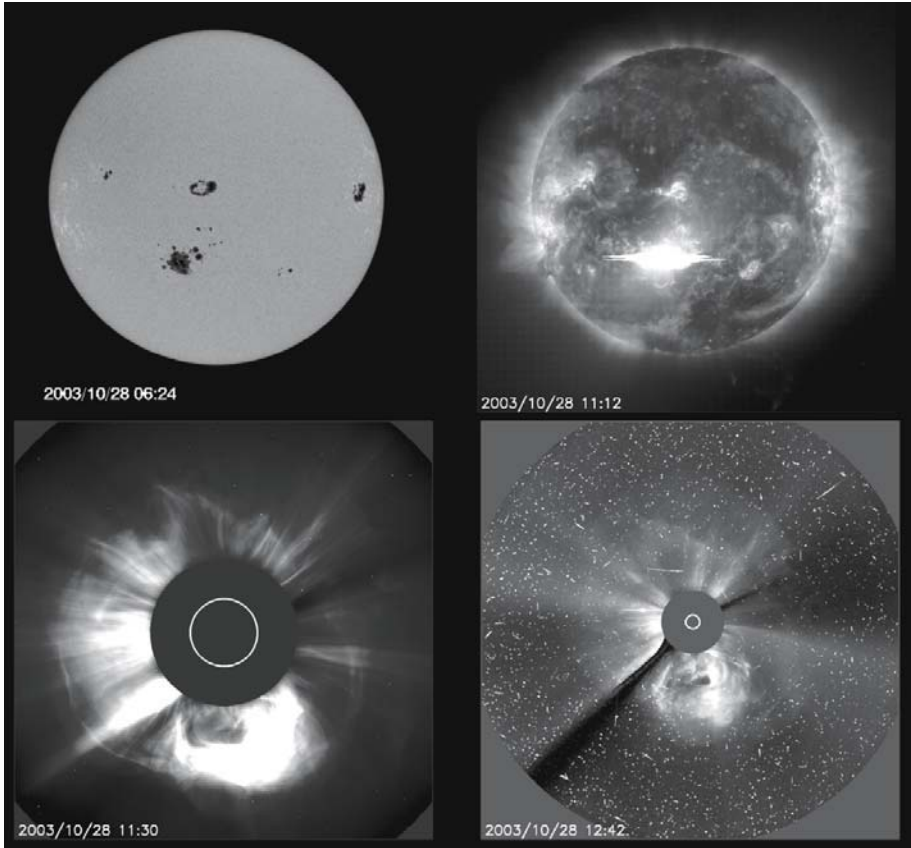
Figure 2. An X17 flare and its related halo CME observed on 28 October 2002 onboard the SOHO spacecraft. The upper left panel is a photospheric image taken by MDI showing a roundish large active region on the south-east hemisphere; the upper right panel is an EUV image taken with EIT which shows the flare, while the lower panels show the ensuing halo CME as observed by the LASCO coronagraphs (C2: left panel, C3: right panel). The 'snow storm' in the C3 image is caused by the impact of solar energetic particles (SEP), accelerated in the flare, onto the CCD. Courtesy of SOHO (ESA & NASA).

CME Catalog (`http://cdaw.gsfc.nasa.gov/CME_list/`), which, besides the basic data (position angle, start time, angular width) contains height-time plots and fitted velocities, direct and running difference movies, provides a comprehensive database for CME studies.

2.1. NEAR-SURFACE CME SIGNATURES

In connection with CMEs, Hα, He 10830 Å and microwave observations show the disappearance of filaments and the subsequent formation of flare ribbons on both sides of the magnetic inversion line.

Erupting filaments can be traced in microwave radio emission (observed e.g. at Nobeyama Radio Observatory, see `http://solar.nro.nao.ac.jp`) as they rise above the limb to become the bright core of white-light CMEs in SOHO/LASCO images.

In EUV (SOHO/EIT, TRACE) movies one can see the eruption of the dark filament followed by the formation of an arcade of bright flare loops in its wake. The post-eruption arcade is well seen in Yohkoh/SXT and GOES/SXI X-ray images and movies. These signatures pinpoint the source region and lift-off time of CMEs.

Another important near-surface signature of CMEs is the formation of the so-called *dimming regions*, which show up best in difference (pre-event image subtracted) 195 Å EIT images. They were first noticed in HAO K coronameter images (Rust and Hildner, 1976). Rust (1983) called them transient coronal holes. Dimmings normally appear on both sides of the post-eruption arcade. The fact that the corona becomes darker may indicate the decrease of density or temperature or both. However, dimmings are interpreted as depletion of coronal material, because the radiative cooling time for their temperature and spatial extent exceeds their observed time scales (Hudson *et al.*, 1996). Material escapes along magnetic field lines which became 'open' towards the interplanetary space due to the CME eruption, and that later becomes the CME in the coronagraph images (Rust and Hildner, 1976). Blue-shift observed in dimming regions using SOHO/CDS data provides direct evidence that the dimmings are associated with outflowing material (Harra and Sterling, 2001). Dimmings mark out the footprints of CMEs! Dimmings can appear widely apart, even on two opposite hemispheres, due to the interaction of the erupting CME structure with overlying large-scale loops, which can lead to the opening of large-scale field lines and the ensuing depletion of coronal material (Manoharan *et al.*, 1996; van Driel-Gesztelyi *et al.*, 2000).

The *EIT transients*, the so-called *'EIT waves'* are recently discovered low-coronal signatures of the early phase of CMEs (Thompson *et al.*, 1998, 1999). They are characterised by a bright front which expands circularly (or along an arc) from a flaring (CME source) region with a speed of a few hundred km s^{-1}. Behind the bright front a dimming is seen. Their origin is still debated. One interpretation is that 'EIT waves' are fast-mode MHD waves associated with eruptions and they eventually produce shocks manifested by type II radio bursts (Klassen *et al.*, 2000). 'EIT waves' are interpreted as shocks when they have a 'bow' structure (Gopalswamy, 2000) and are associated with so-called Moreton waves observed in Hα (Smith and Harvey, 1971) and metric type II bursts, which are shock signatures (Thompson *et al.*, 2000; Warmuth *et al.*, 2001). A transient similar in nature to 'EIT waves' was also observed in soft X-rays and it was noted to appear

together with a type II burst (Khan and Hudson, 2000).

Pohjolainen *et al.* (2001) provided observational evidence for good correspondence between 'EIT waves', Moreton waves and type II bursts indicating a blast-wave like nature. However, blast waves are expected to be correlated with large flares. Burkenpile argued in the interview-review paper of Cliver and Hudson (2002) that 'EIT waves' are associated with flares of all GOES classes from A to X (10^{-8} to $>10^{-4}$ W m^{-2}). Using Thompson's list of 170 'EIT wave' events, selecting 51 with $> 51\%$ confidence level, she found one event associated with a GOES class A-flare, 18 with B-flares, 15 with C-flares, 10 with M-flares and 6 with X-flares. Note that big events are rare, so their association with 'EIT waves' is good, while for small flares the association is poor. However, the fact that EIT transients appear to be associated with at least a few small flares suggests that they are not blast waves.

Plunkett in the paper of Cliver and Hudson (2002) reminds us that there are many CMEs without waves and there are also waves with no associated CMEs (example: 3 waves, but no CME on 25 April 1997)! However, all of the EIT wave observations with no associated CME are disc events, when the (halo) CME might be missed.

An alternative interpretation was proposed by Delannée and Aulanier (1999), namely that EIT waves are due to compression of the plasma at low height in the solar corona in the region surrounding *magnetic field opening*. They note that many EIT waves are stationary fronts! Furthermore, they warn that though the EIT sequence has a low temporal resolution, the running difference images are made without correction for rotation, which can easily create artifacts.

Another newly discovered low-coronal CME signature is the so-called *global enhancement*, which has been observed both in EUV and X-rays (Gopalswamy *et al.*, 1999, 2000). Such enhancement of coronal brightness was reported during filament eruption, and its extension appears to be much larger than that of the post-eruption arcade. It was interpreted as an early form of the CME itself, and though it is a weak signature, it could be used to detect disc CMEs.

2.2. HIGH-CORONAL AND INTERPLANETARY SIGNATURES OF CMES

Using the LASCO C2 and C3 coronagraphs one can follow the evolution of CMEs in white-light between 1.7–6 R$_\odot$ and 3.7–32 R$_\odot$, respectively. However, since the Earth is in 215 R$_\odot$ distance from the Sun, we need other means to follow CMEs in the interplanetary medium (IPM).

When a flare and CME-related disturbance, such as an electron beam or shock moves through the coronal plasma, local electrons get displaced with respect to the ions, and start to oscillate around their equilibrium posi-
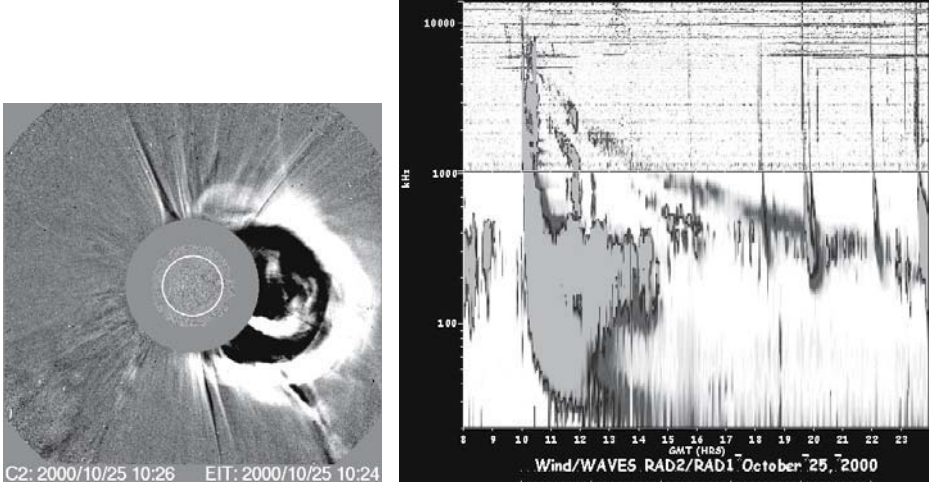
Figure 3. A fast west-limb CME observed with LASCO/C2 (difference image; left panel) and dynamic radio spectrum (frequency versus time) of the related radio bursts as observed with the WAVES instrument onboard the WIND spacecraft (right panel). The broad-band burst which starts at about 10 UT and drifts fast in frequency is a type III burst. The slower-drifting two parallel bursts represent a type II burst – emission appears both at the fundamental (lower, weaker line) and harmonic (upper, stronger line) frequencies. Courtesy of SOHO (ESA & NASA) and the WIND/WAVES consortium.

tion. The natural frequency of this oscillation, called the plasma frequency, depends on the electron density: $f_p = 9\sqrt{n_e}$ (f in kHz, n_e in cm^{-3}). As the disturbance moves outward through the progressively rarified coronal plasma, it excites radiation at lower and lower frequencies. E.g., low in the solar corona, where $n_e \approx 10^8$ cm^{-3}, the plasma frequency is $f_p = 90$ MHz. At 1 AU, close to solar minimum $n_e \approx 10$ cm^{-3} and $f_p = 28$ kHz – the latter can only be observed from space. Since the plasma frequency of the ionosphere is 10 MHz, radio waves with a frequency lower than this are reflected by the ionosphere – enabling world-wide radio communication on Earth, but also mirroring low-frequency radio waves coming from the Sun and the IPM.

Long-wavelength radio emission enables us to track disturbances related to CMEs in the interplanetary space. In Figure 3 a fast west-limb CME observed with LASCO/C2 is shown and next to it is the dynamic radio spectrum (frequency versus time) of the related radio bursts as observed with the WAVES instrument (Bougeret *et al.*, 1995) onboard the WIND spacecraft. The broad-band burst which starts at about 10 UT and drifts fast in frequency is a type III burst. Type III bursts are related to fast ($0.2\,c \lesssim v \lesssim 0.8\,c$, where c is the speed of light) quasi-continuous electron beams travelling along field lines open towards the IPM. The slower-drifting

two parallel lines are signatures of a type II burst, which is thought to be excited by a shock travelling in the IPM. Emission appears both at the fundamental (lower, weaker line) and harmonic (upper, stronger line $f_H = 2f_F$) frequencies. Since the frequency of the radio emission depends on electron density only, having a density model, one can compute the true velocity from the frequency drift of even the Earth-directed halo CMEs.

The highly structured lower corona has a heterogeneous temperature and density structure. The densities in equatorial and polar regions, active regions, coronal holes and streamers may differ by three orders of magnitude. However, all these structures appear to follow the barometric isothermal density law in an unmagnetized plasma characteristic for their temperature: $n_e(r) = n_e(R_\odot) \exp[-(1 - R_\odot/r)R_\odot/H_\odot]$. Here $H_\odot = kT/\mu m_p g_\odot$ is the density scale height, k Boltzmann's constant, $g_\odot$ the gravitational acceleration at the solar surface, m_p the proton rest mass, $\mu = 0.6$ the mean molecular weight. The reference density at the base of the corona is $n_e(R_\odot)$. For more details on the lower coronal density structure see Démoulin and Klein (2000).

For the interplanetary space, LeBlanc *et al.* (1998) derived the following electron density model: $n_e = 3.3 \times 10^5\, r^{-2} + 4.1 \times 10^6\, r^{-4} + 8.0 \times 10^7\, r^{-6}$ (cm^{-3}), with r in units of $R_\odot$. This density model is normalized for a density at 1 AU to be $n(215\,R_\odot) = 7.2$ cm^{-3} (the average value at the minimum of solar activity when the measurements were made; n_e during maximum can be seven times higher). For other densities at 1 AU the coefficients in the equation need to be multiplied by $n_e(1\,\mathrm{AU})/7.2$. At large heliocentric distances the 2nd and 3rd terms in the density model fall off, therefore the density in the interplanetary space scales approximately as $n_e \sim r^{-2}$. Knowing that for fundamental radio emission $f_p = 9\sqrt{n_e}$ (in kHz), one can see that the plasma frequency, on average, scales as $1/r$ in the IPM. Reading out the frequency-time points from the dynamic radio spectrum one can estimate the speed of the shock: $v = \Delta r/\Delta t = 9\sqrt{n_e}\, r_{1\mathrm{AU}}/\Delta t \times (1/f_2 - 1/f_1)$.

In case of the CME/type II burst event seen in Figure 3, having $n_e = 46$ cm^{-3} (this observation was taken during solar maximum), one can estimate a speed of $v \sim 770$ km s^{-1}, which is in good agreement with the CME speed given in the SOHO LASCO CME Catalog for this event.

However, not all CMEs lead to the appearance of type II bursts: as Gopalswamy *et al.* (2001) showed, mainly the fast (≥ 900 km s^{-1}) and broad (mean width: $100°$) CMEs have such linked burst activity. Such CMEs appear to be more geoeffective when Earth-directed.

CME material propagating in the IPM makes natural radio sources scintillate, so by observing a large number of radio sources it is possible to produce all-sky *interplanetary scintillation* (IPS) maps and track the

propagation of interplanetary disturbances even in 3-D (Manoharan *et al.*, 1995; Tokumaru *et al.*, 2000).

Earth-directed (or the ones travelling in Ulysses's direction) CMEs can be sampled *in situ* by various spacecraft. They measure, among others, solar wind speed, density, magnetic field strength, rotation and azimuthal angle. They detect interplanetary shocks. If the 'ejecta' contains an ordered (rotating) magnetic field and its plasma is significantly cooler than the surrounding solar wind, then it is called a 'magnetic cloud' (Burlaga *et al.*, 1981). Sometimes there is cool and dense material observed at the back of IP ejecta, that resembles the prominence close to the bottom of the coronal cavity in three-part CMEs. However, this is a rare case, indicating that the prominence material gets heated up during the eruption process.

2.3. CME STATISTICS

Statistical works on CMEs analyze their occurrence rate, mass, disc location, angular width, speed and acceleration as measured in the plane of the sky (e.g. St. Cyr *et al.*, 2000; Webb, 2002; Moon *et al.*, 2002b; Gopalswamy *et al.*, 2003). As observational datasets are getting longer, attempts are made to derive a cycle dependence of these CME properties.

Typical properties of CMEs:

– CMEs are large-scale structures carrying plasma and magnetic field from the Sun.
– Typical mass: 10^{15} g.
– Speed: $20 \lesssim v \lesssim 2000$ km s^{-1}. The average speed increases towards solar maximum from 300 to 500 km s^{-1}. Flare-associated CMEs are, on average, faster (median speed: 760 km s^{-1}) than the ones associated with filament eruption without flare (median speed: 510 km s^{-1}).
– Dynamics: slow-starting CMEs accelerate, fast CMEs decelerate, others show $v = const$ in the fields of view of the LASCO coronagraphs.
– Typical kinetic energy: 10^{25} J.
– Temperature: 8000 K in the CME core, 2×10^6 K in the frontal part and even in the cavity.
– Typical width: 70°. The width distribution becomes wider during solar maximum.
– Daily rate: $\nu_{CME} \approx 0.5$ day^{-1} during solar minimum, while around the maximum of the cycle it can be as high as $\nu_{CME} \approx 4.5$ day^{-1}.
– The CME mass shows no dependence on the solar cycle.
– The cycle influences the latitudinal distribution: during solar minimum CMEs are concentrated around the equator, while during solar maximum they originate from a wide range of latitudes.

– CMEs are associated with flares, filament eruptions, shocks, radio
  bursts, solar energetic particle (SEP) events and severe geomagnetic
  storms.

2.4. CME SOURCE REGIONS

About 93% of the flare activity (only part of them are eruptive!) arises
in active regions which contain sunspots (Dodson and Hedeman, 1970),
while the span of CME activity is much longer and well extends into the
phase of active region evolution when the magnetic field is dispersed and the
region is frequently classified as quiet solar region, which contains a filament
(van Driel-Gesztelyi *et al.*, 1999). The two classes of CMEs, namely flare-
related CME events and CMEs associated with filament (or, on the limb,
prominence) eruption are well reflected in the evolution described above:
in a young active region with major sunspots mainly flare-related CMEs
appear, and as the magnetic flux of the active region is getting dispersed, the
non-flare, filament-eruption related CMEs will become dominant. However,
since filaments are present even in active regions which still contain strong
magnetic field concentrations (spots), and flare events in such regions are
associated with the eruption of the filament, mixed cases are not rare. A
small statistical study of 32 CME source regions by Subramaniam and Dere
(2001) showed that 41% CMEs were associated with active regions and had
no filament eruptions, 44% were associated with eruptions of prominences
embedded in active regions, and 15% of CMEs were associated with promi-
nence eruptions from 'quiet' regions. However, the sample of this study was
relatively small. Earlier studies based on Skylab and SMM data had more
limited supporting multiwavelength observations, which are much needed
for such studies.

CMEs mainly originate from closed-field regions, so they do not origi-
nate from coronal holes. However, filaments in the vicinity of coronal holes
have a tendency to be CME-active (Bhatnagar, 1996).

3. CME models

Like during the lecture, I will follow Klimchuck's (2000) classification of
CME models (Table 1).

Thermal blast is a directly driven CME model, which involves a sudden
release of thermal energy in the low corona. Then, the greatly enhanced
gas pressure can not be contained by the magnetic field, so the corona is
literally blown open. This model was the first explanation given to CMEs
and it was inspired by the flare-CME association (Dryer, 1982; Wu, 1982).
As CMEs generally start before the associated flare, this model does not

TABLE I. Classification of CME models (Klimchuk, 2000).

Directly driven		Storage and release		
Thermal blast	Dynamo	Mass loading	Tether release	Tether straining

appear to be correct in most of the cases, though in some flare/CME events the timing is very close (e.g. Dryer, 1996; Delannée *et al.*, 2000).

Directly driven models are also the so-called *'dynamo'* models, in which real-time stressing of the field involves the rapid generation of coronal magnetic flux ('flux injection'). A sudden increase of the magnetic shear leads to increased magnetic pressure, which inflates the system. The resulting picture may resemble a CME. The main advocate of dynamo models is Chen (e.g. 1989, 2000) and Chen and Krall (2003). These models involve either fast twisting of pre-existing field lines or fast emergence of a twisted flux tube (on an hour time scale). Problems with these models are that (i) sudden emergence is prohibited by the frozen-in conditions of the solar plasma, (ii) shearing and twisting should be two orders of magnitudes faster than those observed in order to produce a CME-like eruption, and (iii) the emergence of highly twisted field lines is difficult, therefore slow, since, due to their geometry, they can not drain the dense material they carry from the sub-photospheric layers while emerging.

'Storage and release' models represent the bulk of more recent theoretical work on CMEs. They are characterized by a slow build-up of magnetic stress before the eruption begins. The build-up process involves (i) shearing or twisting of magnetic footpoints, and (ii) mass loading in the corona.

In the *'mass loading'* models the pre-eruption magnetic field is presumed to be metastable. Then, the coronal (prominence) field is compressed by increasing mass loaded on it (e.g. Low and Smith, 1993). A CME can be achieved with these models if unloading of large amount of mass occurs. In these models the eruption is gravitationally powered (like a spring compressed by heavy weight), with no need for the magnetic energy to decrease after the eruption. Since it is a well-known observational fact that filaments get darker before they erupt, mass loading appears a viable mechanism, though the fact that during CMEs most of the material is rising instead of falling, contradicts it.

In the *'tether release'* models mass plays no significant role. The magnetically dominated configuration involves a force balance between magnetic pressure (upward) and magnetic tension (downward). The field lines that provide the tension are called tethers. The analogy used by Klimchuk (2000) is a compressed spring held down by tethers. When the tethers are 'cut' (get

reconnected), the spring is released and a CME occurs. In these models the magnetic stresses are constant before the eruption, but they are distributed over fewer and fewer tethers. Tether release models involve the following scenario:

– There is a flux rope embedded in an arcade field (tethers) which keeps the flux rope from rising.
– Opposite polarity footpoints of the arcade are slowly brought together by a converging flow, they meet at the magnetic inversion line and reconnect, forming a circular (spiral in 3-D) field line disconnected from the photosphere.
– After enough arcade field lines have been transferred to flux rope field lines, equilibrium is lost and the rope rises (Forbes and Isenberg, 1991; Isenberg *et al.*, 1993; Lin *et al.*, 1998, and for a fully time-dependent 3-D model Mikic and Linker, 1999; Amari *et al.*, 2000).

Converging motion of opposite polarities and consequent cancellation along the magnetic inversion line before CMEs have been observed (e.g. van Driel-Gesztelyi *et al.*, 2002).

In the *'tether straining'* model the number of 'tethers' is constant, but the stress increases on them. The so-called break-out models belong to this class (Antiochos, 1998; Antiochos *et al.*, 1999). Tether straining models involve the following scenario:

– The basic magnetic configuration is quadrupolar: bipolar arcade embedded in an oppositely directed large-scale (unsheared) bipolar field – the latter represents the tethers.
– Strong footpoint shearing motions along the central arcade increase magnetic stresses there and the arcade inflates, forming a current sheet where it meets the large-scale oppositely directed stabilising field lines.
– Reconnection starts in the current sheet above the inflating central arcade, removing 'tethers'.
– The highly stressed core field erupts. Reconnection under the erupting flux rope will start after the eruption, forming a post-eruption arcade.

These models require reconnection above the erupting arcade prior to the CME eruption. Multiwavelength observations combined with modelling provided a convincing example that break-out is indeed a viable model for CMEs (Aulanier *et al.*, 2000).

In the break-out models the quadrupolar magnetic configuration is a necessary condition. Indeed, most CMEs occur in complex magnetic configuration. However, it is still a question whether topological complexity is indispensable for CMEs or not. Is the loss of equilibrium of a flux rope, in which the twist exceeded a threshold level (see Török and Kliem, 2003, and
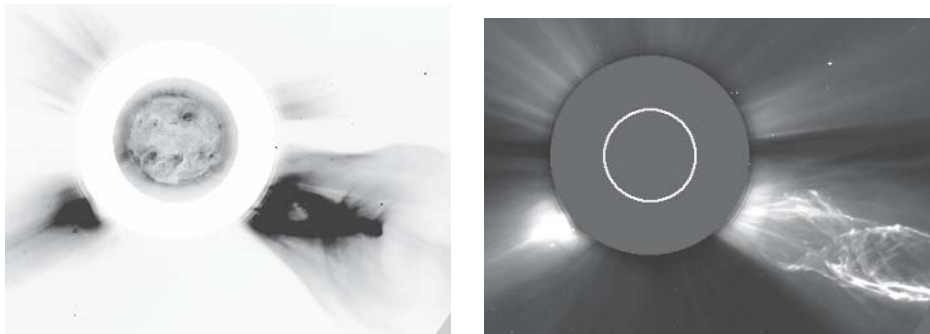
Figure 4.   The bright core region of a CME on 2 June 1998 at 11:27 UT (left panel, EIT image in the centre, reversed colours) and at 13:31 UT (right panel) shows clearly a twisted internal structure as well as a concave-out morphology – signatures of an erupting flux rope. The estimated fraction of CMEs showing such concave-out morphology is about 36–48% (St. Cyr *et al.*, 2000). LASCO/C2 images. Courtesy of SOHO (ESA & NASA).

references within), a sufficient condition for a CME? The Sun is complex, so more than one CME model might be correct!

It has been a long-standing question what comes first: the flare or the CME? Both observations and models suggest that an inflation of the magnetic structure due to increasing magnetic stresses is the first step – this makes observers say that the CME starts before the flare. The main flare energy release occurs during the reconnection of field lines extended by the eruption, which, again, points towards a scenario in which the CME should come first. However, both in the tether cutting (flux rope) and the tether straining (break-out) models pre-eruption reconnection is required under or above, respectively, of the erupting twisted/sheared magnetic structure (filament). In the break-out model this pre-eruption reconnection is expected to occur high in the corona in a region of weak field, releasing too little energy to be observed. However, if the reconnection occurs in a strong field region, like in a complex active region, where the tethers are not external weak fields overlying the sheared core field but they are part of the active region having a quadrupolar configuration, the released magnetic energy can be high enough to qualify as flare. Therefore, we find that (an impulsive, quadrupolar) flare precedes the CME, the latter includes a filament eruption and a related two-ribbon flare representing the post-eruption arcade. Such an observation was reported by Gary and Moore (2004).

In any case, in the models most relevant to observations (storage and release models) the build-up of magnetic stresses, i.e. strong shear and twist are necessary conditions for a CME to occur. In observations twisted CME structures are frequently seen (Figure 4) and there is evidence that a

considerable amount of twist is being carried away from the Sun by CMEs. These facts emphasize the importance of magnetic helicity in the CME process, which will be discussed in the second part of this review.

4. What is magnetic helicity?

Magnetic helicity quantifies how the magnetic field is sheared or twisted compared to its lowest energy state (potential field). Observations provide plenty of evidence for the existence of such stresses in the solar magnetic field and their association to e.g. flare and CME activity, but its precise role in such activity events is far from being clear.

Magnetic helicity is one of the few global quantities, which is conserved even in resistive MHD on a timescale less than the global diffusion timescale (Berger, 1984). Thus, as magnetic flux travels from the tachocline through the convection zone, emerges through the photosphere into the corona and is ejected into the interplanetary space during CME events, the magnetic helicity it carries can be traced.

5. Historical background of helicity studies

In 1925, G.E. Hale published a two-page paper in PASP describing vortices seen in Hα around sunspots, which he called sunspot whirls. Investigating data extending over three solar cycles he found no relationship between the direction of these vortices and spot polarity, and he found no reversal of the whirl direction with the general reversal of spot polarities at cycle changes. He found a cycle-invariant rule, however: about 80% of sunspot whirls are counter-clockwise on the northern hemisphere and clockwise in the south. Drawing a parallel with the hemispheric rule known for terrestrial cyclones, he concluded that these whirls are hydrodynamical rather than electromagnetic phenomena, i.e. they are related to the solar rotation. Richardson (1941) repeated the investigation on data extending over four solar cycles and confirmed Hale's results. In addition, he pointed out that whirls are observed only in $\sim$16% (32% if he made allowances for defective plates and poor seeing) of sunspots which are sufficiently large ($\geq$ 200 MSH [millionth of the solar hemisphere]) to show them clearly on the Mt. Wilson plates.

The subject remained dormant until the 90s, when hemispheric chirality or handedness patterns independent of the sunspot cycle were discovered in active regions, coronal loops, filaments, coronal arcades and interplanetary magnetic clouds (MCs) (Leroy *et al.*, 1983; Seehafer, 1990; Martin *et al.*, 1994; Rust, 1994; Pevtsov *et al.*, 1995; Abramenko *et al.*, 1996; Rust and Kumar, 1996; Martin and McAllister, 1997; Canfield *et al.*, 1999; for a

most recent review see the paper by Pevtsov and Balasubramaniam, 2003, and references therein). A quantitative, mathematical measure of the chiral properties of these structures is the magnetic helicity (Berger and Field, 1984; Berger, 1999). These chirality patterns indicate that the Sun preferentially exhibits left-handed features in its northern and right-handed features in the southern hemisphere. A right-handed twist and a clockwise rotation of the loops, when viewed from above, implies positive helicity, and vice versa for negative helicity, so the recent results agree with those of Hale and Richardson. However, it is noteworthy that in the formation of sunspot whirls, besides or instead of helicity (Nakagawa *et al.*, 1971), the Coriolis force acting on the Evershed flow and its interaction with the magnetic field (Peter, 1996) can play an important role.

Although exceptions to these helicity rules occur in most categories of solar activity at a significant percentage (20–35%), the Sun's preference for features adhering to these rules motivates the search for an underlying mechanism that is, evidently, global in scope. Where and by what kind of mechanism(s) is magnetic helicity generated? The main candidates are the dynamo, helical turbulence (the α or the Σ effect) and differential rotation (both sub-surface and photospheric, the Ω effect). However, theoretical works analyzing the efficiency and even the ability of some of these mechanisms to create the *observed* dominant hemispheric helicity pattern have produced highly controversial results (Seehafer, 1990; Berger and Ruzmaikin, 2000; DeVore, 2000; Démoulin *et al.*, 2002a; Brandenburg and Blackman, 2003; Longcope and Pevtsov, 2003; Seehafer *et al.*, 2003).

When theory is producing confusing results the task of observers is to do their best to provide constraining data. The appearance of quantitative observational works on magnetic helicity has been a very recent development in solar physics.

6. Comparison of magnetic and current helicities

Note that magnetic helicity is different from current helicity, which has been extensively used in establishing the hemispheric helicity rules. The magnetic helicity H_m is defined by the volume integral

$$H_m = \int_V \vec{A} \cdot \vec{B} \, dV, \tag{1}$$

where $\vec{A}$ is the magnetic vector potential and $\vec{B} = \vec{\nabla} \times \vec{A}$ the magnetic field. The current helicity H_c is defined as

$$H_c = \int_V \vec{B} \cdot \vec{j} \, dV, \tag{2}$$

with $\mu_0 \vec{j} = \vec{\nabla} \times \vec{B}$. While, in general, H_m is gauge dependent through $\vec{A}$ (see next Section), there is no gauge freedom with H_c ($\vec{\nabla} \cdot \vec{B} = 0$). Furthermore, while H_m is a conserved MHD quantity, this is not the case for H_c! However, it is usually true that H_m and H_c have the same sign.

Furthermore, we should be aware of the fact that observationally derived values of H_c represent only a fraction of its full value. The volume integral can be written out with its components as

$$H_c = \int_V \vec{B} \cdot \vec{j} \, dV = \int_V (B_x \, j_x + B_y \, j_y + B_z \, j_z) \, dV, \qquad (3)$$

and *only* the last component can be deduced from observations. Though using photospheric vector magnetograms all three components of $\vec{B}$ are available, only the vertical component of $\vec{j}$ can be computed (via the horizontal derivatives of $\vec{B}$). Thus, what we can observationally determine as current helicity is merely the following *surface integral*:

$$h_c = \int_{\text{photosphere}} B_z \, j_z \, dS. \qquad (4)$$

The general relationship between magnetic and current helicities is not known. However, they are both commonly regarded as proxies for twist in magnetic fields.

7. Definition of relative magnetic helicity

Computation of magnetic helicity $H_m = \int_V \vec{A} \cdot \vec{B} dV$ is physically meaningful only when $\vec{B}$ is fully contained inside the volume V. However, when this is not the case (when the normal component $B_n \neq 0$ along the boundary S), following Berger and Field (1984), a relative magnetic helicity H_r, which is gauge independent, can be computed by subtracting the helicity of a reference field $\vec{B}_0$, which has the same B_n distribution on S as $\vec{B}$:

$$H_r = \int_V \vec{A} \cdot \vec{B} \, dV - \int_V \vec{A}_0 \cdot \vec{B}_0 \, dV, \qquad (5)$$

with $\vec{A}_0$ satisfying $\vec{B}_0 = \vec{\nabla} \times \vec{A}_0$. Since H_r is well conserved under solar conditions, the only way helicity can be modified inside V is by helicity flux crossing the boundary S (Berger and Field, 1984):

$$\frac{dH_r}{dt} = -2 \int_S \left[\left(\vec{A}_0 \cdot \vec{v} \right) \vec{B} - \left(\vec{A}_0 \cdot \vec{B} \right) \vec{v} \right] \cdot d\vec{S}, \qquad (6)$$

where $\vec{v}$ is the velocity of the plasma. The first term corresponds to helicity flux by footpoint motions parallel to S (shear term), while the second term

denotes inflow and outflow of helicity through the boundary S (advection term).

The shear term involves helicity injection by footpoint motions in the photosphere like twisting, shearing (special case: differential rotation) and braiding, while the advection term includes emerging motions (but also submergence!) through the photospheric boundary as well as ejection of helicity via CMEs through the coronal boundary of the magnetic volume.

8. Quantitative observational analyses of magnetic helicity

8.1. MAGNETIC HELICITY INJECTED BY DIFFERENTIAL ROTATION

For the computation of magnetic helicity injected by photospheric plasma motions, Berger (1984, 1988) derived an expression for dH_r/dt which depends only on observable photospheric quantities (B_n and $\vec{v}$). DeVore (2000) calculated magnetic helicity injection by differential rotation and found that this time-independent shearing flow, surprisingly, does not provide a monotonous input of magnetic helicity: after 2–2.5 solar rotations it even changes sign! Berger (1986) showed that the helicity injection rate can be understood as the summation of the rotation rate of all the individual elementary flux pairs weighted by their magnetic flux: $dH_r/dt = -1/\pi \int_S \int_{S'} \vec{R} \times \vec{v}(\vec{r})/R^2|_n B_n(\vec{r}) B_n(\vec{r'})\, dS\, dS'$, where $\vec{R} = \vec{r} - \vec{r'}$ is the difference in spatial positions on the photospheric plane. Using this result, Démoulin *et al.* (2002b) have shown that horizontal photospheric plasma motions imply two different helicity terms: the rotation of each polarity introduces 'twist' helicity, while the relative rotation of opposite polarity flux concentrations injects 'writhe' helicity:

$$\Delta H_r(t) = \Delta H_r(t)|_{\text{twist}} + \Delta H_r(t)|_{\text{writhe}}. \tag{7}$$

In case of a shear-flow like differential rotation, the twist and writhe helicity fluxes partially cancel, since they always have opposite signs, while their magnitudes are similar. The relative importance of twist and writhe helicity injection by differential rotation depends mainly on the orientation of the bipole. Twist (writhe) helicity dominates when the bipole axis is parallel (perpendicular) to the equator; these two terms are of the same magnitude and therefore cancel for a bipole tilt of about 45°. As the tilt angle of a bipolar AR is changing, due to the shearing effect of the differential rotation flow, the helicity injection rate is changing as well.

The evolution of the helicity injection rate in a typical AR (NOAA 7978, Jul–Nov 1996), which was initially parallel to the equator and was only deformed by differential rotation, was computed by Démoulin *et al.* (2002a). In this south hemispheric AR differential rotation injected positive helicity,

in accordance with the hemispheric helicity sign; however, the injection rate was low even initially and decreased with time. During six solar rotations differential rotation injected only a total of 8.3×10^{42} Mx^2 which is about the maximum that it can provide to this AR.

Another study by Green *et al.* (2002) of a peculiar AR (NOAA 8100, Nov 1997–Feb 1998), in which the main polarities were rotating around one another by about 150°, showed a very different history of helicity injection. Since the AR, due to its rotation, had passed the critical 45° orientation between its second and third rotation, helicity injection changed sign by the third rotation and became opposite (negative) to the dominant hemispheric helicity sign for the southern hemisphere (see Figure 6 in Green *et al.*, 2002).

Due to the (partial) cancellation between twist and writhe helicities, photospheric differential rotation was shown to be very *inefficient* to provide magnetic helicity on the AR-scale (Démoulin *et al.*, 2002a,b; Green *et al.*, 2002; Nindos and Zhang, 2002). The *maximum total helicity* injected into a bipolar AR that is initially parallel to the equator, having a magnetic flux $\Phi \approx 10^{22}$ Mx, is about 10^{43} Mx^2 (see Figure 5 in Démoulin *et al.*, 2002b). Note that this value refers to helicity injected during the *entire* lifetime of an AR!

However, the conclusion is different in the convective zone for both a solar cycle and a global spatial scale. Berger and Ruzmaikin (2000) evaluated helicity generation by differential rotation using 22 years of magnetogram data (1976–1998) and differential rotation curves. They found that the helicity production in the interior by differential rotation had the correct sign compared to observations of coronal structures (the magnetic helicity conservation is satisfied by the natural generation of the same amount, but of opposite sign, in both hemispheres). The net helicity flow into each hemisphere over this 22-year magnetic cycle was found to be approximately 4×10^{46} Mx^2.

8.2. HELICITY INJECTION BY PHOTOSPHERIC FOOTPOINT MOTIONS

Several authors computed helicity injection at the photospheric level using the shear term, determining transverse velocities of magnetic flux concentrations in active regions by applying a local correlation tracking method (Chae 2001; Chae *et al.*, 2002; Kusano *et al.*, 2002; Moon *et al.*, 2002; Nindos and Zhang, 2002). For these studies line-of-sight magnetic field maps of SOHO/MDI were used, and Kusano *et al.* (2002) used also the transverse field measurements of the Solar Flare Telescope (Mitaka, Japan). To correct for foreshortening, a rotational mapping to the central meridian was applied. To determine B_n from the longitudinal field the ARs were taken close to the centre disc. Furthermore, a small correction is applied

to correct from the off disc centre position: it is generally assumed that magnetic fields in the photosphere are predominantly vertical.

The horizontal photospheric velocities are determined by tracking the position of magnetic flux tubes. The most widely used local correlation tracking (LCT) method was developed by November and Simon (1988). The photospheric velocities are determined by cross-correlating a small fraction of two subsequent images shifted with a variable spatial shift. The relative displacement is given by the highest correlation among the shifts, which provides an estimation for the velocities. Two important parameters in LCT have to be properly chosen: the FWHM (full width at half maximum), w, of the apodizing function and the time interval, ΔT, between the two images to be compared. An optimal value of w should be bigger than the size of the smallest feature seen in the data, so it is related to the resolution of the magnetograms used. In most of the above-mentioned papers an FWHM of $\sim 8''$ was chosen. The choice of ΔT is constrained by the characteristic horizontal velocities in the photosphere. During this ΔT time displacements should (i) be large enough to be well determined by the LCT, but (ii) at the same time be much smaller than the apodizing window size. Velocities ≥ 1–2 km s^{-1} are normally considered unphysical. In these published works ΔT was chosen to be 15 or 20 minutes.

Helicity injected by photospheric footpoint motions and differential rotation during the analyzed periods can be expressed in two units, one is the usual unit of 10^{42} Mx^2, the other is a "natural" unit of helicity expressed as the square of the total magnetic flux of the AR (Φ^2). The latter is very convenient: the helicity of a flux rope having N number of turns is simply N in this natural unit. Expressing helicity in this way also provides a convenient diagnostics for the stability of the twisted flux tube, since simulations show that above a critical end-to-end twist in the range of 2.5–2.75 π no equilibrium can be found, and the rope ascends rapidly (Török and Kliem, 2003, and references therein). The studied intervals by Chae (2001), Chae *et al.* (2002), Kusano *et al.* (2002), Moon *et al.* (2002), and Nindos and Zhang (2002) range from 6.5–120 hours and during such period LCT gave a sum of helicity injected by footpoint motions at most 0.2 Φ^2 (Nindos and Zhang, 2002). During the same time differential rotation injected only 0.02 Φ^2 helicity. All of the results show that photospheric footpoint motions (during the intervals studied) do not provide enough helicity to bring the flux tube twist close to the critical value (1.3–1.4). This low efficiency can be due to the lack of a coherent pattern: areas where positive or negative helicity is injected co-exist at any time, significant shearing motions may last for a relatively short period during the lifetime of an AR, and may even reverse direction.

Active regions cover only a minor fraction of the solar surface. Quiet

Sun areas have low magnetic flux density, but they harbor a huge amount of flux. Flux concentrations are in continuous motion following a random walk along random lattices (Lawrence and Schrijver, 1993). So it is important to find out how much helicity is injected by them. Using a tracking algorithm applied to high cadence ($\sim$5 min), high resolution ($0.61''$/pixel, smoothed over $\sim$3 pixels) SOHO/MDI magnetograms, Welsch and Longcope (2003) obtained an injection rate of $\sim$5 $\times$ 10^{19} Mx^2 cm^{-2} s^{-1} for the mutual magnetic helicity (the helicity coming from the winding of field lines from different flux elements about each other) in the quiet Sun, which corresponds to a whole-cycle, hemispheric mutual helicity flux of $\sim$$10^{42}$ Mx^2. The results of Welsch and Longcope (2003) indicate that the contribution of the quiet Sun to helicity injection by footpoint motions is negligible.

However, it is well possible that these tracking methods, which have serious limitations, largely underestimate the amount of helicity injected by the shear term. Démoulin and Berger (2003) pointed out that the apparent horizontal velocity field of intensity features in magnetograms, $\vec{u}$, is not necessarily identical to the plasma velocity field tangent to the surface, $\vec{v}_t$, though others have treated the two as equivalent. They derived what has since become known as the *Démoulin and Berger relation*: $\vec{u} = \vec{v}_t - \vec{B}_t v_n / B_n$, where vector components normal (n) and tangential (t) to the photosphere are denoted accordingly. They note that the flow field derived from LCT is only an estimate of $\vec{u}$, and discuss the inaccuracies of using LCT. One of the main limitations is low spatial resolution, which limits the obtained velocities to the velocity of group motion of the unresolved bunch of thin ($\leq$100 km) flux tubes covered by a pixel. Also, tracking motions may have great difficulties in areas lacking significant contrast, like sunspot umbrae. The latter may lead to a serious underestimation of the helicity flux, since most of the magnetic flux of the AR is located in such areas in the young active regions analyzed. Furthermore, a large class of motions leave B_n unchanged (i.e. twisting along isocontours) so they remain undetectable by these tracking methods. Another problem is linked to the ΔT and w parameters of the LCT method, which prevent tracking of fast motions and have a smoothing effect on the velocities, because the correlated sub-parts, for which a mean velocity is derived, are typically 2–5 times larger than the spatial resolution of the magnetogram.

Besides problems of velocity determination, there are also problems with the determination of B_n. It was discovered recently that SOHO/MDI underestimates magnetic flux densities by a factor of 0.64–0.69 (Berger and Lites, 2003), which means that all the helicity values obtained earlier using MDI have to be multiplied by a factor of $\sim$2. However, in areas with high magnetic flux density ($\geq$1300 G), the response of MDI becomes non-linear, which amplifies the underestimation of the helicity flux in strong umbrae.

8.3. COMPUTATIONS OF THE ADVECTION TERM

Computations of the advection term $2 \int_S (\vec{A_0} \cdot \vec{B})\vec{v} \cdot d\vec{S}$ from observations involves measurements of the transverse components of the magnetic field and longitudinal velocities, from which B_t and v_n can be determined. Vector magnetograms (after calibration and removal of the 180° ambiguity) can be transformed to provide photospheric maps of B_n and B_t. Longitudinal velocities are classically derived from the Doppler shift of spectral lines. However, since there is no safe way to transform them to v_n, they only provide useful data at disc center. Furthermore, in emerging magnetic field regions, where the advection term should be the largest, both upflows and downflows are present (convective collapse!), and the downflows may be 2–5 times stronger than the upflows (Lites *et al.*, 1998, and references therein); therefore there is no safe way to deduce v_n from Doppler measurements.

The first quantitative estimate of the helicity injection into an observed solar active region was made by Wang (1996), who deduced that 10^{43} Mx^2 of helicity was produced in an emerging flux region (AR 6233) over a period of just a few hours. He calculated changes in magnetic helicity density using vector magnetograms and tracing the change of α, the force-free parameter.

Kusano *et al.* (2002) developed a new method to derive helicity flux through the photosphere in active region NOAA 8100 by using observations of $\vec{B}$ and v_t (using a correlation tracking method) and computing v_n from the induction equation. Though the first results seemed contradictory, the method is promising, and information deduced from the induction equation could be used in the future to compute a more precise helicity flux through the photosphere.

However, a correlation tracking method is not measuring the plasma motions, but rather the displacement of the photospheric cuts of magnetic flux tubes. Such displacement is the result of both horizontal and vertical plasma motions. Démoulin and Berger (2003) show that both the shear and advection terms can be combined in one single term, in which the displacement velocity is used. More precisely, using the velocity deduced from a correlation tracking method, we get the full helicity flux (within the limitations of the observations). Thus, Démoulin and Berger (2003) show that it is not correct to add the helicity flux associated to vertical plasma motions to the helicity flux deduced from the velocities of photospheric footpoint motions.

8.4. COMPUTATIONS OF RELATIVE MAGNETIC HELICITY IN THE CORONA

Démoulin *et al.* (2002a) and Green *et al.* (2002) worked out a method to compute coronal relative magnetic helicity from observations. They used

SOHO/MDI magnetograms taken close to the central meridian passages of the studied ARs as boundary conditions for linear force-free field (lfff) magnetic extrapolations ($\vec{\nabla} \times \vec{B} = \alpha \vec{B}$; $\alpha = $ const). The extrapolated field lines were fitted with coronal loops observed with Yohkoh/SXT. The α value giving the best general fit between the models and observations was adopted for computation of the coronal helicity following Berger (1985): $H_r = 2\alpha \sum_{n_x=1}^{N_x} \sum_{n_y=1}^{N_y} |\widetilde{B}_{n_x,n_y}^2|/l(k_x^2 + k_y^2)$, where $\widetilde{B}_{n_x,n_y}$ is the Fourier amplitude of the field component B_n, $l = (k_x^2 + k_y^2 - \alpha^2)^{1/2}$, $k_x = 2\pi n_x/L$, $k_y = 2\pi n_y/L$ with L the horizontal extension of the computational box.

The coronal magnetic helicity content of an AR depends on the photospheric flux distribution and on the value of α. Even though in all their extrapolations α stays below its resonant value (which would give unrealistically high magnetic helicity), these authors used a linearized expression in α for the helicity computations (see Green *et al.*, 2002). Since they analyzed the evolution of coronal magnetic helicity in ARs as they evolved, it was important to keep the computational box of the same extension centered on the AR in all the cases. These computations of coronal relative magnetic helicity (Démoulin *et al.*, 2002a; Green *et al.*, 2002) carry the problems of lfff models, which are imperfect representations of the coronal field. However, the order of magnitude obtained for large ARs ($5 \times 10^{42} - 2 \times 10^{43}$ Mx^2) agrees quite well with theoretical expectations, thus they appear to be reasonably good estimates.

8.5. MAGNETIC HELICITY EJECTED VIA CMES

A CME is the result of an instability of the coronal field, so it will carry away part of the magnetic helicity of its source magnetic field. There is increasing evidence that the helicity sign of magnetic clouds (MCs) matches that of their source region, i.e. their associated erupting filament (Bothmer and Schwenn, 1994; Rust, 1994; Marubashi, 1997; Yurchyshyn *et al.*, 2001). Assuming a one to one correspondence between CMEs and MCs, i.e. interplanetary twisted flux tubes (e.g. Webb *et al.*, 2000), the helicity ejected in a CME can be evaluated using *in situ* measurements of the interplanetary magnetic field. DeVore (2000) computed the relative helicity per *unit length* in a twisted interplanetary flux tube using a numerically integrated form of Berger's (1999) equation, and the average values of the axial magnetic field $B_0 = (2.0 \pm 0.7) \times 10^{-4}$ G and radius $R = (2.1 \pm 0.7) \times 10^{12}$ cm for a set of 18 clouds studied by Lepping *et al.* (1990). The same computation was done for another sample of 23 clouds analyzed by Zhao *et al.* (2001), $B_0 = (2.4 \pm 0.8) \times 10^{-4}$ G and $R = (1.7 \pm 0.8) \times 10^{12}$ cm. For the length of the interplanetary flux tube two values were used: $L_1 = 0.5$ AU (DeVore, 2000) which yielded $H_r \approx 2 \times 10^{42}$ Mx^2, and $L_2 = 2$ AU (the cloud is still

connected to the Sun; see e.g. Richardson, 1997) which gives four times as much helicity for an average-size MC, i.e. CME. These mean helicity values have to be multiplied by the number of CMEs to obtain the total magnetic helicity ejected from an AR.

During the entire lifetime of two ARs (6 and 5 solar rotations, respectively) such counts have been made: NOAA 7978 was found to be the source region of 31 CMEs (Démoulin *et al.*, 2002a), while NOAA 8100 produced 65 CMEs (Green *et al.*, 2002). These numbers include corrections for data gaps and far-side locations of the ARs. They are much higher than previously thought based on pre-SOHO observations (4–5/AR/lifetime; e.g. DeVore, 2000), and imply a huge amount of (unsigned) helicity ejected from these ARs into the interplanetary space: $(62 - 248) \times 10^{42}$ Mx^2 (AR 7978) and $(130 - 520) \times 10^{42}$ Mx^2 (AR 8100), where the lower/upper estimates imply a flux tube length of 0.5/2 AU.

Nindos and Zhang (2002) studied a MC which was linked to a CME originating in AR 9165, in which they studied helicity injection by photospheric motions. Using the method of DeVore (2000) and B_0 and R measurements for this MC, the magnetic helicity was found as large as 32 (resp. 127) $\times 10^{42}$ Mx^2 with a flux tube length of 0.5 (resp. 2) AU! However, taking the average of MCs observed in the year 2000 they obtained an average magnetic helicity per cloud of 3.9 (resp. 15.4) $\times 10^{42}$ Mx^2, about a factor 2 above the mean values obtained from averaging well observed clouds!

There is a very large uncertainty in these helicity numbers, thus they should be regarded as rough approximative values. The greatest unknown is the length of the flux tube in a MC. Furthermore, even well-observed MCs, like the ones contained in the two samples used for the computations, show a great spread (van Driel-Gesztelyi *et al.*, 2003). Magnetic helicity depends on the third power of R and the second power of B_0, so their spread is amplified in the helicity results. Currently, we do not know the distribution of twist along the interplanetary flux rope, whether it is uniform, or concentrated in its front or its legs, which adds to the uncertainties.

8.6. MAGNETIC HELICITY BUDGET OF ACTIVE REGIONS

The total helicity budget of an active region may be written as:

$$H_{\text{flux from photospheric motions}} = \Delta H_{\text{corona}} + N H_{\text{CME}},$$

where Δ denotes the variation of the helicity, N is the number of the CMEs and H_{CME} is the mean helicity carried away per CME event.

Three groups have drawn the helicity budget of ARs, deriving from observations: (i) the helicity injection at the photospheric level by differential rotation and/or local footpoint motions, (ii) the changes in the coronal

helicity, as well as (iii) the helicity carried away by CMEs (Démoulin *et al.*, 2002a; Green *et al.*, 2002; Nindos and Zhang, 2002).

Their results are in good accordance: (i) helicity injected at the photospheric level by differential rotation is a minor contributor to the global helicity budget: CMEs remove at least 10 times more helicity than the one injected by differential rotation; (ii) photospheric shearing motions may inject much more helicity than the differential rotation, but present studies are – among other problems – limited to a few days and also by the spatial resolution of the observations; (iii) consequently the main source of magnetic helicity carried away in CMEs is still undetected at the photospheric level.

For example, for NOAA 7978 which was a simple isolated bipolar AR, Démoulin *et al.* (2002a) found that an amount of $\Delta H = 49 - 235 \times 10^{42}$ Mx^2 of magnetic helicity should be provided to the corona in order to account for all the CMEs. Expressing this in the "natural" units of helicity, i.e. in the square of the total magnetic flux of the AR, we obtain 0.25–1 Φ^2, since the magnetic flux of AR 7978 was $\Phi \sim 1.5 \times 10^{22}$ Mx (note that all these numbers are corrected for flux underestimation by MDI as derived by Berger and Lites, 2002). Since helicity expressed in this natural unit reveals the number of turns a flux rope has end-to-end, it actually shows that 31 CMEs carried away the equivalent helicity contained in the flux tube forming the AR having about one turn (if uniformly twisted across the flux tube).

This total helicity appears to be consistent with previous theoretical results. Moreno-Insertis and Emonet (1996) and Emonet and Moreno-Insertis (1998) showed that flux tubes, to be able to survive their rise through the convection zone, need to be twisted by a few turns. Though recent simulations by Abbett *et al.* (2001) indicated that the Coriolis force may also have a stabilizing effect on rising flux tubes, the need for them to be twisted did not disappear. Thus, the twist obtained from the helicity budgets seems to be in the right range.

9. Conclusions and perspectives

A complete CME would contain a shock (signatures: radio burst and discontinuity in velocity and density in situ data), a bright and dense frontal feature (white-light), a cavity (white-light), a core (Hα, EUV, X-rays, microwave, in-situ), then should be followed by the formation of a post-eruption arcade (X-rays, EUV, Hα). However, no CME has ever shown all possible signatures nor is there any particular signature which is found in all CMEs.

Multiwavelength and multi-instrument data are needed to obtain a complete picture of CMEs – the wider the wavelength range the better. However, we need to keep in mind that in our images we see two-dimensional projections of three-dimensional structures and it is often difficult to disentangle overlapping features. The STEREO mission will change this in the near future.

What is the underlying cause of CMEs? In the most successful CME models the build-up of magnetic stresses, i.e. strong shear and twist are necessary conditions for a CME to occur. In observations twisted CME structures are frequently seen and there is substantial evidence that a considerable amount of twist is carried away from the Sun by CMEs. There is also evidence rising that magnetic twist and shear (i.e. magnetic helicity) is the key to understand CMEs: they go off when too much helicity has built up in the corona. However, we need improved helicity measurements from the photosphere to 1 AU to prove this.

Direct observations, like helioseismology, do not seem to be able to put constraints on sub-surface generation of magnetic helicity in the near future. However, hopes are raised by the recent development of dynamo theories which are incorporating the analysis (and constraint) of magnetic helicity (e.g. Brandenburg, 2001). Moreover, a combination of theoretical advances in simulations of thin flux tubes and better photospheric observations can advance our knowledge on flux tubes in the convective zone, in particular on their twist/writhe magnetic helicity.

Improving photospheric measurements of $\vec{B}$ and $\vec{v}$ are crucial for a more precise determination of the helicity fluxes. High resolution vector magnetographs, like ASP, THEMIS and SOLAR B will provide suitable data for that. Combining photospheric and chromospheric vector magnetograms would make it possible to derive the vertical derivatives of the magnetic field, and this, combined with information deduced from the induction equation, could be used to compute a more precise helicity flux through the photosphere.

For a better determination of coronal helicity we need improved magnetic field extrapolations and high resolution multi-wavelength coronal loop observations.

For better heliospheric helicity estimates we need more realistic models of MCs, and to advance our knowledge on the length of field lines in MCs (to be able to trace field lines, e.g. Larson *et al.*, 1997). It would also be important to find out how uniform the twist is along an interplanetary twisted flux tube, which we may be able to measure if the same MC would pass by STEREO A and B.

For an improved link between helicity in the solar corona and heliosphere we have to associate a given CME to a given MC, which will have a better

chance when STEREO and its SECCHI heliospheric imager are operational. Finally, we need to combine global and local measurements to achieve our goal of having a complete budget of magnetic helicity, which, in turn will advance our understanding of CMEs.

Acknowledgements

References

Abbett, W.P., Fisher, G.H., and Fan, Y.: 2001, *Astrophys. J.* **546**, 1194.

Abramenko, V.I., Wang, T., and Yurchishin, V.B.: 1996, *Solar Phys.* **168**, 75.

Amari, T., Luciani, J.F., Mikić, Z., and Linker, J.A.: 2000, *Astrophys. J.* **529**, L49.

Antiochos, S.K.: 1998, *Astrophys. J.* **502**, L181.

Antiochos, S.K., DeVore, C.R., and Klimchuk, J.A.: 1999, *Astrophys. J.* **510**, 485.

Aulanier, G., DeLuca, E.E., Antiochos, S.K., McMullen, R.A., and Golub, L.: 2000, *Astrophys. J.* **540**, 1126.

Berger, M.A.: 1984, *Geophys. Astrophys. Fluid Dynamics* **30**, 79.

Berger, M.A.: 1985, *Astrophys. J. Suppl. Ser.* **59**, 433.

Berger, M.A.: 1986, *Geophys. Astrophys. Fluid Dynamics* **34**, 265.

Berger, M.A.: 1988, *Astron. Astrophys.* **201**, 355.

Berger, M.A.: 1999, in M.R. Brown, R.C. Canfield, and A.A. Pevtsov (eds.), *Magnetic Helicity in Space and Laboratory Plasmas*, Geophys. Monograph 111, A.G.U., 1.

Berger, M.A. and Field, G.B.: 1984, *J. Fluid Mech.* **147**, 133.

Berger, M.A. and Ruzmaikin, A.: 2000, *J. Geophys. Res.* **105**, A5, 10481.

Berger, T.E. and Lites, B.W.: 2003, *Solar Phys.* **213**, 213.

Bhatnagar, A.: 1996, *Astrophys. Space Sci.* **243**, 105.

Bothmer, V. and Schwenn, R.: 1994, *Space Sci. Rev.* **70**, 215.

Bougeret, J.-L., Kaiser, M.L., Kellogg, P.J. *et al.*: 1995, *Space Sci. Rev.* **71**, 231.

Brandenburg, A.: 2001, *Astrophys. J.* **550**, 824.

Brandenburg, A. and Blackman, E.G.: 2003, *Astrophys. J.* **579**, 99.

Burlaga, L., Sittler, E., Mariani, F., and Schwenn, R.: 1981, *J. Geophys. Res.* **86**, 6673.

Canfield, R.C., Hudson, H.S. and McKenzie, D.E.: 1999, *Geophys. Res. Lett.* **26**, 627.

Chae, J., 2001, *Astrophys. J.* **560**, L95.

Chae, J., Wang, H., Qiu, J., Goode, P.R., Strous, L., and Yun, H.S.: 2001, *Astrophys. J.* **560**, 476.

Chen, J.: 1989, *Astrophys. J.* **338**, 453.

Chen, J.: 2001, *Space Sci. Rev.* **95**, 165.

Chen, J. and Krall, J.: 2003, *J. Geophys. Res.* **108**, A11, SSH 2-1.

Cliver, E.W. and Hudson, H.S.: 2002, *J. Atm. Solar-Terr. Phys.* **64**, 231.

Delannée, C. and Aulanier, G.: 1999, *Solar Phys.* **190**, 107.

Delannée, C., Delabudiniére, J.-P., and Lamy, P.: 2000, *Astron. Astrophys.* **355**, 725.

Démoulin P. and Berger, M.A.: 2003, *Solar Phys.* **215**, 203.

Démoulin, P. and Klein, K.-L.: 2000, in J.P. Rozelot, L. Klein, and J.-C. Vial (eds.), *Transport and Energy Conversion in the Heliosphere*, Lecture Notes in Physics, vol. 553, 99.

Démoulin P., Mandrini, C.H., van Driel-Gesztelyi, L. *et al.*: 2002a, *Astron. Astrophys.* **382**, 650.

Démoulin P., Mandrini, C.H., van Driel-Gesztelyi, L., López Fuentes, M.C., and Aulanier, G.: 2002b, *Solar Phys.* **207**, 87.

DeVore, C.R.: 2000 *Astrophys. J.* **539**, 944.

Dodson, H.W. and Hedeman, E.R., 1970, Solar Phys., **13**, 401.

Dryer, M.: 1982, *Space Sci. Rev.* **33**, 233.

Dryer, M.: 1996, *Solar Phys.* **169**, 421.

Eddy, J.A.: 1974, *Astron. Astrophys.* **34**, 235.

Emonet, T. and Moreno-Insertis, F.: 1998, *Astrophys. J.* **492**, 804.

Forbes, T.G. and Isenberg, P.A.: 1991, *Astrophys. J.* **373**, 294.

Gary, G.A. and Moore, R.L.: 2004, *Astrophys. J.*, in press.

Green L.G., López-Fuentes, M.C., Mandrini, C.H. *et al.*, *Solar Phys.* **208**, 43.

Gopalswamy, N.: 2003, *Adv. Space Res.* **31**, no. 4, 869.

Gopalswamy, N., Nitta, N., Manoharan, P.K., Raoult, A., and Pick, M.: 1999, *Astron. Astrophys.* **347**, 684.

Gopalswamy, N., Kaiser, M.L., Thompson, B.J. *et al.*: 2000, *Geophys. Res. Lett.* **27**, 1427.

Gopalswamy, N., Yashiro, S., Kaiser, M.L., Howard, R.A., and Bougeret, J.-L.: 2001, *J. Geophys. Res.* **106**, A12, 29219.

Gopalswamy, N., Shimojo, M., Lu, W. *et al.*: 2003, *Astrophys. J.* **586**, 562.

Gosling, J.T.: 2000, in B.L. Dingus, D.B. Kieda, and M.H. Salamon (eds.), Proc. 26th International Cosmic Ray Conference, AIP Conf. Proc. no. 516, American Inst. Phys. Press, New York, 59.

Gosling, J.T., Hildner, E., MacQueen, R.M., Munro, R.H., Poland, A.I., and Ross, C.L.: 1976, *Solar Phys.* **48**, 389.

Hale, G.E.: 1925, *Publ. Astron. Soc. Pacific* **37**, 268.

Harra, L.K. and Sterling, A.C.: 2001, *Astrophys. J.* **561**, L215.

Howard, R.A., Michels, D.J., Sheeley, N.R., Jr., and Koomen, M.J.: 1982, *Astrophys. J.* **263**, L101.

Hudson, H.S., Acton, L.W., and Freeland, S.L.: 1996, *Astrophys. J.* **470**, 629.

Hundhausen, A.: 1997, in N. Crooker, J.A. Joselyn, and J. Feynman (eds.), *Coronal Mass Ejections*, Geophys. Monograph 99, A.G.U., 1.

Hundhausen, A.: 1999, in K.T. Strong, J.L.R. Saba, B.M. Haisch, and J.T. Schmelz (eds.), *The Many Faces of the Sun: A Summary of the Results from NASA's Solar Maximum Mission*, Springer, New York, 143.

Isenberg, P.A., Forbes, T.G., and Démoulin, P.: 1993, *Astrophys. J.* **417**, 368.

Khan, J.I. and Hudson, H.S.: 2000, *Geophys. Res. Lett.* **27**, no. 8, 1083.

Klassen, A., Aurass, H., Mann, G., and Thompson, B.J.: 2000, *Astron. Astrophys. Suppl. Ser.* **141**, 357.

Klimchuk, J.A.: 2000, in P. Song, G. Siscoe, and H. Singer (eds.), AGU Monograph Series, AGU, Washington, 143.

Kusano, K., Maeshiro, T., Yokoyama, T., and Sakurai, T.: 2002, *Astrophys. J.* **577**, 501.

Larson, D.E., Lin, R.P., McTiernan, J.M. *et al.*: 1997, *Geophys. Res. Lett.* **24**, 1911.

Lawrence, J.K. and Schrijver, C.J.: 1993, *Astrophys. J.* **411**, 402.

Leblanc, Y., Dulk, G.A., and Bougeret, J.-L.: 1998, *Solar Phys.* **183**, 165.

Lepping, R.P., Burlaga, L.F., and Jones, J.A.: 1990, *J. Geophys. Res.* **95**, 11957.

Leroy, J.L., Bommier, V., and Sahal-Bréchot, S.: 1983, *Solar Phys.* **83**, 135.

Lin, J., Forbes, T.G., Isenberg, P.A., and Démoulin, P.: 1998, *Astrophys. J.* **504**, 1006.

Lites, B.W., Skumanich, A., and Martínez Pillet, V.: 1998, *Astron. Astrophys.* **333**, 1053.

Longcope, D.W. and Pevtsov, A.A.: 2003, *Adv. Space Res.* **32**, no. 10, 1845.

Low, B.C. and Smith, D.F.: 1993, *Astrophys. J.* **410**, 412.

MacQueen, R.M., Eddy, J.A., Gosling, J.T. *et al.*: 1974, *Astrophys. J.* **187**, L85.

Manoharan, P.K., Ananthakrishnan, S., Dryer, M. *et al.*: 1995, *Solar Phys.* **156**, 377.

Manoharan, P.K., van Driel-Gesztelyi, L., Pick, M., and Démoulin, P.: 1996, *Astrophys. J.* **468**, L73.

Marubashi, K.: 1997, in N. Crooker, J.A. Joselyn, and J. Feynman (eds.), *Coronal Mass Ejections*, Geophys. Monograph 99, A.G.U., 147.

Martin, S.F., Bilimoria, R., and Tracadas, P.W.: 1994, in R.J. Rutten and C.J. Schrijver (eds.), *Solar Surface Magnetism*, Kluwer, Dordrecht, 303.

Martin, S.F. and McAllister, A.H.: 1997, in N. Crooker, J. A. Joselyn, and J. Feynman (eds.), *Coronal Mass Ejections*, Geophys. Monograph 99, A.G.U., 127.

Mikić, Z. and Linker, J.A.: 1999, *Bull. Am. Astron. Soc.* **31**, 918.

Moon, Y.-J., Chae, J., Choe *et al.*: 2002a, *Astrophys. J.* **574**, 1066.

Moon, Y.-J., Choe, G.S., Wang, H. *et al.*: 2002b, *Astrophys. J.* **581**, 694.

Moreno-Insertis, F. and Emonet, T.: 1996, *Astrophys. J.* **472**, L53.

Nakagawa, Y., Raadu, M.A., Billings, D.E., and McNamara, D.: 1971, *Solar Phys.* **19**, 72.

Nindos, A. and Zhang, H.: 2002, *Astrophys. J.* **573**, L133.

Nindos, A., Zhang, J., and Zhang, H.: 2003, *Astrophys. J.* **594**, 1033.

November, L.J. and Simon, G.W.: 1988, *Astrophys. J.* **333**, 427.

Peter, H.: 1996, *Mon. Not. Royal Astron. Soc.* **278**, 821.

Pevtsov, A.A. and Balasubramaniam, K.S.: 2003, *Adv. Space Res.* **32**, no. 10, 1867.

Pevtsov, A.A., Canfield, R.C., and Metcalf, T.R.: 1995, *Astrophys. J.* **440**, L109.

Pevtsov, A.A., Maleev, V.M., and Longcope, D.W.: 2003, *Astrophys. J.* **593**, 1217.

Pohjolainen, S., Maia, D., Pick, M. *et al.*: 2001, *Astrophys. J.*, **556**, 421.

Richardson, I.G.: 1997, in N. Crooker, J.A. Joselyn, and J. Feynman (eds.), *Coronal Mass Ejections*, Geophys. Monograph 99, A.G.U., 189.

Richardson, R.S.: 1941, *Astrophys. J.* **93**, 24.

Rust, D.M.: 1983, *Space Sci. Rev.* **34**, 21.

Rust, D.M.: 1994, *Geophys. Res. Lett.* **21**, 241.

Rust, D.M. and Hildner, E.: 1976, *Solar Phys.* **48**, 381.

Rust, D.M. and Kumar, A.: 1996, *Astrophys. J.* **464**, L199.

Schwenn, R.: 1995, in D. Winterhalter *et al.* (eds.), *Solar Wind Eight*, AIP Conf. Proc. 382, 426.

Seehafer, N.: 1990, *Solar Phys.* **125**, 219.

Seehafer, N., Gellert, M., Kuzanyan, K.M., and Pipin, V.V.: 2003, *Adv. Space Res.* **32**, no. 10, 1819.

Smith, S.F., Harvey, K.L.: 1971, in C.J Macris (ed.), *Physics of the Solar Corona*, Reidel, Dordrecht, 156.

St. Cyr, O.C., Howard, R.A., Sheeley, N.R. ıet al.: 2000, *J. Geophys. Res.* **105**, no. A8, 18169.

Subramaniam, P. and Dere, K.P.: 2001, *Astrophys. J.* **561**, 372.

Thompson, B.J., Plunkett, S.P., Gurman, J.B., Newmark, J.S., St. Cyr, O.C., and Michels, D.J.: 1998, *J. Geophys. Res. Lett.* **25**, 2465.

Thompson, B.J., Gurman, J.B., Neupert, W.M. *et al.*: 1999, *Astrophys. J.* **517**, 151.

Thompson, B.J., Reynolds, B., Aurass, H. *et al.*: 2000, *Solar Phys.* **193**, 161.

Tokumaru, M., Kojima, M., Fujiki, K., and Yokobe, A.: 2000, *J. Geophys. Res.* **105**, A5, 10435.

Török, T. and Kliem, B.: 2003, *Astron. Astrophys.* **406**, 1043.

Tousey, R.: 1973, *Bull. American Astron. Soc.* **5**, 419.

Török, T. and Kliem, B.: 2003, *Astron. Astrophys.* **406**, 1043.

van Driel-Gesztelyi L., Mandrini, C.H., Thompson, B.J. *et al.*: 1999, in B. Schmieder, A. Hofmann, and J. Staude (eds.), *Magnetic Fields and Oscillations*, ASP Conf. Ser. 184, 302.

van Driel-Gesztelyi, L., Manoharan, P.K., Démoulin, P. *et al.*: 2000, *J. Atm. Solar-Terr. Phys.* **62**, no. 16, 1437.

van Driel-Gesztelyi L., Schmieder B., and Poedts S.: 2002, in H. Sawaya-Lacoste (ed.), Proc. Second Solar Cycle and Space Weather Euroconference, ESA SP-477, 47.

van Driel-Gesztelyi, L., Démoulin, P., and Mandrini, C.H.: 2003, *Adv. Space Res.* **32**, no. 10, 1855.

Wang, J.: 1996, *Solar Phys.* **63**, 319.

Warmuth, A., Vršnak, B., Aurass, H., and Hanslmeier, A.: 2001, *Astrophys. J.* **560**, L105.

Webb, D.F.: 2002, in A. Wilson (ed.), *From Solar Min to Max: Half a Solar Cycle with SOHO*, Proc. SOHO 11 Symposium, ESA SP-508, 409.

Webb, D.F., Cliver, E W., Crooker, N.U., St. Cry, O.C., and Thompson, B.J.: 2000, *Geophys. Res. Lett.* **105**, A4, 7491.

Welsch, B.T. and Longcope, D.W.: 2003, *Astrophys. J.* **588**, 620.

Wu, S.T.: 1982, *Space Sci. Rev.* **32**, 115.

Yurchyshyn, V.B., Wang, H., Goode, P.R., and Deng, Y.: 2001, *Astrophys. J.* **563**, 381.

Zhao, X.P., Hoeksema, J.T., and Marubashi, K.: 2001, *J. Geophys. Res.* **106**, 15643.

HIGH ENERGY RADIATION FROM THE SUN

J.C. BROWN
Department of Physics and Astronomy
University of Glasgow, Glasgow G12 8QQ, Scotland

Abstract. This article is a summary of 6 lectures given at the Summer School & Workshop *Solar Magnetic Phenomena* at Kanzelhöhe Solar Observatory, 25th August to 5th September 2003. It addresses observations and theory of high energy radiation from the sun, with the emphasis almost entirely on hard X-rays (HXR) from flares but with brief mention of γ-rays and of nonthermal processes in the non-flaring sun. Following an outline of hard X-ray instrumentation, some relevant plasma properties are briefly discussed, and the importance of HXR data to flare theory explained.

There then follows a more detailed discussion of HXR source theory and data interpretation. The discussion is oriented toward the fact that since February 2002 data have been on stream from the RHESSI Mission providing high resolution HXR (and γ-ray) imaging spectrometry for the first time by combining Ge detectors with rotating modulation collimators.

Volume integrated source spectra are first discussed under the headings:

- bremsstrahlung cross-sections $Q(\epsilon, E)$,
- total photon spectrum $J(\epsilon)$ and mean source ('thin target') electron spectrum, $\bar{F}(E)$, for homogeneous and inhomogeneous sources,
- $J(\epsilon)$ for various parametric $\bar{F}(E)$ and $Q(\epsilon, E)$,
- inversion of $J(\epsilon)$ to find $\bar{F}(E)$ and dependence on $Q(\epsilon, E)$,
- sensitivity of $\bar{F}(E)$ to noise in $J(\epsilon)$.

Next, large scale issues of electron beam propagation are discussed including:

- HXR source spatial structure,
- transport effects and the collisional thick target model injection spectrum $\mathcal{F}_0(E_0)$, including sensitivity to $J(\epsilon)$,
- beam electrodynamics,
- beam heating of the flare plasma, including chromospheric evaporation and Neupert Effect,
- micro-events.

Finally, a short list of RHESSI discovery highlights is presented.

1. Introduction

These lectures are concerned with 'high' energy solar radiation, a term which will be taken here loosely to mean photons of energy ϵ high enough

that a plasma of solar abundances has negligible atomic line contribution – essentially above the Iron line complex near $\epsilon \approx 7$ keV. By coincidence this is also the sort of energy above which electron mean free paths in the corona begin to approach flare loop lengths. Consequently by 'high energy' or 'hard' we also mean that we are approaching the regime where the plasma/particles are 'nonthermal'. Whether or not particles are nonthermal is a somewhat gray area but also one which is absolutely crucial in issues of particle energy budget and its role in flare heating. This is because most of the power in the typically steep particle spectra lies at the low energy end where the thermal/nonthermal uncertainty lies.

At the high energy end, MeV and above, lie γ-rays. Continuum γ-rays are distinct (but not distinguishable) from HXR continuum photons in having their origins in nuclear processes, as do γ-ray lines, while the HXR continuum is of 'atomic' origin – collisional bremsstrahlung or free-free radiation. Solar γ-ray line studies is a major field in itself and will be touched on only briefly here. Fortunately between the dates of presentation of these lectures and of writing this text, the sun shone kindly on the γ-ray community by indulging in a late-cycle outburst of major flare activity with superb aurora and increasing the number of strong RHESSI γ-ray events from one to at least four.

More generally solar 'high energy' radiation could be taken to include solar cosmic rays and neutrons and perhaps even radio emission insofar as radio photons, while of low energy, are often emitted by high energy electrons and so are a high energy electron diagnostic. None of these is covered in these lectures, except in passing.

2. Some basics

2.1. HXR INSTRUMENTATION

Early HXR detection/spectrometry was done with proportional counters then with scintillation counters on satellites like NASA's OGO and OSO series and ESRO TD1A. Such detectors were also carried aboard several interplanetary probes (e.g. ISEE 3 and PVO) enabling some early 'stereo' studies of HXR source geometry and directivity. Spectrometry with such detectors is fairly crude, with resolution $\Delta\epsilon/\epsilon \approx 0.3$ – sufficient to allow measurement of a parametric hardness indicator like the spectral index γ for spectrum $J(\epsilon) \propto \epsilon^{-\gamma}$ (small/large $\gamma \leftrightarrow$ hard/soft spectrum). In events with good count statistics a general change in γ with energy could also sometimes be seen. However, the data were of nowhere near the resolution $\Delta\epsilon/\epsilon$ needed for application of the inverse diagnostic spectrometry approach first advocated by Brown (1971). The advent of solid state Ge detectors and their application to solar physics, first on a balloon (Lin and Schwartz, 1987)

then combined with imaging on RHESSI (Lin *et al.*, 2002) transformed high energy spectrometry with energy resolution $\Delta\epsilon \approx 1$ keV corresponding to up to $\Delta\epsilon/\epsilon \approx 0.1$ at 10 keV and ≈ 0.001 at 1 MeV, limited in practice by photon count statistics.

The technology of direct imaging by grazing incidence optics has progressed amazingly in recent years (XMM and Chandra) but the ϵ^{-3} dependence of the necessary grazing angle rules it out for imaging the truly hard X-rays being discussed here – Fresnel lenses likewise at present. This leaves various forms of collimator device for HXR and γ-ray imaging. A pinhole camera is a sort of collimation device, each 'pixel' on the image plane corresponding to the direction of the pinhole (diameter d) at distance D. The problem is that to get good angular resolution requires $d/D \ll 1$ which implies very large D for reasonable collecting area $\approx d^2$ though such a mission (POF) was studied by NASA. A single collimator 'tube' of length D and hole size d provides the same resolution but with a one pixel field of view and the same tiny collecting area. The HXIS (Hard X-ray Imaging Spectrometer) instrument aboard SMM (Solar Maximum Mission) tackled this problem with a multicollimator assembly. A set of miniproportional counter 'pixels' covered the field of view, each being fed photons through a collimator, and each of these pointing in slightly different directions on the sun. Each collimator consisted of a large set of N parallel subcollimators of large D but very small d. Each collimator thus achieved resolution d/D but with collecting area Nd^2.

A distinct approach is to view the sun with a set of detectors each fed photons through a range of masks of different patterns and to reconstruct the original source image by comparing the signals in each of the detectors, rather akin to radio image reconstruction from the elements of an interferometer array. Such mask techniques take many forms (Skinner and Ponman, 1995) and was first used in Hinotori then in Yohkoh for solar HXR imaging. One of the simplest to understand is the case of a set of rotating grids of different spacings and orientations. A simple analogy illustrates the idea. A fluorescent tube observed through the fingers of a moving hand gives a signal which modulates differently according to how open the finger grid spacing is and to the orientation of the hand. Signals from a set of detectors behind a suitable set of such moving grids allows Fourier-like reconstruction of the scene behind the hand. This is the principle behind the Ramaty High Energy Spectroscopic Imager RHESSI (Lin *et al.*, 2002) which has rotation modulation collimators. Since the imaging is not direct, image reconstruction is limited by signal to noise and, for a time varying source, by the satellite rotation rate. For more on this imaging technique see Hurford *et al.* (2002) and `http://hesperia.gsfc.nasa.gov/hessi/`.

2.2. SOME BASIC SOLAR PLASMA PROPERTIES

To set the context of solar HXR sources, it is useful to be aware of typical flare plasma parameters (density n, temperature T) in the low and high solar atmosphere:

Chromosphere $n \approx 10^{12} - 10^{14}$ cm^{-3}, $T \approx 10^4$ K,

Corona $n \approx 10^9 - 10^{11}$ cm^{-3}, $T \approx 10^7$ K.

The magnetic field strength B in the photosphere can be several kilogauss in sunspots. In absolute value it declines with altitude but the plasma density and pressure decline faster so the field pressure and energy density dominate in the corona (low β plasma) where the field, though very hard to detect directly, is thought to be in the range of hundreds of gauss.

The overall dimension of a flare region is $L \approx 10^9$ cm with associated volume $V \approx L^3 \approx 10^{27}$ cm^3. Thus the magnetic energy available from a non-potential field component B is

$$\mathcal{E}_B = \frac{B^2 V}{8\pi} \approx 4 \times 10^{30} B_2^2 L_9^3 \quad (\text{erg}) \tag{1}$$

and the total number of particles in V is

$$\mathcal{N} = nL^3 \approx 10^{37} n_{10} L_9^3, \tag{2}$$

where $B_2 = B/10^2$, $L_9 = L/10^9$, $n_{10} = n/10^{10}$, etc. Consequently the mean energy released per particle is

$$\bar{E} = \frac{B^2}{8\pi n} \approx 25 \frac{B_2^2}{n_{10}} \quad (\text{keV}). \tag{3}$$

These numbers show that one expects a huge number of energetic particles at deka-keV as observed. At such energies the collisional mean free path (see below) is huge compared to current sheet thicknesses and comparable with the size L of the whole region. Thus the particle distribution is likely to be substantially non-Maxwellian and a pure MHD approach to reconnection theory is suspect.

If one simply adopts the observed field dissipation timescale τ then the expected EMF across L is, by Faraday's law

$$EMF \approx \frac{BL^2}{\tau} \approx \frac{B_2 L_9^2}{\tau_2} \quad (\text{GV}), \tag{4}$$

showing that the potential exists to accelerate particles out of the mean distribution up to the highest solar cosmic ray energies observed (subject to radiative losses which severely limit electron acceleration).

The reconnection theory of τ is still far from satisfactory. The resistive dissipation timescale associated with a simple current sheet of thickness l can be obtained from Ampere's law, Faraday's law, and Ohm's law

$$\nabla \times \nabla \times \mathbf{B} = \nabla \times \frac{\mathbf{j}}{c} = \nabla \times \frac{\sigma \mathbf{E}}{c} = \frac{\sigma}{c} \frac{\partial \mathbf{B}}{\partial t} \tag{5}$$

so that with $\nabla \approx 1/l$ and $\partial/\partial t \approx 1/\tau_{\text{rec}}$ we get

$$\tau_{\text{rec}} \approx \frac{\sigma l^2}{c} \approx 30 \, l^2 \ (\text{sec}) \,. \tag{6}$$

Thus flare observations would demand a sheet thickness l around 1 cm!!

Propagation of individual particles is governed by two main characteristic lengths:

(a) that of their spiralling gyro motion around the field with characteristic Larmor radius r_L given for mass m and perpendicular speed v by

$$\frac{mv^2}{r_L} = \frac{evB}{c} \quad \rightarrow \quad r_L \approx \frac{2}{B_2} \frac{mv}{m_e c} \ (\text{cm}) \,. \tag{7}$$

The B field thus guides particles tightly and can also result in their being mirrored/trapped if the field convergence is sufficient or the longitudinal speed is small (large pitch angle).

(b) their collisional mean free path. For Coulomb collisions the fast electron mean free path is

$$\lambda_{\text{coll}} = \frac{E}{dE/dz} = \frac{E^2}{K} \approx 5 \times 10^9 \frac{(E/10 \text{ keV})^2}{n_{10}} \ (\text{cm}) \,, \tag{8}$$

where $K = 2\pi e^4 \Lambda$ and the Coulomb logarithm $\Lambda \approx 20$. The corresponding stopping time and column density are

$$t_{\text{coll}} = \frac{\lambda_{\text{coll}}}{v} \approx (E/10 \text{ keV})^{3/2} \ (\text{sec}) \tag{9}$$

and

$$N_{\text{coll}} = \lambda_{\text{coll}} \, n \approx 5 \times 10^{19} \frac{(E/10 \text{ keV})^2}{n_{10}} \ (\text{cm}^{-2}) \,. \tag{10}$$

In practice, the typically high particle flux involved means that the fast electrons may behave collectively generating plasma waves (which emit radio waves and may extract beam energy) and drive return currents in the plasma to satisfy the overall beam electrodynamics as mentioned again later. Note that beam electrodynamics is very different from MHD because the timescales etc. involved are such that the displacement current (charge

conservation) term $\partial E/\partial t$ in Ampere's law cannot be ignored. Important parameters here are the electron plasma period

$$\tau_{\rm pe} \approx 10^{-9}\, n_{10}^{-1/2}\ ({\rm sec}) \tag{11}$$

and the Debye length

$$\lambda_{\rm D} \approx v_{\rm th} \times \frac{\tau_{\rm pe}}{2\pi} \approx 0.15\, n_{10}^{1/2} T_7^{1/2}\ ({\rm cm}) \tag{12}$$

where the electron thermal speed is

$$v_{\rm th} = (kT/m_e)^{1/2} \approx 10^9\, T_7^{1/2}\ ({\rm cm\ s^{-1}})\,.$$

2.3. COULOMB COLLISIONS AND BREMSSTRAHLUNG HARD X-RAYS

Coulomb collisions are encounters between charged particles. Here we will be concerned mainly with fast electrons as the test particles. To understand the theory of HXR sources it is important to appreciate the distinctive properties (in classical terms) of short and long range encounters and also of electron-ion (e-i) as against electron-electron (e-e) collisions. In long range e-i encounters, the effect is almost elastic deflection of the electron because ions are very massive, but the electron does lose a little energy by radiation (*bremsstrahlung*) as it is 'braked'. For very close encounters the radiated photons can approach energy $\epsilon = E$ for electron energy E (short wavelength limit). In the case of e-atom encounters long range collisions are affected by screening, and by inelastic processes (ionisation and excitation) but energetic bremsstrahlung-emitting short range collisions of fast electrons are unaffected by the presence of orbital electrons. The inelastic energy losses on atomic electrons are very similar to losses on free electrons except that the binding of atomic electrons reduces the energy loss by a factor of around 2.6. The main energy loss of average individual fast electrons is in fact very long range e-e collisions with impact parameter near its maximum limit (typically the smaller of r_L, λ_D which are both of order 1 cm). The energy loss in one such collision is fantastically small and it takes of order 10^{20} of them to stop a 20 keV electron. However, the cumulative energy loss by such collisions is of order 10^5 times greater than that lost to short range collision bremsstrahlung. There is of course also energy lost by bremsstrahlung at $\epsilon \ll E$ in long range encounters but, since electron spectra are so steep, most HXR radiation at energy ϵ comes from electrons of E just above ϵ.

In summary, the key collisional effects undergone by a fast electron are
- e-i long range collisions which deflect electrons (and emit low energy bremsstrahlung),

  – long range e-e and e-atom collisions which result in kinetic energy
    exchange (plasma heating) and energy loss from fast electrons,
  – short range e-i and e-atom collisions which emit high energy brems-
    strahlung.

   It should also be noted that:
(a) e-e bremsstrahlung becomes important at energies of order $m_e c^2$.
(b) The above applies to fast electrons moving in a cold background. When
    the entire electron population is hot, there is on average no e-e energy
    exchange and the only energy loss is by bremsstrahlung provided the
    high pressure plasma is contained magnetically. In principle this can
    result in a much more efficient source of HXR radiation as in various
    'thermal' models – see below.

2.4. HXR SOURCE 'CARTOONS' AND THE IMPORTANCE OF HXR DATA

HXR bursts are typically of tens of seconds duration and part of the impul-
sive phase of flares. They are a particularly important diagnostic of flare
electron heating and acceleration because the solar atmosphere down to the
photosphere is optically thin at these energies and the radiation process is
simple, (unlike radio bursts) involving no plasma collective effects. Conse-
quently HXR source structure in space and time and the HXR spectrum
are fairly direct indicators of electron acceleration and propagation though
not without considerable ambiguity as discussed below. Flare luminosity in
HXRs themselves is very small ($L_{HXR} \approx 10^{24}$ erg s^{-1} above 20 keV) but,
as noted above, for every bremsstrahlung emitting close e-i collision there
are numerous long range energy losing e-e ones. Consequently the electron
power above 20 keV needed to produce this L_{HXR} is $P_e \approx 10^{29}$ erg s^{-1},
comparable to the total flare power. This is the origin of the widely held
view that fast electrons play a key role in flare impulsive phase heating
and energy transport. This value of $P_e \approx 10^{29}$ erg s^{-1} is based on the
assumption of fast electrons in a cool background $kT \ll E$ and could be
much lower if the HXR spectrum is thermally dominated up to energies
substantially above 20 keV.
   HXR images in general have quite complex structure but many cases
follow a basic pattern of two bright footpoints at the ends of a magnetic
loop, sometimes with some fainter emission at or above the looptop. This
is in line with the early (pre-imaging) cartoon models proposed. These
comprised

  – the coronal magnetic trap model (Takakura and Kai, 1966),
  – the trap plus precipitation model (Kane, 1974),
  – the thick target model (Brown, 1971; Hudson, 1972),

—   the thermal model (Chubb, Friedman, and Kreplin, 1966; Brown, 1974), all of which have been developed in great detail since.

3. Theory of whole source HXR spectra

3.1. BASIC RELATION BETWEEN $J(\epsilon)$, $\bar{F}(E)$ AND $Q(\epsilon, E)$

For a fast electron distribution of density dn_e/dE per unit energy E in a plasma of total hydrogen density n_p the rate of bremsstrahlung photon emission per unit volume per unit photon energy ϵ from electrons in $E, E + dE$ is $dj(\epsilon, E) \propto n_p v(E)(dn_e/dE)dE$ where $v(E)$ is the electron speed. The proportionality constant $Q(\epsilon, E)$ is the bremsstrahlung cross section differential in ϵ. $Q(\epsilon, E)$ here includes a factor ≈ 1.6 to allow for e-i bremsstrahlung from ions and atoms heavier than hydrogen and can also include e-e bremsstrahlung. In general we should also recognise that $Q(\epsilon, E)$, and hence j, depends on direction. Such directivity of emission is an interesting diagnostic in itself but at low energies the directivity observed (by statistics of fluxes across the solar disk and from stereo data) is small and most treatments ignore it, the electrons being approximated as isotropic.

To obtain the total j for all electron energies we integrate over all $E \geq \epsilon$ to give

$$j(\epsilon) = \frac{Q_0 m_e c^2 n_p}{\epsilon} \int_\epsilon^\infty \frac{F(E)}{E} q(\epsilon, E)\, dE \,, \tag{13}$$

where $F(E) = v(E)dn_e/dE$ is the electron flux density spectrum (cm^{-2} s^{-1} per unit E) and we have defined the dimensionless cross section function q by

$$Q(\epsilon, E) = \frac{Q_0 m_e c^2}{\epsilon E} q(\epsilon, E) \tag{14}$$

with $Q_0 \approx \zeta \alpha r_e^2$ where r_e is the classical electron radius, α is the fine structure constant and ζ the heavy ion correction factor. In general q is complicated (Koch and Motz, 1959) but for present illustration purposes two simple approximations will suffice. These are the Kramers approximation

$$q_k(\epsilon, E) = \begin{cases} 1 & : \ E \geq \epsilon, \\ 0 & : \ E < \epsilon. \end{cases} \tag{15}$$

and the Bethe Heitler approximation

$$q_{\mathrm{BH}}(\epsilon, E) = \begin{cases} \log \frac{1+\sqrt{(1-\epsilon/E)}}{1-\sqrt{(1-\epsilon/E)}} & : \ E \geq \epsilon, \\ 0 & : \ E < \epsilon. \end{cases} \tag{16}$$
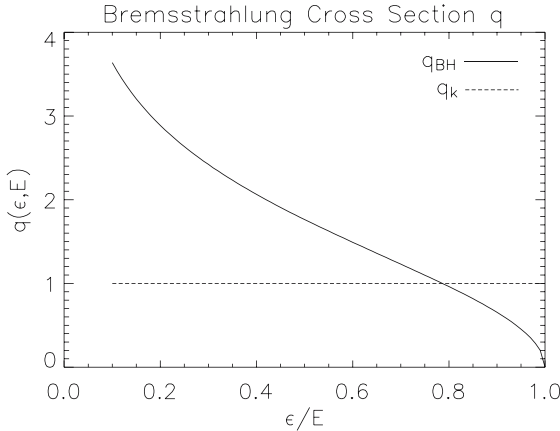
Figure 1. Dimensionless cross section $q(\epsilon, E)$ for the Kramers (labelled q_k) and Bethe Heitler (labelled q_{BH}) approximations. These are shown for one value of electron energy E with q versus $\epsilon/E \leq 1$. The curves also show the shape of $L_k(\epsilon/E_1)/(A/E_1)$ and of $L_{BH}(\epsilon/E_1)/(A/E_1)$ from Equations (23) and (24).

Note that q_k is finite at the short wavelength limit $\epsilon \to E$ while $q_{BH} \to 0$ there (see Figure 1). Though plots of Q_{BH} and Q_k look quite similar, the difference between q_{BH} and q_k is very important in inferring $F(E)$ from $j(\epsilon)$ as shown below.

In a general extended source the total emission from the source volume V is $J = \int_V j\,dV$ with $n_p = n_p(\mathbf{r})$ and $F(E) = F(E, \mathbf{r})$ varying with position $\mathbf{r}$ in V, thus

$$J(\epsilon) = \frac{Q_0 m_e c^2}{\epsilon} \int_V n_p(\mathbf{r}) \int_\epsilon^\infty \frac{F(E, \mathbf{r})}{E} q(\epsilon, E)\,dE\,dV. \qquad (17)$$

For a homogeneous source

$$J(\epsilon) = \frac{Q_0 m_e c^2 n_p V}{\epsilon} \int_\epsilon^\infty \frac{F(E)}{E} q(\epsilon, E)\,dE. \qquad (18)$$

It is clear that for the inhomogeneous case, infinitely many different combinations of functions $n_p(\mathbf{r}), F(E, \mathbf{r})$ can yield the same volume integrated spectrum $J(\epsilon)$. Brown (1971) pointed out that all that determines $J(\epsilon)$ for given q (and all that can be inferred about the electron spectrum from $J(\epsilon)$) is the density weighted volumetric average $\bar{F}(E)$ of $F(E, \mathbf{r})$ defined by

$$\bar{F}(E) = \frac{1}{\bar{n}_p V} \int_V F(E, \mathbf{r}) n_p(\mathbf{r})\,dV, \qquad (19)$$

where $\bar{n}_p = \int_V n_p\,dV/V$. This means that in general the spectrum $J(\epsilon)$ we see is that of an equivalent homogeneous source with electron spectrum

$\bar{F}(E)$ since

$$J(\epsilon) = \frac{Q_0 m_e c^2 \bar{n}_p V}{\epsilon} \int_\epsilon^\infty \frac{\bar{F}(E)}{E} q(\epsilon, E) \, dE \,. \tag{20}$$

The function $\bar{F}(E)$ is also sometimes called the 'thin target' spectrum since it is the (equivalent homogeneous) electron spectrum radiating at any instant, irrespective of how it is produced. One could get a specified $\bar{F}(E)$ in many different ways. These include (a) injection of some spectrum of particles subsequently modified during propagation or (b) integration/summation of the locally Maxwellian spectra in a thermal but non-isothermal source, as discussed further below.

To streamline subsequent equations it is convenient to express the spectrum in terms of

$$L(\epsilon) = \frac{\epsilon J(\epsilon)}{Q_0 m_e c^2 \bar{n}_p V} \,, \tag{21}$$

so that

$$L(\epsilon) = \int_\epsilon^\infty \frac{\bar{F}(E)}{E} q(\epsilon, E) \, dE \,. \tag{22}$$

3.2. SOME PARAMETRIC $\bar{F}(E)$ AND ASSOCIATED $J(\epsilon)$

3.2.1. *δ-function:* $\bar{F}(E) = A\delta(E - E_1)$
For this case $L(\epsilon) = Aq(\epsilon, E_1)$ which, for $\epsilon \le E_1$, gives for $q = q_k$

$$L_k = \frac{A}{E_1} \tag{23}$$

while for $q = q_{\mathrm{BH}}$ it is

$$L_{\mathrm{BH}} = \frac{A}{E_1} \log \frac{1 + \sqrt{(1 - \epsilon/E_1)}}{1 - \sqrt{(1 - \epsilon/E_1)}} \,. \tag{24}$$

which are very different – see Figure 1.

3.2.2. *Power-law:* $\bar{F}(E) = CE^{-\delta}$
This is the most widely used parametric form. The constant C can be expressed in terms of the total flux of electrons of $E \ge E_1$. That is,

$$\bar{F}(E) = CE^{-\delta} = (\delta - 1)\frac{F_1}{E_1}\left(\frac{E}{E_1}\right)^{-\delta} \,. \tag{25}$$

For general q

$$L(\epsilon) = C \int_\epsilon^\infty q(\epsilon, E) E^{-\delta} dE \,. \tag{26}$$

If we restrict ourselves to forms $q = q(\epsilon/E)$ then with change of variable to $x = \epsilon/E$, we get

$$L(\epsilon) = C\epsilon^{-\delta} \int_0^1 x^{\delta-1} q(x)\, dx\,. \tag{27}$$

Consequently, L is also a power-law for any such q. Note that the bremsstrahlung photon flux spectrum $J(\epsilon) \propto \epsilon^{-\gamma}$ in this case has index $\gamma = (\delta + 1)$, so is softer than the source electron index. For $q = q_k$ the integral is just $1/\delta$ while for q_{BH} it is $B(\delta - 1, 1/2)/\delta$ where B is the beta function.

3.2.3. Isothermal hot plasma with temperature T

In this case all the electrons are involved and $n_e \approx n_p$ with Maxwellian

$$F(E, \mathbf{r}) = n_p(\mathbf{r}) \left(\frac{2}{\pi m_e}\right)^{1/2} \frac{E}{(kT(\mathbf{r}))^{3/2}}\, e^{-E/kT(\mathbf{r})}\,. \tag{28}$$

The resulting spectrum is then

$$\epsilon J(\epsilon) = \left(\frac{2}{\pi m_e}\right)^{1/2} Q_0 m_e c^2 \int_V n_p^2(\mathbf{r}) \int_\epsilon^\infty q(\epsilon, E) \frac{e^{-E/kT(\mathbf{r})}}{(kT(\mathbf{r}))^{3/2}}\, dE\, dV\,. \tag{29}$$

For uniform T and with $q = q_k$ this reduces to

$$\epsilon J(\epsilon) = \left(\frac{2m_e}{\pi}\right)^{1/2} Q_0 c^2 EM \frac{e^{-E/kT}}{(kT)^{1/2}}\,, \tag{30}$$

where the *emission measure* EM is

$$EM = \int_V n_p^2\, dV\,. \tag{31}$$

No closed analytic form seems to exist for the isothermal $\epsilon J(\epsilon)$ for $q = q_{\mathrm{BH}}$ or more complex forms.

3.2.4. Non-isothermal plasma: $T = T(\mathbf{r})$

Here we can use the isothermal result dL for a small range dT of T in which the emission measure is $dEM(T) = DEM(T)\, dT$ where, loosely, $DEM(T) = d(EM)/dT$ is the *differential emission measure* (per unit T) defined rigorously by Craig and Brown (1976). Integrating up over all T we then get

$$\epsilon J(\epsilon) = \left(\frac{2m_e}{\pi}\right)^{1/2} Q_0 c^2 \int_0^\infty DEM(T) \frac{e^{-E/kT}}{(kT)^{1/2}}\, dT\,. \tag{32}$$

It is left as an exercise for the reader to show that if $DEM(T) \propto T^{-a}$, with constant a, the resulting thermal photon spectrum is a power-law – usually assumed to indicate a nonthermal source (Brown, 1974).

3.3. THE INVERSE PROBLEM: INFERRING $\bar{F}(E)$ FROM $J(\epsilon)$

Instead of using parametric forms of $\bar{F}(E)$ to predict parametric $L(\epsilon)$ one can regard the spectral equation

$$L(\epsilon) = \int_{\epsilon}^{\infty} \frac{\bar{F}(E)}{E} q(\epsilon, E) \, dE \tag{33}$$

as a Volterra integral equation to be solved for $\bar{F}(E)$ for an observed photon spectrum $L(\epsilon)$ and with $q(\epsilon, E)$ as known kernel function (Craig and Brown, 1986). The equation can also be written in operator terms as a functional equation

$$\mathcal{Q}[\bar{F}(E)/E; \epsilon] = L(\epsilon) \tag{34}$$

with formal solution

$$\bar{F}(E)/E = \mathcal{Q}^{-1}[L(\epsilon); E] \tag{35}$$

with $\mathcal{Q}^{-1}$ the inverse operator. Depending on $q(\epsilon, E)$ the following situations can arise:

- $\mathcal{Q}^{-1}$ does not exist for some $J(\epsilon)$,
- $\mathcal{Q}^{-1}$ exists but is not unique for some $J(\epsilon)$,
- $\mathcal{Q}^{-1}$ exists and is unique but is unstable to small changes in $J(\epsilon)$,
- $\mathcal{Q}^{-1}$ exists but is unphysical ($\bar{F}$ negative) for some $J(\epsilon)$, i.e. this form of $J(\epsilon)$ cannot be produced by bremsstrahlung with that q.

In the real world one does not deal with spectral functions but with discretized source and data vectors $(\mathbf{F}, \mathbf{L})$ and a kernel matrix $\mathbf{Q}$ so that

$$\mathbf{Q}\mathbf{F} = \mathbf{L} . \tag{36}$$

This inevitable discretisation further compounds issues of non-uniqueness and instability (Craig and Brown, 1986).

Solution of the integral equation is very simple for the case $q = q_k$. Differentiation with respect to ϵ at once yields the solution

$$\frac{\bar{F}(E)}{E} = \left[-\frac{dL}{d\epsilon} \right]_{\epsilon = E} . \tag{37}$$

Note that for any physical $\bar{F} \geq 0$ the bremsstrahlung spectrum must be monotonic decreasing.

Brown (1971) showed that an analytic integral (Abel equation) inversion also exists for $q = q_{\text{BH}}$ which is considerably more complicated. Most cross sections are only amenable to numerical inversion methods.

3.4. SPECTRAL THERMALITY TEST

For a non-isothermal source we have

$$L(\epsilon) = D \int_0^\infty DEM(T) \frac{e^{-E/kT}}{(kT)^{1/2}} \, dT \,, \tag{38}$$

where D is a constant. Note that if we differentiate L j times the result has sign $(-1)^j$. Consequently, in the Kramers approximation, the spectrum from *any* physical thermal source ($DEM \geq 0$) must have this derivative property. Brown and Emslie (1988) called this the thermality test.

We also note that by changing variable from T to $t = 1/kT$ the thermal spectrum integral relationship takes the form (with f, g related to L, DEM, respectively)

$$f(x) = \int_0^\infty g(y) \exp(-xy) \, dy \tag{39}$$

which is the Laplace transform (again in the Kramers approximation).

3.5. IMPORTANCE OF CORRECT $Q(\epsilon, E)$

To illustrate the seriousness of 'errors' in inverse problems we use here a simple example to show the importance of using the best possible description for q. (In practice we cannot know q exactly since it depends on the unknown emission direction).

Suppose that $q_{BH}(\epsilon, E)$ were an adequate model for q and that the source electron spectrum $\bar{F}(E)$ were in fact a δ-function. Then the photon spectrum observed would be as given by Eq. (24). Suppose next that we chose to be lazy and, to infer $\bar{F}(E)$, we decide just to use inversion Eq. (37) appropriate to q_k. Applying this to Eq. (24) and simplifying we find that instead of the true δ-function this would lead us to infer for $\bar{F}(E)$

$$\bar{F}(E) = \frac{A}{E_1 \sqrt{(1 - E/E_1)}} \,, \tag{40}$$

which, apart from tending to ∞ at $E \to E_1$, is quite unlike the true δ-function, being finite at all energies $E \leq E_1$ down to zero – see Figure 2.

3.6. EFFECT OF NOISE IN $J(\epsilon)$ ON INFERRED $\bar{F}(E)$ AND $DEM(T)$

Since the inverse operator $\mathcal{Q}^{-1}$ (e.g. Eq. (37), and Brown, 1971) involves derivatives, errors in the data $L(\epsilon)$ in general are greatly magnified in the solution for $\bar{F}(E)$. Noise tends to be of high frequency and so to have large derivatives even if of small amplitude. To see this write

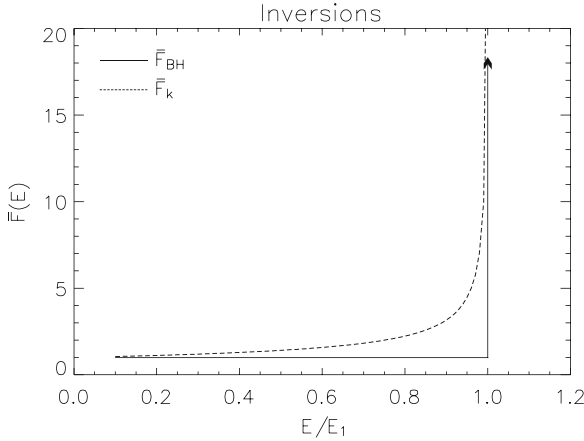$$L(\epsilon) = L_0(\epsilon) + L_1 \exp(i\omega\epsilon) \,, \tag{41}$$

Figure 2.   The electron spectrum $\bar{F}(E)$ with E in units of E_1 recovered by deconvolving $J(\epsilon)$ through q for the correct $q = q_{\mathrm{BH}}$, which gives the true δ-function form of $\bar{F}(E)$ at $E/E_1 = 1$, and the incorrect form of $\bar{F}(E)$ inferred when q_k is used.

where $i = \sqrt{(-1)}$ and ω is the noise angular 'frequency' in energy space. Then for the Kramer's solution, for example, we get

$$\frac{\bar{F}(E)}{E} = -L_0'(E) - i\omega L_1 \exp(i\omega\epsilon) , \qquad (42)$$

so the amplitude $\Delta\bar{F}$ of the noise in $\bar{F}$ is

$$\frac{\Delta F}{\bar{F}} = \omega \frac{L_1}{L_0} , \qquad (43)$$

which approaches ∞ as $\omega \to \infty$ for any non-zero noise amplitude L_1, however small. That is, noise of sufficiently high frequency will always swamp the solution. Put another way this means that any sharp (high frequency) structure in $\bar{F}(E)$ is suppressed in $L(\epsilon)$ by the filtering action of the broad (in E) kernel q when the bremsstrahlung integral over E is performed. It follows that it is essential to have both high spectral resolution *and* high signal to noise if we are to recover from noisy data $L(\epsilon)$ any details in $\bar{F}(E)$.

The filtering action of an integral operator is related to the Riemann-Lebesque lemma which is particularly simple in the non-isothermal problem relating $DEM(T)$ to $L(\epsilon)$ for the Kramers q_k. We saw that by change of variable the integral can be written as the Laplace transform

$$f(x) = \int_0^\infty g(y) \exp(-xy) dy . \qquad (44)$$

If we now consider a Fourier component of the (DEM related) function g namely

$$g_\omega(y) = a_\omega \exp(i\omega y) , \qquad (45)$$

then its contribution to the data is

$$f_\omega(x) = a_\omega \left[\frac{\exp((i\omega - x)y)}{i\omega - x} \right] = \frac{a_\omega(i\omega + x)}{\omega^2 + x^2} . \qquad (46)$$

One sees that for both the real and imaginary parts the amplitude of the signal component $f_\omega(x)$ due to the term g_ω in g at frequency ω goes to zero as $\omega \to \infty$. That is, sharp structure in the source function $DEM(T)$ will be lost in the noise in the data $L(\epsilon)$.

3.7. ALBEDO AND OTHER COMPLICATIONS

Besides the issue of directionality of emission already mentioned, a complicating factor in interpreting $L(\epsilon)$ in terms of $\bar{F}(E)$ is that the photosphere has quite a high albedo at deka-keV energies. Thus what we observe is not just the primary source $L(\epsilon)$ in the 'upward' direction but also some of the 'downward' HXR flux backscattered from the photosphere. If the primary HXR emission is significantly downward beamed (e.g. Brown, 1972) then what we see may be dominated by the albedo component. The albedo is a function of photon energy and is actually dependent on the form of $L(\epsilon)$ since it involves Compton scattering and atomic absorption. Correcting for it is therefore complex. Alexander and Brown (2002) offered a simplified approach and discussed its impact on inversions to find $\bar{F}(E)$.

4. Spatial and global HXR source issues

How the volume averaged radiating $\bar{F}(E)$ is related to the electron acceleration and/or heating processes depends on how the electrons propagate, in particular what Coulomb collisional and other energy loss processes they undergo (e.g. plasma wave generation, gyro-synchrotron radiation) along the 'path' from the acceleration 'site' through the radiation volume. Note that there is no real basis for this separation of acceleration and emission regions though it is a widely utilised notion. In particular it is common, for simplicity, to think of accelerated electrons being accelerated in one location (low density so little radiation) and injected into a propagation/radiation region. If the acceleration spectrum is $\mathcal{F}_0(E_0)$ electrons per sec per unit E_0, then an important problem is to relate $\mathcal{F}_0(E_0)$ to $\bar{F}(E)$. In the limit where the energy losses undergone in traversing the source are small ($\Delta E \ll E_0$) the situation is termed *thin target* while if the electrons lose all their energy the situation is *thick target*. Of course, in reality, the electrons will ultimately lose all their energy in any source and it is really a matter of time scales. If one makes an observation in a time $\ll$ the electron stopping time then the target is thin while if one integrates for $\gg$ the stopping time it is

thick. In particular the term 'thick target model' usually refers to the scenario proposed by Brown (1971) where electrons accelerated in the corona are injected downward reaching the chromosphere in $\ll 1$ s and stopping there collisionally in an even shorter time. Since these times are typically shorter than most observational integration times, what we see is a thick target in a quasi-steady state with a time varying injection rate. It must be noted, however, that time of flight effects are marginally detectable and have been studied extensively by Aschwanden, Schwartz, and Alt (1996). These and observed HXR source spatial structure are important tests of the model.

4.1. TRANSPORT EFFECTS AND THE THICK TARGET MODEL

Consider one electron, injected with energy E_0. As it propagates, in time interval dt around position $\mathbf{r}(t)$ it will emit a number of photons per unit ϵ given by $n_p(\mathbf{r})Q_B(\epsilon, E(\mathbf{r}(t)))v(E(\mathbf{r}(t)))dt$. Thus, over its lifetime, it will emit a number of photons per unit ϵ given by

$$
\begin{aligned}
\phi(\epsilon, E_0) &= \int_t n_p(\mathbf{r}) Q_B(\epsilon, E(\mathbf{r}(t))) v(E(\mathbf{r}(t))) dt \\
&= \int_\epsilon^\infty \frac{n_p(\mathbf{r}) Q_B(\epsilon, E(\mathbf{r}(t))) v(E(\mathbf{r}(t)))}{|dE/dt|} dE.
\end{aligned}
\tag{47}
$$

For injection of electrons at total rate $\mathcal{F}_0(E_0)$ (per second per unit E_0), the bremsstrahlung emission rate J (photons per second per unit ϵ) is then given by

$$
J_{\text{thick}}(\epsilon) = \int_\epsilon^\infty \mathcal{F}_0(E_0) \int_\epsilon^{E_0} \frac{Q_B(\epsilon, E)}{Q_E(E)} dE \, dE_0,
\tag{48}
$$

where the effective energy loss cross section $Q_E(E)$ is defined by

$$
\frac{1}{E} \frac{dE}{dt} = -n_p v Q_E(E).
\tag{49}
$$

Defining the column density N (cm^{-2}) along the electron path by $N(s) = \int_0^s n_p(s) \, ds$, and noting that $dN = n_p v \, dt$, then

$$
\frac{1}{E} \frac{dE}{dN} = -Q_E(E).
\tag{50}
$$

In general $Q_E(E)$ will be complex and depend on many things like plasma wave level etc. at the point $\mathbf{r}$ where the energy is E. However, in the specific case of a collisional thick target where Coulomb e-e collisions dominate the energy loss the result is simple

$$
Q_E(E) = Q_c(E) = \frac{K}{E^2},
\tag{51}
$$

where K is as previously and we have

$$\frac{1}{E}\frac{dE}{dN} = -\frac{K}{E^2} , \tag{52}$$

so

$$E(N) = (E_0^2 - 2KN)^{1/2} , \tag{53}$$

leading to

$$\begin{aligned}
\epsilon J_{\text{thick}}(\epsilon) &= \frac{Q_0 m_e c^2}{K} \int_\epsilon^\infty \mathcal{F}_0(E_0) \int_\epsilon^{E_0} q(\epsilon, E) \, dE \, dE_0 \\
&= \frac{Q_0 m_e c^2}{K} \int_\epsilon^\infty q(\epsilon, E) \int_\epsilon^\infty \mathcal{F}_0(E_0) \, dE_0 \, dE .
\end{aligned} \tag{54}$$

Comparing Equations (53) and (20) we see that the mean source spectrum $\bar{F}(E)$ for a thick target is related to $\mathcal{F}_0(E_0)$ by

$$\bar{F}(E) = \frac{E}{K \bar{n}_p V} \int_E^\infty \mathcal{F}_0(E_0) dE_0 \tag{55}$$

or, conversely using Eq. (37)

$$\mathcal{F}_0(E_0) = K \bar{n}_p V \left[-\frac{d}{dE}\left(\frac{\bar{F}(E)}{E}\right) \right]_{E=E_0} = \frac{K}{Q_0 m_e c^2} \left[-\frac{d^2(\epsilon J)}{d\epsilon^2} \right]_{\epsilon=E_0} . \tag{56}$$

The following are important points to note:

1. $\mathcal{F}_0(E_0)$ is VERY sensitive to noise in J.
2. $\mathcal{F}_0(E_0)$ is only physical (≥ 0) for those $J(\epsilon)$ which are monotonic decreasing and concave up.
3. $J(\epsilon)$ for a collisional thick target is independent of the distribution of $n_p(\mathbf{r})$. This surprising result is due to the fact that any change in n_p results in a change of collisional bremsstrahlung emission rate but also a proportional change of total collisional energy loss rate and the two effects cancel, only the total column density traversed being important.
4. From Eq. (47) we see that the ratio of total HXR emission rate $\approx \epsilon J$ to total electron injection rate $\approx E_0 \mathcal{F}_0(E_0)$ is (using $E_0 \approx E \approx \epsilon$)

$$\frac{Q_0 m_e c^2 \epsilon}{K} \approx \frac{\zeta \alpha r_e^2 m_e c^2 \epsilon}{2\pi e^4 \Lambda} \approx \frac{\zeta \alpha E}{2\Lambda m_e c^2} \approx 10^{-5} \tag{57}$$

at 10 keV.

This means, as mentioned earlier, that collisional bremsstrahlung of fast electrons in a cold target is very inefficient, requiring 10^5 erg of electron input for each erg of HXR output because of the large preponderance of

long range e-e collisions over short range e-i ones. In a pure hot Maxwellian gas with no particle escape (if such could ever be realised) the efficiency can be 10^5 times greater with bremsstrahlung the sole energy loss. It is left as an exercise for the reader to prove that for $\mathcal{F}_0(E_0)$ a power-law $\propto E_0^{-\delta}$ with any $q = q(\epsilon/E)$ the resulting $J(\epsilon) \propto \epsilon^{-\gamma}$ where $\gamma = (\delta - 1)$ so that the HXRs are one power harder than the injected electrons in contrast with the thin target case where they are one power softer than the source electrons, $\gamma = (\delta + 1)$. This is due to the collisional hardening ($Q_C = K/E^2$) of the electron spectrum as it propagates to create $\bar{F}(E)$. In reality this power-law relationship is not quite true because K is not really constant along the path, falling by a factor of 2.6 from the ionised to the near neutral chromosphere. This causes a 'chicane' in the power-law J (Brown, 1973a) with important consequences for interpreting HXR spectra (Brown et al., 2000; Kontar, Brown, and McArthur, 2002).

Of course much more information is carried by HXR imaging spectroscopy than by volume integrated spectroscopy alone, even though spectroscopic image reconstruction with a modulation collimator is far from easy (Skinner and Ponman, 1995). Brown and McClymont (1975) were the first to predict the height structure of a thick target HXR source and their predictions compared with the first data obtained using stereo occultation data by Kane (see Brown, Carlaw, and Kane, 1983). The essence is that there should be only rather weak emission from the tenuous thin target corona and very intense emission from the dense chromospheric footpoints. This seems to be the case in many flares though there are cases of substantial HXR emission at very high altitude (Kane, 1983; Masuda et al., 1995) and of very dense loops producing thick target emission there (Veronig and Brown, 2004). A relatively simple case of physically modelling actual imaging data for a 1-D loop of constant cross-section was treated by Brown, Kontar, and Aschwanden (2002) and applied to RHESSI data by Aschwanden, Brown, and Kontar (2002). The energy/height (z) distribution $\partial^2 J/\partial z \partial \epsilon$ dependency of the HXR emission depends on three unknown functions: the electron injection spectrum $\mathcal{F}_0(E_0)$; the effective energy loss cross section $Q_E(E)$ which depends on local plasma conditions at z; the distribution of these conditions with z along the electron path. It is impossible to learn all three of these from data on the bivariate spectral image function $\partial^2 J/\partial z \partial \epsilon$ so an assumption has to be made. What Aschwanden, Brown, and Kontar (2002) did was actually to make two assumptions: a power-law $\mathcal{F}_0(E_0)$ and also that the energy losses are purely collisional $Q_E(E) = K/E^2$. Then one can best fit the noisy data $\partial^2 J/\partial z \partial \epsilon$ to find the thick target plasma density structure $n_p(z)$ – a new way of probing the solar atmosphere if the assumptions are correct. Roughly speaking this amounts to saying that, since photons of energy ϵ come mainly from electrons of

$E \approx \epsilon$, then HXRs of energy ϵ will be seen mainly from collisional stopping depth $N(\epsilon) \approx \epsilon^2/2K$. So if we see photons of energy ϵ mainly from height $z(\epsilon)$ we then have $N(z(\epsilon))$. But $n_p = dN/dz$ hence we have $n_p(z)$.

4.2. BEAM ELECTRODYNAMICS

All of the above treats fast electrons as if they moved like individual test particles. The reasonably good agreement between the predictions of the collisional thick target model and data from RHESSI and elsewhere suggest that much of the electron behaviour is roughly consistent with this. This is really rather surprising given the enormous intensities of the beams required to produce a typical HXR burst flux. We noted earlier that thick target interpretation requires a beam power 10^5 times the HXR luminosity or about 10^{29} erg s^{-1} above 20 keV in a large flare or approaching 10^{37} electrons per second. A typical flare flux tube in the corona, of cross section $S \approx 10^{18}$ cm^2 and length $l \approx 10^9$ cm, contains $n L S \approx 10^{37} n_{10}$ electrons. The fact that the total flow rate $\mathcal{F}_{\mathrm{tot}}$ of electrons would empty such a tube in a second while in fact HXR bursts last minutes has been claimed by some to refute the thick target model because of the *number problem*. This is a fallacy – there is no electron number supply problem as such, though there are open questions concerning electrodynamics issues like current closure. (The myth that there is continues to exist, furthered by total misunderstanding of the physics such as that expounded by Zirker, 2001.) This is because, in a plasma, a relatively tenuous propagating beam automatically creates a dense slow plasma drift return current which replenishes the electrons leaving the acceleration site. To see why this happens consider a beam of radius R carrying a current I propagating in a vacuum or neutral gas. At the edge of the beam there is a toroidal magnetic field $B = I/2\pi Rc$ which exerts a force on electrons in the beam deflecting them sideways with Larmor radius $r_L = m_e vc/eB$. Clearly, if $r_L \ll R$ the beam does not propagate longitudinally but disintegrates laterally due to its self field. (A net beam charge density would also cause the beam to explode by electrostatic repulsion). The (Alfven-Lawson) limiting current I_{AL} for which $r_L = R$ is

$$I_{\mathrm{AL}} = \frac{2\pi m_e vc^2}{e} \approx 17000 \text{ A} . \tag{58}$$

If the HXR $\mathcal{F}_{\mathrm{tot}}$ were collimated it would have a beam current $\mathcal{F}_{\mathrm{tot}} e \approx 10^{18} A \approx 10^{14} I_{\mathrm{AL}}$!! One can look at this another way. If one could inject a 'bare beam' 10^9 cm in radius with $I \approx 10^{18}$ A it would have a self field $B \approx 2 \times 10^7$ G at its edge. Such a field would have an energy density enormously higher than the kinetic energy density of the beam which created it, which is physically impossible. In consequence, intense charged beams

cannot propagate in a vacuum or in a neutral gas (unless, in the latter case an ionised channel is first created by a laser pulse, as is done with charged beam weapons). However, when a beam is launched into a plasma the induced and electrostatic E fields generated by the rising current and charge act (Lenz's law) to drive a plasma drift return current which neutralises the beam current and charge (see e.g. Colgate, 1978; Brown and Bingham, 1984; Spicer and Sudan, 1984; Miller, 1998; van den Oord, 1990). For beam and plasma densities n_b, n respectively, and a beam of speed $v = \mathcal{F}_{tot}/Sn_b$ the necessary plasma drift speed to ensure neutralisation $j = j_0$ is $v_0 = vn_b/n$. Since $n_b/n \ll 1$, the drift current is slow but driving it extracts energy from the beam because:

− the plasma has a finite resistivity η so that Ohm's law requires an electric field $E = \eta j = \eta j_0$ to drive the return current against the resistance. This E slows the beam, in addition to direct Coulomb collisions of the beam particles themselves. One can alternatively think of the return current ohmic dissipation ηj_0^2 per unit volume as extracting power from the beam.

− if the plasma drift v_0 is too high, plasma waves are excited and enhance η above its Coulomb value, thus adding to beam deceleration (cf. Duijveman, Hoyng, and Ionson, 1981; Cromwell, McQuillan, and Brown, 1988). If these effect were large, because Q_E would be increased, the thick target bremsstrahlung efficiency would be even lower and an impossibly large beam power required to produce a HXR burst. The absolute upper limit before wave generation occurs for sure is $v_0 \approx v_{th}$ with the plasma electron thermal speed. This has to be compared with the required plasma drift speed

$$v_0 = 10^9 \frac{\mathcal{F}_{tot}/10^{37}}{(S/10^{17})(n_0/10^{11})}.$$

So the criterion for return current stability is

$$\frac{\mathcal{F}_{tot}/10^{37}}{(S/10^{17})(n_0/10^{11})} \leq 1. \tag{59}$$

The fact that this limit involves $\mathcal{F}_{tot}$ so close to the maximum observed values suggests that return current instability may well act to limit flare beam acceleration rates (Brown and Melrose, 1977).
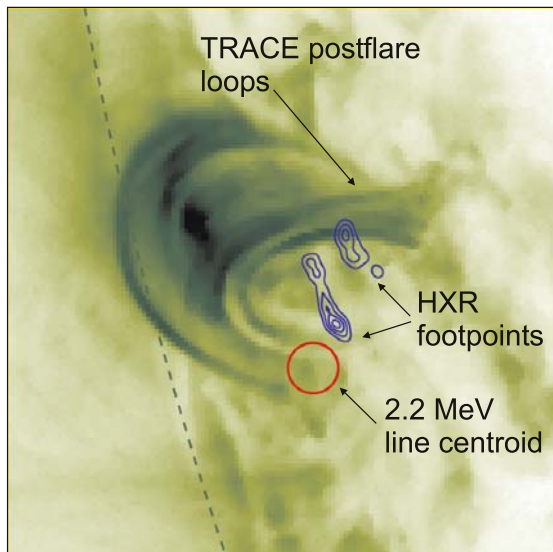
Figure 3.   Image of the July 23, 2002 flare showing distinct location of RHESSI HXR and 2.2 MeV line emission (Hurford *et al.*, 2003) against TRACE image of post flare loops (image courtesy of Peter Gallagher).

4.3. ENERGETIC PARTICLE/BEAM HEATING OF FLARE PLASMA

4.3.1. *Basic evidence*

There is considerable evidence that electron beams, and possibly ion beams (though they are much harder to detect), may play a key role in flare impulsive phase atmospheric heating:

1. HXR light curves often show synchronism with impulsive chromospheric emissions (EUV, Hα).
2. If the thick target power-law electron injection spectrum $\mathcal{F}_0(E_0)$ extends down to 20 keV or so, as is consistent (though not uniquely so) with HXR spectra, the total beam power is adequate to cause much of the flare heating.
3. The speed $v \approx 10^{10}$ cm s^{-1} of 20 keV electrons is fast enough to synchronise footpoints of a loop within a few 100 ms as observed. Thermal conduction and Alfven speeds are too slow.
4. While the power in ions below 1 MeV or so per nucleon may also be enough to contribute to heating, they cannot produce HXRs directly (cf. Emslie and Brown, 1988; Simnett and Haines, 1990; Karlický *et al.*, 2000). At present, ion diagnostic imaging and timing etc. (γ-rays, Hα impact polarisation), though advancing spectacularly, are not a quantitative test of ion heated models.
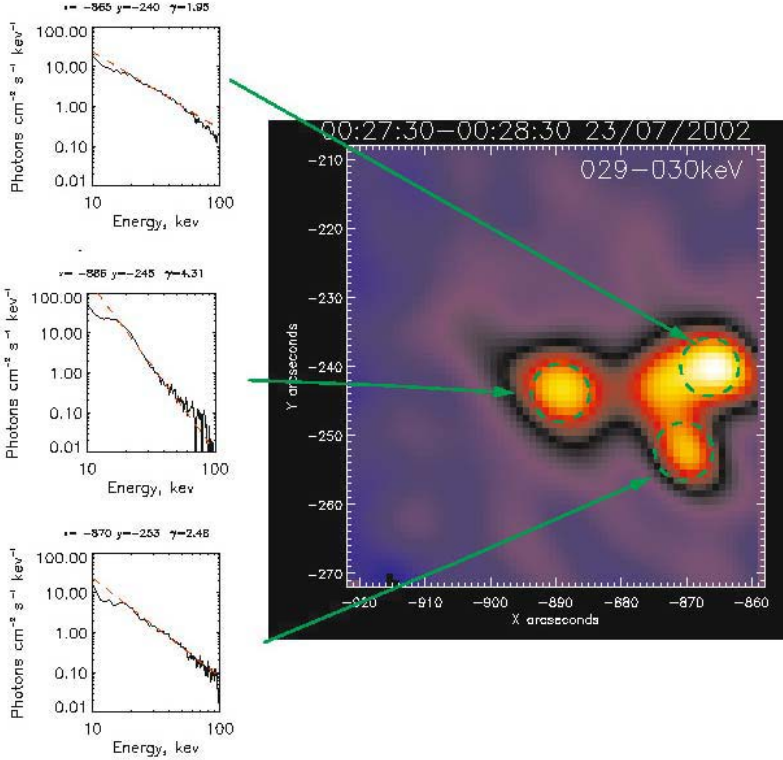
Figure 4.   RHESSI HXR image from Emslie *et al.* (2003) of the event of July 23, 2002 with local spectral indices indicated showing the loop top to be softer than the footpoints as predicted for a collisional thick target model.

4.3.2.   *Theory of electron beam collisional heating of the atmosphere*

The basic theory was given by Brown (1973b). For an electron beam of injection flux spectrum $F_0(E_0) = \mathcal{F}_0(E_0)/S$ (with S the beam area) and $F(E, N)$ at depth N where the plasma density is $n_p(N)$ the collisional heating rate per unit volume is

$$I_B(N) = \int_0^\infty F(E, N) Q_C(E) E n_p(N)\, dE \,. \tag{60}$$

For power-law $F_0(E_0)$ of index δ and total flux $F_1(E \geq E_1)$ and with continuity equation (neglecting pitch angle scattering) $F(E, N) = F_0(E_0) dE_0/dE$ and $E^2 = E_0^2 - 2KN$ as before one finds
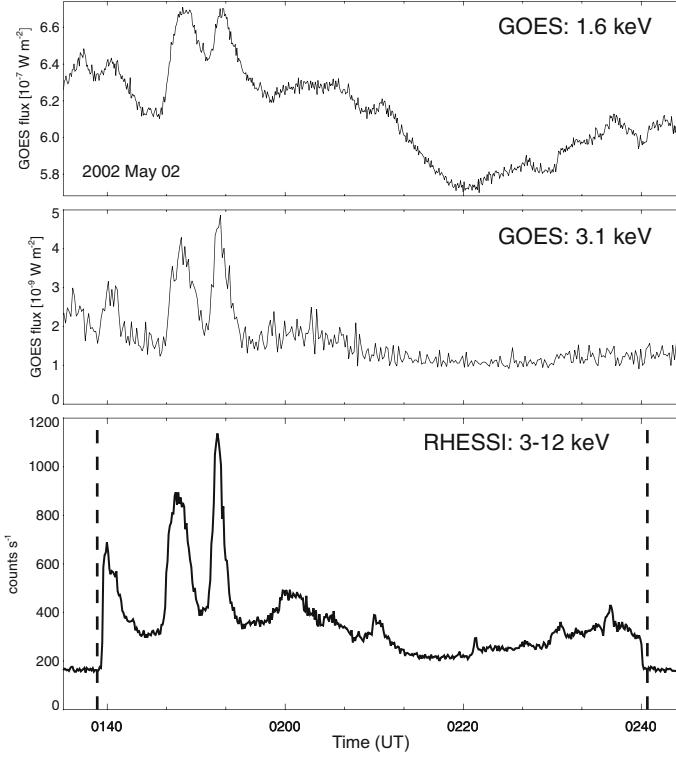
Figure 5. Results from Krucker *et al.* (2002) showing recurring microbursts of nonthermal HXRs around 10 keV from active regions. (Dashed lines indicate the end/beginning of RHESSI night time.)

$$I_B(N) = \begin{cases} (\delta - 1)Kn_p(N)\frac{F_1}{E_1} \int\limits_{\sqrt{2\bar{K}\bar{N}}}^{\infty} \left(\frac{E_0}{E_1}\right)^{-\delta} \frac{dE_0}{\sqrt{E_0^2 - 2\bar{K}\bar{N}}} & : N \geq N_1, \\ (\delta - 1)Kn_p(N)\frac{F_1}{E_1} \int\limits_{E_1}^{\infty} \left(\frac{E_0}{E_1}\right)^{-\delta} \frac{dE_0}{\sqrt{E_0^2 - 2\bar{K}\bar{N}}} & : N \leq N_1. \end{cases}$$

(61)

Note that this can be expressed, using change of variable $E_0 = x\sqrt{2\bar{K}\bar{N}}$ in terms of Beta functions, with $N_1 = E_1^2/2K$.

Provided $N_1 \leq N_*$, the column density at the transition zone, then the first expression applies to chromospheric heating and varies as $I_B(N) \propto n_p(N)N^{-\delta/2} = Cn_p(N)N^{-\delta/2}$. Consequently:

1. Electrons of $E_0 \leq \sqrt{2\bar{K}\bar{N}_*}$ heat the coronal loop region. This has low n_p and rather long radiative and conductive cooling times. If the beam is rather impulsive the coronal matter should then heat up with a time
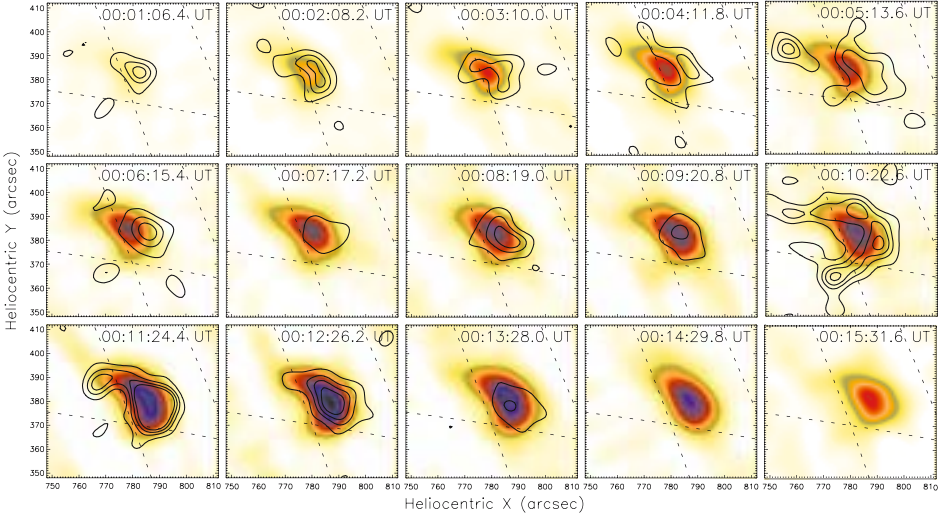
Figure 6. RHESSI image sequence for the 14/15 April 2002 flare from Veronig and Brown (2004). Gray scale images represent 6–12 keV RHESSI images, contours indicate the corresponding images at 25–50 keV. Images and contour levels (at 17, 30, 40, and 50%) are normalized to the respective maxima of the time series.

profile of thermal energy content (plus losses) correlated with the time integral of the total beam power input there. This is the theoretical *Neupert Effect* (Veronig *et al.*, 2004).

2. Electrons of $E_0 \geq \sqrt{2KN_*}$ heat the chromosphere. In particular, the upper layers are heated to above the critical radiative instability temperature $T_* \approx 60,000K$ (e.g. Cox and Tucker, 1969). Note that this radiative instability is the fundamental reason for the existence of the sharp transition region jump in T and for the corona being so hot (cf. discussion in Brown *et al.*, 2000). This causes the top of the preflare chromosphere to heat rapidly and expand upward till it joins the hot SXR emitting coronal plasma, increasing N_*. This process was first mentioned by Sweet (1969) and modelled by Brown (1973b), Shmeleva and Syrovatskii (1973) and later by Antiochos and Sturrock (1987) who coined the term *chromospheric evaporation*. The increase of N_* increases E_* and rapidly reduces the effectiveness of beam driven evaporation as time progresses, if the electron beam persists in the same site. Fletcher and Hudson (2002) have pointed out that if the beam impact site moves with time, this self-quenching of beam driven evaporation is reduced or eliminated. The critical level N_* is determined by energy balance at the critical temperature

$$n_p^2(N_*)f_{\rm rad}(T_*) = Cn_p(N_*)N_*^{-\delta/2}, \qquad (62)$$
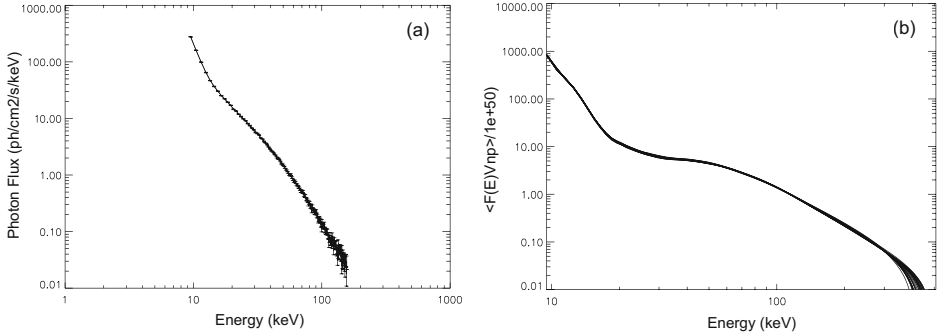
Figure 7. a) RHESSI photon spectrum of the February 26 (~10:26 UT), 2002 flare accumulated near the peak over 20 s interval with error bars. b) The resulting electron spectrum obtained inverting the photon spectrum using first order regularization algorithm (Kontar *et al.*, 2004). The multiple lines present various realizations of the regularized solution within the errors of the photon spectrum.

which, since (roughly) $n_p \propto N$ implies that the transition region depth in an electron heated flare should vary as

$$N_* \propto F_1^{\frac{2}{\delta+2}}.$$

4.3.3. *Micro-events and the coronal heating/supply problem*

The occurrence distribution of flares over event size (total energy release) increases toward low energies. This has led to the idea that a large number of very small flare-like events (micro/nano-flares) may be responsible for coronal heating (e.g. Krucker and Benz, 1998). In addition, a more detailed study of some individual micro-events by Brown *et al.* (2000) suggests that the evaporation in them must be driven nonthermally (i.e. not by conduction). They also suggested that, if the nonthermal driver were low energy (10 keV) nonthermal electrons then the associated HXR emission might be detectable by RHESSI. Whether or not the 'quiet' sun micro HXR events discovered by RHESSI (Krucker *et al.*, 2002) involve evaporated masses consistent with the electron heating expected from their HXR fluxes is a question currently being addressed by the author and collaborators.

5. **Highlights of RHESSI**

The influx of pioneering results from RHESSI continues unabated at the time of writing and there will be many more discoveries while this is in press. Some of the discoveries to date at that time were mentioned in the lectures. Rather than reading here an outdated list, the reader should refer to the two special RHESSI journal issues already out: Solar Physics Vol. 210 (2002)

and Astrophysical Journal Letters Vol. 595 (2003) but most importantly to the RHESSI Website `http://hesperia.gsfc.nasa.gov/hessi/`. But to give a brief flavour of the excitement, as someone who has worked for 35 years on the theory, I would list among my favourite RHESSI results so far:

– the discovery of distinct locations of HXR and γ-ray line sources (Hurford *et al.*, 2003) – cf. Figure 3,
– the broad consistency of footpoint event imaging spectroscopy with the predictions of the collisional thick target model (Emslie *et al.*, 2003) – cf. Figure 4,
– the discovery of micro-event HXRs from the 'quiet' sun (Krucker *et al.*, 2002) – cf. Figure 5,
– the discovery of thick (60 keV) target coronal HXR loops (Veronig and Brown, 2004) – cf. Figure 6 – and of very high altitude HXR sources (Kane and Hurford, 2003),
– the production of simultaneous movies linking HXR events to TRACE evaporation and jet events, Type III bursts, and interplanetary electrons and waves (see `http://sprg.ssl.berkeley.edu/~krucker/hessi/typeIII_july19.html`),
– detailed progress on the inversion of HXR spectra to yield flare electron spectra (Piana *et al.*, 2003; Massone *et al.*, 2003) – cf. Figure 7.

May all the Kanzelhöhe students and readers of this article get as much pleasure from the high energy sun as I have!

Acknowledgements

References

Alexander, R.C. and Brown, J.C.: 2002, *Solar Phys.* **210**, 407.
Antiochos, S.K. and Sturrock, P.A.: 1978, *Astrophys. J.* **220**, 1137.
Aschwanden, M.J., Schwartz, R.A., and Alt, D.M.: 1996, *Astrophys. J.* **447**, 923.
Aschwanden, M.J., Brown, J.C., and Kontar, E.P.: 2002, *Solar Phys.* **210**, 383.
Brown, J.C.: 1971, *Solar Phys.* **18**, 489.
Brown, J.C.: 1972, *Solar Phys.* **26**, 441.
Brown, J.C.: 1973a, *Solar Phys.* **28**, 151.
Brown, J.C.: 1973b, *Solar Phys.* **31**, 143.
Brown, J.C.: 1974, in G.A. Newkirk (ed.), *Coronal Disturbances*, Proc. IAU Symposium no. 57, Dordrecht, Boston: Reidel, 395.

Brown, J.C. and Bingham, R.L. *Astron. Astrophys.* l3l, Lll.

Brown, J.C. and Emslie, A.G.: 1988, *Astrophys. J.* **331**, 554.

Brown, J.C. and McClymont, A.N.: 1975, *Solar Phys.* **4**l, l35.

Brown, J.C. and Melrose, D.B.: 1977, *Solar Phys.* **52**, ll7.

Brown, J.C., Emslie, A.G., and Kontar, E.P.: 2003, *Astrophys. J.* **595**, L115.

Brown J.C., Kontar, E.P., and Aschwanden, M.J.: 2002, *Solar Phys.* **210**, 373.

Brown, J.C., Carlaw, V.A., Cromwell, D., and Kane, S.R.: 1983, *Solar Phys.* **88**, 28l.

Brown J.C., McArthur G., Barrett R.K., McIntosh S.W., and Emslie A.G.: 1998, *Solar Phys.* **179**, 379.

Brown, J.C., Krucker, S., Güdel, M, and Benz, A.O.: 2000, *Astroph. Astrophys.* **359**, 1185.

Chubb, T.A., Friedman, H., and Kreplin, R.W.: 1966, *J. Geophys. Res.* **71**, 3611.

Colgate, S.A.: 1978, *Astrophys. J.* **221**, 1068.

Cox, D.P. and Tucker, W.H.: 1969, *Astrophys. J.* **157**, 1157.

Craig, I.J.D. and Brown, J.C.: 1976, *Astron. Astrophys.* **49**, 239.

Craig, I.J.D. and Brown, J.C.: 1986, *Inverse Problems in Astronomy: A Guide to Inversion Strategies for Remotely Sensed Data*, Bristol, Boston: Hilger.

Cromwell, D., McQuillan, P. and Brown, J.C.: l988, *Solar Phys.* **115**, 289.

Duijveman, A., Hoyng, P., and Ionson, J.A.: 1981, *Astrophys. J.* **245**, 721.

Emslie, A.G. and Brown, J.C.: l985, *Astrophys. J.* **245**, 648.

Emslie, A.G., Kontar, E.P., Krucker, S., and Lin, R.P.: 2003, *Astrophys. J.* **595**, L107.

Fletcher, L. and Hudson, H.S.: 2002, *Solar Phys.* **210**, 307.

Hurford, G. J., and 13 co-authors: 2002, *Solar Phys.* **210**, 61.

Hurford, G.J., Schwartz, R.A., Krucker, S., Lin, R.P., Smith, D.M., and Vilmer, N.: 2003, *Astrophys. J.* **595**, L77.

Hudson, H.S.: 1972, *Solar Phys.* **24**, 414.

Kane, S.R.: 1974, in G.A. Newkirk (ed.), *Coronal Disturbances*, Proc. IAU Symposium no. 57, Dordrecht, Boston: Reidel, 105.

Kane, S.R.: 1983, *Solar Phys.* **86**, 355.

Kane, S.R. and Hurford, G.J.: 2003, *Adv. Space Res.* **32**, no. 12, 2489.

Karlický, M., Brown, J.C., Conway, A.J., and Penny, G.: 2000, *Astron. Astrophys.* **353**, 729.

Koch, H.W. and Motz, J.W.: 1959, *Rev. Mod. Phys.* **31**, 920.

Kontar, E.P., Brown, J.C., and McArthur, G.K.: 2002, *Solar Phys.* **210**, 419.

Kontar, E.P. *et al.* 2004, preprint.

Krucker, S. and Benz, A.O.: 1997, *Astrophys. J.* **501**, L213.

Krucker, S., Christe, S., Lin, R.P., Hurford, G.J., and Schwartz, R.A.: 2002, *Solar Phys.* **210**, 445.

Lin, R.P. and Schwartz, R.A.: 1987, *Astrophys. J.* **312**, 462.

Lin, R.P., and 65 co-authors: 2002, *Solar Phys.* **210**, 3.

Massone, A.M., Piana, M., Conway, A.J., and Eves, B.: 2003, *Astron. Astrophys.* **405**, 325.

Masuda, S., Kosugi, T., Hara, H., Sakao, T., Shibata, K., and Tsuneta, S.: 1995, *Publ. Astron. Soc. Japan* **47**, 677.

Miller, J.A.: 1998, *Space Sci. Rev.* **86**, 79.

Piana, M., Massone, A.M., Kontar, E.C., Emslie, A.G., Brown, J.C., and Schwartz, R.A.: 2003, *Astrophys. J.* **595**, L127.

Shmeleva, O.P. and Syrovatskii, S.I.: 1973, *Solar Phys.* **33**, 341.

Simnett, G.M. and Haines, M.G.: 1990, *Solar Phys.* **130**, 253.

Skinner, G.K. and Ponman T.J.: 1995, *Inverse Problems* **11**, 655.

Spicer, D.S. and Sudan, R.: 1984, *Astrophys. J.* **280**, 448.

Sweet, P. A.: 1969, *Ann. Rev. Astron. Astrophys.* **7**, 149.

Takakura, T. and Kai, K.: 1966, *Publ. Astron. Soc. Japan* **18**, 57.

van den Oord, G.H.J: 1990, *Astron. Astrophys.* **234**, 496.

Veronig, A. and Brown, J.C: 2004, *Astrophys. J.* **603**, L117.

Veronig, A., Brown, J.C., Dennis B.R., Schwartz, R.A., Sui, L., and Tolbert, A.K.: 2004, *Astrophys. J.*, submitted.

Zirker, J.B.: 2001, *Journey from the Center of the Sun*, Princeton University Press, Princeton.

PHYSICS OF SOLAR PROMINENCES

P. HEINZEL

Astronomical Institute
Academy of Sciences of the Czech Republic
CZ-25165 Ondřejov, Czech Republic

U. ANZER

Max-Planck-Institut für Astrophysik
Karl-Schwarzschild-Strasse 1
D-85740 Garching, Germany

Abstract. We present the fundamental equations which govern the physics of quiescent solar prominences. The mechanical equilibrium of prominences is described by the equations of magneto-hydrostatics. The radiative properties of the structures have to be modelled by non-LTE equations. In addition one has to prescribe the energetics of the cool prominence material in the coronal environment. The magneto-hydrodynamic equations allow us to construct 1D slab and 2D thread models. We then also discuss the aspects of magnetic dips. Furthermore, modern techniques of solving the complex set of non-LTE radiative transfer equations are described in some detail. Finally, new models resulting from a combination of magneto-hydrostatics and radiative transfer are outlined and their relevance for observations is discussed.

1. Introduction

Solar prominences are relatively cool plasma structures located inside the hot solar corona. The prominence plasma contains roughly 90% of hydrogen, which is partially ionized in the central coolest parts of prominences. Typical temperatures in these parts are between about 6000 – 8500 K, but some authors give the lower limit as low as 4300 K. Inside the boundary parts the temperature rapidly increases up to coronal values exceeding one million degrees. This particular region is called the Prominence-Corona Transition Region (PCTR). The plasma density in the central cool parts is about two orders of magnitude larger than that in the corona and thus the presence of the magnetic field is also crucial for the prominence support and stability. The coronal magnetic field penetrates the whole prominence and keeps it in a quasi-static state, supporting its dense plasma against the solar gravity. The intensity of this field is not very large, according to

current determinations it ranges from a few Gauss to few tens of Gauss. However, at this point we have to distinguish between the so-called *quiescent* and *active* prominences. Quiescent prominences usually last in the corona for many days and even weeks (finally they may be activated and disappear), while active prominences are usually very dynamic phenomena with rather short life-time (minutes or hours). Also the magnetic field in active prominences is typically stronger, its intensity reaches tens of Gauss or even more. Characteristic conditions prevailing in quiescent prominences are summarised in the so-called 'Hvar Reference Atmosphere of Quiescent Prominences' (Engvold *et al.* 1990). A pictorial atlas of solar prominences can be found at `http://www.astro.uni.wroc.pl/prominatlas.html`.

Prominences are thus tightly connected with the presence of magnetic fields and are, to a certain degree, also related to active regions on the Sun. This is why they are more numerous around the solar maximum. Prominences are very well visible above the solar limb, projected against the dark sky. The best contrast can be reached using the coronagraph equipped with an Hα filter. Due to solar rotation, prominences visible on the eastern limb move across the solar disk toward the western limb and during this period we can observe them in projection against the disk as dark features called *filaments*. Both prominences and filaments represent the same kind of an active solar structure, but seen in different projections. This also makes a significant difference in their emitted radiation as we shall see later.

Although solar prominences are well described already since the 19th century (see drawings by Secchi, 1875) and were intensively studied during the last decades, they still represent a subject of wide interest for solar physicists. This is mainly due to fast development of various observing techniques. With the help of the largest solar telescopes (located, e.g., on Canary Islands) one can resolve prominences or filaments on spatial scales reaching tens of km. Moreover, using space instruments it is possible to observe them also in ultraviolet (UV) or extreme-UV (EUV) which is not accessible from the ground. UV and EUV data provide us with rich diagnostic information. However, any quantitative analysis of these modern prominence observations requires the development of appropriate numerical models (simulations) based on an adequate theory of the plasma in a magnetic field and the theory of its interaction with radiation. It is the main objective of these lectures to present such a theory and to discuss various aspects of its applicability in the context of current prominence research. We concentrate on a tutorial description of basic physical principles and applications used, rather than making an exhaustive review of the whole field.

There exists a vast literature on prominences and filaments. Our basic

understanding of the prominence physics is well described in the monograph of Tandberg-Hanssen: *The Nature of Solar Prominences* (1995). Important are also the proceedings from the IAU Colloquia on prominences no. 117 and 167 held on Hvar in 1989 (Ruždjak and Tandberg-Hanssen, 1990) and in Aussois in 1997 (Webb, Rust and Schmieder, 1998), respectively, together with the proceedings from the IAU Colloquium no. 144 held in 1993 in Slovakia (Rušin, Heinzel and Vial, 1994). One can also find many interesting papers in the proceedings from the last two European Solar Physics Meetings held in 1999 in Florence (Wilson, 1999) and in 2002 in Prague (Wilson, 2002), respectively. Many exciting results were obtained analysing data from the SOlar and Heliospheric Observatory – SOHO. A new class of ground-based observations is represented by polarisation measurements in both prominences and filaments which are aimed at determining the vector magnetic field.

2. MHD structure of prominences

We will start our theoretical description with classical magneto-hydrodynamic (MHD) prominence models. These models contain the basic physics of the mutual interaction between the plasma and coronal magnetic field in which the prominences form.

2.1. BASIC EQUATIONS

Basic principles of solar MHD are explained in the textbook of Priest (1982). The relevant equations are:

Equation of motion (momentum equation):

$$\rho \frac{d\mathbf{v}}{dt} = -\nabla p + \frac{1}{c}\mathbf{j} \times \mathbf{B} + \rho \mathbf{g}\,, \tag{1}$$

where $\mathbf{B}$ and $\mathbf{j}$ have to obey the relations

$$\nabla.\mathbf{B} = 0 \tag{2}$$

and

$$\mathbf{j} = \frac{c}{4\pi}\nabla \times \mathbf{B}\,. \tag{3}$$

Continuity equation:

$$\frac{d\rho}{dt} + \rho\nabla.\mathbf{v} = 0\,. \tag{4}$$

Equation of state:

$$p_\mathrm{g} = p_\mathrm{g}(\rho, T, \overline{m}) = \rho k T / \overline{m}\,. \tag{5}$$

Turbulent pressure:

$$p_\mathrm{t} = \frac{1}{2}\rho v_\mathrm{t}^2\,. \tag{6}$$

Individual quantities have the following meaning:

ρ – plasma density
p – total plasma pressure, $p = p_\mathrm{g} + p_\mathrm{t}$
$\mathbf{v}$ – flow velocity
v_t – mean turbulent velocity
T – kinetic temperature
$\overline{m}$ – mean molecular mass
$\mathbf{j}$ – current density
$\mathbf{B}$ – magnetic field vector
$\mathbf{g}$ – gravitational acceleration on solar surface

∇p – force due to pressure gradients
$(1/c)\,\mathbf{j} \times \mathbf{B}$ – Lorentz force
$\rho\mathbf{g}$ – gravity force

For a given temperature structure, one can solve these equations to obtain p, ρ and $\mathbf{v}$. The temperature structure follows from the energy-balance condition and the ionization degree is obtained by solving the non-LTE equations of radiative transfer (to be discussed later).

In the simplest case, solar prominences can be viewed as static structures and thus we shall use the magneto-hydrostatic (MHS) approximation with $\mathbf{v} = 0$ and the equilibrium equation

$$\nabla p = \frac{1}{4\pi}(\nabla \times \mathbf{B}) \times \mathbf{B} + \rho\mathbf{g}\,. \tag{7}$$

Since we shall be mostly interested in quiescent prominences where the macroscopic velocities are small, this MHS approximation will give us a very good description of the physical situation.

2.2. MHS MODEL OF KIPPENHAHN AND SCHLÜTER

Prominences are mostly located along the so-called *neutral lines* where the vertical photospheric magnetic field changes its sign and thus the vertical component of that field is zero along such a line. The field lines which extend to coronal altitudes and penetrate the prominence body may have the same orientation as the field which is obtained inside the prominence and we thus deal with a simple magnetic arcade - this configuration is of *normal* or *N*-polarity. If the orientations are opposite we speak about *inverse* or *I*-polarity prominences. The latter were observationally discovered by Leroy, Bommier and Sahal-Bréchot (1984) and a detailed statistical analysis of Bommier and Leroy (1998) showed that a large majority of quiescent prominences is actually of *I*-polarity type. Inverse-polarity configuration was studied theoretically by Kuperus and Raadu (1974).

Now we shall describe one of the first MHS prominence models which was suggested by Kippenhahn and Schlüter (1957). This 'KS' model of *N*-polarity prominences demonstrates well the basic properties of interaction of the cool dense plasma with the magnetic field. First, we shall use it to illustrate how one can construct global prominence models. Second, in Section 7 we shall outline a generalisation of this classical model to two dimensions and briefly describe how it can be used to study the prominence fine structure.

Here we shall consider a one-dimensional (1D) plasma slab oriented vertically with respect to the solar surface and having the finite geometrical thickness D. This slab is embedded in the coronal magnetic field and its weight is balanced by the Lorentz force acting against the gravity. For our modelling we take a Cartesian coordinate system with x perpendicular to the prominence slab, y along the prominence slab and z in the vertical direction perpendicular to the solar surface. The basic assumption is that all quantities are independent of y and z. For simplicity we take $B_y = 0$, the generalisation to a non-zero, constant B_y is straightforward. The equilibrium is then given by the equations

$$\frac{\partial B_x}{\partial x} = 0 \Rightarrow B_x = \text{constant}\,, \tag{8}$$

$$\frac{\partial p}{\partial x} = -\frac{1}{4\pi} B_z \frac{\partial B_z}{\partial x}\,, \tag{9}$$

$$\frac{\partial p}{\partial z} = \frac{1}{4\pi} B_x \frac{\partial B_z}{\partial x} - \rho g = 0\,. \tag{10}$$

Combination of the last two equations gives

$$\frac{\partial p}{\partial x} = -\rho g \frac{B_z}{B_x}\,. \tag{11}$$

For the sake of simplicity we shall now put $p = p_g$. The solution of the above two equations has the form

$$B_z = B_{z1} \tanh \left(\frac{B_{z1}}{B_x} \frac{x}{2H} \right) \tag{12}$$

and

$$\rho = \frac{B_{z1}^2}{8\pi} \frac{g}{H} \left[\cosh^2 \left(\frac{B_{z1}}{B_x} \frac{x}{2H} \right) \right]^{-1}, \tag{13}$$

where

$$H = \frac{kT}{g\overline{m}} \tag{14}$$

is the hydrostatic pressure scale height and B_{z1} the vertical field component at the surface of the prominence. These solutions have been obtained for constant T and $\overline{m}$. The width of the prominence is approximately equal to

$$D \simeq 4 \frac{B_x}{B_{z1}} H. \tag{15}$$

Poland and Anzer (1971) gave a generalisation for the case that both T and $\overline{m}$ are prescribed functions of x.

2.3. SOLUTION OF MHS EQUATIONS USING THE COLUMN-MASS SCALE

The equations for equilibrium become considerably simpler if one uses instead of x the column-mass coordinate m, defined by the relation

$$dm = -\rho dx \tag{16}$$

with $m = 0$ at one surface of the prominence slab and $m = M$ at the other. Then one obtains the equations

$$\frac{dp}{dm} = g \frac{B_z}{B_x} \tag{17}$$

and

$$\frac{dB_z}{dm} = -\frac{4\pi g}{B_x}. \tag{18}$$

These equations can now easily be integrated and have the following solution

$$B_z(m) = -\frac{4\pi}{B_x} gm + \text{constant},$$

$$B_z(M/2) = 0 \Rightarrow \text{constant} = \frac{4\pi}{B_x} g \frac{M}{2},$$

$$B_z(m) = \frac{4\pi g}{B_x}\left(\frac{M}{2} - m\right),$$

$$\frac{dp}{dm} = \frac{4\pi g^2}{B_x^2}\left(\frac{M}{2} - m\right),$$

$$p(m) = \frac{4\pi g^2}{B_x^2}\left(\frac{M}{2}m - \frac{m^2}{2}\right) + \text{constant}, \tag{19}$$

$$p(m) = 4p_c\frac{m}{M}\left(1 - \frac{m}{M}\right) + p_0, \tag{20}$$

where p_0 is the coronal pressure at the slab surfaces (this equation was first derived by Heasley and Mihalas, 1976). At the slab surface one has $B_z \equiv B_{z1}$ which gives

$$M = \frac{B_x B_{z1}}{2\pi g}. \tag{21}$$

Using this formula, we obtain for p_c

$$p_c = \frac{\pi g^2}{B_x^2}\frac{M^2}{2} = \frac{B_{z1}^2}{8\pi}. \tag{22}$$

The quantity p_c can be interpreted in the following way: at the slab centre we have the pressure

$$p_{\text{cen}} = p(M/2) = p_c + p_0. \tag{23}$$

If p_0 would be zero, then $p_{\text{cen}} = p_c = B_{z1}^2/8\pi$, which is the magnetic pressure. Therefore, in this case the gas pressure at the slab centre will be equal to the magnetic pressure calculated with $B = B_{z1}$.

These equations based upon the column-mass coordinate m are very simple, but in order to obtain the true spatial structure of the prominence (i. e. the density and other quantities as functions of x and the magnetic field geometry) one has to integrate Eq. (16) . In almost all cases this can be done only numerically. Only for the special case of $T = \text{constant}$ and $\overline{m} = \text{constant}$ one recovers the analytical solutions given by Eqs. (12) – (14). To get the density $\rho(m)$ we use the state equation (5) with the mean molecular mass

$$\overline{m} = \frac{1 + 4\alpha}{1 + \alpha + i}m_H, \tag{24}$$

where i is the ionisation degree of hydrogen, $i = n_p/n_H$ (n_p and n_H are the proton and hydrogen densities, respectively), α the helium abundance relative to hydrogen and m_H the hydrogen atom mass. i varies between

zero (neutral gas) and unity (fully-ionised plasma). Inside the prominence with a PCTR, one can take the following schematic relation for i

$$i = 1 - (1 - i_c) \left(\frac{T_{\text{tr}} - T}{T_{\text{tr}} - T_{\text{cen}}} \right)^2 , \tag{25}$$

where i_c is the ionisation degree at the centre of the prominence. However, for a given prominence model the ionisation-degree structure results from rather complex non-LTE radiative-transfer calculations which are discussed below.

Global parameters of the slab

Here we summarise the basic parameters of the 1D prominence slab in MHS equilibrium. Besides the total column mass M and the mean temperature T we have:

Mean gas pressure $\bar{p}$:

$$\bar{p} = \frac{1}{M} \int_0^M p \, dm = \frac{2}{3} p_c + p_0 . \tag{26}$$

Mean gas density $\bar{\rho}$:

$$\bar{\rho} = \frac{1}{M} \int_0^M \rho \, dm . \tag{27}$$

Total geometrical thickness:

$$D_{\text{tot}} = \int_0^M \frac{dm}{\rho} . \tag{28}$$

A representative value for the thickness D:

$$D = \frac{M}{\bar{\rho}} . \tag{29}$$

Neglecting the coronal pressure p_0, we can express D in terms of T, M and central gas pressure p_{cen} as

$$D = \frac{3k}{2\overline{m}} \left(\frac{TM}{p_{\text{cen}}} \right) . \tag{30}$$

3. Magnetic dips in quiescent prominences

The weight of the prominence itself will lead to dips in the magnetic field. If we use the one dimensional slab model we get the vertical equilibrium

condition given by Equation (10). The investigations of Bommier *et al.* (1994) showed that in many of their prominences B_{z1} is comparable to the total horizontal field which we denote by $B_{\mathrm{h}} = \sqrt{B_x^2 + B_y^2}$. The field vector was determined using linear-polarisation measurements and applying the theory of the Hanle effect. The latter means that the degree of the linear polarisation of radiation which is scattered by the prominence is lowered in the presence of the magnetic field. These measurements imply that the column mass in the prominence has to be sufficiently large to produce these deep dips. They also show that the inclination angles of the magnetic field in these prominences are at least one order of magnitude larger than the coronal values. By the latter we mean the magnetic dips which are very shallow and appear in the magnetic field topology of a quiescent prominence when one neglects the weight of the cool plasma (they exist as a result of the equilibrium between the magnetic-pressure gradient and the magnetic-tension force). In other words, we can say that such coronal dips exist in cases of very low plasma β, which is the ratio between the gas pressure and the magnetic pressure. Such configurations were recently studied using the linear force-free-field ($lfff$) extrapolations (Aulanier and Démoulin, 1998). For discussion of various dip configurations see a review by Anzer (2002) where a brief summary of the prominence *formation models* is also given.

It is intuitively clear that the larger β, the deeper the dips produced by the weight of the prominence plasma. We shall now derive a simple analytic relation between the field line inclination and the value of the plasma β inside the prominence. In our one dimensional slab models one has

$$\beta(x) = \frac{8\pi p(x)}{B_x^2 + B_y^2 + B_z^2(x)} \,. \tag{31}$$

For simplicity we again assume $B_y = 0$; the generalisation to the case $B_y \neq 0$ can be easily obtained. The equilibrium in the x-direction gives a condition on the total pressure

$$\frac{d}{dx}\left[p(x) + \frac{B_x^2 + B_z^2(x)}{8\pi} \right] = 0 \,. \tag{32}$$

This leads to the relation

$$p(x) = p_0 + \frac{B_{z1}^2 - B_z^2(x)}{8\pi} \,, \tag{33}$$

where p_0 (as in the previous sections) is the pressure at the surface of the prominence. For the plasma β at the surface we then obtain

$$\beta_0 = \frac{8\pi p_0}{B_x^2 + B_{z1}^2} \,. \tag{34}$$

From these equations one can derive the following basic relation between the local plasma β and the field line inclination angle ψ (the angle between the vertical axis z and the magnetic-field vector)

$$\beta(x) = (\beta_0 + \cos^2 \psi_1) \frac{B^2(x_1)}{B^2(x)} - \cos^2 \psi(x). \tag{35}$$

The local value of ψ is given by $\cos \psi(x) = B_z(x)/B(x)$ and $B^2(x) = B_x^2 + B_z^2(x)$. This will lead to a central value of β

$$\beta_c = \frac{\beta_0}{\sin^2 \psi_1} + \cot^2 \psi_1. \tag{36}$$

Since usually $\beta_0 \ll 1$ holds, Equation (36) can be simplified to

$$\beta_c \simeq \cot^2 \psi_1. \tag{37}$$

This simple relation derived by Heinzel and Anzer (1999) demonstrates that in general the value of β inside prominences will not be negligible. For example if $\psi_1 = 45°$ one obtains $\beta_c = 1$. From the observations of Bommier *et al.* (1994) one finds that the values $\beta \simeq 1$ are relatively frequent. Equations (36) and (37) were derived from a 1D slab model. But a similar relation can be obtained if the prominence consists of individual vertical threads. The details of such thread models are presented in a paper by Heinzel and Anzer (2001) and here we shall only give a brief description. In such models the column mass, the field vector and the width are assumed to vary along the prominence axis. But the total pressure $p_T = p + B^2/8\pi$ has to be constant and the magnetic field is *laminar*, i.e. the field lines lie in parallel planes which requires that $B_y/B_x = $ constant everywhere. In this case Equation (10) will hold along each individual field line; but now the quantities ψ, x, and also $\mathbf{B}$ can all be functions of the y-coordinate. From these results one can conclude that the relations (36) – (37) which were originally derived for the special case of a 1D slab can also be applied to much more general configurations. Therefore, we expect that the results which we have obtained for simple 1D slabs in MHS equilibrium are valid quite generally.

4. Interpreting prominence spectra

The radiation which prominences or filaments emit and which we observe in the form of monochromatic images or spectra has two-fold importance for prominence physics. First, it provides us with the diagnostics of the prominence structure – this means that using rather sophisticated tools discussed below one can determine the basic thermodynamic quantities

like temperature, density, pressure, ionisation, but also the intensity of the magnetic field. On the other hand, the radiation field plays a crucial role in the global energy budget of prominence structures and has to be considered when evaluating self-consistently the prominence internal structure. Here we have in mind theoretical *ab initio* models which also include the plasma dynamics in a magnetic field. For this we normally use the MHD approach described in the previous section. We shall now start with the prominence spectral diagnostics and show how the *spectral lines* can be modelled.

4.1. BASIC EQUATIONS OF RADIATIVE TRANSFER

The *Radiative Transfer Equation* (RTE) tells us how much the *specific intensity* of radiation $I(\nu)$ is changed along an elementary geometrical path ds due to absorption and emission processes (ν is the frequency)

$$\frac{dI_\nu}{ds} = -\chi_\nu I_\nu + \eta_\nu. \tag{38}$$

The absorption and emission coefficients are denoted as χ_ν and η_ν, respectively. Using x as the reference coordinate in a 1D prominence slab

$$\frac{dx}{ds} = \cos\theta \equiv \mu \tag{39}$$

and τ_ν as the *optical depth* at frequency ν

$$d\tau_\nu = -\chi_\nu dx \tag{40}$$

we can write the transfer equation in its standard form

$$\mu\frac{dI_\nu}{d\tau_\nu} = I_\nu - S_\nu. \tag{41}$$

Here we have introduced the so-called *source function* as

$$S_\nu \equiv \frac{\eta_\nu}{\chi_\nu}. \tag{42}$$

Solving the transfer equation is a non-trivial task and must be done numerically. The problem is that in general the source function depends on the radiation intensity. Only in the case when we already know the source function, the integration of the transfer equation is relatively simple (so-called formal solution). We shall return to this point later on.

4.2. OPACITY AND EMISSIVITY

Now we shall show how χ_ν and η_ν can be derived in the case of a spectral line (for the sake of simplicity we shall not deal here with continua which are less used for the prominence diagnostics but are still very important for determining the excitation and ionisation balance). First we introduce the notion of the absorption profile

$$\phi_\nu = \frac{1}{\sqrt{\pi}\Delta\nu_{\mathrm{D}}} H(a, x),\tag{43}$$

where $H(a, x)$ is the Voigt function, a is the damping parameter $a = a_i + a_j$ pertinent to the respective atomic levels i and j and $x = \Delta\nu/\Delta\nu_{\mathrm{D}}$ is the frequency displacement from the line centre expressed in units of the Doppler width. The line profile is normalised:

$$\int_0^\infty \phi_\nu \, d\nu = 1 \,.\tag{44}$$

The energy absorbed by the line absorption is $h\nu_{ij} = E_j - E_i$, where E is the excitation energy of a given atomic level and ν_{ij} is the line-centre frequency.

Using the Einstein coefficients for absorption (B_{ij}), spontaneous emission (A_{ji}) and stimulated emission (B_{ji}), the absorption coefficient corrected for stimulated emission is written as

$$\chi_\nu = n_i B_{ij} \frac{h\nu_{ij}}{4\pi} \phi_\nu - n_j B_{ji} \frac{h\nu_{ij}}{4\pi} \psi_\nu \,,\tag{45}$$

and the emission coefficient

$$\eta_\nu = n_j A_{ji} \frac{h\nu_{ij}}{4\pi} \psi_\nu \,.\tag{46}$$

In these relations n_i and n_j are the atomic level populations (density of atoms in a given quantum state). The frequency dependence of the absorption and emission processes is given by the profiles ϕ_ν and ψ_ν, respectively. In most practical cases we assume that $\psi_\nu \equiv \phi_\nu$ and this approximation is called complete redistribution (see below). As shown above, the line source function is defined as the ratio of emission and absorption coefficients, i.e.

$$S_\nu = \frac{n_j A_{ji} \psi_\nu}{n_i B_{ij} \phi_\nu - n_j B_{ji} \psi_\nu} \simeq \frac{n_j A_{ji}}{n_i B_{ij} - n_j B_{ji}} \rho_{ij}(\nu)\tag{47}$$

with $\rho_{ij}(\nu) \equiv \psi_\nu/\phi_\nu$. This corresponds to the so-called non-LTE situation normally met in prominences and filaments, where the atomic level populations and $\rho_{ij}(\nu)$ depend on the radiation intensity and thus are coupled to

the radiative-transfer equation. Contrary to that in *Local Thermodynamic Equilibrium* (LTE) the level populations are given by the Boltzmann distribution and the source function is simply equal to the Planck function. Unfortunately, LTE is of no use in the prominence physics because of rather low plasma densities. Basic concepts of the non-LTE physics are well explained in the textbook of Mihalas (1978).

4.3. FORMAL SOLUTION OF THE TRANSFER EQUATION IN A FINITE 1D SLAB

Before we show how the line source function can be obtained by the solution of the full non-LTE problem, we shall discuss simple formal solutions of the transfer equation. For this we use two kinds of 1D plasma slabs of a finite geometrical thickness, oriented either vertically above the solar surface and irradiated symmetrically on both sides (the case of prominences seen on the limb) or oriented horizontally (parallel to the solar surface) and irradiated only from one side – the bottom surface is illuminated by the Sun and no incident radiation from the corona is expected in spectral lines of interest (the case of filaments). These approximate geometries are schematic, more rigorous transfer has to be done in 2D or even 3D geometries as we shall discuss later.

To obtain the outgoing radiation intensity at the slab surface (i.e. for $\tau = 0$) and in direction μ, we can formally solve the transfer equation (41) and obtain

$$I(0, \mu) = I_0(\tau, \mu) \exp(-\tau/\mu) + \int_0^\tau S(t) \exp(-t/\mu) dt/\mu, \qquad (48)$$

where $I_0(\tau, \mu)$ is the *incident radiation* on the other side of the slab.

Assuming a constant source function, we get analytically

$$I(0, \mu) = I_0(\tau, \mu) \exp(-\tau/\mu) + S[1 - \exp(-\tau/\mu)]. \qquad (49)$$

Then two limiting cases are important

$$\tau \ll 1 \;\Rightarrow\; S[1 - \exp(-\tau/\mu)] \simeq S\tau/\mu \,, \qquad (50)$$
$$\tau \gg 1 \;\Rightarrow\; S[1 - \exp(-\tau/\mu)] \simeq S \,. \qquad (51)$$

Prominence on the limb:

The spectral line is in emission ($I_0 = 0$, no background radiation), for $\mu = 1$ we get

$$I(0) = S[1 - \exp(-\tau)] \,. \qquad (52)$$

As a special case of an *optically-thin slab* we have

$$I(0) \simeq S\tau = \eta D, \tag{53}$$

where $\tau \ll 1$ and D is the geometrical thickness of the slab. However, we have to remember that I_0 from other directions drives the source function or η and plays a crucial role in determining these quantities. This is a standard situation in central cool parts of prominences where the scattering of the line radiation is the dominant radiation process. On the other hand, inside the PCTR the temperature is steeply increasing and emission lines are mostly optically-thin and the collisional excitation followed by spontaneous emission plays an important role in the line-formation process.

Filament on the disk:

The spectral lines are normally in absorption (e.g. the hydrogen Hα line), for $\mu = 1$ we get

$$I(0) = I_0 \exp(-\tau) + S[1 - \exp(-\tau)]. \tag{54}$$

Since the line source function is mainly controlled by the photon scattering in low-density prominence and filament plasmas, we can approximately write

$$S \simeq \frac{1}{2}I_0, \tag{55}$$

where $1/2$ is the *dilution factor* by which the incident solar-disk radiation I_0 has to be multiplied because there is roughly only one half of the prominence or filament surrounding from which the incident radiation illuminates it (no radiation from the corona). For filaments seen against the disk we express their intensity contrast as

$$\frac{I(0)}{I_0} = \frac{1}{2}[1 + \exp(-\tau)], \tag{56}$$

and in two limiting situations we get

$$\tau \ll 1 \implies \frac{I(0)}{I_0} \simeq 1,$$
$$\tau \gg 1 \implies \frac{I(0)}{I_0} \simeq \frac{1}{2}.$$

Therefore, for an optically-thin filament, the line-centre contrast approaches unity and in the case of a large optical thickness it goes to $1/2$. This is why we can see Hα filaments as dark structures relative to the background chromosphere. Since τ depends on frequency (or wavelength), in the line

wings it is largely reduced and we can no longer see the dark filament – this is exactly the effect of shifting the narrow-band filter out of the line centre.

The reason why we see Hα prominences on the limb in emission and filaments on the disk in absorption is the following. Cool prominence plasma absorbs the radiation coming from the solar disk and scatters it in all directions. Because there is no coronal background in Hα (corona is dark), we see on the limb only the scattered radiation and the Hα line is thus in emission. On the other hand, the chromospheric background of the filament is the absorption line which becomes even darker due to filament absorption. The radiation scattered in the direction toward the observer represents only a small fraction of the absorbed one and thus cannot compensate for the absorption. We thus see filaments darker than the background chromosphere.

4.4. STATISTICAL EQUILIBRIUM EQUATIONS

In general, the non-LTE line source function is not known in advance (and also not constant with depth in the slab) and thus it must be computed by solving the transfer problem. Since the absorption and emission coefficients depend on the atomic level populations, we have to compute them using the *Equations of Statistical Equilibrium* (ESE) which replace the Boltzmann equation used in LTE. A general form of ESE is

$$\frac{dn_i}{dt} = \sum n_j(R_{ji} + C_{ji}) - n_i \sum (R_{ij} + C_{ij}), \qquad (57)$$

$$\frac{dn_i}{dt} = \frac{\partial n_i}{\partial t} + \frac{\partial n_i v}{\partial x}.$$

R_{ij} are the radiative rates, those for absorption and stimulated emission depend on the line intensity. $C_{ij} = n_{\rm e}\Omega_{ij}(T)$ are the collisional rates proportional to the electron density $n_{\rm e}$ and dependent on temperature T through the function $\Omega(T)$. The time-derivative on the left hand side splits into the local temporal variations of n_i (e.g. due to time-dependent heating processes) and the divergence of the flux of atoms in the state i (v is the macroscopic flow velocity of the prominence plasma). Other equations to be used are the charge-conservation equation $\sum N_k Z_k = n_{\rm e}$ and total particle-number (N) evaluation which comes from the state equation for the gas pressure $p_{\rm g}$

$$p_{\rm g} = NkT. \qquad (58)$$

Here Z_k is the ionisation degree of the k-th species and $N = \sum N_k + n_{\rm e}$ (N_k is the total density of atoms in a given ionisation state k). Finally,

knowing N, the electron density and the atomic abundances together with the atomic masses, one can compute the gas density ρ.

To be more specific, we write the radiative rates in the form $R_{ij} = B_{ij}\overline{J}_{ij}$ for absorption, $R_{ji}(\text{spont}) = A_{ji}$ for spontaneous emission and $R_{ji}(\text{stim}) = B_{ji}\overline{J}_{ij}$ for stimulated emission. Then $R_{ji} = R_{ji}(\text{spont}) + R_{ji}(\text{stim})$.

$$\overline{J}_{ij} = \int_0^\infty J_\nu \phi_\nu \, d\nu \tag{59}$$

is the integrated spatially averaged *mean intensity* weighted by the absorption profile. This quantity tells us how many line photons are actually absorbed from the mean radiation field, owing to the frequency dependence of the absorption coefficient represented by the line profile function ϕ_ν.

Finally, we can define the *net radiative rates* as

$$R_{ij}^{\text{net}} \equiv n_j A_{ji} - (n_i B_{ij} - n_j B_{ji})\overline{J}_{ij}. \tag{60}$$

4.5. MULTILEVEL ACCELERATED LAMBDA ITERATIONS (MALI)

The solution of the mutually coupled RTE and ESE (non-LTE problem) represents a difficult numerical task demanding powerful computing resources. Various methods can be found in the textbook of Mihalas (1978). During the last two decades, new techniques called *Accelerated Lambda Iterations* (ALI) have been developed for stellar atmospheric modelling and are now routinely used (see Hubeny, Mihalas and Werner, 2003). For prominences they have been first applied by Auer and Paletou (1994) in the frame of a two-level atom. To describe them briefly, we write the formal solution of RTE at a given depth in terms of the *Lambda operator* as

$$I_{\nu\mu} = \Lambda_{\nu\mu} S_{\nu\mu}. \tag{61}$$

This is used in *lambda iterations* (LI) to solve the non-LTE problem, i.e. we can write

$$\overline{J}_{ij}^n = \Lambda S^{n-1}, \tag{62}$$

where the integrated mean intensity $\overline{J}_{ij}$ which is needed to compute the radiative rates in ESE is obtained at the n-th iteration from the source function taken from the previous iteration. This, however, leads to very inefficient and extremely slow convergence rates and thus LI's are of no practical use (see Mihalas, 1978). Therefore, it has been suggested to use the accelerated lambda iterations which are based on the idea of the Lambda-operator splitting (Cannon, 1973)

$$\Lambda = \Lambda^* + (\Lambda - \Lambda^*), \tag{63}$$

where Λ^* is the *Approximate Lambda Operator* (ALO). Then the iterative solution can be written as

$$\overline{J}^n_{ij} = \Lambda^* S^n + (\Lambda - \Lambda^*)[S^{n-1}] = \Lambda^* S^n + \Delta\overline{J}^{n-1}_{ij}. \tag{64}$$

We can immediately see that in this case $\overline{J}^n_{ij}$ is consistent with the current source function S^n and only a correction to it is computed using the lagged source function S^{n-1}. Although the coupling between $\overline{J}^n_{ij}$ and S^n is only approximate (because of the use of Λ^* instead of the exact operator), the correction term improves the solution within a limited number of iterations and the final solution is exact. Further, one can insert this into the ESE and thus *precondition* them as suggested by Rybicki and Hummer (1991). Using the formula (47) for the line source function, we can express R^{net}_{ij} as

$$R^{\mathrm{net}}_{ij} = n_j A_{ji}(1 - \Lambda^*) - (n_i B_{ij} - n_j B_{ji})\Delta\overline{J}^{n-1}_{ij}, \tag{65}$$

where Λ^* and $\Delta\overline{J}$ are the angle and frequency-averaged quantities. In this way the net radiative rates no longer depend on the current radiation intensity which represents a great advantage for the speed of convergence. For multilevel atoms, this approach was called the MALI method by Rybicki and Hummer (1991). For prominences is was first applied by Heinzel (1995) and with generalisation to 2D geometry by Paletou (1995).

4.6. PARTIALLY-COHERENT SCATTERING IN PROMINENCE PLASMAS

As we have seen above, the solar radiation absorbed by the prominence plasma is most probably scattered into all directions. In general, the emission profile which describes the line-photon scattering differs from the absorption one and this is why we have introduced the function ρ

$$\rho_\nu = \frac{\psi_\nu}{\phi_\nu}, \tag{66}$$

where ψ_ν is the normalised emission profile and ϕ_ν normalised absorption profile. ψ_ν is expressed in terms of the so-called *scattering integral*

$$\psi_\nu = \frac{\int_0^\infty R_{\nu',\nu} J_{\nu'} d\nu'}{\overline{J}}, \tag{67}$$

where $R_{\nu',\nu}$ is the *redistribution function*, i.e. the probability that the radiation absorbed at frequency ν' will be reemitted at frequency ν. If there is such a correlation between both frequencies we speak about partially-coherent scattering (*Partial Redistribution* – PRD).

As we have already mentioned, the *Complete Redistribution* – CRD assumes that $\rho = 1$. In such a case the redistribution function has the

simple form $R_{\nu',\nu} = \phi_{\nu'}\phi_\nu$ and when inserted into Equation (68) one gets $\psi_\nu \equiv \phi_\nu$. The photon frequencies are completely uncorrelated in this case.

For resonance lines (transitions from the ground state) one has

$$R_{\nu',\nu} = \gamma R_{II} + (1 - \gamma)R_{III}\,, \tag{68}$$

$$\gamma = \frac{A_{21}}{A_{21} + Q_E}\,.$$

The function R_{II} follows from purely coherent scattering in the atom's frame while R_{III} reflects the complete redistribution in the atom's frame due to elastic collisions having the rate Q_E. γ is the branching ratio, i.e. the probability that the coherence in the atom's frame is destroyed by collisional perturbation of the upper atomic state. $R_{\nu',\nu}$ is the velocity-averaged redistribution function, here also averaged over all directions. The critical importance of PRD for resonance lines like hydrogen Lyman α emitted by quiescent prominences was first demonstrated by Heinzel, Gouttebroze and Vial (1987). However, the subordinate lines like Hα which arise between two excited atomic levels can be well described by the CRD approximation – the coherence is partially destroyed by the lower-level broadening.

1D non-LTE models of both prominences and filaments have been constructed, using the PRD approach for first two Lyman lines (for higher members of the Lyman series the coherence effects become less important and one can use CRD). A large grid of such models was computed by Gouttebroze, Heinzel and Vial (1993) assuming vertical isobaric and isothermal slabs symmetrically irradiated on both sides by the solar radiation. This grid demonstrates systematic trends in the behaviour of various plasma and radiation quantities. The prominence-plasma diagnostics based on UV and EUV spectral observations obtained on board SOHO was recently reviewed by Patsourakos and Vial (2002).

5. Energy balance in solar prominences

The simplest energy balance is called the *radiative equilibrium*. This means that the radiative flux F_r integrated over all frequencies is conserved inside the prominence slab

$$\frac{dF_r}{dx} = 0\,, \tag{69}$$

$$F_r = \int_0^\infty F_\nu\, d\nu\,,$$

$$F_\nu = \frac{1}{2} \int_{-1}^{1} I_{\nu,\mu}\mu\, d\mu\,.$$

In other words, the total radiation energy emitted at a given point must be exactly equal to that absorbed, i.e.

$$L = 4\pi \int_0^\infty (\eta_\nu - \chi_\nu J_\nu)d\nu = 4\pi \int_0^\infty \chi_\nu (S_\nu - J_\nu)d\nu = 0 \,. \qquad (70)$$

As we shall see in the next section, this situation was investigated theoretically but doesn't seem to be realistic in solar prominences. If the radiative equilibrium is violated, then there must exist sources of heating and cooling which finally will establish a more general energy equilibrium

$$\frac{dF_{\rm c}}{dx} = L - H \,, \qquad (71)$$

in which $F_{\rm c}$ represents the conductive flux and L are the so-called radiation losses given by Equation (71). $L = 0$ only in the case of radiative equilibrium. Other possible sources of the heating are included in the term H (wave heating, enthalpy flux divergence, magnetic reconnection, etc.). The solution of the energy-balance equation gives us the temperature structure of the prominence slab. The conductive-heating term in Equation (72) can be generalised by assuming that the prominence outermost layers are also heated due to the *ambipolar diffusion*. This was studied in detail by Fontenla *et al.* (1996) who have demonstrated the importance of the ambipolar diffusion for the prominence energy balance.

6.   Coupling MHD and non-LTE in 1D prominence slabs

Theoretical prominence models can be constructed using the MHS equations discussed in Section 2 where in the 1D case we have obtained an analytical solution for the pressure-balance equilibrium. This was done using the column-mass scale. However, to describe the model on geometrical scale, one has to know the spatial variations of the temperature and the ionisation degree which both appear in the state equation. These two quantities are needed to relate the gas pressure and density. As briefly explained in the previous section, the temperature structure is derived from the energy-balance equation, which is represented by the radiative equilibrium in its simplest form. One can also use some kind of *empirical temperature structure* derived from typical observational constrains. On the other hand, the ionisation structure must be computed consistently with the internal temperature structure, electron density and the radiation field which determine the ionisation equilibrium of the plasma via the equations of statistical equilibrium (plus other constraint relations). Therefore, a full non-LTE radiative-transfer treatment must be used, together with proper specifications of the prominence boundary conditions, i.e. the radiation incident on the slab surfaces.

Such a coupled MHS and non-LTE problem was first solved in a simplified way by Poland and Anzer (1971), who have studied the basic properties of KS models. A much more detailed approach was used by Heasley and Mihalas (1976), who solved all coupled equations of MHD, non-LTE and energy balance by the so-called *complete linearisation* method (see Mihalas, 1978). MHS models of the KS-type in radiative equilibrium were found to be geometrically narrow (a few hundreds km) which is due to relatively high pressures used by these authors. This result can be easily understood using Eq. (30), where the slab thickness D is inversely proportional to the gas pressure. Also the temperature at the slab centre which corresponds to radiative equilibrium is rather low, around or even below 5000 K. This is in conflict with the typically higher values obtained from spectral analyses, and thus the problem of radiation equilibrium in the central cool parts of prominences has to be reconsidered. If the empirical temperatures are indeed higher than those of radiation equilibrium, one needs a substantial prominence heating and the actual nature of this is not well understood.

Modelling similar to that of Heasley and Mihalas (1976) was recently performed by Anzer and Heinzel (1999), who also studied the prominence energy balance using empirical temperature variations and detailed computations of radiation losses. They presented altogether 12 different models in MHS equilibrium, one half of them having also rather small thickness $D \simeq 400 - 500$ km. Their models were aimed at representing the whole prominence slab as in Heasley and Mihalas (1976), but the class of geometrically narrow models can also be viewed as a certain kind of prototype for the fine-structure models.

7. Coupling MHD and non-LTE in prominence fine structures

Magnetic dips of the KS-type which contain enough cool plasma were discussed so far as models of the *whole* prominence of N-polarity type. However, it is now well known that prominences consist of fine structures which have dimensions of the order of or below one arc sec, which is the resolution limit of medium-size telescopes. These structures are observed by large solar-tower telescopes or coronagraphs and they cannot be neglected in current prominence modelling. A straightforward generalisation of the KS models to fine structures is if one considers them as purely *local* MHS equilibria, producing many local magnetic dips everywhere. Such a scenario was first proposed by Poland and Mariska (1988) who considered local magnetic dips due to the cool plasma weight and these dips were propagated vertically to form narrow vertical plasma threads. Such threads are frequently observed in quiescent prominences (see `http://www.astro.uni.wroc.pl/prominatlas.html`) and their puzzling behaviour is that they are almost

vertical while the magnetic field derived from polarisation measurements is predominantly horizontal (Leroy, 1989). A first approximation to such vertical threads is to consider them vertically infinite and homogeneous, while their horizontal cross-section is obtained from the solution of 2D MHS equilibria of the KS-type, coupled to non-LTE radiative transfer in two dimensions. This approach was first used by Heinzel and Anzer (2001), who presented the basic equations of 2D equilibria and performed numerical solutions of 2D radiative transfer for the multilevel hydrogen atom. The method used to solve the 2D transfer problem is that of Auer and Paletou (1994) and Paletou (1995). However, the equilibrium *along* the magnetic field lines is expressed using the the m-scale as in 1D (see Eq. (20)), while the 2D transfer is performed on a Cartesian mesh. A transformation between m-scale and geometrical x-scale is thus needed and is performed iteratively after the ionisation-structure has converged for each such iteration step (Heinzel and Anzer, 2003). The results of these 2D computations allow us to view the fine-structure threads from different directions, in particular along the x-axis which is parallel to the projected field lines and along the y-axis which is perpendicular to them. This also invokes quite different PCTR structures due to the different thermal conductivity along and across the field lines. The spectral profiles of selected hydrogen lines were synthesised for these two viewing directions and their significant differences were demonstrated (Heinzel and Anzer, 2001). Note finally that *locally* near the central dip the I-polarity model will have practically the same structure and, therefore, in the context of fine-structure modelling both configurations will give the same results. This is why we have considered only the KS type models.

8. Conclusions

In these lectures we have presented the basic physical approaches which are used to understand the behaviour of the cool and dense plasma in the prominence magnetic field and its radiation properties. The corresponding models can explain the prominence fine structure in the form of magnetic dips filled by a dense plasma. Although such dips seem to be consistent with the measurements of the magnetic-field vector in several prominences (Bommier *et al.*, 1994), some new measurements (see Paletou *et al.* (2001) and Aulanier (2003) reporting the THEMIS observations) or new interpretations of some archive data (López Ariste and Casini, 2003) lead to conclusions that the magnetic field in prominences can be much stronger, reaching a few tens of Gauss. A similar result was also obtained from the analysis of Aulanier and Démoulin (2003) who show that some prominences of their sample may have stronger fields and others not. But at present it is not clear whether

all these measurements refer to truly quiescent prominences or some of
them are actually active region prominences; such an important question
will require a more systematic study. This issue is of critical importance for
future modelling of the prominence magnetic structure since it is related to
the actual values of the plasma β. A field of the order of 5 Gauss and a gas
pressure of 1 dyn cm^{-2} give $\beta \simeq 1$. The latter gas pressure may represent
an upper limit deduced from spectral diagnostics and non-LTE modelling.
But even considering pressures an order of magnitude lower still leads to
non-negligible β and thus favours the formation of dips due to prominence
weight. However, if the field strengths are increased by a factor $5 - 10$, β
becomes very small and thus the dips will be rather shallow although still
more pronounced than the so-called coronal dips which result from the $lfff$
extrapolations of Aulanier and Démoulin (2003). This can be easily shown
by using Equation (37). Note that the problem of coronal dips is that the
field lines are extremely flat and the dips are also very shallow. Therefore,
such configurations would lead to very wide prominences which are rather
unstable. In contrast to the MHS models discussed in these lectures, the
models based on $lfff$ extrapolations have not yet been studied in terms
of quantitative plasma opacities and radiation properties. In summary,
new precise measurements of the vector magnetic fields in prominences
are highly needed, together with improved spectroscopic determinations
of the basic thermodynamic quantities, namely the gas pressure, density
and temperature. The temperature is crucial for our understanding of the
prominence energy budget. The non-LTE models which take into account
a strong external irradiation of prominences give us also the ionisation
structure of the prominence plasma which is important for the evaluation
of MHS equilibria. Finally, note that the cool plasma which is supposed
to exist in the magnetic dips may extend far beyond the regions where we
see it e.g. in the Hα line (thin dark filaments on the disk). Such extended
structures are visible in UV and EUV lines (SOHO, TRACE) and their
proper interpretation represents a new challenge.

References

Anzer, U.: 2002, in A. Wilson (ed.), *Solar Variability: From Core to Outer Frontiers*, Proc. 10th European Solar Physics Meeting, ESA SP-506, 389.

Anzer, U. and Heinzel, P.: 1999, *Astron. Astrophys.* **349**, 974.

Auer, L.H. and Paletou, F.: 1994, *Astron. Astrophys.* **285**, 675.

Aulanier, G.: 2003, in F. Combes, D. Barret, T. Contini and L. Pagani (eds.), *Scientific Highlights 2003*, SF2A 2003, 237.

Aulanier, G. and Démoulin, P.: 1998, *Astron. Astrophys.* **329**, 1125.

Aulanier, G. and Démoulin, P.: 2003, *Astron. Astrophys.* **402**, 769.

Bommier, V., Landi Degl'Innocenti, E., Leroy, J.-L., and Sahal-Bréchot, S.: 1994, *Solar Phys.* **154**, 231.

Bommier, V. and Leroy, J.-L.: 1998, in D. Webb, D. Rust and B. Schmieder (eds.), *New Perspectives on Solar Prominences*, Proc. IAU Coll. 167, ASP Conf. Ser., Vol. 150, 434.

Cannon, C.J.: 1973, *Astrophys. J.* **185**, 621.

Engvold, O., Hirayama, T., Leroy, J.-L., Priest, E.R., and Tandberg-Hanssen, E.: 1990, in V. Ruždjak and E. Tandberg-Hanssen (eds.), *Dynamics of Quiescent Prominences*, Proc. IAU Coll. 117, Lecture Notes in Physics 363, Springer-Verlag, Berlin, 294.

Fontenla, J.M., Rovira, M., Vial, J.-C., and Gouttebroze, P.: 1996, *Astrophys. J.* **466**, 496.

Gouttebroze, P., Heinzel, P., and Vial, J.-C.: 1993, *Astron. Astrophys. Suppl. Ser.* **99**, 513.

Heasley, J.N. and Mihalas, D.: 1976, *Astrophys. J.* **205**, 273.

Heinzel, P.: 1995, *Astron. Astrophys.* **299**, 563.

Heinzel, P. and Anzer, U.: 1999, *Solar Phys.* **184**, 103.

Heinzel, P. and Anzer, U.: 2001, *Astron. Astrophys.* **375**, 1082.

Heinzel, P. and Anzer, U.: 2003, in I. Hubeny, D. Mihalas and K. Werner (eds.), *Stellar Atmosphere Modelling*, ASP Conf. Ser., Vol. 288, 441.

Heinzel, P., Gouttebroze, P., and Vial, J.-C.: 1987, *Astron. Astrophys.* **183**, 351.

Hubeny, I., Mihalas, D., and Werner, K. (eds.): 2003, *Stellar Atmosphere Modelling*, ASP Conf. Ser., Vol. 288.

Kippenhahn, R. and Schlüter, A.: 1957, *Z. Astrophys.* **43**, 36.

Kuperus, M. and Raadu, M.A.: 1974, *Astron. Astrophys.* **31**, 189.

Leroy, J.-L.: 1989, in E.R. Priest (ed.), *Dynamics and Structure of Quiescent Solar Prominences*, Kluwer Acad. Publ., Dordrecht, 77.

Leroy, J.-L., Bommier, V., and Sahal-Bréchot, S.: 1984, *Astron. Astrophys.* **131**, 33.

López Ariste, A. and Casini, R.: 2003, *Astrophys. J.* **582**, L51.

Mihalas, D.: 1978, *Stellar Atmospheres*, W.H. Freeman, San Francisco.

Paletou, F.: 1995, *Astron. Astrophys.* **302**, 587.

Paletou, F., López Ariste, A., Bommier, V., and Semel, M.: 2001, *Astron. Astrophys.* **375**, L39.

Patsourakos, S. and Vial, J.-C.: 2002, *Solar Phys.* **208**, 253.

Poland, A.I. and Anzer, U.: 1971, *Solar Phys.* **19**, 401.

Poland, A.I. and Mariska, J.T.: 1988, in J.L. Ballester and E.R. Priest (eds.), *Dynamics and Structure of Solar Prominences*, Université des Illes Baléares, 133.

Priest, E.R.: 1982, *Solar Magnetohydrodynamics*, D. Reidel Publ. Co., Dordrecht.

Rybicki, G.B. and Hummer, D.G.: 1991, *Astron. Astrophys.* **245**, 171.

Rušin, V., Heinzel, P., and Vial, J.-C. (eds.): 1994, *Solar Coronal Structures*, Proc. IAU Coll. 144, Veda Publ. House, Slovak Acad. Sci.

Ruždjak, V. and Tandberg-Hanssen, E. (eds.): 1990, *Dynamics of Quiescent Prominences*, Proc. IAU Coll. 117, Lecture Notes in Physics 363, Springer-Verlag, Berlin, 294.

Secchi, A.: 1875, *Le Soleil*, Gauthier-Villars, Paris.

Tandberg-Hanssen, E.: 1995, *The Nature of Solar Prominences*, Kluwer Acad. Publ., Dordrecht.

Webb, D., Rust, D., and Schmieder, B. (eds.): 1998, *New Perspectives on Solar Prominences*, Proc. IAU Coll. 167, ASP Conf. Ser., Vol. 150.

Wilson, A. (ed.): 1999, *Magnetic Fields and Solar Processes*, Proc. 9th European Meeting on Solar Physics, ESA SP-448.

Wilson, A. (ed.): 2002, *Solar Variability: From Core to Outer Frontiers*, Proc. 10th European Solar Physics Meeting, ESA SP-506.

EIGHT YEARS OF SOHO: SOME HIGHLIGHTS

B. FLECK

ESA Research and Scientific Support Department
c/o NASA/GSFC, Mailcode 682.3, Greenbelt, MD 20771, USA

Abstract. Since its launch on 2 December 1995, the joint ESA/NASA SOHO mission
has provided a wealth of information about the Sun, from its interior, through the hot
and dynamic atmosphere, to the solar wind and its interaction with the interstellar
medium. Analysis of the helioseismology data from SOHO has provided the first images
of structures and flows below the Sun's surface and has shed new light on a number of
structural and dynamic phenomena in the solar interior, such as the absence of differential
rotation in the radiative zone, subsurface zonal and meridional flows, and sub-convection-
zone mixing. Evidence for an upward transfer of magnetic energy from the Sun's surface
toward the corona has been established. The ultraviolet imagers and spectrometers have
revealed an extremely dynamic solar atmosphere where plasma flows play an important
role. Electrons in coronal holes were found to be relatively "cool", whereas heavy ions
are extremely hot and have highly anisotropic velocity distributions. The source regions
for the high speed solar wind have been identified and the acceleration profiles of both
the slow and fast solar wind have been measured. SOHO has also revolutionized our
space weather forecasting capabilities by providing a continuous stream of images of the
dynamic atmosphere, extended corona, and activity on the far side of the Sun. At the
same time, SOHO's easily accessible images and movies have captured the imagination
of the science community and the general public alike. This article summarizes some of
the key findings from eight years of SOHO.

1. Introduction

The Solar and Heliospheric Observatory (SOHO) is a project of interna-
tional cooperation between ESA and NASA to study the Sun, from its
deep core to the outer corona, and the solar wind (Domingo *et al.*, 1995).
It carries a complement of twelve sophisticated instruments, developed
and furnished by twelve international PI consortia involving 39 institutes
from fifteen countries (Belgium, Denmark, Finland, France, Germany, Ire-
land, Italy, Japan, Netherlands, Norway, Russia, Spain, Switzerland, United
Kingdom, and the United States). Detailed descriptions of all the twelve in-
struments on board SOHO as well as a description of the SOHO ground sys-
tem, science operations and data products together with a mission overview
can be found in Fleck *et al.* (1995).

1.1. MISSION STATUS

SOHO was launched by an Atlas II-AS from Cape Canaveral Air Station on 2 December 1995, and was inserted into its halo orbit around the L1 Lagrangian point on 14 February 1996. The launch was so accurate and the orbital manoeuvres were so efficient that enough fuel remains on board to maintain the halo orbit for several decades, many times the lifetime originally foreseen (up to six years). An extension of the SOHO mission for a period of five years beyond its nominal lifetime, i.e. until March 2003, was approved by ESA's Science Programme Committee in 1997, and a further extension until March 2007 was approved in February 2002.

An unexpected loss of contact occurred on 25 June 1998. Fortunately, the mission could be completely recovered in one of the most dramatic rescue efforts in space, and normal operations could be resumed in mid-November after the successful recommissioning of the spacecraft and all twelve instruments. When the last on-board gyro failed on 21 December 1998, SOHO went into Emergency Sun Reacquisition (ESR) mode. In a race against time – the ESR thruster firings consumed an average of about 7 kg of hydrazine per week – engineers at ESTEC and Matra Marconi Space developed software to exit ESR mode without a gyro and allow gyroless operation of the spacecraft. The first gyroless reaction wheel management and station keeping manoeuvre was performed on 1 February 1999, making SOHO the first three-axis-stabilised spacecraft to be operated without a gyro. A new Coarse Roll Pointing (CRP) mode, which uses the reaction wheel speed measurements to monitor and compensate for roll rate changes, was successfully commissioned in September 1999. The CRP mode is almost two orders of magnitude more stable than using gyros. It also acts as an additional safety net between the normal mode and ESR mode, making SOHO perhaps more robust than ever.

In early May 2003, the East-West pointing mechanism of SOHO's High Gain Antenna (HGA) started missing steps; by late June it appeared stuck. Using both primary and redundant motor windings simultaneously, the mechanism was parked in a position that maximises the time it can be used throughout a 6-month halo orbit, with the spacecraft rotated by 180 degrees for half of each orbit and with "keyhole periods" twice per orbit. During the keyholes the Low Gain Antenna can be used with larger DSN stations to receive science telemetry, but data losses of varying magnitude occur depending on the competition for these resources.

1.2. OPERATIONS

The SOHO Experimenters' Operations Facility (EOF), located at NASA's Goddard Space Flight Center (GSFC), serves as the focal point for mission

science planning and instrument operations. At the EOF, the experiment teams receive real-time and playback telemetry, process these data to determine instrument commands, and send commands directly from their workstations through the ground system to their instruments, both in near real-time and on a delayed execution basis.

From the very beginning of the mission, much of the observing time of the SOHO experiments has been devoted to coordinated campaigns. As of mid-February 2004, the SOHO campaign database lists a total of 955 coordinated campaigns. Of these, 315 involved ground-based observatories, 110 involved Yohkoh, and 365 involved TRACE.

With over 1500 articles in the refereed literature and even more articles in conference proceedings and other publications, it is impossible to cover adequately all the exciting work that has been done in the past eight years. Instead, we can only touch upon some selected results.

2. Irradiance variations

The total solar irradiance (TSI) is measured by the VIRGO experiment with two types of radiometers, PMO6V and DIARAD, allowing a first independent and internally consistent determination of possible long-term changes. By comparing the VIRGO measurements with ACRIM-II on UARS, Fröhlich (2002) estimates the uncertainty of the long-term precision over the first 7 years of the SOHO mission to less than ± 15 ppm, or about 2 ppm/yr.

Fröhlich and Lean (2002) compiled the composite TSI from 1978 through 2002 with an overall precision of order $0.05 \, \text{W m}^{-2}$ and a secular trend uncertainty of ± 3 ppm/year (Figure 1). They did not find any significant trend of TSI over the past 24 years. Willson and Mordvinov (2003), who neglect the corrections of the NIMBUS-7 HF instrument data set during the period of the gap between ACRIM-I and II, disagree. They instead claim a secular increase of TSI of about the amount of the HF correction. Interpretation of the TSI record, whether as a steady cycle with no underlying secular change or as showing an increasing trend, has broad social and political impacts as governments make decisions on their responses (if any) to global warming.

In recent years there has been significant effort in modeling the TSI variations by several groups (see e.g. Krivova *et al.*, 2003, and references therein). Their models reconstruct irradiance variations from model atmospheres for the quiet Sun, sunspot umbrae and penumbrae, and faculae, with a contrast depending on the magnetic field strength. The areas of faculae and network are determined empirically from MDI magnetograms, and the areas of sunspot umbrae and penumbrae from MDI intensity images. While some would argue that such a "superficialist" interpretation of
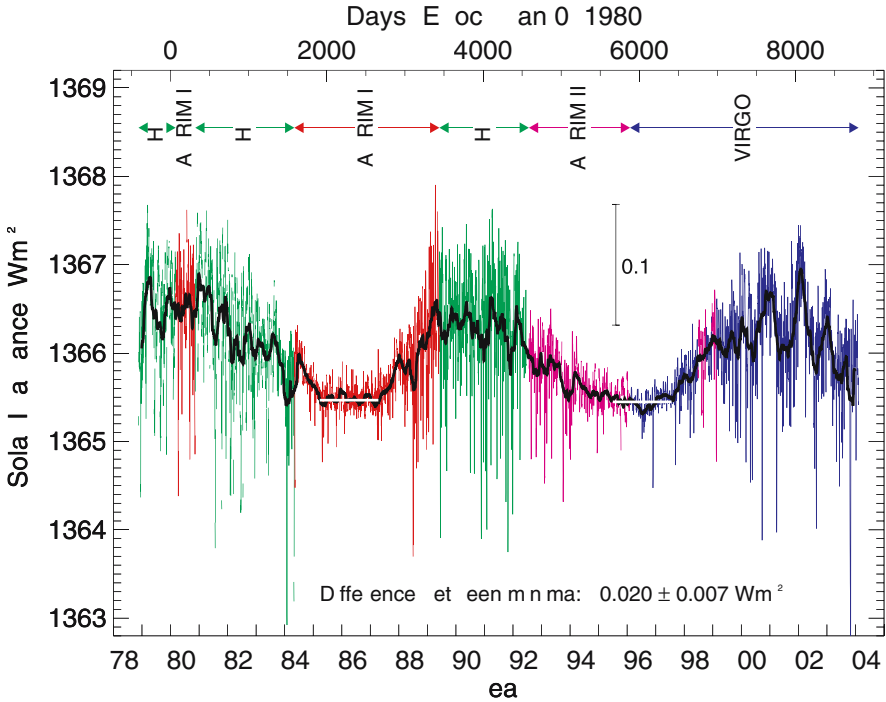
Figure 1.   The composite TSI from 1978 through early 2004. Courtesy C. Fröh-lich/VIRGO.

the origin of irradiance variations ignores potentially important subsurface physics, the agreement of model and observations in Figure 2 is remarkable.

3. Solar interior dynamics and flows

3.1. SOLAR MODELS AND NEUTRINO FLUX

For many decades the solar neutrino puzzle has been one of the most fundamental unsolved problems in astrophysics (e.g. Bahcall and Ostriker, 1997). Helioseismology, by putting ever more stringent constraints on the neutrino flux emitted by nuclear reactions in the core (e.g. Turck-Chièze *et al.*, 2001), has played a key role in solving this puzzle. Turck-Chièze *et al.* (2001) have used sound speed and density profiles inferred from GOLF and MDI data to construct a spherically symmetric seismically adjusted model. Critically important in that work was the prior identification of low-order low degree modes ($n < 9$, $l = 0, 1, 2$), which are relatively insensitive to the uncertain structure and dynamics of the turbulent surface layers of the Sun. They determined the emitted neutrino flux of their seismic model and
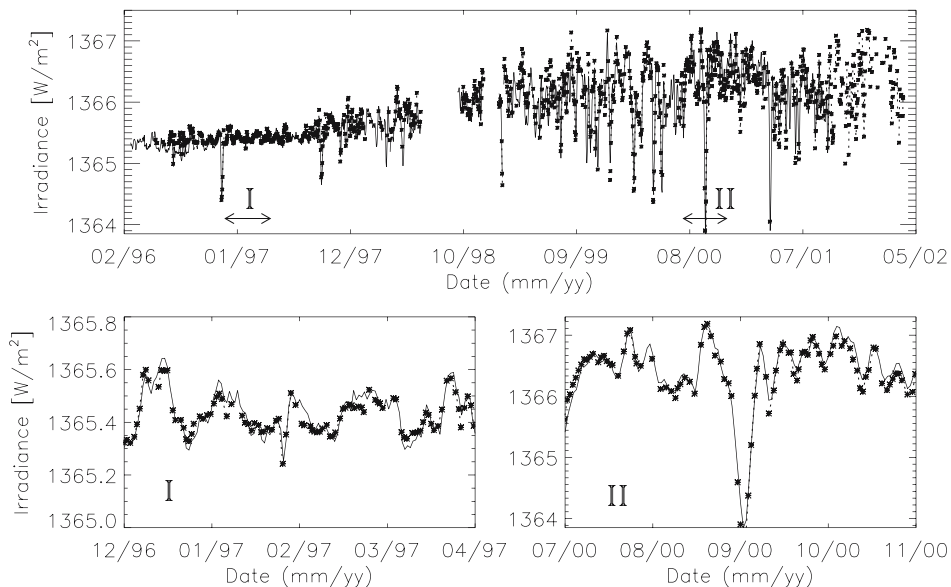
Figure 2. Top panel: Reconstruction (asterisks connected by dotted curve when there are no data gaps) of total solar irradiance for about 1500 individual days between 1996 and 2002, i.e. from the minimum of cycle 23 to its maximum. The irradiance record measured by VIRGO is represented by the solid line. The bottom panels show a zoom-in to two shorter intervals at different activity levels labeled I and II in the top panel. The agreement between measurements and reconstructions is remarkable. From Krivova *et al.* (2003).

demonstrated that it is unlikely that the deficit of the neutrino flux measured on Earth can be explained by a spherically symmetric classical model without neutrino flavor transitions. The neutrino problem was eventually put to rest by the Sudbury Neutrino Observatory (SNO) measurements, which provided strong evidence for solar ν_e flavor transformation (Ahmad *et al.*, 2002).

3.2. STILL NO G-MODES

Gabriel *et al.* (2002) performed a critical statistical analysis of over five years of GOLF data and found no statistically significant evidence for g-mode oscillations in the observed range of 150–400 μHz. They could set a new upper limit for the velocity amplitudes at the solar surface of 6 mm/s. The previous upper limit based on work by the Phoebus group (Appourchaux *et al.*, 2000) was 10 mm/s. Gabriel *et al.* found three possible peaks at 209.974 μHz, 218.374 μHz, and 284.666 μHz, with the last one tentatively identified as one member of the $m = \pm 1$ multiplet of the $n = 1$, $l = 1$

p-mode. The statistical significance of the other two peaks, previously tentatively identified as possible g-mode candidates from GOLF data, is shown to be insufficient, within the present assumptions regarding the nature of the signal.

3.3. CORE ROTATION

Couvidat *et al.* (2003) derived the radial rotation profile of the deep interior of the Sun from the analysis of low-order GOLF and MDI sectoral modes ($l \leq 3$, $6 \leq n \leq 15$, $|m| = l$) and LOWL data ($l > 3$). After removing the effects of the latitudinal variation of the rotation in the convection zone, they obtain a flat rotation profile down to $0.2\,\mathrm{R}_\odot$. This puts strong constraints on the redistribution of angular momentum. Without the correction of the splittings to account for the differential rotation in the convection zone, the inferred rotation rate near the core shows a decrease.

3.4. CONVECTION ZONE ROTATION

The nearly uninterrupted MDI data yield oscillation power spectra with an unprecedented signal-to-noise ratio that allow the determination of the frequency splittings of the global resonant acoustic modes of the Sun with exceptional accuracy. The inversions of these data have confirmed that the decrease of the angular velocity Ω with latitude seen at the surface extends with little radial variation through much of the convection zone, at the base of which is an adjustment layer, called the "tachocline", leading to nearly uniform rotation deeper in the radiative interior (Schou *et al.*, 1998). Further a prominent rotational shearing layer in which Ω increases just below the surface is discernible at low to mid latitudes. Schou *et al.* (1998) have also been able to study the solar rotation closer to the poles than has been achieved in previous investigations. The data have revealed that the angular velocity is distinctly lower at high latitudes than the values previously extrapolated from measurements at lower latitudes based on surface Doppler observations and helioseismology.

3.5. TACHOCLINE OSCILLATIONS

Using data from MDI and the GONG network, Howe *et al.* (2000b) detected changes in the rotation of the Sun near the base of the convection zone, with unexpected periods of ≈ 1.3 year near the equator, possibly faster (≈ 1 year) at high latitudes. Inversion of the global-mode frequency splittings revealed temporal changes in the angular velocity Ω of up to 6 nHz above and below the tachocline, with the peak amplitude at $0.72\,\mathrm{R}_\odot$ and an anticorrelated variation at $0.63\,\mathrm{R}_\odot$. The changes are most pronounced near the equator

and at high latitudes and are a substantial fraction of the average 30 nHz difference in Ω with radius across the tachocline at the equator. The 1.3-year periodicity is in stark contrast to the 11-year period of the sunspot cycle. More recent work by Howe (2003) indicates that the amplitude of the 1.3-year variations of the rotation rate near the tachocline has been greatly reduced in recent years. It is interesting to note that this reduction coincided with higher solar acitity, and it will be interesting to see whether this periodicity will show up again during the decreasing part of the solar cycle.

3.6. ZONAL FLOWS

From f-mode frequency splittings of MDI data, Kosovichev and Schou (1997) detected zonal variations of the Sun's differential rotation, superposed on the relatively smooth latitudinal variation in Ω. These alternating zonal bands of slightly faster and slower rotation show velocity variations of about $\pm 5\,\text{m/s}$ at a depth of 2–9 Mm beneath the surface and extend some 10 to 15° in latitude. They appear to coincide with the evolving pattern of "torsional oscillations" reported from earlier surface Doppler studies. Later studies (e.g. Howe *et al.*, 2000a) showed that these relatively weak flows are not merely a near-surface phenomenon, but extend downward at least 60 Mm (some 8% of the solar radius), and thus are evident over a significant fraction of the nearly 200 Mm depth of the solar convection zone. Indeed, Vorontsov *et al.* (2002), by applying a novel inversion method to the MDI rotational splitting data of 1996–2002, found evidence that these zonal shear flows (or "torsional oscillations") can penetrate to the bottom of the convection zone. It appears that the entire solar convective envelope is involved in the torsional oscillations, with phase propagating poleward and equatorward from midlatitudes at all depths. This challenges the previous models of torsional oscillations as a secondary effect of migrating sunspot zones.

3.7. MERIDIONAL FLOWS

Meridional flows from the equator to the poles have been observed before on the solar surface in direct Doppler shift measurements (e.g. Duvall, 1979). The time-distance measurements by Giles *et al.* (1997) provided the first evidence that such flows persist to great depths, and therefore may play an important role in the 11-year solar cycle. They found the meridional flow to persist to a depth of at least 26 Mm, with a depth averaged velocity of $23.5\pm0.6\,\text{m/s}$ at mid-latitude. Since then several methods of local helioseismology have been used to measure the meridional flows in the upper convection zone and their changes with the solar cycle (e.g. Beck *et al.*, 2002; Haber *et al.*, 2002). These flows play a key role in flux-transport dynamo

Meridional Circulation Cells
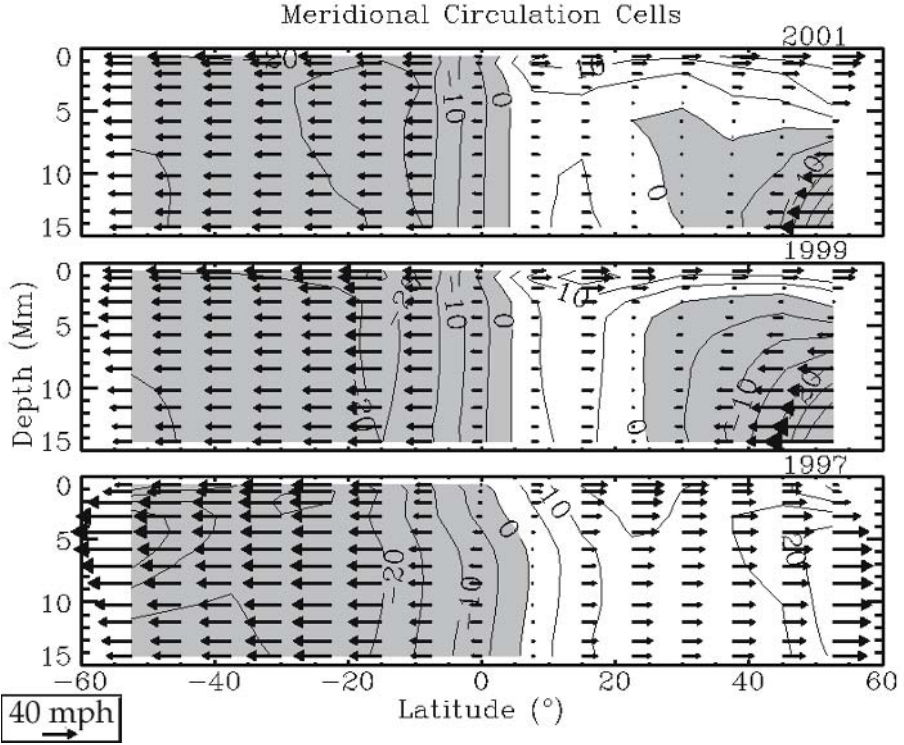
Figure 3. Meridional flow averaged in time and longitude, shown as a function of latitude and depth during the rising phase of cycle 23 (years 1997, 1999, and 2001). Underlying the vector fields are contours of constant meridional flow, with contours labeled in m/s. Regions of southerly flow are indicated by negative contours and are shaded gray. Starting in 1998, an additional circulation cell appears in the northern hemisphere (positive latitudes). This cell manifests as a submerged region of equatorward flow lying below poleward flow at the surface and appearing as the gray zone within the northern hemisphere. The breaking of symmetry between the southern hemisphere, which has a fairly uniform flow, and the northern hemisphere, which has varying multiple cells, is quite striking. Courtesy of D. Haber.

models of the cycle, by transporting the magnetic flux to the polar regions and causing the polarity reversals. The common result is that the meridional circulation slows down when the activity level is higher because of the additional flows converging around active regions in the activity belts. In addition, Haber *et al.* (2002) have studied how meridional circulation varies with depth over time, and found surprising evidence of the appearance and evolution of a submerged meridional cell during the years 1998–2001, which arose in the northern hemisphere and disrupted the orderly poleward flow and symmetry about the equator that is typically observed (Figure 3).
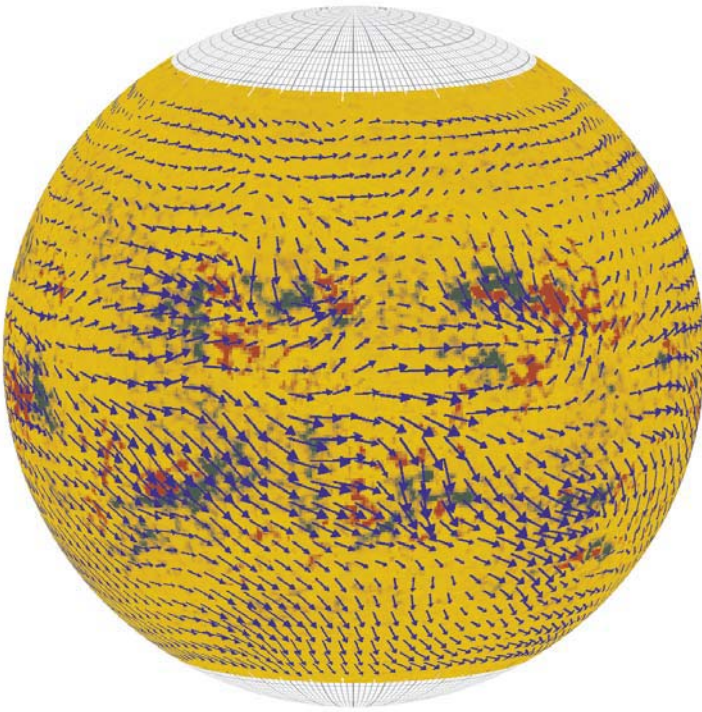
Figure 4.   Large-scale flows in the upper convection zone obtained by ring-diagram analysis of 28 days of MDI Dynamics data from April 2002, superposed on an MDI magnetogram. Courtesy of D. Haber.

3.8. SOLAR SUBSURFACE WEATHER

The "ring diagram" analysis of MDI Dynamics data by Haber *et al.* (2002) has also revealed persistent patterns of large-scale flows in the upper convection zone (Figure 4). These results led to a new concept of "Solar Subsurface Weather" connecting the effects of the synoptic flows to the development of solar activity. The initial results are promising, and may result in a new approach to long-term space weather forecasting, based on the dynamics of the upper convection zone.

3.9. FARSIDE IMAGING

Just a little over 4 years after the launch of SOHO, Lindsey and Brown (2000) published an astonishing result: the first successful, holographic reconstruction of solar farside features from p-mode oscillations observed on the visible hemisphere with MDI. In the meantime, the astonishing has

become routine, and the SOHO MDI offers daily farside images on the Web[1].

Another method to monitor solar activity on the far side of the Sun was developed by the SWAN team (Bertaux *et al.*, 2000). SWAN monitors the whole sky in Ly-α light from the Sun, as it is reflected off neutral hydrogen seeping into the heliosphere from the outside. Since active regions are brighter than quiet regions, parts of the sky facing an active region are brighter than those facing a quiet region. Just as a rotating lighthouse beam will illuminate different patches of fog, the Sun's rotation produces a changing pattern of illumination on the sky behind the Sun's far side.

3.10. SUBSURFACE STRUCTURE OF SUNSPOTS

The high-resolution data from MDI have allowed new investigations about the structure and flows beneath sunspots (Kosovichev *et al.*, 2000; Zhao *et al.*, 2001). Kosovichev *et al.* (2000) found sunspot "fingers" – long, narrow structures at a depth of about 4 Mm, which connect the sunspot with surrounding pores of the same polarity. Pores which have the opposite polarity are not connected to the spot. The work by Zhao *et al.* (2001) provided new clues to a longstanding problem in solar physics: Why do sunspots stay organised for several weeks, instead of disintegrating much more rapidly? The answer appears to be sub-surface inflows. Zhao *et al.* detected strong converging and downward directed flows at depths of 1.5–5 Mm, which they tentatively identified with the downdrafts and vortex flows that were suggested by Parker (1979) for a cluster model of sunspots. In deeper layers, 6–9 Mm, the sunspot region is occupied by a ring of upflows with almost zero velocity at the center. Strong outflows extending more than 30 Mm are found below the downward and converging flows. The analysis by Zhao *et al.* also suggests that sunspots might be a relatively shallow phenomenon, with a depth of 5–6 Mm, as defined by its thermal and hydrodynamic properties. They also found a strong mass flow across the sunspot at depths of 9–12 Mm, which they interpret as more evidence in support of the cluster model, as opposed to the monolithic sunspot model.

3.11. EMERGING ACTIVE REGIONS

There have been several attempts to detect emerging active regions in the convection zone before they appeared on the surface (e.g. Kosovichev *et al.*, 2000). It was found that the emerging flux propagates very rapidly in the upper 20 Mm, with a speed exceeding 1 km/s. Early detection of emerging

---

[1] `http://soi.stanford.edu/data/farside/`

active regions, therefore, may prove difficult without probing deeper into the convection zone.

3.12. SUPERGRANULATION

By applying the new technique of time-distance helioseismology to high resolution MDI data, Duvall *et al.* (1997) were able to generate the first maps of horizontal and vertical flow velocities as well as sound speed variations in the convection zone just below the visible surface. They found that in the upper layers, 2–3 Mm deep, the horizontal flow is organized in supergranular cells, with outflows from the cell centers. The characteristic size of these cells is 20–30 Mm and the cell boundaries were found to coincide with the areas of enhanced magnetic field. The supergranulation outflow pattern disappears at a depth of approximately 5 Mm. This suggests that supergranules, which have a characteristic horizontal cell size of 20–30 Mm, are a relatively shallow phenomenon.

The importance of supergranular flows for the distribution of solar magnetic flux and the formation of magnetic network is well known. By using long series (up to 9 days) of subsurface flow maps obtained from MDI Dynamics data by time-distance helioseismology, Gizon *et al.* (2003) have studied the global dynamics of the supergranular flow pattern. They concluded that it has a significant, wave-like component that may explain why this pattern rotates faster than magnetic features in the photosphere, and also why advection may be suppressed by meridional flows.

3.13. SEISMIC WAVES

MDI has also made the first observations of seismic waves from a solar flare (Kosovichev and Zharkova, 1998), opening up possibilities of studying both flares and the solar interior. During the impulsive phase of the X2.6 class flare of 9 July 1996 a high-energy electron beam heated the chromosphere, resulting in explosive evaporation of chromospheric plasma at supersonic velocities. The upward motion was balanced by a downward recoil in the lower chromosphere which excited propagating waves in the solar interior. On the surface the outgoing circular flare waves resembled ripples from a pebble thrown into a pond. The seismic wave propagated to at least 120,000 km from the flare epicenter with an average speed of about 50 km/s on the solar surface.

3.14. SOLAR OBLATENESS

High precision MDI measurements of the Sun's shape and brightness obtained during two special 360° roll manoeuvres of the SOHO spacecraft

have produced the most precise determination of solar oblateness ever (Kuhn *et al.*, 1998). There is no excess oblateness. These measurements unambiguously rule out the possibility of a rapidly rotating core, and any significant solar cycle variation in the oblateness.

4. Transition region and corona

4.1. UV AND EUV SPECTRAL ATLASES

A far-ultraviolet and extreme-ultraviolet spectral atlas of the Sun between 670 Å and 1609 Å, derived from observations obtained with the SUMER spectrograph (Figure 5), identifies over 1100 distinct emission lines, of which more than 150 had not been recorded or identified before (Curdt *et al.*, 2001). The atlas contains spectra of the average quiet Sun, a coronal hole and an active region on the disk, providing a rich source of new diagnostic tools to study the physical parameters in the chromosphere, the transition region and the corona. In particular, the wavelength range below 1100 Å as observed by SUMER represents a significant improvement over the spectra produced in the past.

Brooks *et al.* (1999) present the extreme-ultraviolet spectrum as observed in normal incidence by CDS. It covers the wavelength ranges 308–381 Å and 513–633 Å. In all over 200 spectral lines have been measured and about 50% identified.

These two atlases will be a very valuable product for many years to come, for both solar and stellar communities.

4.2. EXPLOSIVE EVENTS AND BLINKERS

Explosive events have been studied extensively by a number of authors (e.g. Innes *et al.*, 1997; Chae *et al.*, 1998), who provided strong evidence that these features are the result of magnetic reconnection. Innes *et al.* (1997) report explosive events that show spatially separated blue shifted and red shifted jets and some that show transverse motion of blue and red shifts, as predicted if reconnection was the source. Chae *et al.* (1998) provide further evidence of the magnetic reconnection origin of explosive events by comparing their SUMER observations with MDI magnetograms and magnetograms obtained at Big Bear Solar Observatory. The explosive events are found to rarely occur in the interior of strong magnetic flux concentrations. They are preferentially found in regions with weak and mixed polarity, and the majority of these events occur during "cancellation" of photospheric magnetic flux (Chae *et al.*, 1998).

Harrison *et al.* (1999) present a thorough and comprehensive study of EUV flashes, also known as "blinkers" (Harrison, 1997), which were
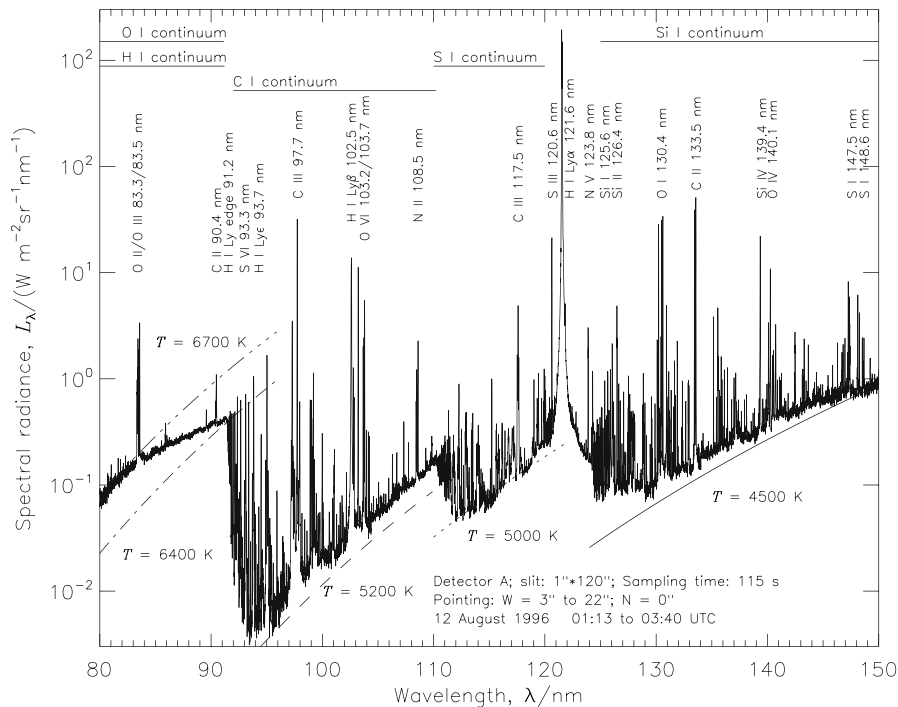
Figure 5.   SUMER radiance spectrum of a quiet-Sun region in first order of diffraction (second-order lines have been removed manually). Prominent lines and continua are identified. Some black-body radiation levels are shown to provide an estimate of the radiation temperatures of the continua. From Wilhelm *et al.* (2002).

identified in quiet Sun network as intensity enhancements of order 10–40% using CDS. They have analyzed 97 blinker events and identified blinker spectral, temporal and spatial characteristics, their distribution, frequency and general properties, across a broad range of temperatures, from 20,000 K to 1,200,000 K. The blinkers are most pronounced in the transition region lines O III, O IV and O V, with modest or no detectable signature at higher and lower temperatures. A typical blinker has a duration of about 1000 s. Due to a long tail of longer duration events, the average duration is 2400 s, though. Comparison to plasma cooling times led to the conclusion that there must be continuous energy input throughout the blinker event. The projected blinker onset rate for the entire solar surface is $1.24\,\mathrm{s}^{-1}$, i.e. at any one time there are about 3000 blinker events in progress. Remarkably, line ratios from O III, O IV and O V show no significant change throughout the blinker event, suggesting that the intensity increase is not a temperature effect but predominantly caused by increases in density or filling factor. The authors estimate the thermal energy content of an average blinker at 2×10^{25} erg.

4.3. ACTIVE REGION DYNAMICS

EIT, SUMER, and CDS observations have clearly demonstrated that the solar transition region and corona is extremely dynamic and time variable in nature. This has become even more evident with the advent of the spectacular high resolution time lapse sequences obtained by the Transition Region and Coronal Explorer (TRACE) (Schrijver *et al.*, 1999). A comprehensive investigation of active region flows by Kjeldseth-Moe and Brekke (1998) demonstrated that high Doppler shifts are common in active region loops. Strong shifts are present in parts of loops for temperatures up to 0.5 MK. Regions with both red and blue shifts are seen. While typical values correspond to velocities of ± 50–100 km/s, shifts approaching 200 km/s have been detected. At temperatures T $\geq$ 1 MK, i.e. in Mg IX 368 Å or Fe XVI 360 Å, only small shifts are seen. Thus, the high Doppler shifts seem to be restricted to the chromosphere and transition region.

Fludra *et al.* (1997) show that loops with different temperatures can co-exist within an active region, sometimes very close to each other, but not really co-spatial, i.e. they occupy different volumes.

4.4. CORONAL HOLE TEMPERATURES

Using the two SOHO spectrometers CDS and SUMER, David *et al.* (1998) have measured the electron temperature as a function of height above the limb in a polar coronal hole. Temperatures of around 0.8 MK were found close to the limb, rising to a maximum of less than 1 MK at 1.15 R$_\odot$, then falling to around 0.4 MK at 1.3 R$_\odot$. In equatorial streamers, on the other hand, the temperature was found to rise constantly with increasing distance, from about 1 MK close to the limb to over 3 MK at 1.3 R$_\odot$. With these low temperatures, the classical Parker mechanisms cannot alone explain the high wind velocities, which must therefore be due to the direct transfer of momentum from MHD waves to the ambient plasma.

Wilhelm *et al.* (1998) determined the electron temperatures, densities and ion velocities in plumes and interplume regions of polar coronal holes from SUMER spectroscopic observations of the Mg IX $706/750$ Å and Si VIII $1440/1445$ Å line pairs. They find the electron temperature T_e to be less than $800{,}000$ K in a plume in the range from r $= 1.03$ to 1.60 R$_\odot$, decreasing with height to about $330{,}000$ K. In the interplume lanes, the electron temperature is also low, but stays between $750{,}000$ and $880{,}000$ K in the same height interval. Doppler widths of O VI lines are narrower in the plumes ($v_{1/e} \approx 43$ km/s) than in the interplumes ($v_{1/e} \approx 55$ km/s). Thermal and turbulent ion speeds of Si VIII reach values up to 80 km/s, corresponding to a kinetic ion temperature of 10^7 K.
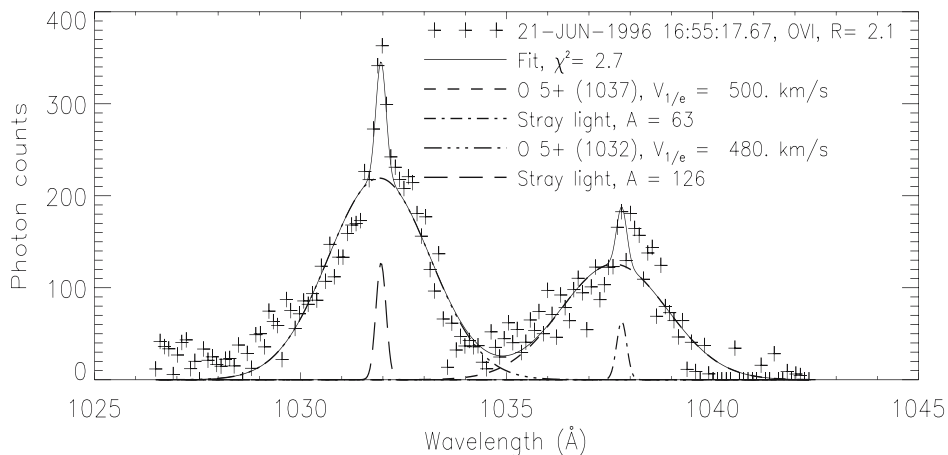
Figure 6. UVCS observations of O VI 1032 Å and 1037 Å above the north polar coronal hole at $2.1\,R_\odot$. The narrow peaks are due to straylight. The data points are shown as crosses, the fitted profile by a solid line. From Kohl *et al.* (1997).

One of the most surprising results from SOHO has been the extremely broad coronal profiles of highly ionized elements such as oxygen and magnesium (Kohl *et al.*, 1997, 1999; Figure 6). Kohl *et al.* (1998) and Cranmer *et al.* (1999a) present a self-consistent empirical model of a polar coronal hole near solar minimum, based on H I and O VI UVCS spectroscopic observations. Their model describes the radial and latitudinal distribution of the density of electrons, H I and O VI as well as the outflow velocity and unresolved anisotropic most probable velocities for H I and O VI. It provides strong evidence of anisotropic velocity distributions for protons and O VI in polar coronal holes (Figure 7) and indicates proton outflow speeds of $190 \pm 50\,\mathrm{km/s}$ and larger outflow speeds of $350 \pm 100\,\mathrm{km/s}$ for O VI at 2.5 $R_\odot$. While the protons (which are closely coupled to H I atoms by charge transfer in the inner corona) are only mildly anisotropic above 2–$3\,R_\odot$ and never exceed $3\,\mathrm{MK}$, the O VI ions are strongly anisotropic at these heights, with perpendicular kinetic temperatures approaching $200\,\mathrm{MK}$ at $3\,R_\odot$ and $(T_\perp/T_\parallel) \approx 10$–$100$ (Kohl *et al.*, 1997, 1998). The measured O VI and Mg X "temperatures" are neither mass proportional nor mass-to-charge proportional when compared to H I (Esser *et al.*, 1999; Zangrilli *et al.*, 1999). This and the highly anisotropic velocity distributions rule out thermal (common temperature) Doppler motions and bulk transverse wave motions along the line of sight as dominant line-broadening mechanisms. Clearly, additional energy deposition is required which preferentially broadens the perpendicular velocity of the heavier ions (cf. Section 4.8).

In summary, SOHO measurements have clearly established that the
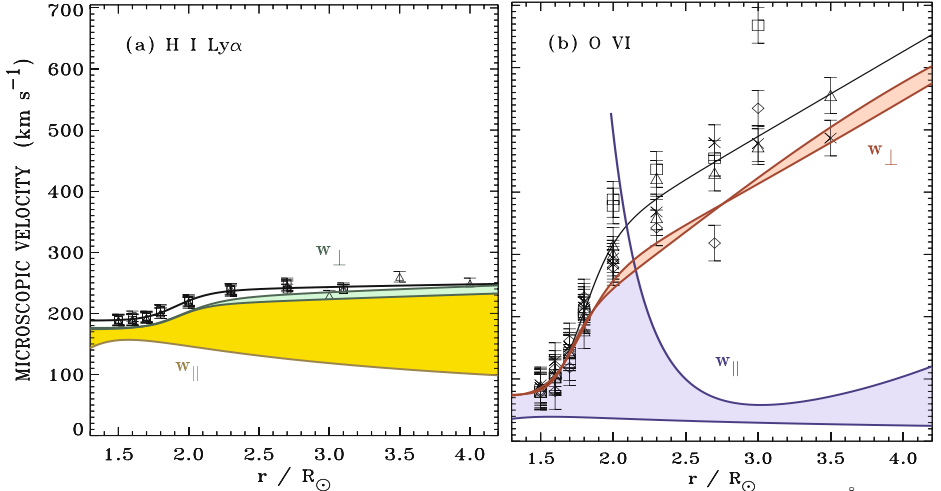
Figure 7. $v_{1/e}$ and most probable speeds for H I Lyα (left) and O VI 1032 Å (right). Squares: north polar holes, triangles: south polar holes. Solid line: best fit to data. Dotted line: most probable speed w_e corresponding to the electron temperature. From Kohl *et al.* (1998).

ions in coronal holes are extremely "hot" and the electrons much "cooler". They also clearly demonstrate that local thermal equilibrium does not exist in polar coronal holes and that the assumption of Collisional Ionization Equilibrium (CIE) and the common notion that $T_e \approx T_{ion}$ can no longer be made in models of coronal holes.

It seems difficult to reconcile these low electron temperatures measured in coronal holes with the freezing-in temperatures deduced from ionic charge composition data (e.g. Geiss *et al.*, 1995). The freezing-in concept, however, assumes that the adjacent charge states are in ionization equilibrium. A critical re-evaluation of this concept appears to be justified.

4.5. CORONAL HEATING

A promising theoretical explanation for the high temperatures of heavy ions and their strong velocity anisotropies is the efficient dissipation of high-frequency waves that are resonant with ion-cyclotron Larmor motions about the coronal magnetic field lines. This effect has been studied in detail by Cranmer *et al.* (1999b), who constructed theoretical models of the nonequilibrium plasma state of the polar solar corona using empirical ion velocity distributions derived from UVCS and SUMER. They found that the dissipation of relatively small amplitude high-frequency Alfvén waves (10–10,000 Hz) via gyroresonance with ion cyclotron Larmor motions can explain many of the kinetic properties of the plasma, in particular the strong

anisotropies, the greater than mass proportional temperatures, and the faster outflow of heavy ions in the high speed solar wind. Because different ions have different resonant frequencies, they receive different amounts of heating and acceleration as a function of radius, exactly what is required to understand the different features of the H I and O VI velocity distributions. Further, because the ion cyclotron wave dissipation is rapid, the extended heating seems to demand a constantly replenished population of waves over several solar radii. This suggests that the waves are generated gradually throughout the wind rather than propagate up from the base of the corona.

In addition to measuring velocity and intensity oscillation, MDI also measures the line-of-sight component of the photospheric magnetic field. In long, uninterrupted MDI magnetogram series a continuous flux emergence of small bipolar regions has been observed (Schrijver *et al.*, 1997, 1998). Small magnetic bipolar flux elements are continually emerging at seemingly random locations. These elements are rapidly swept by granular and mesogranular flows to supergranular cell boundaries where they cancel and replace existing flux. The rate of flux generation of this "magnetic carpet" is such that all of the flux is replaced in about 40 hours (Schrijver *et al.*, 1998), with profound implications for coronal heating on the top side and questions of local field generation on the lower side of the photosphere. Estimates of the energy supplied to the corona by "braiding" of large-scale coronal field through small-scale flux replacement indicate that it is much larger than that associated with granular braiding (Schrijver *et al.*, 1998).

4.6. POLAR PLUMES

Previously, plumes were considered to be the source regions of the high speed solar wind. Given the narrower line widths in plumes and the absence of any significant motions in plumes, Wilhelm *et al.* (1998) suggested that the source regions of the fast solar wind are the interplume lanes rather than the plumes, since conditions there are far more suitable for a strong acceleration than those prevailing in plumes. Teriaca *et al.* (2003), by applying the Doppler dimming technique to SUMER and UVCS O VI and H I data, present further evidence that is indeed the interplume areas that are the source regions of the fast wind stream. Contrary to that and other published results (e.g. Giordano *et al.*, 2000), Gabriel *et al.* (2003), by applying the Doppler dimming technique to SUMER observations of plumes in the height range of $1.05 – 1.35\,R_\odot$, find that outflow velocities in plumes *exceed* those in the interplume regions. Clearly, the question about the physical nature of plumes and interplumes and their respective role for the acceleration of the fast wind streams is still far from settled.

DeForest and Gurman (1998) observed quasi-periodic compressive waves in solar polar plumes in EIT Fe IX/X 171 Å time sequences. The pertur-
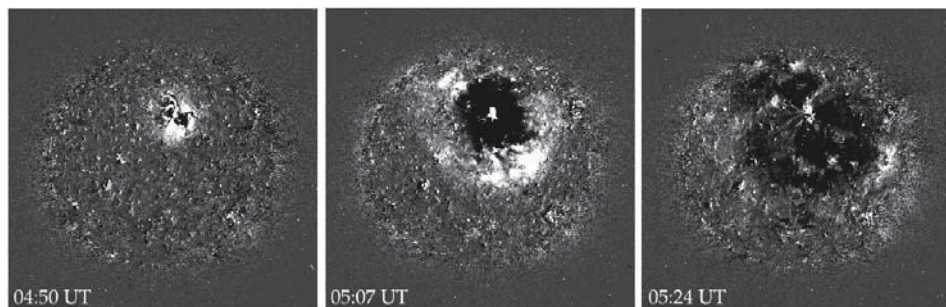
Figure 8.   SOHO/EIT 195 Å running difference images of the EIT-wave event of 12 May 1997. The brightest regions exceed 200 percent increase in emission measure. From Thompson *et al.* (1998).

bations amount to 10–20% of the plumes' overall intensity and propagate outward at 75–150 km/s, taking the form of wave trains with periods of 10–15 minutes and envelopes of several cycles. The authors conclude that the perturbations are compressive waves (such as sound waves or slow-mode acoustic waves) propagating along the plumes. Assuming that the waves are sonic yields a mechanical flux of $1.5–4 \times 10^5$ ergs cm^{-2} s^{-1} in the plumes. The energy flux required to heat a coronal hole is about 10^6 ergs cm^{-2} s^{-1}.

4.7. EIT WAVES

EIT has discovered large-scale transient waves in the corona, sometimes also called "Coronal Moreton Waves", propagating outward from active regions below CMEs (Thompson *et al.*, 1998, 1999). These events are usually recorded in the Fe XII 195 Å bandpass, during high-cadence (≤ 20 min) observations. Their appearance is stunning in that they usually affect most of the visible solar disk (Figure 8). They generally propagate at speeds of 200–500 km/s, traversing a solar diameter in less than an hour. Active regions distort the waves locally, bending them toward the lower Alfvén speed regions. On the basis of speed and propagation characteristics, Thompson *et al.* (1998, 1999) associate the "EIT waves" with fast-mode MHD waves. Another interesting aspect of these waves is their association with the acceleration and injection of high energy electrons and protons (Torsti *et al.*, 1999).

4.8. HOT LOOP OSCILLATIONS

Kliem *et al.* (2002) have discovered strong Doppler shift oscillations in SUMER observations of hot loops above active regions (Figure 9). Wang *et al.* (2003) give an extensive overview of hot coronal loop oscillations and identify them with slow magnetoacoustic standing waves in the loops. The
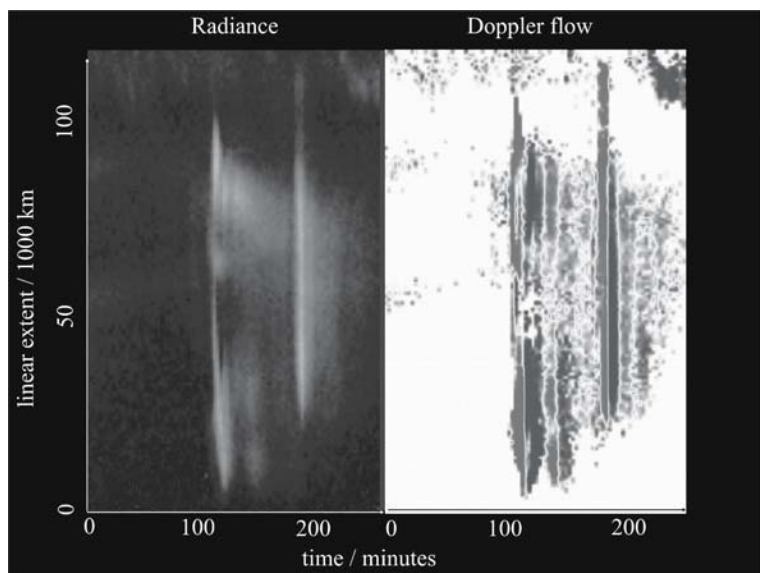
Figure 9. Hot loop oscillations as observed by SUMER in Fe XIX 1118 Å. Left: intensity; right: velocity. Time goes from left to right in each half. Courtesy W. Curdt/SUMER.

periods are typically around 10 to 20 minutes, with a comparable decay time scale. The oscillations are seen only in hot flare lines (>6 MK, e.g. Fe XVII, Fe XIX, Fe XXI). Lines formed at "normal" coronal temperatures (1 MK, e.g. Fe XII, Ca XIII, Ca X) do not show any signature of these oscillations. These new and previously unexpected results may help to understand the heating of coronal loops, and open a new area of coronal seismology.

5. Solar wind

5.1. ORIGIN AND ACCELERATION OF THE FAST SOLAR WIND

Coronal hole outflow velocity maps obtained with the SUMER instrument in the Ne VIII emission line at 770 Å show a clear relationship between coronal hole outflow velocity and the chromospheric network structure, with the largest outflow velocities occuring along network boundaries and at the intersection of network boundaries (Hassler *et al.*, 1999). This can be considered the first direct spectroscopic determination of the source regions of the fast solar wind in coronal holes.

Proton and O^{5+} outflow velocities in coronal holes have been measured by UVCS using the Doppler dimming method (Kohl *et al.*, 1997, 1998; Cranmer *et al.*, 1999a). The O^{5+} outflow velocity was found to be significantly higher than the proton velocity, with a very steep increase between
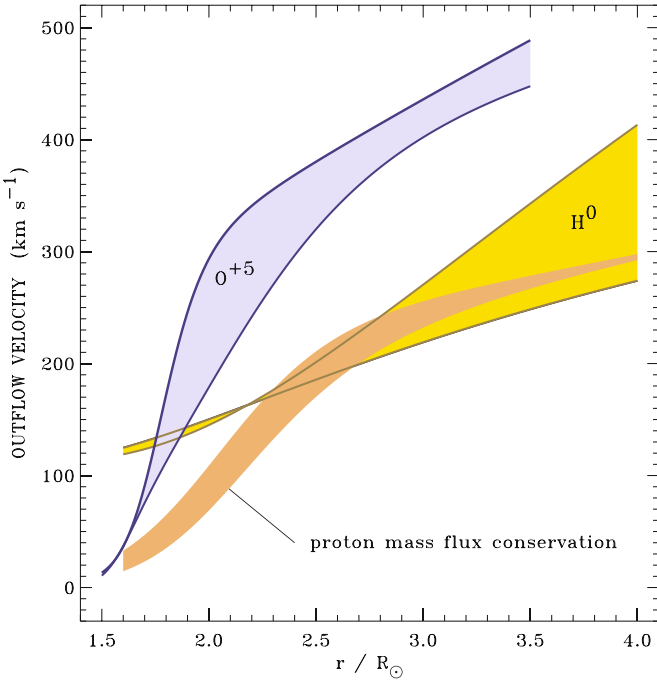
Figure 10.   Empirical outflow velocity of O VI and H I in polar coronal holes, with gray regions corresponding to lower/upper limits of $w_{||}$. From Kohl *et al.* (1998).

1.5 and $2.5 \, R_\odot$, reaching outflow velocities of 300 km/s already around $2 \, R_\odot$ (Figure 10). While the hydrogen outflow velocities are still consistent with some conventional theoretical models for polar wind acceleration, the higher oxygen flow speeds cannot be explained by these models. A possible explanation is offered by the dissipation of high-frequency Alfvén waves via gyroresonance with ion-cyclotron Larmor motions, which can heat and accelerate ions differently depending on their charge and mass (Cranmer *et al.*, 1999b, and references therein).

5.2. ACCELERATION, ORIGIN AND COMPOSITION OF THE SLOW SOLAR WIND

Time-lapse sequences of LASCO white-light coronagraph images give the impression of a continuous outflow of material in the streamer belt. Density enhancements, or "blobs" form near the cusps of helmet streamers and appear to be carried outward by the ambient solar wind. Sheeley *et al.* (1997), using data from the LASCO C2 and C3 coronagraphs, have traced a large number of such "blobs" from 2 to over 25 solar radii. Assuming that these "blobs" are carried away by the solar wind like leaves on the river,

they have measured the acceleration profile of the slow solar wind, which typically doubles from $150\,\mathrm{km/s}$ near $5\,\mathrm{R}_\odot$ to $300\,\mathrm{km/s}$ near $25\,\mathrm{R}_\odot$. They found a constant acceleration of about $4\,\mathrm{m\,s^{-2}}$ through most of the $30\,\mathrm{R}_\odot$ field-of-view. The speed profile is consistent with an isothermal solar wind expansion at a temperature of about $1.1\,\mathrm{MK}$ and a sonic point near $5\,\mathrm{R}_\odot$.

Raymond *et al.* (1997) analyzed UVCS data to measure the composition of coronal streamers. They found strong variations from streamer to streamer, and even within streamers. The FIP effect is present in streamers, and the helium abundance lower than in the photosphere. In the core of quiescent equatorial streamers, oxygen and other high-FIP elements are depleted by an order of magnitude compared to photospheric abundances, while they are depleted by only a factor of 3 along the edges of the streamers. They suggest that gravitational settling may be responsible for the low abundances of heavy elements in the static core region of closed magnetic field. The abundance along the edges of the streamer ("legs") resemble elemental abundances measured in the slow solar wind, suggesting the identification of streamers as the source regions of that wind component.

Uzzo *et al.* (2003) combined UVCS and CELIAS measurements to determine abundances of oxygen, silicon, and magnesium in streamers and the slow solar wind on an almost daily basis over more than 2 months during solar minimum conditions (summer of 1996). The agreement between remote sensing and *in-situ* measurements provides further evidence that active-region streamers and the outer "leg" structural component of quiescent streamers are contributors to the slow solar wind.

Kallenbach *et al.* (1997), using CELIAS/MTOF data, has made the first *in-situ* determination of the solar wind calcium isotopic composition, which is important for studies of stellar modelling and solar system formation, because the present-day solar Ca isotopic abundances are unchanged from their original isotopic composition in the solar nebula. The isotopic ratios $^{40}\mathrm{Ca}/^{42}\mathrm{Ca}$ and $^{40}\mathrm{Ca}/^{44}\mathrm{Ca}$ measured in the solar wind are consistent with terrestrial values.

The first in-situ determination of the isotopic composition of nitrogen in the solar wind has been made by Kallenbach *et al.* (1998), also based on CELIAS/MTOF data. They found an isotope ratio $^{14}\mathrm{N}/^{15}\mathrm{N} = 200 \pm 60$, indicating a depletion of $^{15}\mathrm{N}$ in the terrestrial atmosphere compared to solar matter.

Ipavich *et al.* (2001) report relative abundances of the iron isotopes $^{54}\mathrm{Fe}$, $^{56}\mathrm{Fe}$, and $^{57}\mathrm{Fe}$. Their results agree with terrestrial values. Bochsler *et al.* (2000) have measured the abundance of aluminum in the solar wind. The Al/Mg abundance ratio is important because it provides an excellent test case for investigating possible fractionation processes among low FIP elements in the solar wind. In interstream solar wind regimes they measured

a ratio of 0.081 ± 0.012, and in a coronal hole associated high speed wind stream 0.076 ± 0.011. A comparison with the solar system ratio of 0.079 ± 0.005 gives no indication of fractionation occurring among low FIP elements in the solar wind.

6. CMEs and space weather

The LASCO team has compiled an extensive list[2] and catalog[3] (Yashiro et al., 2004) of the more than 6000 coronal mass ejections observed with SOHO since launch. The on-line catalog of Yashiro et al. (2004) documents the observed properties of all CMEs observed by LASCO, such as central position angle, angular width in the plane of sky, heliocentric distance with time, average speed, and acceleration.

St. Cyr et al. (2000) report the properties of all the 841 CMEs observed by the LASCO C2 and C3 white-light coronagraphs from January 1996 through the SOHO mission interruption in June 1998 and compare those properties to previous observations by other instruments. The CME rate for solar minimum conditions was slightly higher than had been reported for previous solar cycles, but both the rate and the distribution of apparent locations of CMEs varied during this period as expected. The general shape of the distribution of apparent sizes for LASCO CMEs is similar to those of earlier reports, but the average (median) apparent size of $72°$ ($50°$) is significantly larger.

St. Cyr et al. (2000) also report on a population of CMEs with large apparent sizes, which appear to have a significant longitudinal component directed along the Sun-Earth line, either toward or away from the Earth (so-called "halo" CMEs). Using full disk EIT images they found that 40 out of 92 of these events might have been directed toward the Earth. A comparison of the timing of those events with the Kp geomagnetic storm index in the days following the CME yielded that 15 out of 21 (71%) of the $Kp > 6$ storms could be accounted for as SOHO LASCO/EIT frontside halo CMEs. Eliminating three Kp storms that occurred following LASCO/EIT data gaps brings the possible association rate to 18 out of 21 (86%).

Fox et al. (1998) describe the first ever end to end tracking of a space storm (6–10 January 1997 event), from its eruption on the Sun to its impact at Earth.

Gopalswamy et al. (2003) studied the solar cycle variations of various properties of CMEs, such as daily CME rate, mean and median speeds, and the latitude of solar sources for cycle 23 (1996–2002). They find that

---

[2] http://lasco-www.nrl.navy.mil/cmelist.html
[3] http://cdaw.gsfc.nasa.gov/CME_list/

(1) there is an order of magnitude increase in CME rate from the solar minimum (0.5/day) to maximum (6/day), (2) the maximum rate is significantly higher than previous estimates, (3) the mean and median speeds of CMEs also increase from minimum to maximum by a factor of 2, (3) the latitude distribution of CMEs separate the prominence-associated (high-latitude) and active-region associated CMEs, and (4) the rate of high-latitude CMEs shows north-south asymmetry and the cessation eruptions in the north and south roughly mark the polarity reversals. They also compared the rates of the fast-and-wide CMEs, major solar flares, interplanetary shocks, long-wavelength type II bursts and large SEP events and conclude that all these phenomena (except the major flares, which are too frequent) have a close physical relationship.

Simnett *et al.* (2002) compared the release time of near-relativistic electron beams (≈ 40–$300\,\mathrm{keV}$) measured by ACE with the timing of coronal activity measured by LASCO. They found that the near-relativistic electron injection time was typically delayed by approximately 20 minutes from the CME launch time and greater than 10 minutes after the onset of the electromagnetic radio and X-ray signatures of the flare (when present). Therefore, the near-relativistic electrons that must be present to produce the chromospheric electromagnetic emission do not escape promptly (at least in detectable quantities). The radial distance of most CMEs at the electron release time was between 1.5 and 3.5 $R_\odot$. Both the peak electron flux and the spectral hardness of the electrons were positively correlated with the CME speed, a signature of shock acceleration. They therefore suggest that most of the near-relativistic electrons seen by ACE/EPAM are accelerated by the shock driven by the coronal transient and are released at a radial distance around 2–3 $R_\odot$.

Torsti *et al.* (2002) present the first ever measurement of the ^{3}He energy spectrum of an event with an exceptionally high ^{3}He enhancement (^{3}He/^{4}He > 1). The particle event was associated with an impulsive flare and an interplanetary shock wave. The analysis shows that the high-energy ^{3}He-rich event refers to the flare material reaccelerated by the interplanetary CME. Onset of the high-energy ^{3}He-rich event was observed in the far upstream region, when the CME-driven shock was at about 0.3 AU from the Sun.

7. Heliosphere

The Sun is moving through the Local Interstellar Cloud (LIC) at a velocity of about $26\,\mathrm{km/s}$. The solar wind builds a cavity, the heliosphere, within the ionized gas component of the LIC. The neutral gas component at of the LIC however passes through the heliopause and into the heliosphere,

where it can be observed by SWAN. Costa *et al.* (1999) analysed SWAN
H-cell data and compared them with a simple hot model of the interstellar
H flow in the inner heliosphere. They found hydrogen temperatures T_0 of
$11,500 \pm 1500$ K, i.e. significantly above the temperature of the interstellar
He flow (6000 ± 1000 K), requiring a strong heating of more than 3500 K
at the heliosphere interface. Part of this excess temperature probably is
due to radiative transfer effects. They also measured a deceleration of the
interstellar hydrogen at the heliopause of 3.5 ± 1.0 km/s.

Quémerais *et al.* (1999), in an independent study using data from the
SWAN hydrogen absorption cell, determined the apparent interstellar hy-
drogen velocity in the up- and downwind direction to -25.4 ± 1 km/s and
$+21.6\pm1.3$ km/s, respectively. They also presented the most precise, model
independent determination of the H flow direction. Their new estimate of
the upwind direction is $252.3° \pm 0.73°$ and $8.7° \pm 0.90°$ in ecliptic coordi-
nates, which is off by about $3°$–$4°$ from the He flow direction. The authors
speculate that this might be a sign of an asymmetry of the heliospheric
interface due to the ambient interstellar magnetic field.

Comparing the above hydrogen temperature and velocity measurements
by SWAN with heliospheric models leads to an estimate of the interstellar
plasma density of $n_e \approx 0.04$ cm^{-3} (Lallement, 1999). It is interesting to
note that the plasma frequency for $n_e = 0.04$ cm^{-3} is 1.8 kHz, i.e. exactly
the value of the remarkably stable cut-off frequency observed by Voyager.

8. Comets

SOHO is providing new measurements not only about the Sun. As of the end
of 2003 LASCO has detected over 700 comets, most of them so-called sun-
grazers. One comet was discovered by SWAN in Ly-α emission (Mäkinen
et al., 2000).

Biesecker *et al.* (2002) used LASCO observations of comets to obtain
quantitative light curves of sungrazing comets. The light curves reveal an
anomalous brightening as the comets approach the Sun, followed by a
rapid dimming when the comets pass beyond ≈ 11 R$_\odot$, suggesting break-up
around this distance.

Thanks to rapid communication from the LASCO group and the near-
realtime observing capabilities of the SOHO instruments due to the unique
operations concept, UVCS could make spectroscopy measurements of sev-
eral comets on the day of their discovery. UVCS spectroscopic measure-
ments of comet C/1996Y1 obtained at 6.8 R$_\odot$ confirmed the predictions
of models of the cometary bow shock driven by mass-loading as cometary
molecules are ionized and swept up in the solar wind. From the width and
shift of the line profiles, the solar wind speed at 6.8 R$_\odot$ could be determined

(640 km/s). The outgassing rate of the comet was estimated at 20 kg/s, implying an active area of the nucleus of only about 6.7 m in diameter and a mass of about 120,000 kg (Raymond *et al.*, 1998).

Uzzo *et al.* (2001) report UVCS Ly-α observations of comet C/2000 C6, a member of the Kreutz family of sungrazing comets, which was in the UVCS field-of-view on 9 and 10 February 2000. A tail nearly 0.5 R$_\odot$ in length was detected in Ly-α emission. From the Ly-α intensity and its rate of fading due to H I ionization they estimated the streamer density at 4.56 R$_\odot$ to 0.68×10^5 cm^{-3}. They also determined the outgassing rate at various heights, which in turn gives an estimate of the diameter of the nucleus (12 m). Further, between 5.7 and 4.6 R$_\odot$ a sudden brightening was observed, which is interpreted as fragmentation of the nucleus.

Mäkinen *et al.* (2001) used the SWAN instrument to monitor the break-up of comet C/1999 S4 (LINEAR). The total amount of water vapour observed by SWAN from 25 May through 12 August 2000 was estimated at 3.3×10^9 kg. Only about 1% of this was left on 6 August, when observations by the Hubble Space Telescope of the dying comet's fragments gave an estimate of the total volume of the fragments. Combining the two numbers gives a remarkably low value for the density – about $15 \, \text{kg/m}^3$, compared with $917 \, \text{kg/m}^3$ for familiar non-porous ice. Even allowing for an equal amount of dust grains, $30 \, \text{kg/m}^3$ is far less than the $500 \, \text{kg/m}^3$ often assumed by cometary scientists.

Combi *et al.* (2000) observed the structure and evolution of the hydrogen Ly-α coma of comet Hale-Bopp (1995 O1) during its perihelion passage in the spring of 1997. The coma was more than 100 million kilometers wide, far exceeding the great comet's visible tail. Although generated by a comet nucleus perhaps only 40 km in diameter, the hydrogen cloud was 70 times wider than the Sun itself and ten times wider than the hydrogen cloud of Comet Hyakutake observed by SWAN in 1996. The water evaporation rate of Hale-Bopp was measured at more than 200 million tons per day. For comparison, comet Wirtanen, the original target of ESA's Rosetta mission, pumped out water vapour at a rate of 20,000 tons per day during its most recent visit to the Sun, according to SWAN data. The SWAN observations of Hale-Bopp have also shown something else extraordinary – the biggest feature ever observed in our solar system, namely the shadow of comet Hale-Bopp's coma projected on the sky behind it.

The analysis of high-resolution spectroscopic observations of comet C/2002 X5 (Kudo-Fujikawa) from UVCS has revealed a quasi-spherical cloud of neutral hydrogen and a variable tail of ionized carbon (C$^+$ and C^{2+}) that disconnected from the comet and subsequently regenerated (Povich *et al.*, 2003). C^{2+} has never been observed in a comet before. The high abundance of C^{2+} and C$^+$ relative to water (24%) found is unexplainable

by photodissociation of carbon monoxide but instead attributed to the evaporation and subsequent photoionization of atomic carbon from organic refractory compounds present in the cometary dust grains.

Because Venus has no appreciable magnetic field, the solar wind interacts directly with the planetary atmosphere and ionosphere much as with a cometary coma. In fact, several people have pointed out similarities of the tails of Venus and comets. In June 1996, Venus passed through a very close inferior conjunction with the Sun. Close to that time the CELIAS/CTOF sensor registered three intervals of unusal fluxes of O^+ and C^+ (Grünwaldt *et al.*, 1997). The C^+ abundance was $\approx$10% of O^+. The energy distributions resembled those of tail rays originating in the Venus ionosphere or ionopause region, i.e. Venus tail rays have been identified in the solar wind some 45 million km downstream of Venus.

Acknowledgements

References

Ahmad, Q.R., Allen, R.C., and Andersen, T.C. *et al.*: 2002, *Phys. Rev. Lett.* **89**, 011301.
Appourchaux, T., Froehlich, C., and Andersen, B. *et al.*: 2000, *Astrophys. J.* **538**, 401.
Bahcall, J.N. and Ostriker, J.P.: 1997, *Unsolved Problems in Astrophysics*, Princeton Univ. Press.
Beck, J.G., Gizon, L., and Duvall, T.L., Jr.: 2002, *Astrophys. J.* **575**, L47.
Bertaux, J.-L., Quémerais, E., and Lallement, R. *et al.*: 2000, *Geophys. Res. Lett.* **27**, 1331.
Biesecker, D.A., Lamy, P., St.Cyr, O.C. *et al.*: 2002, *Icarus* **157**, 323.
Bochsler, P., Ipavich, F.M., Paquette, J.A., Weygand, J.M., and Wurz, P.: 2000, *J. Geophys. Res.* **105**, no. A6, 12659.
Brooks, D.H., Fischbacher, G.A., Fludra, A. *et al.*: 1999, *Astron. Astrophys.* **347**, 277.
Chae, J., Wang, H. , Lee, C.-Y., Goode, P.R., and Schühle, U.: 1998, *Astrophys. J.* **497**, L109.
Combi, M.R., Reinard, A.A., Bertaux, J.-L. *et al.*: 2000, *Icarus* **144**, 191.
Costa, J., Lallement, R., Quémerais, E., Bertaux, J.-L., Kyrölä, E., and Schmidt, W.: 1999, *Astron. Astrophys.* **349**, 660.
Couvidat, S., García, R.A., and Turck-Chièze, S. *et al.*: 2003, *Astrophys. J.* **597**, L77.
Cranmer, S.R., Kohl, J.L., Noci, G. *et al.*: 1999a, *Astrophys. J.* **511**, 481.
Cranmer, S.R., Field, G.B., and Kohl, J.L.: 1999b, *Astrophys. J.* **518**, 937.
Curdt, W., Brekke, P., Feldman, U. *et al.*: 2001, *Astron. Astrophys.* **375**, 591
David, C., Gabriel, A.H., Bely-Dubau, F., Fludra, A., Lemaire, P., and Wilhelm, K.: 1998, *Astron. Astrophys.* **336**, L90.

DeForest, C.E. and Gurman, J.B.: 1998, *Astrophys. J.* **501**, L217.

Domingo,V., Fleck, B., and Poland, A.I.: 1995, *Solar Phys.* **162**, 1.

Duvall, T.L., Jr.: 1979, *Solar. Phys.* **63**, 3.

Duvall, T.L., Jr., Kosovichev, A.G., Scherrer, P.H. *et al.*: 1997, *Solar Phys.* **170**, 63

Esser, R., Fineschi, S., Dobrzycka, D. *et al.*: 1999, *Astrophys. J.* **510**, L63.

Fleck, B., Domingo, V., and Poland, A.I. (eds.): 1995, The SOHO Mission, *Solar Phys.* **162**, Nos. 1–2.

Fludra, A., Brekke, P., Harrison, R.A. *et al.*: 1997, *Solar Phys.* **175**, 487.

Fox, N.J., Peredo, M., and Thompson, B.J.: 1998, *Geophys. Res. Lett.*, **Vol. 25, no. 14**, 2461.

Fröhlich, C.: 2003, *Metrologia* **40**, 60

Fröhlich, C. and Lean, J.: 2002, *Astron. Nachr.* **323**, 203.

Gabriel, A.H., Baudin, F., Boumier, P. *et al.*: 2002, *Astron. Astrophys.* **390**, 1119.

Gabriel, A.H., Bely-Dubau, F., and Lemaire, P.: 2003, *Astrophys. J.* **589**, 623

Geiss, J., Gloeckler, G., von Steiger, R. *et al.*: 1995, *Science* **268**, 1033.

Giles, P.M., Duvall, T.L., Jr., and Scherrer, P.H.: 1997, *Nature* **390**, 52.

Giordano,S., Antonucci, E., Noci, G., Romoli, M., and Kohl, J.L.: 2000, *Astrophys. J.* **531**, L79.

Gizon, L., Duvall, T.L., Jr., and Schou, J.: 2003, *Nature* **421**, 43.

Gopalswamy, N. Lara, A., Yashiiro, S., Nunes, S., and Howard, R.A.: 2003, ESA SP-535, 403.

Grünwaldt, H., Neugebauer, M., Hilchenbach, M. *et al.*: 1997, *Geophys. Res. Lett.* **24**, no. 10, 1163.

Haber, D.A., Hindman, B.W., Toomre, J. *et al.*: 2002, *Astrophys. J.* **570**, 855.

Hassler, D.M., Dammasch, I., Lemaire, P. *et al.*: 1999, *Science* **283**, 810.

Harrison, R.A.: 1997, *Solar Phys.* **175**, 467.

Harrison, R.A., Lang, J., Brooks, D.H., and Innes, D.E.: 1999, *Astron. Astrophys.* **351**, 1115.

Howe, R.: 2003, ESA SP-517, p. 81.

Howe, R., Christensen-Dalsgaard, J., and Hill, F. *et al.*: 2000a, *Astrophys. J.* **533**, L163.

Howe, R., Christensen-Dalsgaard, J., Hill, F. *et al.*: 2000b, *Science* **287**, 2456.

Innes, D.E., Inhester, B., Axford, W.I., and Wilhelm, K.: 1997, *Nature* **386**, 811.

Ipavich, F.M., Paquette, J.A., Bochsler, P., Lasley, S.E., Wurz, P.: 2001, in R.F. Wimmer-Schweingruber (ed.), *Solar and Galactic Composition*, CP598, p. 121.

Kallenbach, R., Ipavich, F.M., Bochsler, P., *et al.*: 1997, *Astrophys. J.* **498**, L75.

Kallenbach, R., Geiss, J., Ipavich, F.M. *et al.*: 1998, *Astrophys. J.* **507**, L185.

Kjeldseth-Moe, O. and Brekke, P.: 1998, *Solar Phys.* **182**, 73.

Kliem, B., Dammasch, I.E., Curdt, W., and Wilhelm, K.: 2002, *Astrophys. J.* **568**, L61.

Kohl, J.-L., Noci, G., and Antonucci, E. *et al.*: 1997, *Solar Phys.* **175**, 613.

Kohl, J.-L., Noci, G., Antonucci, E. *et al.*: 1998, *Astrophys. J.* **501**, L127.

Kohl, J.-L., Esser, R., and Cranmer, S.R. *et al.*: 1999, *Astrophys. J.* **510**, L59.

Kosovichev, A.G., Duvall, T.L., and Scherrer, P.H.: 2000, *Solar Phys.*, **192**, 159

Kosovichev, A.G. and Schou, J.: 1997, *Astrophys. J.* **482**, L207.

Kosovichev, A.G. and Zharkova, V.V.: 1998, *Nature* **393**, 317.

Krivova, N.A., Solanki, S.K., Fligge, M., and Unruh, Y.C.: 2003, *Astron. Astrophys.* **399**, L1.

Kuhn, J.R., Bush, R.I., Scheick, X., and Scherrer, P.H.: 1998, *Nature* **392**, 155.

Lallement, R.: 1999, in S. Habbal (ed.), *Proc. Solar Wind 9*, AIP Conf. Proc. 471, 205.

Lindsey, C. and Braun, D.C.: 2000, *Science* **287**, 1799.

Mäkinen, T., Bertaux, J.-L., and Laakso, H. *et al.*: 2000, *Nature* **405**, 321.

Mäkinen, T., Bertaux, J.-L., Combi, M.R., and Quemerais, E.: 2001, *Science* **292**, 1326.

Parker, E.N.: 1979, *Astrophys. J.* **230**, 905.

Povich, M.S., Raymond, J.C., Jones, G.H. *et al.*: 2003, *Science* **302**, no. 5652, 1949.

Quémerais, E., Bertaux, J.-L., Lallement, R., and Berthé, M.: 1999, *J. Geophys. Res.* **104**, 12 585.

Raymond, J.C., Kohl, J.K., Noci, G. *et al.*: 1997, *Solar Phys.* **175**, 645.

Raymond, J.C., Fineschi, S., Smith, P.L. *et al.*: 1998, *Astrophys. J.* **508**, 410.

Sheeley, N.R. Jr., Wang, Y.-M., Hawley, S.H. *et al.*: 1997, *Astrophys. J.* **484**, 472.

Schou, J., Antia, H.M., Basu, S. *et al.*: 1998, *Astrophys. J.* **505**, 390.

Schrijver, C.J., Title, A.M., van Ballegooijen, A. *et al.*: 1997, *Astrophys. J.* **487**, 424.

Schrijver, C.J., Title, A.M., Harvey, K.L. *et al.*: 1998, *Nature* **394**, 152.

Schrijver, C.J., Title, A.M., Berger, T.E. *et al.*: 1999, *Solar Phys.* **187**, 261.

Simnett, G.M., Roelof, E.C., and Haggerty, D.K.: 2002, *Astrophys. J.* **579**, 854.

St. Cyr, O.C., Plunkett, S.P., Michels, D.J. *et al.*: 2000, *Geophys. Res. Lett.* **105**, no. A8, 18,169.

Teriaca, L., Poletto, G., Romoli, M., and Biesecker, D.A.: 2003, *Astrophys. J.* **588**, 566.

Thompson, B.J., Plunkett, S.P., Gurman, J.B., Newmark, J.S., St.Cyr, O.C., and Michels, D.J.: 1998, *Geophys. Res. Lett.* **25**, 2465. *Geophys. Res. Lett.* **25**, 2465

Thompson, B.J., Gurman, J.B., Neupert, W.M. *et al.*: 1999, *Astrophys. J.* **517**, L151.

Torsti, J., Kocharov, L., Laivola, J., Lehtinen, N., Kaiser, M.L., and Reiner, M.J.: 2002, *Astrophys. J.* **573**, L59.

Torsti, J., Kocharov, L., Teittinen, M., and Thompson, B.J.: 1999, *Astrophys. J.* **510**, 460.

Turck-Chièze, S., Couvidat, S., Kosovichev, A.G. *et al.*: 2001, *Astrophys. J.* **555**, L69.

Uzzo, M., Raymond, J.C., Biesecker, D. *et al.*: 2001, *Astrophys. J.* **558**, 403.

Uzzo, M., Ko, Y.-K., Raymond, J.C., Wurz, P., and Ipavich, F.M.: 2003, *Astrophys. J.* **585**, 1062.

Vorontsov, S.V., Christensen-Dalsgaard, J., Schou, J. *et al.*: 2002, *Science* **296**, 101.

Wilhelm, K., Marsch, E., Dwivedi, B.N. *et al.*: 1998, *Astrophys. J.* **500**, 1023.

Wilhelm, K., Schühle, U., Curdt, W. *et al.*: 2002, in A. Pauluhn *et al.* (eds.), *The Radiometric Calibration of SOHO*, ISSI SR-002, p. 145.

Willson, R.C. and Mordvinov, A.V.: 2003, *Geophys. Res. Lett.* **30**, 1199.

Wang, T.J., Solanki, S.K., Curdt, W., Innes, D.E., Dammasch, I.E., Kliem, B.: 2003, *Astron. Astrophys.* **406**, 1105.

Yashiro, S., Gopalswamy, N., Michalek, G. *et al.*: 2004, *J. Geophys. Res.*, submitted.

Zangrilli, L., Nicolosi, P., Poletto, G. *et al.*: 1999, *Astron. Astrophys.* **342**, 592.

Zhao, J., Kosovichev, A.G., Duvall, T.L., Jr.: 2001, *Astrophys. J.* **557**, 384.

2$\frac{1}{2}$–D COMPRESSIBLE RECONNECTION MODEL

M. SKENDER
Rudjer Bošković Institute
Zagreb, Bijenička 54, HR-10002, Croatia

B. VRŠNAK
Hvar Observatory
Faculty of Geodesy
Zagreb, Kačićeva 26, HR-10000, Croatia

Abstract. The exact solution of the jump conditions on the RD/SMS discontinuity system in a two–and–half–dimensional (2$\frac{1}{2}$–D) symmetrical reconnection model enables one to analyse the outflowing jet characteristics in dependence on the inflow velocity, and to follow changes in transition to the two–dimensional model. Implications arising from the exact solution and its relevance for solar flares are discussed.

1. Introduction

Magnetic reconnection is considered to play a central role in the rapid conversion of the magnetic energy into plasma energy required for initiating solar flares. Petschek (1964) proposed the so–called fast reconnection mechanism: When two regions of plasma containing oppositely directed magnetic fields are placed in contact, magnetic field lines reconnect in a tiny diffusion region, from which two pairs of standing magnetohydrodynamic waves (SMSs) extend and dissipate the magnetic field energy. Petschek and Thorne (1967) discussed the situation when the merging fields are skewed one to the other, and introduced two pairs of large–amplitude Alfvén waves or rotational discontinuities (RDs) in front of SMSs to satisfy the boundary conditions. A comprehensive treatment of this two–and–half–dimensional (2$\frac{1}{2}$–D) problem has been given by Soward (1982) using the approximation of plasma inflowing slowly and perpendicularly to the symmetry axis of the system. The exact solution of the jump conditions for the RD/SMS discontinuity system in a 2$\frac{1}{2}$–D system has recently been obtained by Skender *et al.* (2003). Implications arising from the exact solution are presented in this article.
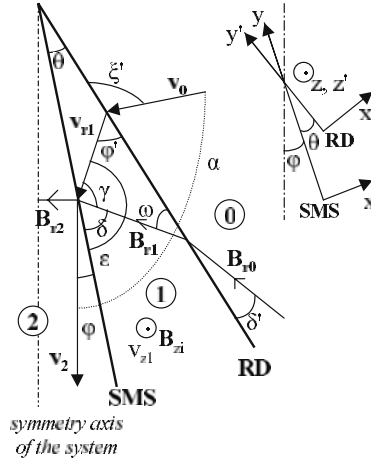
Figure 1.   The geometry of the system of discontinuities in the $2\frac{1}{2}$–D symmetrical reconnection problem, depicted in one quadrant. The quantities in the inflow, intermediate, and outflow regions are designated by subscripts "0", "1", and "2", respectively. The xy-plane components of the magnetic field $\vec{B}$ and the flow velocity $\vec{v}$ are denoted by the subscript "r". The direction of the z-component of $\vec{B}$ and $\vec{v}$ is also indicated. The magnetic field generally has x-, y-, and z-components in all three regions, as does the velocity in region 1, while the velocities in regions 0 and 2 have the xy-plane components only. The magnetic field $\vec{B}_2$ is perpendicular to the velocity $\vec{v}_2$. All quantities in a $2\frac{1}{2}$–D model are independent of the z-axis.

2. Background theory

In region 0 (see Fig. 1), plasma of density ρ_0 and pressure p_0 flows into the RD with velocity $\vec{v}_0$, carrying the magnetic field $\vec{B}_0$. Rotated and accelerated plasma proceeds towards the SMS through region 1. At the SMS plasma is heated, compressed, and further deflected and accelerated.

Jump relations for a RD/SMS discontinuity system are derived from the continuity equation, equation of motion under conditions of electrical neutrality and no influence from gravity and viscosity, energy conservation equation for fully ionized H-plasma, which has the ratio of specific heats $\gamma = 5/3$, magnetic divergence relation, and magnetic flux conservation equation. The general forms of these equations are:

$$\frac{\partial \rho}{\partial t} + \rho \vec{\nabla} \cdot \vec{v} = 0 \,, \tag{1}$$

$$\rho \frac{D\vec{v}}{Dt} = -\vec{\nabla} p + \vec{j} \times \vec{B} \,, \tag{2}$$

$$\vec{\nabla} \cdot \left[\left(\frac{5}{2} p + \frac{1}{2} \rho v^2 \right) \vec{v} \right] + \left(\vec{v} \times \vec{B} \right) \cdot \vec{j} = 0 \,, \tag{3}$$
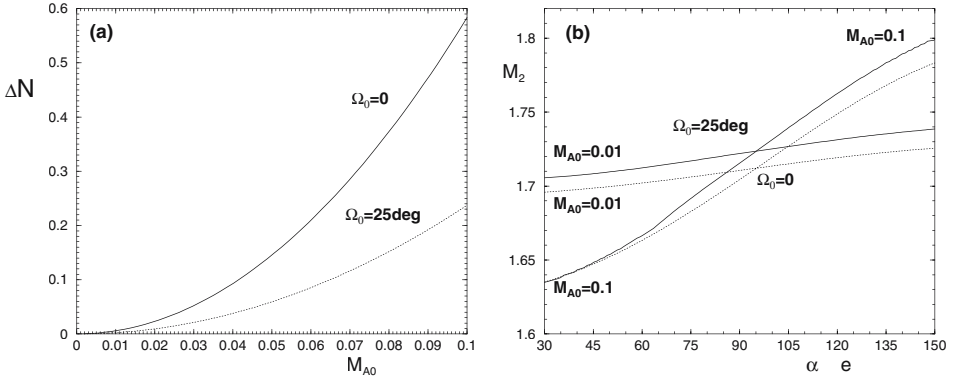
Figure 2. For $\beta_0 = 0.01$, we present the dependence of: (a) the relative difference $\Delta N_\%$ of the compression N and the Soward approximation value N_S; (b) the outflow Mach number M_2 on the incidence angle α for the inflow Mach Alfvén numbers $M_{A0} = 0.01$ and 0.1, combined with $\Omega_0 = 25°$ and $0°$ (2–D case).

$$\vec{\nabla} \cdot \vec{B} = 0 \,, \tag{4}$$

$$\vec{\nabla} \times \vec{E} = 0 \,. \tag{5}$$

The exact solution of the system is used for analyzing the outflow conditions in dependence of the inflow speed and the inflow incidence angle, at a given shear of the magnetic field and the plasma–to–magnetic pressure ratio β_0.

3. Results and discussion

The exact solution of the jump relations on the RD/SMS system provides the possibility of investigating situations when the inflow is not perpendicular to the outflow, as well as situations of relatively fast inflow, which are often met in the coronal environment. In Fig. 2a the deviation of the compression $N = n_2/n_0$ from the value N_S obtained in Soward's approximation is shown in dependence on the inflow Mach Alfvén number M_{A0}, utilizing $\Delta N_\% = 100 \, (N - N_S)/N_S$. The values are obtained for $\beta_0 = 0.01$, appropriate for conditions in solar flares. The value of N increases with increasing Mach Alfvén number M_{A0}, which is more pronounced for smaller angles Ω_0 ($\tan \Omega_0 = B_{z0}/B_{r0}$, see Fig. 1). A similarly weak dependence is found for the temperature jump $T = T_2/T_0$, where the value of T decreases with increasing M_{A0}.

Figure 2b shows the dependence of the outflow magnetosonic Mach number M_2 on the incidence angle α (see Fig. 1). We present the results for $M_{A0} = 0.01$ and 0.1, again taking $\beta_0 = 0.01$, at $\Omega_0 = 0°$ and $25°$. The graph reveals a considerable change of M_2, but only for a comparatively
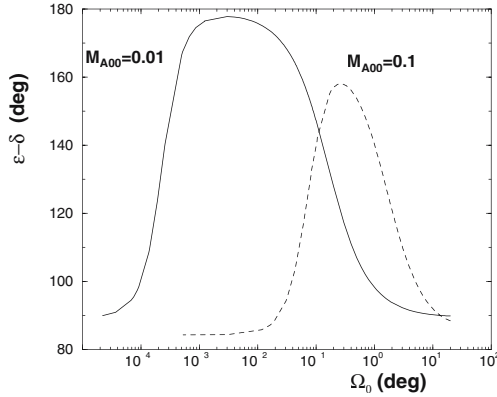
Figure 3.   Illustrative results of dramatic changes in transition from $2\frac{1}{2}$–D to 2–D. The difference of the angles $(\epsilon - \delta)$ in region 1 in dependence on Ω_0 is presented for the perpendicular inflow, at two reconnection rates M_{A00} and $\beta_0 = 0.01$.

large inflow Mach Alfvén number (i.e. also for large reconnection rates). The value of M_2 increases when the inflow has a component in the direction of the outflow, while it decreases for the inflow having a component in the direction opposite to the outflow. It determines whether the outflow jet is sub– or super–magnetosonic. In the case of super–magnetosonic outflow, a quasi–perpendicular fast–mode standing shock forms if the jet encounters an obstacle.

The explicit solutions of the full set of jump relations enable us to follow the changes of the geometry of the system in transition from $2\frac{1}{2}$–D to 2–D, which happens, e.g., in two-ribbon flares when the initially sheared arcade of the magnetic field becomes stretched by an eruption. We have presented that the flow/field geometry changes rapidly within $\Omega_0 \lesssim 1°$. Figure 3 shows how the difference between the angles $(\epsilon - \delta)$ in the intermediate region (see Fig. 1) depends on Ω_0. Obviously, at small Ω_0, a perturbation of the transversal magnetic field component in the inflow region might have consequences on the overall stability of the system. Considering the supersonic outflow, this could straightforwardly explain the stochastic and intermittent electron acceleration such as observed in solar flares.

References

Petschek, H.E.: 1964, in W.N. Hess (ed.), *AAS-NASA Symp. on Physics of Solar Flares*, NASA, Greenbelt, Maryland, 425.

Petschek, H.E. and Thorne, R.M.: 1967, *Astrophys. J.* **147**, 1157.

Soward, A.M.: 1982, *J. Plasma Phys.* **28**, 415.

Skender, M., Vršnak, B., and Martinis, M.: 2003, *Phys. Rev. E* **68**, 46 405.

WAITING TIME DISTRIBUTION OF CMES

C.-T. YEH, M.D. DING and P.F. CHEN
Department of Astronomy
Nanjing University
Nanjing 210093, China

Abstract. Inspired by the fact that the waiting time of solar flares presents a power-law distribution, this paper is aimed to investigate the waiting time distribution of coronal mass ejections (CMEs). SOHO/LASCO data from 1996 to 2001 are collected. It is shown that the observed CMEs reveal a similar power-law behavior as flares, and the power-law indices for both phenomena are almost identical. This finding strongly supports the viewpoint that solar flares and CMEs are different manifestations of the same physical process. Similar to the avalanche model for solar flares, our results suggest that a self-organized mechanism might be also involved in the CME processes.

1. Introduction

Coronal mass ejections (CMEs) are explosions of magnetized plasma which are observed carrying billion tons of plasma away from the Sun. Observations show that CMEs are often accompanied by solar flares. The distribution of the time interval between two successive eruptive events, i.e., the so-called waiting time, has been extensively studied for solar flares (Wheatland *et al.*, 1998; Boffeta *et al.*, 1999). In this paper, we make a statistical study of waiting time distributions (WTDs) of solar flares and CMEs for the same period, with the purpose to show whether the WTD of CMEs presents a power-law behavior similar to that of flares.

2. Data analysis and results

The data examined here include flares and CMEs observed during the period 1996−2001. Flare data are from the GOES soft X-ray flux provided by the National Geophysical Data Center (NGDC). CME data are collected from SOHO/LASCO observations (Brueckner *et al.*, 1995). In order to minimize the ambiguity of the real onset time, full halo CMEs and events with speeds below 100 km s^{-1} are skipped.
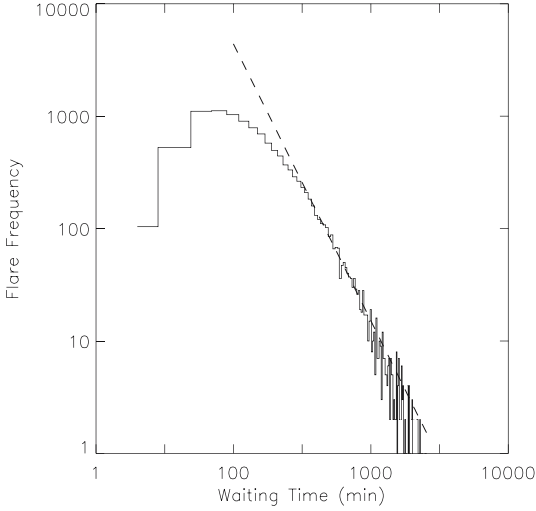
Figure 1. Waiting time distribution of GOES soft X-ray flares during the years 1996−2001 (solid line), which is fitted by a power-law with an index of −2.46 (dashed line) in the range between 6 and 15 hours.

During the period from 1996 to 2001, in total about 11660 flares are identified. The waiting time of all these flares is sampled with an interval of 20 min. The waiting time distribution of flares is shown in Fig. 1. For the power-law index calculation, sample points above 15 hours are skipped because of the large fluctuation that results from the small amount of data, and sample points less than 6 hours are ignored because of the finite resolution of flare detection. The 1490 sample points remaining are fitted by a power-law distribution, with a derived power-law index of -2.46 ± 0.1 (the corresponding χ^2 is below 1.7).

Ignoring full halo CMEs as well as extremely slow CMEs, 4762 out of 5060 CMEs are collected for the same period from 1996 to 2001. The waiting time is sampled with an interval of 40 min. The WTD of CMEs is shown in Fig. 2. Sample points below 10 hours and above 30 hours are skipped in the power-law fitting for the same reasons mentioned above. The remaining sample points are well fitted by a power-law distribution, with an index of -2.37 ± 0.1 (the corresponding χ^2 is below 1.0).

To study whether CMEs with different velocity profiles show different WTD behaviors, we categorize the CMEs into two groups with different speeds, one with speeds larger than 400 km s^{-1}, and the other with speeds smaller than 400 km s^{-1}. Each group contains approximately 2500 sample points. The results are shown in Fig. 3. It is found that the group with higher speed is described by a power-law index of −2.16, and the group with smaller speeds by an index of −2.13. This finding may suggest that
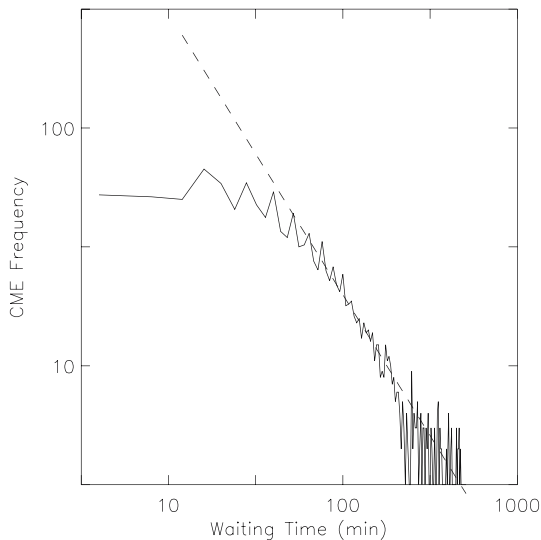
Figure 2. Waiting time distribution of CMEs observed by SOHO/LASCO during the years 1996−2001 (solid line), which is fitted by a power-law with an index of −2.37 (dashed line) in the range between 10 and 30 hours.

flare-associated eruptions and prominence-associated events originate from an identical mechanism.

3. Discussion

In summary, we find that CMEs show a power-law behavior in the waiting time distribution similar to that of solar flares. The corresponding power-law indices are −2.37 ± 0.1 for the former and −2.46 ± 0.1 for the latter, respectively.

The power-law distribution is a standard feature of Self-Organized Criticality (SOC). The basic idea of SOC can be illustrated by the sandpile model. The sandpile simulations in Lu and Hamilton (1991) for the distributions of the total energy, duration and peak flux of flares are in good agreement with observations. It verifies that the dynamics of coronal magnetic activities is analogous to that of a self-organized model. The waiting time in the self-organized model is defined as the time interval between successive avalanches, which also presents a power-law distribution, if the duration for an avalanche is ignored (Bak, 1996).

To conclude, our statistical research indicates that solar flares and CMEs show almost the same power-law behavior in the waiting time distributions. It strongly supports the viewpoint that flares and CMEs are different manifestations of the same physical process. The common power-law behavior
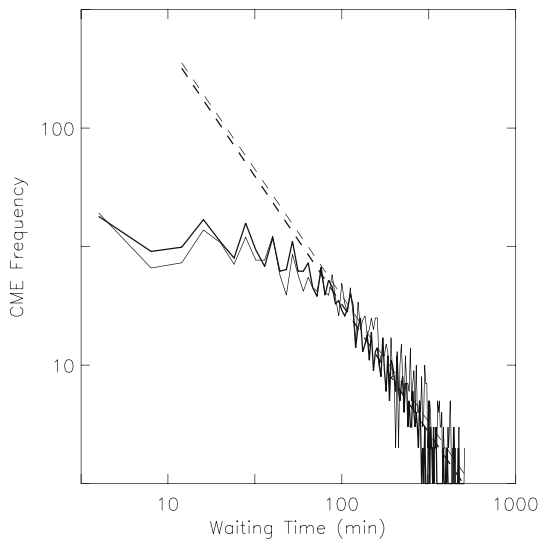
Figure 3. Waiting time distribution of CMEs grouped according to their speeds. The thick line corresponds to CMEs with a speed exceeding 400 km s^{-1}, and the thin line to CMEs with a speed smaller than 400 km s^{-1}. The former has an index of -2.16, while the latter shows an index of -2.13.

suggests that both of them can be statistically described by an avalanche model.

Acknowledgements

References

Bak, P.: 1996, *How Nature Works*, Springer-Verlag.
Boffeta, G., Carbone, V., Veltri, P., and Vulpiani, A.: 1999, *Phys. Rev. Lett.* **83**, 4662.
Brueckner, G.E., Howard, R.A., Koomen, M.J. *et al.*: 1995, *Solar Phys.* **162**, 357.
Lu, E.T. and Hamilton, R.J.: 1991, *Astrophys. J.* **380**, L89.
Wheatland, M.S., Sturrock, P.A., and McTiernan, J.M.: 1998, *Astrophys. J.* **509**, 448.

SIMULTANEOUS VISIBLE AND IR SPECTROPOLARIMETRY OF THE QUIET SUN

I. DOMÍNGUEZ CERDEÑA
Universitäts-Sternwarte Göttingen
Geismarlandstraße 11, D-37083 Göttingen, Germany

J. SÁNCHEZ ALMEIDA
Instituto de Astrofísica de Canarias, E-38205 La Laguna, Spain

F. KNEER
Universitäts-Sternwarte Göttingen
Geismarlandstraße 11, D-37083 Göttingen, Germany

Abstract. This work presents the first quiet Sun spectropolarimetric observations carried out in the visible and the infrared (IR) simultaneously. The Fe ɪ lines at 6301.5, 6302.5, 15648, and 15652 Å were observed co-spatially, and at the same time (with a time lag of only 1 minute), with high sensitive spectropolarimeters operated in two different telescopes (VTT and THEMIS at the Observatorio del Teide). We find Stokes V profiles above noise in 30% of the observed area, showing intrinsic magnetic fields of kG (traced by visible lines) co-existing with sub-kG fields (traced by infrared lines). We also found V profiles with opposite polarity in the visible and the IR in 25% of the pixels under study (8% of the area).

1. Introduction

The quiet Sun far from the network has been traditionally regarded as nonmagnetic. However, in the 70s magnetic fields were observed for the first time in the interior of the network (Livingston and Harvey, 1975; Smithson, 1975), and more recently there has been an increasing interest in these inter-network (IN) magnetic fields, thanks to the improvements in the sensitivity and resolution of the instruments. The IN covers most of the solar surface, and some works suggest that it may harbour a large amount of unsigned magnetic flux (e.g. Stenflo, 1982; Domínguez Cerdeña *et al.*, 2003a).

In recent years, there has been a controversy on the intrinsic strength of the IN magnetic field. With the use of visible lines, a magnetic field of the order of kG is inferred (see e.g, Sánchez Almeida and Lites, 2000; Socas-Navarro and Sánchez Almeida, 2002; Domínguez Cerdeña *et al.*,

2003b), while IR lines show the presence of sub-kG field strengths (see Lin and Rimmele, 1999; Khomenko *et al.*, 2003). A possible explanation was already given by Sánchez Almeida and Lites (2000), pointing out that both sub-kG and kG may exist as a continuous distribution of field strengths. Socas-Navarro and Sánchez Almeida (2003) synthesized visible and IR lines with a particular distribution of magnetic field strengths (with horizontal gradients). When the techniques used in the above mentioned works are applied to such profiles, the visible lines show kG fields while the IR lines show sub-kG.

In these proceedings we summarize the results from a simultaneous observation of IN fields in the visible and the IR. A more extended explanation can be found in Sánchez Almeida *et al.* (2003).

2. Observation

For this observation we used two different telescopes, the Vacuum Tower Telescope (VTT) and THEMIS, both at the Spanish Observatorio del Teide (Tenerife, Spain). Using the Tenerife Infrared Polarimeter (TIP) at the VTT we obtained the four Stokes profiles of the IR lines Fe I $\lambda15648$ ($g_{\mathrm{eff}} = 3$) and Fe I $\lambda15652$ ($g_{\mathrm{eff}} = 1.53$). With the spectropolarimetric mode of THEMIS, the same information was obtained for the visible lines Fe I $\lambda6301.5$ ($g_{\mathrm{eff}} = 1.67$) and Fe I $\lambda6302.5$ ($g_{\mathrm{eff}} = 2.5$). On 2002 August 10, we scanned an IN region at disk center. Integrating 30 s per slit position, we obtained a field of view (FOV) of $30'' \times 35''$ with a step size of $0\rlap{.}''5$.

The co-spatiality of the scans in IR and visible is of the order of $1''$, which corresponds to a time lag of 1 minute (two steps). The spatial resolution of the IR observations was $1''$–$1\rlap{.}''2$, while it was some $1\rlap{.}''5$–$1\rlap{.}''7$ in the visible. The polarization noise of Stokes V is $3 \times 10^{-4} I_c$ for the IR data, and $7 \times 10^{-4} I_c$ for the visible data.

3. Data analysis and results

To analyze the data, we choose those pixels with Stokes V profiles above 3 times the noise level, which correspond to the 30% of the pixels in our FOV. All these Stokes V profiles were classified using principal component analysis (PCA), in a way similar to the one used by Sánchez Almeida and Lites (2000). The classification was done simultaneously for visible and IR profiles, scaling the profiles of each individual pixel to the extremum of the blue lobe of the V profile of Fe I $\lambda6302.5$. The result was 25 different classes with abundance above 0.5%. Figure 1 shows the 10 first classes. A surprising fact is the presence of classes with profiles of opposite polarities in the visible and IR (see classes 4, 7, 8, and 9), resulting that 25% of the
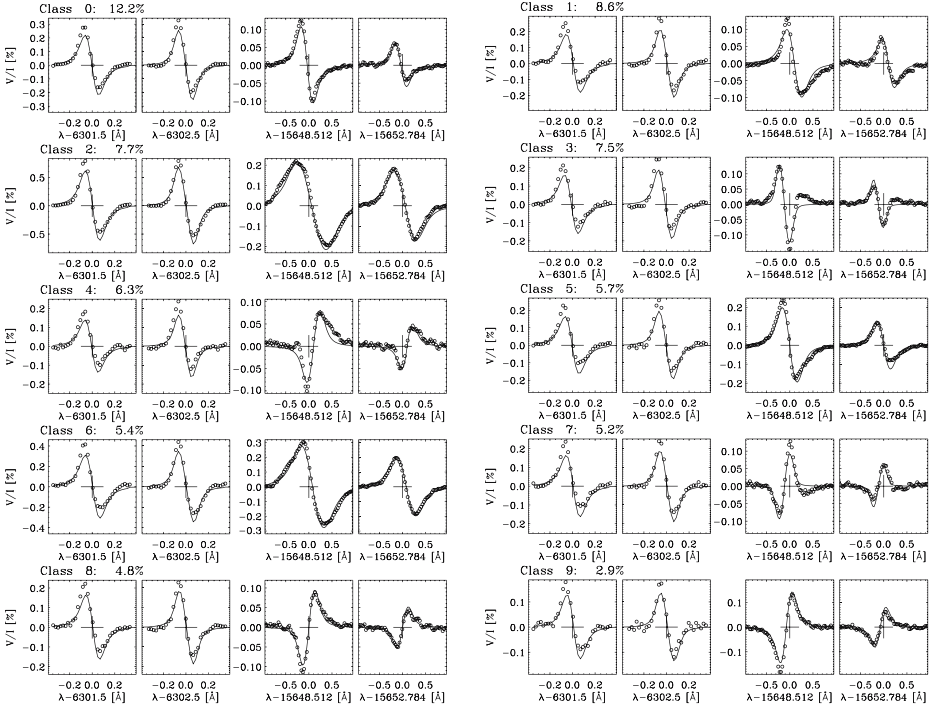
Figure 1.   First 10 classes of Stokes V profiles from the PCA classification, with abundance in percentage. Circles represent observations (mean profile among those in each class), and solid lines are the ME fits.

pixels under study present this effect. It follows that visible and IR lines trace different magnetic structures.

To make a deeper analysis of the data, we performed a Milne-Eddington (ME) inversion on the individual profiles and classes. Such an inversion can give us an estimate of the magnetic field strength. It was carried out using the MILK code from the Community Inversion Codes[1] developed at the High Altitude Observatory (see Socas-Navarro, 2001). The inversion of Stokes I and Stokes V was done independently for the visible and IR pair of lines, so we obtain two values of magnetic fields per pixel.

The result of the inversion is that most of the profiles (classes and individuals) are characterized in the visible by kG fields, while simultaneous IR profiles indicate sub-kG field strengths. Some profiles show strong fields also in the IR (class 2 in Fig. 1), but such profiles correspond to a small network patch in our FOV. The mean magnetic field strength for the visible lines is 1100 G, with a filling factor of 1%, while in the IR it is 300 G filling 2% of the FOV. The unsigned magnetic flux density in the visible (11 G)

---

[1] http://www.ho.ucar.edu/public/research/cic

is larger than in the IR (6 G), despite the better resolution of the IR data (the better the resolution the larger the magnetic flux measured in IN, see Domínguez Cerdeña *et al.*, 2003b). The signed flux in the visible is -1.5 G, while in the IR it is negligible (0.2 G). This net flux was already observed in the visible by Lites (2002), Domínguez Cerdeña *et al.* (2003b), and others.

4. Conclusions

The use of simultaneous visible and IR spectra has revealed some important properties of the IN magnetic fields, where the use of only visible or IR lines biases the result. The use of basic tools demonstrate the co-existence of kG and sub-kG magnetic field strengths in most of the pixels under study (30% of the FOV). IR lines show sub-kG fields while visible lines indicate kG fields, which support the suggestion by Sánchez Almeida and Lites (2000), and Socas-Navarro and Sánchez Almeida (2002, 2003).

It has been found that 25% of the pixels present magnetic fields with opposite polarity in the visible and the IR, which proofs the co-existence of two polarities in 1″5 resolution elements. This was already inferred by Sánchez Almeida and Lites (2000) and Lites (2002).

Finally, the concentration of the flux in strong magnetic fields (75% of the flux for magnetic field strengths above 500 G) is in agreement with the PDF suggested by Socas Navarro and Sánchez Almeida (2003) to be able to explain the discrepancies between the different magnetic field strengths obtained from the visible and IR lines.

References

Domínguez Cerdeña, I., Kneer, F., and Sánchez Almeida, J.: 2003a, *Astrophys. J.* **582**, L55.

Domínguez Cerdeña, I., Sánchez Almeida, J., and Kneer, F.: 2003b, *Astron. Astrophys.* **407**, 741.

Khomenko, E.V., Collados, M., Solanki, S. K., Lagg, A., and Trujillo-Bueno, J.: 2003, *Astron. Astrophys.* **408**, 1115.

Lin, H. and Rimmele, T.: 1999, *Astrophys. J.* **514**, 448.

Lites, B.W.: 2002, *Astrophys. J.* **573**, 431.

Livingston, W.C. and Harvey, J.W.: 1975, *Bull. Am. Astr. Soc.* **7**, 346.

Sánchez Almeida, J. and Lites, B.W.: 2000, *Astrophys. J.* **532**, 1215.

Sánchez Almeida, J., Domínguez Cerdeña, I., and Kneer, F.: 2003, *Astrophys. J.* **597**, L177.

Smithson, R.C.: 1975, *Bull. Am. Astr. Soc.* **7**, 346.

Socas-Navarro, H.: 2001, in M. Sigwarth (ed.), *Advanced Solar Polarimetry – Theory, Observations, and Instrumentation*, ASP Conf. Ser. Vol. 236, San Francisco: ASP, 487.

Socas-Navarro, H. and Sánchez Almeida, J.: 2002, *Astrophys. J.* **565**, 1323.

Socas-Navarro, H. and Sánchez Almeida, J.: 2003, *Astrophys. J.* **593**, 581.

Stenflo, J.O. 1982, *Solar Phys.* **80**, 209.

A SIMPLE TOPOLOGICAL MODEL OF THE BASTILLE DAY FLARE (JULY 14, 2000)

I.V. ORESHINA and B.V. SOMOV
Sternberg Astronomical Institute
Moscow State University
Universitetskii pr. 13, Moscow, 119992, Russia

Abstract. We present a topological model of the active region NOAA 9077, where the large two-ribbon flare (3B/X5.7) occurred on July 14, 2000. The coronal magnetic field was reconstructed on the basis of SOHO magnetograms. The model interprets the two-ribbon structure of the flare, the location and the form of the bright chromospheric ribbons and the appearance of bright kernels on the ribbons' ends, observed in different wavelengths by YOHKOH and TRACE. It is shown that such features are a consequence of the magnetic-field topology. The electric field, arising as a result of the magnetic-flux change through the separators, is also estimated. The advantage of our model consists in simplicity and clearness.

1. Introduction

The aims of our study are (1) to explain the two-ribbon structure of the flare, the location and form of the bright chromospheric ribbons and the appearance of bright kernels on the ribbons' ends, observed in different wavelengths by YOHKOH and TRACE, and (2) to estimate the electric field in the flare. For this, we address two main problems: (1) to develop a topological model of the active region, i.e. to separate the coronal magnetic field into interacting fluxes and to find separators; (2) to examine the evolution of the magnetic field before the flare and to estimate the electric field arising as a result of the magnetic-flux change through the separators.

Our basic assumptions are the following: the coronal field is potential (the validity of this approximation in solar active regions was shown by Somov, 1992); the flare is caused by magnetic reconnection in the current layer on the separator (Somov, 1992; Oreshina and Somov, 2000).

a)   b)
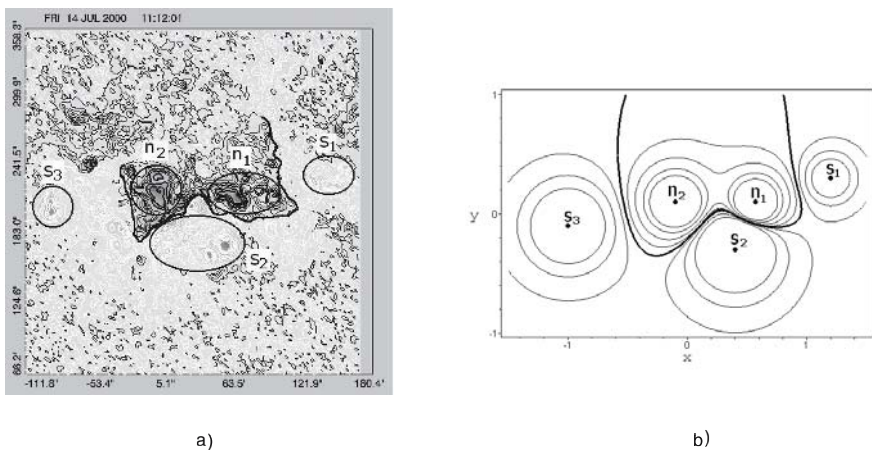
Figure 1.   a) Observed magnetogram from MDI/SOHO. b) Model magnetogram.

2. The model

Let us first address problem number one. Our model consists of the following (Gorbachev and Somov, 1988). The magnetic field $\mathbf{B}$ is created by effective charges, situated below the photosphere:

$$\mathbf{B}(x, y, z) = \sum_{i=1}^{5} \frac{e_i}{|\mathbf{r} - \mathbf{r}_i|} \frac{\mathbf{r} - \mathbf{r}_i}{|\mathbf{r} - \mathbf{r}_i|}, \tag{1}$$

where e_i denote the values of the charges and $\mathbf{r}_i$ their radius-vectors. The photosphere is the plane $z = 0$.

The reconstruction of the coronal magnetic field has been performed by numerical integration of the field-line equations:

$$\frac{\mathrm{d}x}{B_x} = \frac{\mathrm{d}y}{B_y} = \frac{\mathrm{d}z}{B_z}, \tag{2}$$

where $(\mathrm{d}x, \mathrm{d}y, \mathrm{d}z)$ is an element along a field line, and $\mathbf{B}$ is defined by Eq. (1). The solution scheme of the system Eq. (2) is based on the Euler method.

Let us apply this model to the Bastille Day Flare, July 14, 2000, active region NOAA 9077. The corresponding observed magnetogram is shown in Figure 1a. The black colour corresponds to the north polarity of the magnetic field and the white colour corresponds to its south polarity. The thick black line is the magnetic neutral line. Note, that it has the shape of the Greek letter ω. This situation is reproduced on the model magnetogram (see Figure 1b): 2 charges (n_1 and n_2) model the north magnetic field, 3 charges (s_1, s_2, and s_3) model the south magnetic field, and these charges generate a ω-shaped neutral line.

a) b)
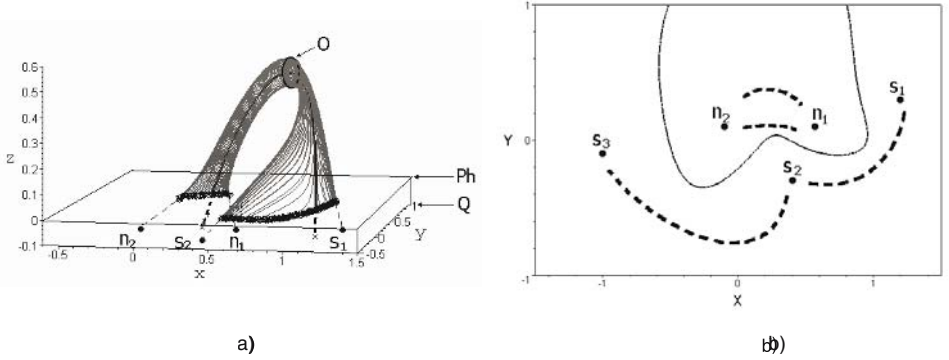
Figure 2.   a) Separator, region of initial energy-release (O) and the flare ribbons on the photosphere (Ph). Q is the plane of the charges. b) Result of the numerical computation of the flare ribbons in the xy-plane.

The values and radius-vectors of the charges used in the model are the following:

$$e_1 = 2.0; \qquad \mathbf{r}_1 = (-0.1, 0.1, -0.1);$$
$$e_2 = 1.5; \qquad \mathbf{r}_2 = (0.57, 0.1, -0.1);$$
$$e_3 = -0.5; \qquad \mathbf{r}_3 = (1.2, 0.3, -0.1);$$
$$e_4 = -4.0; \qquad \mathbf{r}_4 = (0.4, -0.3, -0.1);$$
$$e_5 = -2.6; \qquad \mathbf{r}_5 = (-1.0, -0.1, -0.1).$$

So, we are able to investigate the coronal magnetic field with Eqs. (1) and (2). The small number of the charges makes the model simple and clear and allows us to reproduce the most important features of the MDI/SOHO magnetogram. We separate the coronal magnetic field into interacting fluxes and find separators. Then, we assume that the flare is caused by magnetic reconnection in a current layer (Litvinenko and Somov, 1993; Oreshina and Somov, 2000; Somov, 2000) at the separator top and that the region of the initial energy-release is a small circle (see Figure 2a). Accelerated particles follow the field lines and precipitate to the chromosphere. There, the matter is more dense. The interaction of the particles with the dense matter results in brightening in various wavelengths. Note that the ends of the field lines form the ribbons on the photosphere (see Figure 2b). The majority of lines concentrates on the ribbons ends. Thus, we see the most important brightening on the ends of the ribbons.

Based on the topological model, we examine the evolution of the magnetic field before the flare and estimate the electric field arising as a result of the magnetic-flux change through the separators. The electric field plays an important role in the flare because it contributes to transformation (in current layers) of magnetic energy to thermal energy of the plasma and accelerated particles (Litvinenko and Somov, 1993; Oreshina and Somov,

2000). We assume that the active region had a minimum of magnetic energy after the relatively powerful flare on July 12, and it accumulated the energy during the two following days before July 14 (Somov *et al.*, 2002). The electric field is estimated by the formula

$$\mathbf{E} = \frac{1}{c}\frac{\partial \mathbf{A}}{\partial t}$$

with $\mathbf{A}$ the vector-potential ($\mathbf{B} = \mathrm{rot}\,\mathbf{A}$) and c the velocity of light. The corresponding magnetic flux Ψ is

$$\Psi = \oint_L \mathbf{A}\mathrm{d}\mathbf{l},$$

where L is a separator. Thus, we derive for the electric field:

$$E \approx 10 \text{ V/cm}.$$

This result is in agreement with values of other authors (Somov, 2000).

Acknowledgements

References

Gorbachev, V.S. and Somov, B.V.: 1988, *Solar Phys.* **117**, 77.
Litvinenko, Y.E. and Somov, B.V.: 1993, *Solar Phys.* **146**, 127.
Oreshina, A.V. and Somov, B.V.: 2000, *Astron. Astrophys.* **354**, 703.
Somov, B.V.: 1992, *Physical Processes in Solar Flares*, Kluwer Academic Publ., Dordrecht, Boston, London.
Somov, B.V.: 2000, *Cosmic Plasma Physics*, Kluwer Academic Publ., Dordrecht, Boston, London.
Somov, B.V., Kosugi, T., Hudson, H.S., Sakao, T., and Masuda S.: 2002, *Astrophys. J.* **579**, 863.

SPECTROPOLARIMETRY IN A SUNSPOT PENUMBRA AT HIGH SPATIAL RESOLUTION

N. BELLO GONZÁLEZ, O. OKUNEV and F. KNEER

Universitäts-Sternwarte Göttingen
Geismarlandstrasse 11, D-37083 Göttingen, Germany

Abstract. We present results from polarimetric data on sunspot penumbrae obtained with the Vacuum Tower Telescope at the Observatorio del Teide, Tenerife, using the 'Göttingen' Fabry–Pérot Interferometer. Speckle image reconstruction has been performed giving us a spatial resolution of 0.6″. The observations were taken in the Fe II 6149.2 Å line which, given its particular Zeeman splitting, has no instrumental (Q, U) to V crosstalk and provides us measurements of I and V Stokes profiles to analyse velocities and magnetic fields in penumbrae.

1. Introduction

The 'Evershed effect' (Evershed, 1909) is characterized by a wavelength shift and profile asymmetry observed in photospheric absorption lines which has been interpreted as a radial outflow in sunspot penumbrae. While the cool umbra ($T \simeq 4000$ K) keeps at rest, the penumbra ($T \simeq 5600$ K) shows dark filaments in an almost homogeneous background with nearly horizontal magnetic field, alternating with bright cometary like structures with their 'heads' pointing towards the umbra and magnetic field inclined about 40° to the horizontal (Title, Frank, and Shine, 1993). The Evershed flow evolves outwards of the penumbra and concentrates in thin elevated unresolved channels (Rimmele, 1995).

The origin of the Evershed flow has been explained by the 'siphon model' (Meyer and Schmidt, 1968; Montesinos and Thomas, 1999). In this model the mass flows along magnetic loops and is driven by unbalanced gas pressure due to stronger magnetic fields outside than inside the spot. Another explanation is given by Schlichenmaier, Jahn, and Schmidt (1998) with their 'thin moving flux tube model' of penumbral filaments. This flux tube emerges vertically from the deep penumbra carrying the Evershed flow to the penumbral photosphere where it turns horizontal.
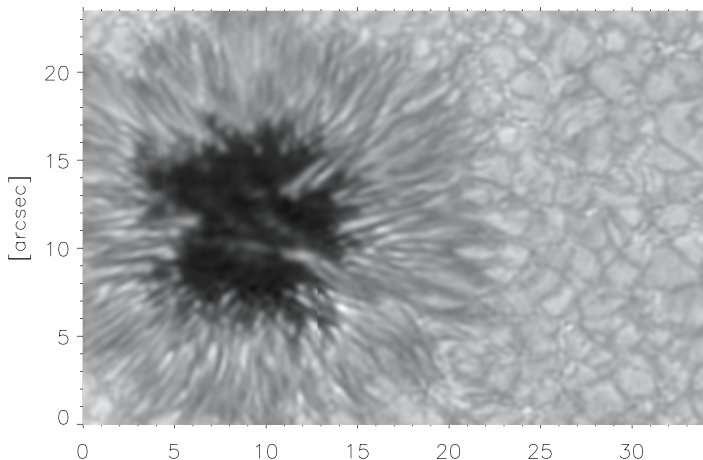
Figure 1.　　Reconstructed broadband image of a sunspot. The spatial resolution is 0.2″.

2.　Observations

The observations were realized on May 2, 2003 with the German Vacuum Tower Telescope (VTT, 70 cm) at the Observatorio del Teide, Tenerife. We used the 'Göttingen' Fabry–Pérot interferometer (FPI) and a Stokes V polarimeter which splits the light into right, $1/2(I+V)$, and left, $1/2(I-V)$, circularly polarized components. We obtained simultaneous 2D broadband and narrowband polarimetric images, scanning along 18 wavelength positions on the Fe II line at 6149 Å. The observed sunspot – NOOA 0346 – was located at off-center position $\theta = 28°$, not far from the disc centre.

This kind of simultaneous data allows us to apply speckle reconstruction to the broadband images (example in Fig. 1) and later, imaging restoration to the narrowband ones with the code by Janßen (2003) to achieve high spatial resolution: 0.2″ (diffraction limit) in broadband images and 0.6″ for the narrowband set. After data reduction and reconstruction, 2D spectropolarimetric data – right and left components – are ready to be added in order to obtain Stokes I and subtracted to obtain Stokes V maps. We refer to Koschinsky, Kneer, and Hirzberger (2001, and references therein) for a detailed description of the instrument and data analysis.

The Fe II 6149 Å line, formed at relatively deep layers, is not strongly sensitive to magnetic field ($g_{\mathrm{eff}} = 1.33$) but possesses a peculiar Zeeman pattern which makes it interesting for our purpose. In the presence of a magnetic field, the π and σ components coincide in wavelength position. This introduces strong simplifications in the radiative transfer equation which lead us to $U = Q = 0$, no linear polarization, and hence a line free of (Q,U) to V crosstalk.
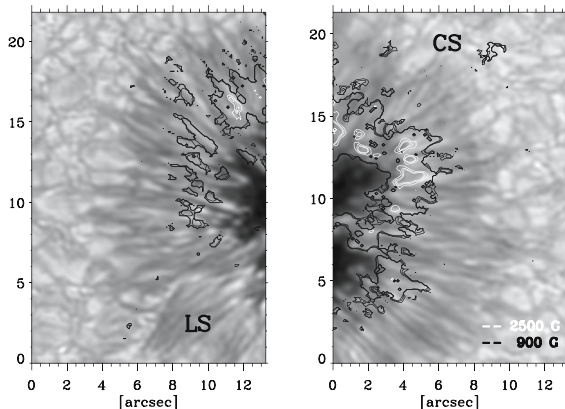
Figure 2.   Line of sight magnetic field distribution overplotted on continuum image. The absence of magnetic signal in the LS penumbra is produced by the magnetic neutral line.

3. Results

Since magnetic fields in sunspots are quite strong, the weak field approximation can not be used. Within the whole 2D field of view we have calculated magnetic field components along the line of sight (LOS) from the lobes of the Stokes V profiles, using a simple atmosphere model. We can detect magnetic fields basically from inner to mid penumbra (Fig. 2). Taking into account the relative small heliocentric angle ($\theta = 28°$), we can interpret that, in this region, the observed signal is associated with more vertical fluxes, and in the outer penumbra, where we detect no V signal above the noise, the fields are oriented perpendicular to the LOS.

Velocity maps have been calculated by two methods: from shifts of bisectors of intensity profiles and from displacements of the zero crossing point of Stokes V profiles. The reference zero velocity is the centre of gravity in the photosphere. We obtain typical values of $\pm 1.5\,\mathrm{km\,s^{-1}}$.

Velocity maps show blueshifts and redshifts in the centre side (CS) and limb side (LS) penumbra, respectively, as we expect from the radial mass outflow. Also, overplotting to continuum images we have observed, from velocity maps in mid layers, some blueshifts alternating with redshifts in the inner penumbra, independently of the azimuthal position. These must correspond to vertical motions.

4. Conclusions

With high spatial resolution 2D spectropolarimetry of a sunspot penumbra we observe clear asymmetries and displacements (Fig. 3) in the Stokes I profiles characteristic of velocity gradients along the LOS and even, in some
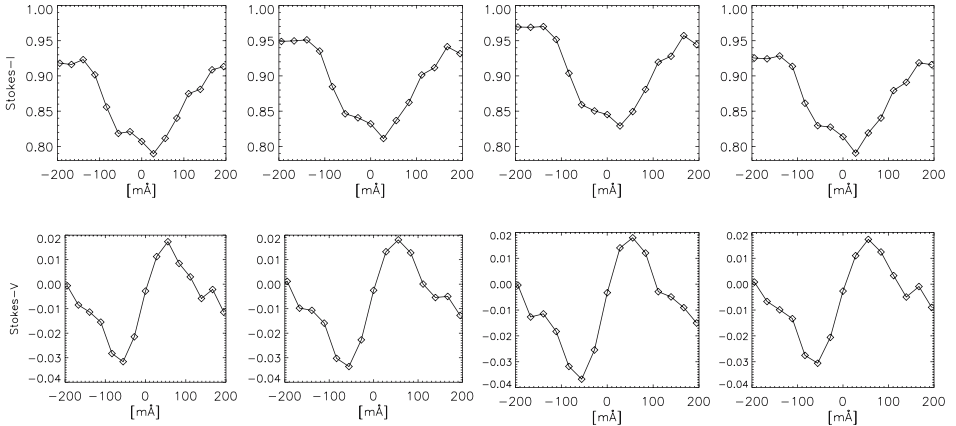
Figure 3. Examples of Stokes *I* and *V* profiles from a centre side (CS) penumbra.

cases, of different unresolved flow components. These asymmetries are more pronounced in profiles associated with dark structures. In bright structures they appear more symmetric except in penumbral grains close to the umbra.

From the calculation of LOS velocities from Stokes *I* (intensity) and Stokes *V* (magnetic), we obtain values of the same order, $\pm 1.5 \, \mathrm{km \, s^{-1}}$, for mid layers, which agrees with the fact that sunspot penumbrae are basically magnetic structures. Also typical radial outflow is observed: blueshifts in the CS and redshifts in the LS penumbra.

Finally, Stokes *V* amplitudes give us LOS components of magnetic fields between 900 and 2500 G, observed basically in the inner-mid penumbra with a higher (more vertical) LOS component and absent in the mid-outer penumbra where the LOS component is too faint (field close to perpendicular) to be observable at $\theta = 28°$.

A deeper analysis of the data must be done. The synthesis of Stokes profiles through an atmosphere model of a sunspot penumbra is being performed to understand the origin of the strong asymmetries and shape of the observed profiles.

References

Evershed, J.: 1909, *Mon. Not. Roy. Astr. Soc.* **69**, 454.
Janßen, K.: 2003, PhD Thesis, Göttingen University.
Koschinsky, M., Kneer, F., and Hirzberger, J.: 2001, *Astron. Astrophys.* **365**, 588.
Meyer, F. and Schmidt, H.U.: 1968, *Mitteilungen der AG* **25**, 194.
Montesinos, B. and Thomas, J.H.: 1999, *Astrophys. Space Sci.* **263**, 323.
Rimmele, T.R.: 1995, *Astron. Astrophys.* **298**, 260.
Schlichenmaier, R., Jahn, K., and Schmidt, H.U.: 1998, *Astron. Astrophys.* **493**, L121.
Title, A., Frank, Z., and Shine, R.: 1993, *Astrophys. J.* **403**, 780.

X-RAY AND Hα EMISSION OF THE 20 AUG 2002 FLARE [*]

J. KAŠPAROVÁ and M. KARLICKÝ
Astronomical Institute AS CR
251 65 Ondřejov, Czech Republic

R.A. SCHWARTZ and B.R. DENNIS
Goddard Space Flight Center
Greenbelt, MD 20771, USA

Abstract. An analysis of the August 20, 2002 flare using RHESSI, Hα, and radio observations is presented. Radio data in the decimetric frequency range showed a type IIId (relativistic) burst at the time of the X-ray maximum. At this time a very flat ($\gamma_{\mathrm{phot}} = 1.8$) X-ray spectrum was measured. Fitted double power-law spectra in the thick-target model revealed an increase of the low energy cutoff in the electron spectrum that rose to as high as 81 keV. This cutoff evolution is interpreted as a possible gap in energies of electrons injected into the X-ray thick-target source and those of the background plasma. Fast changes of Hα intensities were found to be located away from the X-ray sources in the beginning of the Hα flare.

1. Introduction

Accelerated particles in solar flares reveal their presence e.g. in hard X-ray and radio emission, and cause rapid heating of the chromosphere and subsequent emission in the hydrogen Hα line. Recently, Gan *et al.* (2002) found that the low energy cutoff of the electron flux spectrum derived from X-ray spectra can be as high as 97 keV. Time correlation of hard X-ray and Hα emission, predicted by numerical models (e.g. Canfield and Gayley, 1987), was recently analysed (e.g. Trottet *et al.*, 2000). The results indicate that hard X-rays and Hα intensities in flare kernels may exhibit time correlation in the time range from subseconds to 10 s.

2. Event description

The analysed flare was detected by GOES on Aug 20, 2002 at 08:25 UT and reached its maximum at 08:26 UT as an M3.4 flare. The 1B Hα flare

---

[*] This paper is a short version of Kašparová *et al.* (2004)
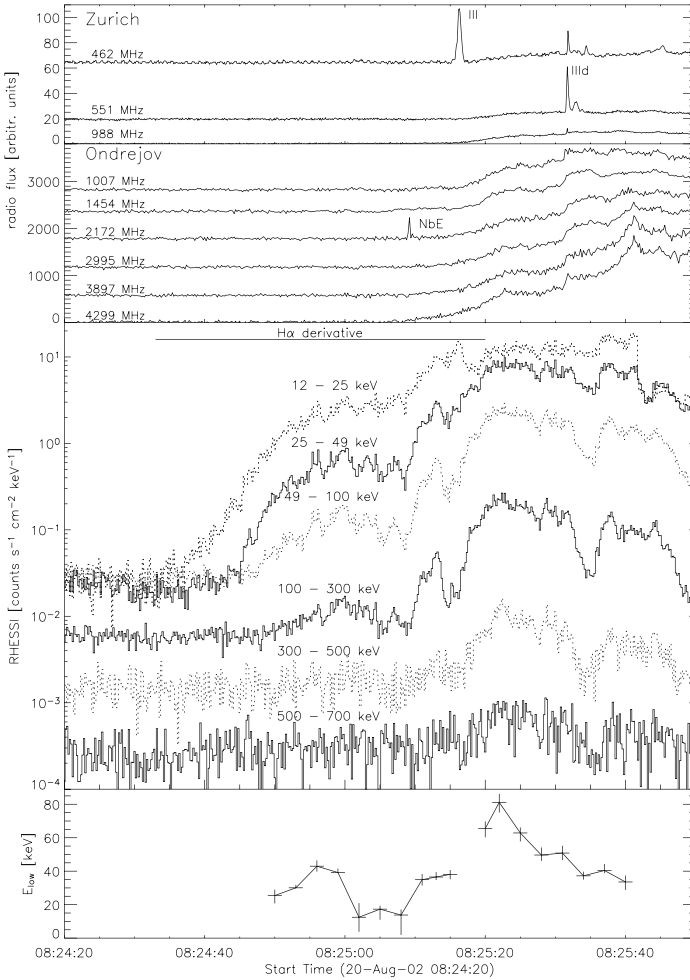
Figure 1. Time evolution of hard X-ray (RHESSI) and radio (Ondřejov and Zürich) fluxes. For display purposes RHESSI count fluxes in the 300–500 keV and 500–700 keV energy band were scaled by factors 1.5 and 0.5, respectively. The time interval in which Hα derivatives were analysed is indicated on top of the RHESSI plot. The bottom panel shows the time evolution of E_{low} of the electron flux distribution. Bars in x-direction correspond to the RHESSI accumulation interval, bars in y-direction to standard errors.

started at 08:25 UT in NOAA AR 0069 at S10W38 (SEC, 2002). A global overview of the flare evolution in dm/m radio waves and RHESSI X-rays is shown in Fig. 1. The RHESSI flare started at 08:24:32 UT as the increase in the 12–25 keV band. Bursts at harder energies up to emission in the 500–700 keV band followed. At the analysed frequencies 0.1–4.5 GHz the starting phase of the flare is nearly without any radio emission. First, narrow band emission (NbE) at ∼2 GHz was registered, then a type III burst below
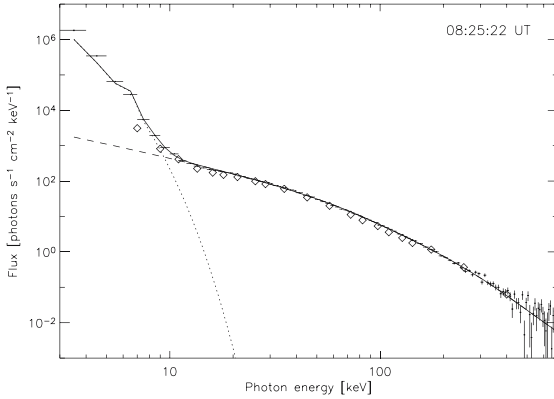
Figure 2. Very flat X-ray spectrum of $\gamma_{\mathrm{phot}} = 1.8$ up to 70 keV. The dotted line shows the fitted thermal part, the dashed line the fitted non-thermal part, and the solid line the fitted total flux. Crosses with error bars represent the observed data. An isothermal plus a double power-law electron flux function was fitted to the data in the energy range 8–600 keV. PIXON photon fluxes are plotted as diamond symbols.

500 MHz followed. A fast drifting (~ -4 GHz s^{-1}) type IIId burst occurred during the time interval when X-ray emission up to 700 keV was detected.

3. X-ray emission at the burst maximum

The background subtracted X-ray spectra were fitted with an isothermal component plus a double power-law electron flux distribution function assuming thick-target bremsstrahlung spectra. The time evolution of one of the derived parameters of the electron flux distribution functions, the low energy cutoff E_{low}, together with error bars is plotted in Fig. 1. Note that E_{low} increases up to 81±6 keV at the burst maximum at 08:25:22 UT. We propose that this high value shows a real gap between the thermal plasma energy and the electron distribution function.

At this time the flare was characterised by an unusually flat X-ray spectrum up to energies of ~ 70 keV (see Fig. 2). Fitting of the photon spectrum with an isothermal component plus a double power-law function gave a spectral index $\gamma_{\mathrm{phot}} = 1.8$ which lies outside of the range of $\gamma_{\mathrm{phot}} = \langle 2, 7 \rangle$ as reported e.g. by Dennis (1985). The solar origin of the spectrum was confirmed by imaging spectroscopy using the PIXON algorithm.

4. Time derivative of Hα intensities

We assume that fast changes of Hα intensity $I_{\mathrm{H}\alpha}$ might indicate locations of a flare which are directly affected by electron beams. According to the atmosphere model of Machado *et al.* (1980), only electrons of energy ≥ 25 keV
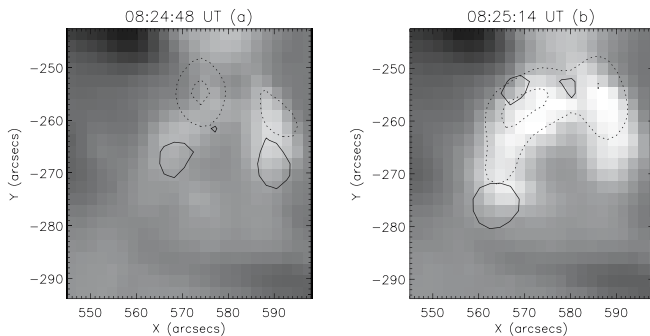
Figure 3.   Locations of $dI_{\mathrm{H}\alpha}/dt$ (full lines) overlayed on Hα images (Kanzelhöhe Solar Observatory, Austria). RHESSI images at 25–40 keV are plotted as dashed contours at 50 and 90% of the maximum of each image.

may penetrate into the layers of Hα formation. Figure 3 shows locations of $dI_{\mathrm{H}\alpha}/dt$ above the chosen threshold and RHESSI images in the 25–40 keV band. Some areas of high $dI_{\mathrm{H}\alpha}/dt$ lie on the boundaries or inside of X-ray sources (Fig. 3b). However, there are other such areas located away from the X-ray sources (Fig. 3a). Since X-ray sources in the 3–12 keV band do not exhibit a significant shift between them and those of the 25–40 keV band, we suggest that these Hα areas might be caused by hot plasma with temperature below 10 MK (minimum temperature detected by RHESSI) or the apparent shift may be due to the low dynamic range of RHESSI (10:1).

Acknowledgements

References

Canfield, R.C. and Gayley, K.G.: 1987, *Astrophys. J.* **363**, 1999.
Dennis, B.R.: 1985, *Solar Phys.* **100**, 465.
Gan, W.Q., Li, Y.P., Chang, J., and McTiernan, J.M.: 2002, *Solar Phys.* **207**, 137.
Kašparová, J., Karlický, M., Schwartz, R.A., and Dennis, B.R.: 2004, *Solar Phys.*, subm.
Machado, M.E., Avrett, E.H., Vernazza, J.E., and Moyes, R.W.: 1980, *Astron. Astrophys.* **242**, 336.
Trottet, G., Rolli, E., Magun, A., Barat, C., Kuznetsov, A., Sunyaev, R., and Terekhov, O.: 2000, *Astron. Astrophys.* **356**, 1067.
SEC: 2002, `http://www.sec.noaa.gov/weekly/pdf/prf1408.pdf`

CENTER-TO-LIMB VARIATION OF FACULAR CONTRAST DERIVED FROM MLSO RISE/PSPT FULL DISK IMAGES

F.L. VOGLER
Institut für Geophysik, Astrophysik und Meteorologie
Karl-Franzens-Universität Graz, Austria

P.N. BRANDT
Kiepenheuer-Institut für Sonnenphysik, Germany

W. OTRUBA
Sonnenobservatorium Kanzelhöhe, Austria

A. HANSLMEIER
Institut für Geophysik, Astrophysik und Meteorologie
Karl-Franzens-Universität Graz, Austria

Abstract. RISE/PSPT full disk solar images ($2\text{k} \times 2\text{k}$) with a resolution of 1 arcsec per pixel, observed in 1999 at Mauna Loa Observatory (MLSO), Hawaii, are used to measure the contrast of facular areas as function of the two variables μ and E_k, where μ is the cosine of the heliocentric angle Θ and E_k is the Ca II K excess. The analysis comprises 60 datasets, each of them consisting of simultaneously taken narrowband images in 3 wavelengths: i.e. λ_k=393.4±0.15 nm (Ca II K), λ_b=409.3±0.15 nm ('blue'), and λ_r=607.2 ±0.25 nm ('red'). The contrast $(I - I_0)/I_0$ is measured in the two wavelengths λ_b and λ_r, while the Ca II K excess is used as a proxy. I_0 represents the 'quiet Sun level'. A multivariate fit yields the compact presentation of the contrast function $C_f(\mu, E_k)$.

1. Introduction

Measurements of the center-to-limb variation (CLV) of facular contrast have been tried for many decades with widely varying results: Kiepenheuer (1953), Foukal (1981), Chapman and Klabunde (1982), Schatten *et al.* (1985, 1986), Lawrence (1988), Lawrence, Chapman and Herzog (1988), Auffret and Muller (1991), Chapman and Ziegler (1996), Ahern and Chapman (2000). In all these publications the CLV of facular contrast was described by functions depending on only one variable, i.e. μ. However, the attempt to completely describe the CLV of facular contrast in dependence on only one variable seems to be either extremely complicated

or even impossible. Frazier (1971) stated already that, for describing the photospheric network and the continuum faculae, the dependence on B (the line-of-sight magnetic flux density) is as important as the dependence on μ, because non-sunspot magnetic fields, continuum faculae, and the 'network' are intimately related. Harvey and White (1999) found that the residual Ca II K intensity is on average proportional to $B^{1/2}$. Following these ideas we decided to select the Ca II K excess E_k, instead of B, as second variable in addition to μ, for describing the function $C_f(\mu, E_k)$.

2. Data and processing

From the time period 1999 May 28 to 1999 July 31, 60 sets of images with the best resolution were selected for final processing. These triple sets of full disk solar images were transformed into rectangular r-φ-presentations and the center-to-limb variation of the quiet Sun was removed; this yielded pixel-congruent images in the 3 wavelengths. E_k was defined as contrast with a chosen maximum of 1.0 (100 percent). The range from 0.0 to 1.0 corresponds to 100 E_k-bins. Pixels at a definite r-φ-position, showing Ca II K excess values within a specific E_k-bin, determined the pixels in the cospatial 'blue' and 'red' images, where the contrast C_f was measured and assigned to μ and E_k. μ ranges from 1.0 at disk center to 0.14 near the limb.

3. Preliminary results

The main results are: i) the contrast of the continuum faculae is increasing almost linearly with E_k for $E_k < 0.3$ and for all μ values, ii) the contrast turns negative beyond a specific E_k threshold described in Sect. 5, and that the contrast increases monotonically towards the limb down to $\mu = 0.2$, while a decrease is indicated beyond. An extended version of this article including figures can be accessed at `http://www.kso.ac.at/IrradVariations/public_info/docs/vogler_etal.pdf`.

3.1. RESULTS OF MULTIVARIATE ANALYSIS

First of all an approach to a closed presentation of $C_f(\mu, E_k)$ was found by a heuristic method. It comprises a mixed polynomial for the two variables μ and E_k, using six coefficients and the auxiliary function $q(E_k)$, viz.

$$C_f(\mu, E_k) = \{\, [\, a_0 + a_1\,\mu + a_2\,\mu^2 + a_3\,q(E_k)\,]^2 + a_4\} \, E_k + a_5\,\mu^2 E_k^2\,,$$

$$q(E_k) = 1.0 - E_k/(\,2.5E_k^2 - E_k + 0.4\,)\,,$$

λ_b: a_0=0.43, a_1=−0.11, a_2=−0.34, a_3=−0.09, a_4=0.06, a_5=−0.15,

λ_r: a_0=0.29, a_1=−0.04, a_2=−0.23, a_3=−0.07, a_4=0.03, a_5=−0.09.

The coefficients were calculated by iterative fit procedures. Unfortunately $q(E_k)$ is a rational function, but it is indispensable for the range of $E_k < 0.3$.

3.2. DEDUCTIONS FOR SIGN CHANGE AND DEPRESSION DOMAIN

The contrast function $C_f(\mu, E_k)$ represents a surface and shows a limited depression domain (a trench) near the origin:

λ_b: $C_f \leq 0$ for $E_k \geq -0.014/\mu^3 + 1.40/\mu^2 - 1.44/\mu + 0.44\mu$; $0.72 \leq \mu \leq 1.0$
λ_r: $C_f \leq 0$ for $E_k \geq -0.009/\mu^3 + 1.07/\mu^2 - 0.86/\mu + 0.17\mu$; $0.71 \leq \mu \leq 1.0$

For fixed values of E_k within the ranges given below and running μ the function passes through a minimum at a specific $\mu_0 = \cos\Theta_0$. If this minimum is interpreted as an accumulation of magnetic flux tubes, with their axes in the direction to the line of sight and therefore showing their 'dark' bottom, Θ_0 must be a measure for the inclination of the magnetic field lines in the photosphere against the local normal to the Sun's surface. The following relations show 'steeper' field lines (less inclination) with rising intensity:

λ_b: $\Theta_0 = 66 \cdot \sqrt{0.215 - E_k}$ $\rightarrow$ $29° \geq \Theta_0 \geq 5°$ for $0.02 \leq E_k \leq 0.21$,
λ_r: $\Theta_0 = 75 \cdot \sqrt{0.125 - E_k}$ $\rightarrow$ $25° \geq \Theta_0 \geq 5°$ for $0.02 \leq E_k \leq 0.12$.

4. Modified Photometric Facular Index Model (MPFI)

Chapman (1984) defined the PFI, to be summed over all solar active regions, PFI $= C_p(1/\mu - 1)(A_p\mu)(3\mu + 2)$, where C_p is constant, $(1/\mu - 1)$ the adopted CLV of facular contrast $C(\mu)$, $(A_p\mu)$ the projected plage area, and $(3\mu + 2)/5$ the solar limb darkening. With our contrast function $C_f(\mu, E_k)$, to act as a substitute for $C(\mu)$, we propose the following modified PFI:

$$\text{MPFI} = \alpha \sum_{i=1}^{m} \sum_{j=1}^{n} C_f \left(\sqrt{1 - r_i^2}, E_k\left(r_i, \varphi_j\right) \right) \left(3\sqrt{1 - r_i^2} + 2 \right) r_i \Delta\,\varphi_j\,\Delta r_i\,.$$

$E_k(r_i, \varphi_j)$ is an (m, n)-array Ca II K image, $r_m{=}0.99$, $\varphi_n{=}2\pi$, $\mu_i{=}\sqrt{(1 - r_i^2)}$, and α contains all constants and radial normalisation factors. At all events, the coefficients a_i in $C_f(\mu, E_k)$ have to be adjusted for an appropriate distribution in λ (color dependence). The advantage is that C_f is described completely by the two variables μ and E_k and that the determination of active areas is performed by the algorithm itself. The definition of active area and of intensity threshold is not required anymore.

5. Summary

The presentation of facular contrast in dependence on the two variables μ and E_k yields better insight in the phenomenology than presentation in dependence on the single variable μ. Our results are principally comparable to those of Frazier (1971), Topka, Tarbell and Title (1992), and Ortiz *et al.* (2002), with the distinction that they used the magnetic flux density B (respectively B/μ) instead of the Ca II K excess E_k as intensity measure, and that they measured at other wavelengths. We tried to use the results of Harvey and White (1999) for substitution, who claim that E_k shows an average proportionality to $B^{1/2}$, to compare our function $C_f(\mu, E_k)$ with the result function $C_{\mathrm{fac}}(\mu, B/\mu)$ of Ortiz *et al.* (2002), but analogy in the representations of the functional dependence could not be found. Our deductions of the inclination of magnetic field lines in dependence on E_k yield angles between $29°$ and $5°$. Frazier (1971) reports a preferred inclination of about $50°$, and Topka, Tarbell and Title (1992) state that an inclination from the local vertical of about $10°$ at the photosphere is common on the Sun. The Modified Photometric Facular Index (MPFI) Model could prove to be an appropriate and easy to apply method for calculating the contribution of faculae to irradiance variations, if the coefficients from $C_f(\mu, E_k)$ are adjusted for an adequate representative determination of the color dependence on the facular contrast.

References

Ahern, S. and Chapman, G.A.: 2000, *Solar Phys.* **191**, 71–84.

Auffret, H. and Muller, R.: 1991, *Astron. Astrophys.* **246**, 264–279.

Chapman, G.A.: 1984, *Nature* **308**, 252–254.

Chapman, G.A. and Klabunde, D.P.: 1982, *Astrophys. J.* **261**, 387–395.

Chapman, G.A. and Ziegler, B.: 1996, *Solar Phys.* **168**, 259–272.

Frazier, E.N.: 1971, *Solar Phys.* **21**, 42–53.

Foukal, P.: 1981, in L.E. Cram and J.H. Thomas (eds.), *The Physics of Sunspots*, National Solar Obs., Sunspot, NM, 391–423.

Harvey, K.L. and White, O.R.: 1999, *Astrophys. J.* **515**, 812–831.

Kiepenheuer, K.O.: 1953, in G. Kuiper (ed.), *The Sun*, 322.

Lawrence, J.K.: 1988, *Solar Phys.* **116**, 17–32.

Lawrence, J.K., Chapman, G.A. and Herzog, A.D.: 1988, *Astrophys. J.* **324**, 1184–1193.

Ortiz, A., Solanki, S.K., Domingo, V., Fligge, M., and Sanahuja, B.: 2002, *Astron. Astrophys.* **388**, 1036–1047.

Schatten, K.H., Miller, N., Sofia, S., Andrew, S.E., Chapman, G.A., and Hickey, J.: 1985, *Astrophys. J.* **294**, 689–696.

Schatten, K.H., Mayr, H.G., Kazem, O., and Mair, E.: 1986, *Astrophys. J.* **311**, 460–473.

Topka, K.P., Tarbell, T.D., and Title, A.M.: 1992, *Astrophys. J.* **396**, 351–363.

THE ACCELERATION–VELOCITY RELATIONSHIP IN 5000 LASCO–CME'S

D. RUŽDJAK, B. VRŠNAK and D. SUDAR
Hvar Observatory
Faculty of Geodesy University of Zagreb
Kačićeva 26, HR–10000 Zagreb, Croatia

Abstract.   Data from the SOHO LASCO CME catalogue are used to investigate the acceleration–velocity relationship of CMEs. We analyse 5012 individual events reported in the catalogue from 1996 to 2001. The dependence of acceleration on velocity is considered using the mean distance and width of CMEs as parameters. The obtained relationship is interpreted in the frame of a magnetohydrodynamic drag. The results are used to estimate the Lorentz force acting on CMEs.

1. Introduction

Large scale structures in the solar corona disrupt and are ejected into the interplanetary space at speeds ranging from 10 to several thousands $\mathrm{km\,s^{-1}}$. This phenomenon is called coronal mass ejection (CME). The motion of CMEs cannot be described by the ballistic expulsion, because some of them are moving outwards slower than the escape speed. Also many CMEs are still accelerated at large distances, so there must be some continuously driving force(s). Gopalswamy *et al.* (2000) found that in the interplanetary space CMEs that are faster than the solar wind decelerate, whereas the slower ones accelerate. This indicates that at large distances the magnetohydrodynamic drag becomes a dominant force.

2. Method

The acceleration of a CME can be written as:

$$a = a_L - g + a_d \tag{1}$$

where a_L is the acceleration due to the Lorentz force, g the gravity acceleration and a_d is the acceleration due to the drag force. Here we assume that
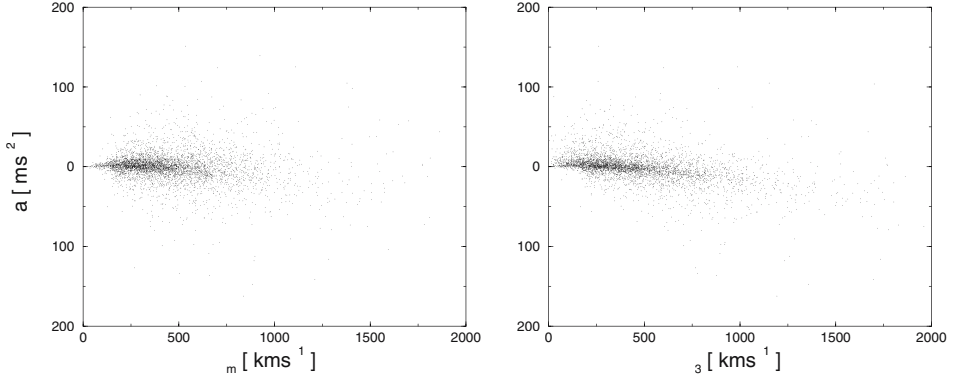
Figure 1. The dependence of acceleration on the velocity v_m (left) and the velocity v_3 (right) for all events.

the CME is much denser than the ambient solar wind. The drag acceleration has the form (Cargill *et al.*, 1996):

$$a_d = -\gamma(v - w)|v - w| \qquad (2)$$

where v is the velocity, w the solar wind speed and γ a parameter dependent on the geometry of the system and density.

For the investigation of the acceleration–velocity relationship we used events that were measured at least at 4 instants. Applying this criterion we were left with 4609 events from the whole sample of 5012 LASCO events. For the analysis we used the mean acceleration a, obtained from the 2nd degree polynomial fit, the mean velocity v_m from the linear fit and the velocity at the heliocentric distance of 3 solar radii ($R = 3$), v_3, obtained from the 2nd degree polynomial fit. In the case of v_3 the number of analysed events was 4463, because for some events the 2nd degree polynomial did not intercept the $R = 3$ level.

The dependence of the acceleration on the velocities v_m and v_3 is presented in Figure 1. In the next step, we divided the data in subsamples according to the mean distance and width. However, there is a crosstalk between these two parameters. To avoid that, the subsamples with different mean distances R_m were chosen to have the same average width W. To accomplish that, some of the events had to be dropped out: we successively excluded the CMEs of smallest/largest widths until the mean width in all subsamples became equal (e.g., $W = 60°$). A similar procedure was used for the subsamples with different widths excluding successively events with the smallest/largest values of R_m.
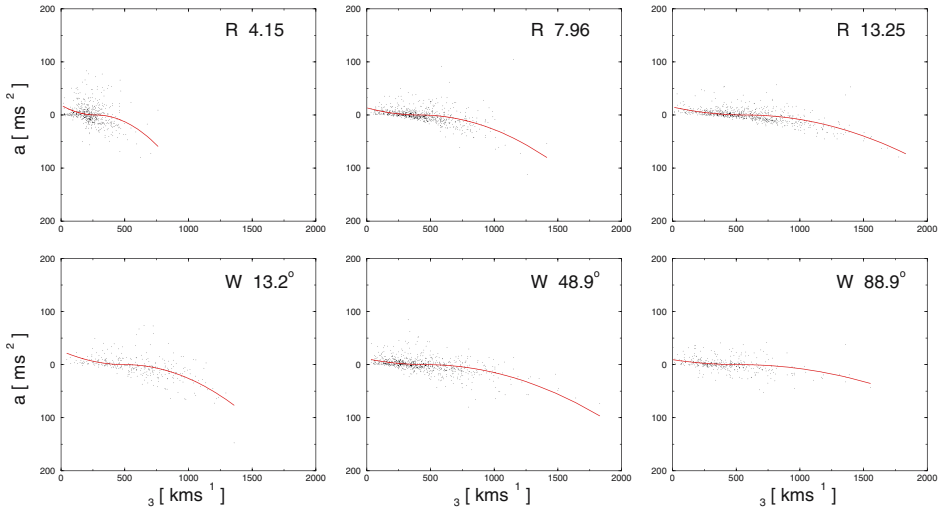
Figure 2.   The dependence of acceleration on the velocity v_3 for various mean distances (upper row, all subsamples have an average width $W = 60°$) and for various widths (lower row, all subsamples have the mean distance $R = 9$).

3. Results

The dependence of acceleration on the velocity v_3, where the mean distance and width are treated as parameters is shown in Figure 2. Solid lines are the least square fits of Equation (2).

The dependence of the obtained parameter γ on the distance R and the width W is presented in Figure 3. The solid lines are power law fits, which yield the dependence of γ on R and W: $\gamma = (2.2 \pm 1.4)R^{-(1.5\pm0.3)}$ and $\gamma = (0.4 \pm 0.2)W^{-(0.5\pm0.1)}$ where γ is expressed in $10^{-6}\,\text{km}^{-1}$.

In Figure 4a the obtained intercept with the x–axis, w_x, is presented as a function of the distance and is compared with the empirical solar wind speed obtained by Sheeley *et al.* (1997). In Figure 4b we present the parameter w_x versus W, showing no dependence (as expected).
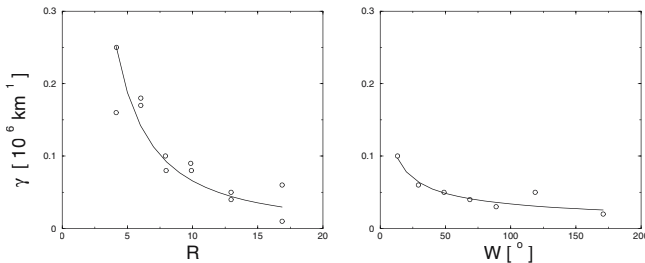
Figure 3.   The dependence of the obtained parameter γ on distance and width.
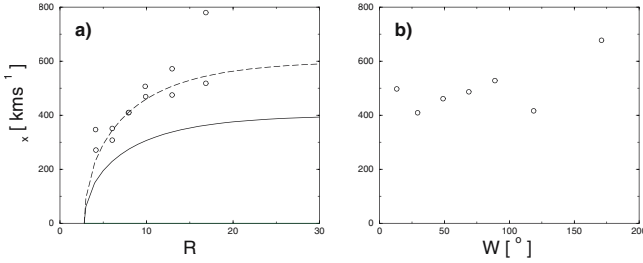
Figure 4. a) The dependence of the parameter w_x on distance compared with the Sheeley *et al.* (1997) model of wind speed with the asymptotic value v_∞=400 km s^{-1} (solid line) and v_∞=600 km s^{-1} (dashed line). b) The dependence of the parameter w_x on the width of the CME.

4. Discussion and conclusion

The results indicate that the parameter γ (and consequently the drag force acceleration) is decreasing with the distance and width of a CME. The decrease with the distance is in agreement with the results of Gopalswamy *et al.* (2000), Vršnak (2001) and Vršnak and Gopalswamy (2002). Since the parameter γ is proportional to the quantity $A\rho_e/M_{\mathrm{CME}}$, where A is the cross section, ρ_e the external density and M_{CME} the mass of the CME, our results indicate that this quantity is proportional to $W^{-\frac{1}{2}}$.

The obtained wind speed is rather high in comparison to the value of approximately 400 km s^{-1} obtained by Sheeley *et al.* (1997) for the asymptotic wind speed. However, those CMEs, having a considerable width could be affected by the fast solar wind. Another possibility is that the Lorentz force is still acting. From the differences of the obtained parameter w_x and the solar wind speed given by Sheeley *et al.* (1997) (i.e., from the shift of the curve upwards in the $a(v)$ graph), we estimate that the values of the acceleration due to the Lorentz force are in the order of 10 m s^{-2}.

The obtained results indicate that the dynamics of CMEs in the range from 3 to 30 solar radii is strongly affected by the magnetohydrodynamic drag.

References

Cargill, P.J., Chen, J., Spicer, D.S., Zalesak, S.T.: 1996, *J. Geophys. Res.* **101**, 4855.
Gopalswamy, N., Lara, A., Lepping, R.P., Kaiser, M.L., Berdichevsky, D., and St. Cyr, O.C.: 2000, *Geophys. Res. Lett.* **27**, 145.
Sheeley, N.R., Jr., et al.: 1997 *Astrophys. J.* **484**, 472.
Vršnak, B.: 2001, *Solar Phys.* **202**, 173.
Vršnak, B. and Gopalswamy, N.: 2002, *J. Geophys. Res.* **107**, 10.1029.

TIME EVOLUTION OF THE SPECTRAL INDEX IN SOLAR FLARES

P.C. GRIGIS, D. BUSER and A.O. BENZ
Institute for Astronomy, ETH Zurich, Switzerland

Abstract. We study RHESSI data for 14 impulsive M class flares which show a soft-hard-soft spectral evolution. The photon spectral index and the flux at a reference energy of 35 keV are in all cases anti-correlated. The data can be fitted by a simple empirical model of a power-law relation between the flux and the spectral index.

1. Introduction

Non-thermal hard X-ray emission during impulsive solar flares is highly variable, often showing activity peaks and dips with durations ranging from seconds up to several minutes. This behaviour can be observed in the largest X class flares as well as in smaller B and C class flares. It was early recognized (Parks and Winckler, 1969; Kane and Anderson, 1970) that the hardness of the photon spectrum can also change with time, and, furthermore, that there is a direct correlation between the hard X-ray flux and the spectral hardness. Since this implies that the flare spectrum starts soft, gets harder as the flux rises and softer again after the peak time, the term *soft-hard-soft* (SHS) was coined to describe this behaviour. Later observations of major flares (Benz, 1977; Brown & Loran 1985) confirmed the SHS pattern. However, flares were observed that systematically hardened with time (Frost and Dennis, 1971; Cliver *et al.*, 1986), thus showing a *soft-hard-harder* (SHH) pattern. The current wisdom seems to indicate that SHH flares represent gradual, long duration events. While it seems to be well established that impulsive flares have a SHS spectral dynamics, much less is known about the *quantitative* relation, if any exists, between the photon spectral index (noted γ) and the X-ray flux during the burst.

In this paper, we analyze RHESSI (Lin *et al.*, 2002) data for 14 M class flares that clearly show the SHS pattern, trying to get a quantitative understanding of this phenomenon. In order to be able to do this, we produce spectra of the flares with a high temporal cadence, and we fit a power law model to the non-thermal part.

2. Data reduction

We have chosen to limit our analysis to flares larger than GOES class M1
and smaller than X1. These have fairly large counts rates, but are not
too heavily affected by the pulse pileup problem. 176 M class flares were
reported in the RHESSI flare list in the period from 13 February 2002 to
31 November 2002 (status: April 2003). We additionally restricted ourselves
to the 79 flares with constant attenuator state of 1 (thin attenuator in) and
no front-segment decimation (Smith *et al.*, 2002). From this selection of 79
flares we dropped the ones which had no emission above the background
in the 25–50 keV band. In order to have enough data for meaningful time
series, we additionally required the peak in the 25–50 keV band being more
than 3 minutes away from any interruption in the data. We also dropped
the flares in which a particle precipitation event was happening during the
time of enhanced emission in the 25–50 keV band. These additional criteria
dropped the number of events to 32. For each event in the list, we generated
spectrograms with a time resolution of 2 seconds, which is approximately
one half of the RHESSI spin period, and an energy resolution of 1 keV.
The data were calibrated using the diagonal elements of the instrument
response matrix (thus we speak of *semi-calibrated data*). For simplicity, we
only fitted the non-thermal part of the emission in an energy range where
the non-thermal emission was clearly dominant over the thermal part. To
determine the suitable energy and time range for the fitting we computed
the derivative of the flux with respect to the energy dF/dE in all the
background-subtracted spectra, and computed the equivalent temperature
$T_{\text{eff}}(E)$ that an isothermal emission would need in order to produce the
measured dF/dE at the energy E. The *non-thermal-dominant* part of the
spectrum was then defined as the energy interval where $T_{\text{eff}} \geq 40$ MK,
and the fitting time interval as the interval in which the flare had a non-
thermal-dominant part. We identify this interval with the *impulsive* phase.
For 18 flares there was not any such interval, and therefore we discarded
these because their non-thermal emission was not strong enough to provide
good fits with the simple approach described above. A more complete and
detailed study, with fully calibrated data and careful fitting of the thermal
component, is underway (Grigis and Benz, 2004).

3. Results

The fitting procedure described above yielded 14 time series of spectral in-
dices with a duration varying from some tens of seconds to several minutes.
Our goal is to compare the spectral indices with the non-thermal flux. From
the simple analysis described above, there is no obvious way to find a value
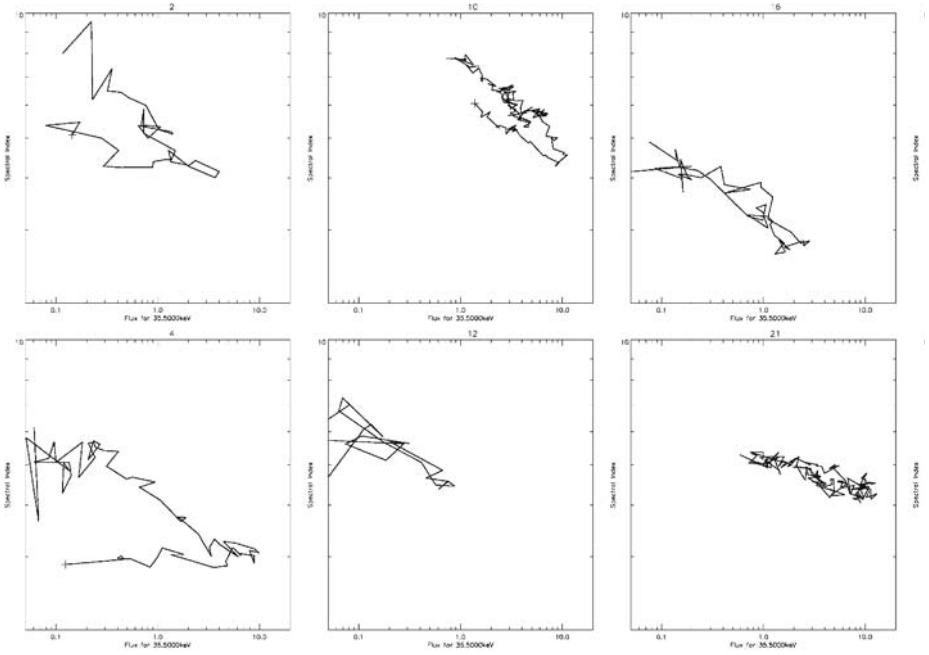
Figure 1. Plots of the fitted power-law index vs. photon flux at 35 keV for six flares.

for the low energy cutoff of the non-thermal part, and hence no way to compute the total non-thermal flux. Therefore we have chosen to compare the spectral index with the flux at some representative energy $E_{\rm rep}$. The choice of $E_{\rm rep}$ is arbitrary, but to provide a meaningful comparison we have chosen a value of $E_{\rm rep} = 35$ keV, which lies near the middle of the energy interval used for the fitting. The cross correlation coefficient of the spectral index $\gamma(t)$ and the flux at 35 keV $F_{35}(t)$ was found to be lower then zero for all flares at a confidence level of 95%. The average value is -0.69. Therefore, F_{35} and γ are clearly anti-correlated. A plot of $\log \gamma$ versus $\log F_{35}$ for each flare clearly show this anti-correlation trend (see Figure 1).

In some flares, there are several peaks in the lightcurve of the 25–50 keV band, lasting about 30 to 120 seconds. We analysed in detail two flares and we found that the SHS trend holds for each peak. If we assume that the SHS behaviour is a fundamental characteristic of the electron acceleration, we can interpret each peak as an *energy release fragment* (ERF), the whole flare being composed of one or more of this fragments. Thus the overall SHS behaviour of the flare is a direct consequence of the properties of the ERFs. The question arises, whether these ERFs are elementary, or can be decomposed in smaller substructures. To test for this, we filtered the data from the two flares mentioned above with a high-pass, and found that the

shortest structures which show anti-correlation of γ and F_{35} were of about 30 seconds duration.

The curves plotted in Fig. 1 follow mostly a rather simple path in the $\log \gamma$–$\log F_{35}$ diagram. As a first approximation, the path consists of two straight lines, the first going from the beginning of the flare to the peak and the second going from the peak to the end. The flares with many peaks show a more complicated structure, which can be ascribed to the SHS behaviour for each peak. A simple empirical model fitting the data for an ERF would therefore be: $\gamma \simeq A \cdot F_{35}^{-\alpha}$, where the parameter α can be different in the rise and decay phase, and A is a constant. We found for α values in the range 0.08–0.23, with an average of 0.151 and a median of 0.143.

4. Conclusions

The SHS pattern is found ubiquitously in impulsive solar flares as well as in subpeaks. RHESSI data are suitable to follow the quantitative evolution of the spectrum with good time cadence. The observed time evolution of the spectral index can be used to put constraints on theoretical electron acceleration models, which must be able to account for the SHS behaviour of the ERFs in a quantitative way. A detailed comparison of observations and models may be possible in the future going beyond the approximate power-law used here.

Acknowledgements

References

Benz, A.O.: 1977, *Astrophys. J.* **211**, 270.
Brown, J.C. and Loran, J. M.: 1985, *Mon. Not. Roy. Astr. Soc.* **212**, 245.
Cliver, E.W., Dennis, B.R., Kiplinger, A.L., et al.: 1986, *Astrophys. J.* **305**, 920.
Frost, K.J. and Dennis, B.R.: 1971, *Astrophys. J.* **165**, 655.
Grigis, P.C. and Benz, A.O.: 2004, in preparation.
Kane, S.R. and Anderson, K.A.: 1970, *Astrophys. J.* **162**, 1003.
Lin, R.P. and Schwartz, R.A.: 1986, *Astrophys. J.* **312**, 462.
Lin, R.P., Dennis, B.R., Hurford, G.J. *et al.*: 2002, *Solar Phys.* **210**, 3.
Parks, G.K. and Winckler, J.R.: 1969, *Astrophys. J.* **155**, 117.
Smith, D.M., Lin, R.P., Turin, P. *et al.*: 2002, *Solar Phys.* **210**, 33.

ANALYSIS OF DOPPLER SHIFTS OF SPECTRAL LINES OBTAINED BY THE CDS/SOHO INSTRUMENT

P. GÖMÖRY, J. RYBÁK and A. KUČERA
Astronomical Institute, Slovak Academy of Sciences
05960 Tatranská Lomnica, Slovakia

W. CURDT
Max-Planck-Institut für Aeronomie
37191 Katlenburg-Lindau, Germany

H. WÖHL
Kiepenheuer-Institut für Sonnenphysik
79104 Freiburg, Germany

Abstract. SOHO/CDS measurements of the quiet Sun chromospheric He I 584.33 Å and transition region O V 629.73 Å spectral lines are used to study the ability of the CDS instrument to detect Doppler shifts of spectral lines in the supergranular network and internetwork using short exposures. A precise analysis revealed that the CDS instrument is not suitable for the detection of mass motion in the internetwork, but in contrast, it is capable for such a detection in the network.

1. Introduction

The launch of SOHO in 1995 brought new opportunities to study small-scale and short-time dynamical events. Explosive events were confirmed by the SUMER spectrometer (Innes *et al.*, 1997) and new types of eruptive events have been also revealed, e.g., blinkers by CDS (Harrison, 1997) and bright points by EIT (Zhang *et al.*, 2001). Now it is aimed to identify all these different types of eruptive events by the same instrument and to describe their dynamics. For this reason it is necessary to obtain not only information about line intensities but also information about Doppler shifts of spectral lines and their absolute calibration. In this contribution it is investigated whether data obtained by the CDS instrument are suitable for such a task.

Emission spectral lines of He I 584.33 Å (2.0×10^4 K) and O V 629.73 Å (2.5×10^5 K) were observed in the quiet Sun supergranular network and
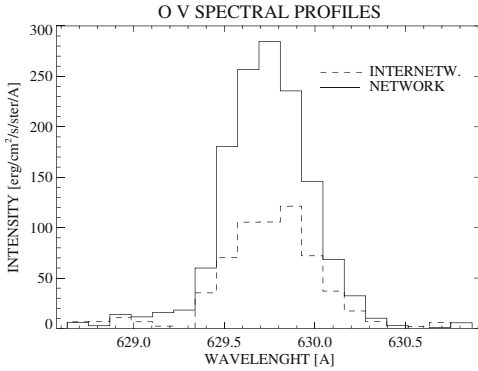
Figure 1. The characteristic spectral profiles of the O v 629.73 Å spectral line of the quiet Sun internetwork (dashed line) and network (solid line) obtained with an exposure time of 5 s.

internetwork near disk center between 23:25 UT and 23:53 UT on May 14, 1998 by the CDS/NIS instrument (Harrison, 1995) using a 'sit-and-stare' observational mode. 190 spectral images were obtained using the $2'' \times 240''$ slit with an exposure time of 5 s and with a cadence of 9.1 s. The spectra were corrected for the instrumental features of the CDS/NIS instrument[1] and converted to the physical units: intensity to $\mathrm{erg\,cm^{-2}\,s^{-1}\,sr^{-1}\,\mathring{A}^{-1}}$ and the Doppler shifts to $\mathrm{km\,s^{-1}}$. The characteristic O v spectral profiles of the internetwork and network are displayed in Figure 1. A single Gaussian profile with linear background was fitted to each spectral profile using relative weights of the data.[2] The wavelength scales were adjusted using the mean redshift of the transition region lines (Peter and Judge, 1999) and their laboratory wavelengths (Macpherson and Jordan, 1999). The resulting 2D maps of O v line intensities and Doppler shifts are given in Figure 2.

2. Results

The absolute calibration of Doppler shifts of spectral lines is very important for identification of the different small-scale eruptive events. Therefore, the mean spectral profiles for network ($5'' \times 190$ exposures) and for internetwork ($7'' \times 190$ exposures) of the He I and O v spectral lines were calculated as the first order approximation. The Doppler shifts of these mean spectral profiles showed that the internetwork (He I $= 5.64 \pm 3.6$ km/s; O v $= 12.3 \pm 4.7$ km/s) is more red-shifted than the network (He I $= 4.62 \pm 2.1$ km/s; O v $= 10.9 \pm 3.2$ km/s). After a careful inspection it was found that

---

[1] Details: `http://solg2.bnsc.rl.ac.uk/software/uguide/uguide.shtml`

[2] CDS Software Note no. 47: `http://orpheus.nascom.nasa.gov/cds/software_notes.html`
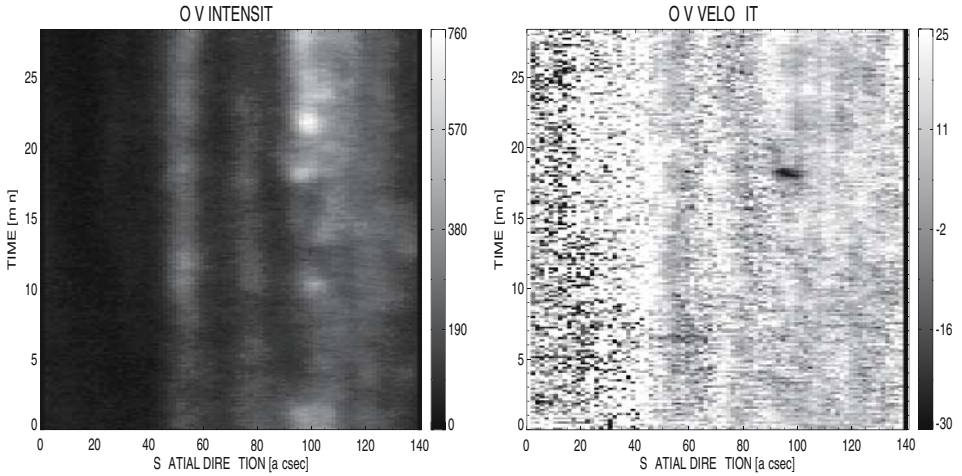
Figure 2. 2D space-time maps of the O V line intensities and the Doppler shifts. The horizontal axis describes spatial direction and the vertical axis describes time. The solar rotation was not compensated, so the vertical axis presents also the spatial extent of the observed solar features. Internetwork area was selected in the area between 62″ and 69″ and network area between 111″ and 116″. Intensities are given in $erg\,cm^{-2}\,s^{-1}\,sr^{-1}\,\text{Å}^{-1}$ and the Doppler shifts in $km\,s^{-1}$. Positive values of the Doppler shifts are toward the solar surface and negative values toward the observer.

this contradictory result is probably caused by weak and noisy spectral profiles, which were included into the averaging. Therefore we estimated the average network Doppler shift errors, which were found to be $\pm2.1\,km/s$ for He I and $\pm3.2\,km/s$ for O V lines respectively. Only the spectral profiles which had smaller errors of the Doppler shifts then the average network Doppler shift errors were selected from the whole data set for averaging. However there were no data with such small errors of the Doppler shift in the internetwork. The dependence of the relative cumulative number of exposures from internetwork and network on the Doppler shift errors for the O V line was constructed (Figure 3, left panel) in order to confirm our idea. Values of the Doppler shifts of O V line in the internetwork and network as a function of the Doppler shifts errors are also shown (Figure 3, right panel). When only spectral data of very small error of the Doppler shift (only few in the internetwork) were used then the network was more red-shifted than the internetwork. Very similar results were obtained also for the He I spectral line. The effect of binning was also studied to obtain more data with small error of the Doppler shift in the internetwork. In particular, binning of area $6.7'' \times 10\,s$ (4 pixels along the slit $\times$ 2 exposures) was made, but the number of applicable spectral profiles has not increased substantially.
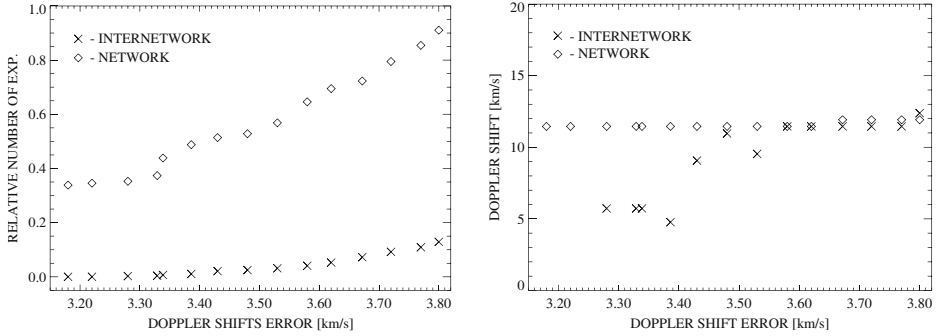
Figure 3.   Left panel: Relative cumulative number of exposures from the internetwork
and network as a function of the Doppler shift errors of O v line. Right panel: Doppler
shifts of the O v spectral line in the internetwork and in the network as a function of the
Doppler shifts errors.

3.   Conclusions

Very short exposure times (less than 10 s) are not suitable for detection of
dynamics of internetwork dynamical events in the quiet Sun by the CDS
instrument because of low S/N ratio even in the most prominent spectral
lines. Nevertheless the Doppler shifts of spectral lines obtained from the
supergranular network are adequate for the identification of small-scale
eruptive events (Gömöry *et al.*, 2003).

Acknowledgements

References

Gömöry, P., Rybák, J., Kučera, A., Curdt, W., and Wöhl, H.: 2003, *Hvar Obs. Bull.* **27**,
    67.
Harrison, R.A., and the CDS team: 1995, *Solar Phys.* **162**, 233.
Harrison, R.A.: 1997, *Solar Phys.* **175**, 467.
Innes, D.E., Brekke, P., Germerott, D., and Wilhelm, K.: 1997, *Solar Phys.* **175**, 341.
Macpherson, K.P. and Jordan, C.: 1999, *MNRAS* **308**, 510.
Peter, H. and Judge, P.G.: 1999, *Astrophys. J.* **522**, 1148.
Zhang, J., Kundu, M.R., and White, S.M.: 2001, *Solar Phys.* **198**, 347.

ON THE BEHAVIOUR OF A BLINKER IN CHROMOSPHERIC AND TRANSITION REGION LAYERS

F. TOMASZ, J. RYBÁK and A. KUČERA
Astronomical Institute, Slovak Academy of Sciences
SK-05960, Tatranská Lomnica, Slovakia

W. CURDT
Max-Planck-Institut für Aeronomie, Max-Planck-Straße 2
D-37191 Katlenburg-Lindau, Germany

H. WÖHL
Kiepenheuer-Institut für Sonnenphysik, Schöneckstraße 6
D-79104, Freiburg, Germany

Abstract. Analysis of a blinker, observed with the SUMER/SOHO spectrometer in the C II 1036.34 Å, C II 1037.01 Å, O VI 1037.61 Å lines and in C I continuum, is presented. We find that the blinker is highly pronounced in both the chromosphere and transition region. Intensities of chromospheric and transition region lines behave similarly although the blinker is more pronounced in the upper transition region.

1. Introduction

Since the late 80-ties the variability of the upper solar atmosphere has been studied on temporal scales of minutes and spatial scales of few arc-seconds using various instruments (e.g., Brueckner and Bartoe, 1983; Dere *et al.*, 1984; Innes *et al.*, 1997; Harrison, 1997; Bewsher *et al.*, 2002; Parnell *et al.*, 2002). Harrison (1997) reported on blinkers to describe EUV brightenings in the quiet Sun transition region. The blinkers were most apparent in the transition region O II 599 Å, O IV 554 Å and O V 629 Å lines and no relevant brightenings in coronal Mg IX 368 Å and Mg X 624 Å lines were detected. Brković *et al.* (2001) found significant flux enhancements in the He I 584 Å lines as well. Bi-directional jets, a non-typical feature of blinkers, were also observed in a particular blinker (Tomasz *et al.*, 2003). An investigation of the response of the chromospheric and the coronal layers to this blinker using TRACE Ly α and Fe IX filtergrams and SUMER H I Ly β spectra showed significant chromospheric effects of the blinker but
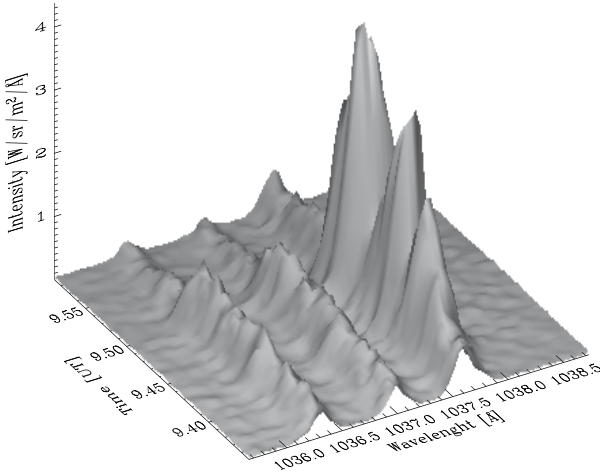
Figure 1.   Time evolution of the spectral profiles of C II and O VI lines during the blinker.

no emission of the coronal plasma was detected (Tomasz *et al.*, 2004). The goal of this paper is to investigate the response of the chromosphere and the lower/upper transition region to this particular blinker using C I continuum, two C II and one O VI lines.

2.   Observations and data analysis

Spectral profiles of C II 1036.34 Å (CII1) and C II 1037.01 Å (CII2) (3×10^4 K) as well as O VI 1037.61 Å (3×10^5 K) lines were acquired on May 5, 1999, using the SUMER/SOHO spectrometer (Wilhelm *et al.*, 1995). In almost 5 hours 1200 spectra were taken using the $0.3'' \times 120''$ slit with an exposure time of 14.25 s. Compensation of the solar rotation was applied in order to track the target on the surface. Standard instrumental corrections were applied to the data. Each spectrum was fitted by a triple Gaussian. The line intensity, the Gaussian width and the Doppler shift of all three lines were calculated after subtraction of the underlying continuum intensity. The most pronounced transient event in the internetwork – identified as blinker (Tomasz *et al.*, 2003) – was selected for this study.

3.   Results

Three enhancements of the O VI intensity are observed during the entire evolution of the blinker (Fig. 1). They appeared due to 'jumping' of the spectrograph slit for $0.38''$ correcting for solar rotation (Tomasz *et al.*, 2003). Line intensities increased gradually only in the C II lines but remarkably in the O VI line. The smallest peak appears at the beginning of
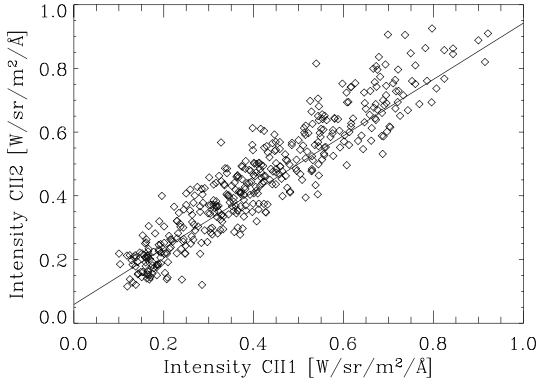
Figure 2. Scatter-plot of the C II line intensities during the blinker. The solid line shows the linear least-square fit to the data.

the blinker, the intermediate peak reveals a more complicated structure with three small intensity decreases in the O VI line. The third peak is the highest one, which falls off rapidly at the end of the blinker.

The dependence of intensities CII1 on CII2 lines during the blinker tends to be linear (Fig. 2). Deviations from linearity increase with increasing line intensities as their uncertainties grow by the square root of the intensities. A linear trend is expected because both lines are emitted from the identical excited level of the same ion. Thus, hereafter only the C II 1037.02 Å line was used for our analysis. Dependencies of the C II line intensity and the C I continuum intensity on the O VI line intensity during the blinker are shown in Fig. 3. Both dependencies are not linear within the whole range of the measured values: for small values of the O VI line intensity a rapid increase of the C II line intensity was detected; for higher values of the O VI line intensity ($\geq 1\,\mathrm{W/sr/m^2/Å}$) only a weak relation was found with few particular pixels for which saturation was deduced; the relation of the C I continuum intensity to the O VI line intensity seems to be more linear but large scatter as well as signatures of saturation for high O VI line intensities were found.

4. Conclusions

Signatures of a blinker were observed in the chromosphere and as well in the lower and upper transition region. The increase of the line intensities was found to be higher in the upper (O VI) than in the lower (C II) transition region, and these increases seem to appear simultaneously. This is in agreement with the results of Brković and Peter (2003). A small but clear increase was also detected in the chromospheric emission (C I continuum) during the
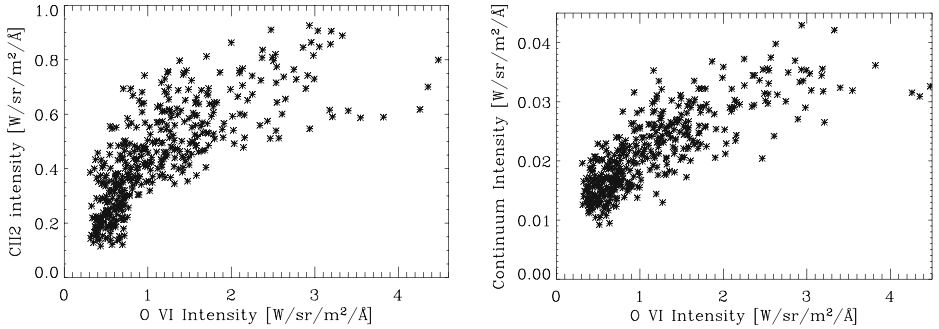
Figure 3.　　Dependencies of the C II 1037.02 Å line intensity (left panel) and the C I continuum intensity (right panel) on the O VI line intensity during the blinker.

blinker. Therefore it can be concluded that an inter-relationship between the upper and the lower transition region and the chromospheric plasmas exists during (this particular) blinker. However, the relations between the studied parameters do not seem to be linear.

5. Acknowledgments

References

Bewsher, D., Parnell, C. E., and Harrison, R. A.: 2002, *Solar Phys.* **206**, 21.
Brković, A. and Peter, H.: 2003, *Astron. Astrophys.* **406**, 363.
Brković, A., Solanki, S. K., and Rüedi, I.: 2001, *Astron. Astrophys.* **373**, 1056.
Brueckner, G. E. and Bartoe, J.-D. F.: 1983, *Astrophys. J.* **272**, 329.
Dere, K. P., Bartoe, J.-D. F., and Brueckner, G. E.: 1984, *Astrophys. J.* **281**, 870.
Innes, D. E., Inhester, B., Axford, W. I., and Wilhelm, K.: 1997, *Nature* **386**, 811.
Harrison, R. A.: 1997, *Solar Phys.* **175**, 467.
Parnell, C. E., Bewsher, D., and Harrison, R. A.: 2002, *Solar Phys.* **206**, 249.
Tomasz, F., Rybák, J., Kučera, A., Curdt, W., and Wöhl, H.: 2003, *Hvar Obs. Bull.* **27**, 75.
Tomasz, F., Rybák, J., Kučera, A., Curdt, W., and Wöhl, H.: 2004, in H. Lacoste (ed.), *Waves, Oscillations and Small Scale Transient Events in the Solar Atmosphere: A Joint View of SOHO and TRACE*, ESA SP-547, 307.
Wilhelm, K., and the SUMER team: 1995, *Solar Phys.* **162**, 189.

ON THE 24- AND 155-DAY PERIODICITY OBSERVED IN SOLAR Hα FLARES

M. TEMMER, A. VERONIG and A. HANSLMEIER

Institute for Geophysics, Astrophysics and Meteorology,
University of Graz, Universitätsplatz 5, A-8010 Graz, Austria

Abstract. We analyze daily numbers of solar Hα flares with regard to their periodical occurrences related to rotational modulations ($\sim20^d$–30^d) and the so-called "activity" periods ($\sim150^d$–160^d). We focus on the separate analysis of the northern and southern solar hemisphere as well as on an energy dependence of the flare events. Our findings suggest that the appearance of the "activity" periods might result due to superposition of two predominant periods of $\sim24^d$ and $\sim28^d$.

1. Introduction

The most striking variation in the analysis of solar activity indices is the 27-day[1] period according to the solar differential rotation. However, when the two hemispheres are studied separately, an asymmetric behavior with slightly differing predominant periods is obtained, namely ~27 days for the northern and ~28 days for the southern hemisphere, respectively (Temmer, Veronig, and Hanslmeier, 2002, and references therein). The investigation of Hα flare occurrences reveals similar results. Furthermore, for high-energetic flare events a ~24-day period for both hemispheres is revealed (Temmer *et al.*, 2003) that was also seen in hard X-ray flares (Bai, 1987). Another striking period in the occurrence rate of major solar flares is within the range of ~150–160 days, first discovered by Rieger *et al.* (1984) for γ-ray events and thereafter confirmed by many authors for various solar flare observations. However, the origin of this period is still unclear (cf. Bai, 2003).

The findings of predominant occurrence rates of 24 and 28 days led to the idea that the ~150–160 day period is due to wave superposition (Bai and Sturrock, 1987): interacting "hotspots" rotating with different rates of $\sim24^d$ and $\sim28^d$ align with one another about every 150–160th day. Here

---

[1] All periods stated in this paper are synodic.

we revisit this hypothesis by means of wavelet analysis which allows us to track the occurrence of predominant periods in time.

2. Data and Methods

Daily occurrence rates of flare events are derived from the Hα flare compilation in the Solar Geophysical Data covering the time span 1955–2002. The analysis is performed separately for the northern and southern hemisphere, as well as separately for all (i.e. covering importance classes 1 to 4 as well as subflares, denoted as S–4) and high-energetic (covering only importance classes 1 to 4, denoted as 1–4) Hα flare events. Because of the inadequate importance classification of flares before 1975 the distinctive analysis for high-energetic events can be done exclusively for the years 1975–2002.

The superposition of two waves with different periods, P_1 and P_2, produces beat phenomena where the period of the variation of the envelope amplitude, P_3, is given by

$$\frac{1}{P_3} = \frac{1}{P_1} - \frac{1}{P_2}. \tag{1}$$

The wavelet transform is used to examine simultaneous occurrences of possible couples of periods in the range from ~24–28 days that might produce beat phenomena with ~150–160 days.

All wavelet power spectra presented in this paper are calculated for the period range from 20–200 days with the "Morlet" wavelet as the analyzing wavelet. As significance tests confidence levels at 90% and 95% are applied. The background spectrum is modeled with red noise. Regions where edge effects become apparent due to dealing with finite-length time series, such as the beginning and the end of the wavelet spectrum, are labeled as cone of influence (COI). The computation of all these parameters is performed in the way described by Torrence and Compo (1998).

3. Results

Fig. 1 shows sample wavelet power spectra where the principle of superposition with simultaneous appearance of $\sim24^d$, $\sim28^d$, and $\sim155^d$ periods is confirmed. The clearest results are found for cycles 20 and 21. Southern events reveal a higher significance of the resulting periods than the northern. For the northern hemisphere better outcomes are obtained considering only high-energetic events, i.e. excluding subflares from the analysis.

Exceptions from the principle of superposition are found for both hemispheres during cycles 19, 22, and 23 showing ~24- and ~28-day periods but none with ~150–160 days. It is worth noting that during these times distinct
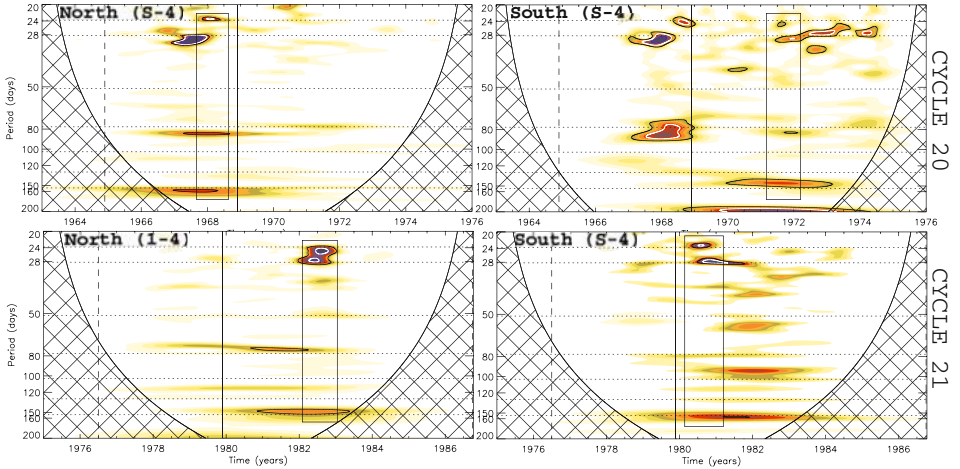
Figure 1. Wavelet power spectra derived from daily Hα flare numbers. Note that the *y*-axis has a logarithmic scale. Grey-scale coding from white to black represents the square root of power on a linear scale. Dashed/solid vertical lines indicate the solar cycle minima/maxima. Black/white contour lines denote the confidence levels at 90%/95%. COIs are given as cross hatched lines. Dotted horizontal lines mark periods of 24, 28, and 155 days, as well as the 2nd to 5th subharmonic of the fundamental period of 25.5 days according to Bai and Sturrock (1993).

periods in the range from 50–100 days are revealed, too, whereas during solar cycles 20 and 21 the decisive periods of ~24, ~28, and ~155 days are most prominent. In general, the periods are intermittent and observed around the solar cycle maxima ($-1.5 \lesssim \max. \lesssim +2.5$ years). The $\sim24^{d}$, $\sim28^{d}$, and $\sim155^{d}$ periods are apparent at different times, i.e. independently, for the northern and southern hemisphere.

Furthermore, it has to be stressed that the produce of beat phenomena within a range of 150–160 days is highly sensitive on the exact value of the causing periods (changes of $\pm0.3^{d}$ in P_1 or P_2 cause changes of $\pm10^{d}$ in P_3, cf. Fig. 1).

4. Discussion and Conclusions

Flares occur preferentially in association with active regions which are subject to the solar differential rotation. In the frame of the anchoring hypothesis, new-born spots represent deeper and thus faster rotating layers (see, e.g., Balthasar, Schüssler, and Wöhl, 1982). Therefore, not only the 28- but also the 24-day period might be related to the rotation of active regions, whereas the ~155-day period is produced by superposition of these two rotational periods. Alternatively, the 24-day period might be related to periodical occurrences of new magnetic flux (see Temmer *et al.*, 2004).

For the rising phase of solar cycle 23, Zięba *et al.* (2001) found in sunspot relative numbers periods of 23.8, 28, and 156 days (after the removal of strong periods in the original data).

A different hypothesis for the 155-day period (Bai and Sturrock, 1993) is that the period of 25.5 days is the fundamental period of an obliquely rotating magnetic pattern with a 153-day period as a subharmonic ($6 \times 25.5^d = 153^d$). However, subharmonics of and the fundamental period of 25.5 days itself were not found simultaneously with the $\sim$153-day period (cf. Fig. 1). Krivova and Solanki (2002) suggested that a 156-day period could be the third harmonic of the 1.3-year periodicity found in helioseismic observations ($3 \times 156^d = 1.28$ years) acting near the bottom of the solar convection zone. Furthermore, they found a high correlation with the strength of the sunspot cycle and concluded that the $\sim$1.3-year period is a harmonic of the 11-year solar cycle itself.

We suggest that the superposition of two predominant periodical occurrence rates in the range of $\sim$24 and $\sim$28 days might produce beat phenomena resulting in periods within $\sim$150–160 days. This principle works if the $\sim$24- and $\sim$28-day occurrence rates of flares operate simultaneously without strong intermediate periods in the range $\sim$50–100 days which may destroy a straight superposition.

Acknowledgements

References

Bai, T.: 1987, *Astrophys. J.* **314**, 795.
Bai, T.: 2003, *Astrophys. J.* **591**, 406.
Bai, T. and Sturrock, P.A.: 1987, *Nature* **327**, 601.
Bai, T. and Sturrock, P.A.: 1993, *Astrophys. J.* **409**, 476.
Balthasar, H., Schüssler, M., and Wöhl, H.: 1982, *Solar Phys.* **76**, 21.
Krivova, N.A. and Solanki, S.: 2002, *Astron. Astrophys.* **394**, 701.
Rieger, E.: 1984, *Nature* **312**, 623.
Temmer, M., Veronig, A., and Hanslmeier, A.: 2002, *Astron. Astrophys.* **390**, 707.
Temmer, M., Veronig, A., Rybák, J., and Hanslmeier, A.: 2003, *Hvar Obs. Bull.* **27**, 59.
Temmer, M., Veronig, A., Rybák, J., Brajša, R., and Hanslmeier, A.: 2004, *Solar Phys.*, in press.
Torrence, C. and Compo, G.P.: 1998, *Bull. Am. Meteorol. Soc.* **79**, 61.
Zięba, S., Masłowski, J., Michalec, A., and Kułak, A.: 2001, *Astron. Astrophys.* **377**, 297.

HE-D$_3$ POLARIZATION OBSERVED IN PROMINENCES

R. RAMELLI and M. BIANDA
Istituto Ricerche Solari Locarno (IRSOL)
6605 Locarno Monti, Switzerland

Abstract. Spectro-polarimetric measurements of the D$_3$-He I 5876 Å line profile in 35 prominences have been performed in 2003 with the Gregory-Coudé Telescope in Locarno. Two different experimental techniques (ZIMPOL and beam exchange method) have been successfully employed to determine all four Stokes components. Both give compatible results. The preliminary results as well as the measurement techniques are reported.

1. Introduction

The understanding of prominence formation is strongly connected with the knowledge of the magnetic fields responsible for their support. Polarimetric observations of the emission lines in prominences allow to study the structure and intensity of their magnetic fields through the Hanle and the Zeeman effect. After the extensive measurements of Athay *et al.* (1983) and Leroy *et al.* (1984), in the last two decades the observational activity in this domain was rather poor. On the other hand the progress in the instrumentation improved remarkably the polarimetric sensitivities that can now be achieved. Recently, new polarimetric observations of few prominences were reported (e.g. Paletou *et al.*, 2001; Wiehr and Bianda, 2003). In the present work we proceed to a more extended observational program.

2. Observations

The evacuated Gregory-Coudé telescope which is used at IRSOL (Istituto Ricerche Solari Locarno), has the advantage to introduce small instrumental polarization and cross-talks (Sanchez *et al.*, 1991). Both are generated mainly from two off-axis flat mirrors, whose effects theoretically cancel out around the equinox. Otherwise they increase almost linearly with declination and stay almost constant over one day of solar observations. At solstice the total instrumental linear polarization reaches almost 3% and the circular polarization is smaller than 1%.

19 prominences were observed from 24th March to 24th April 2003 using the beam exchange technique proposed by Semel *et al.* (1993). This technique allows a measurement free from effects introduced by the detector gain table. The data reduction technique and the instrumental set-up are described by Bianda *et al.* (1998). For each prominence we took various sets of measurements at different locations and times. Each set included typically about 20 exposures of 5 seconds each on a fixed position on the prominences, from which all four Stokes components were extracted.

A second observation series was performed using the Zurich Imaging Polarimeter ZIMPOL II (Stenflo *et al.*, 1992; Povel, 1995; Gandorfer and Povel, 1997; Gandorfer, 1999), which allows to get polarization measurements free from seeing effects. 16 prominences were observed from 22nd May to 26th September 2003. The image was rotated with a Dove prism set after the analyzer in order to keep the limb parallel to the spectrograph slit. Various sets of measurements were taken at different locations. Each set included typically 100 images of 10 seconds exposure each.

In both observing techniques additional measurements were regularly performed for calibration purposes. The light originating at the center of the solar disc was assumed to be unpolarized and therefore used as reference to establish the correction for the instrumental polarization. The background intensity profile was determined observing a quiet region of the halo near the prominence. We sometimes measured a nonzero polarization in the background light in a particular region (NE) above the solar limb (values up to 7%). This is believed to come from spurious reflections within the telescope. The full Stokes vector of the background light was therefore subtracted from the total measured Stokes vector.

In order to account for the cross-talk from the linear polarization to the circular polarization (values up to about 18% at solstice) measurements were performed applying a linear polarization filter in different positions before the entrance window of the telescope. The cross-talk from the circular to the linear polarization was not taken into account since it was expected to be negligible.

3. Results

An example of the four Stokes spectral images resulting from the measurement of one prominence with the ZIMPOL II system is shown in Fig. 1 (left panel). In this preliminary analysis we look at the spectro-polarimetric profiles obtained integrating over the spatial region where the signal intensity is at least 50% of the maximum intensity. The profiles of Stokes Q, U and V divided by I_{max} (the maximum of the intensity profile) are shown in the right panel of Fig. 1. Two resolved multiplet components can be observed: a
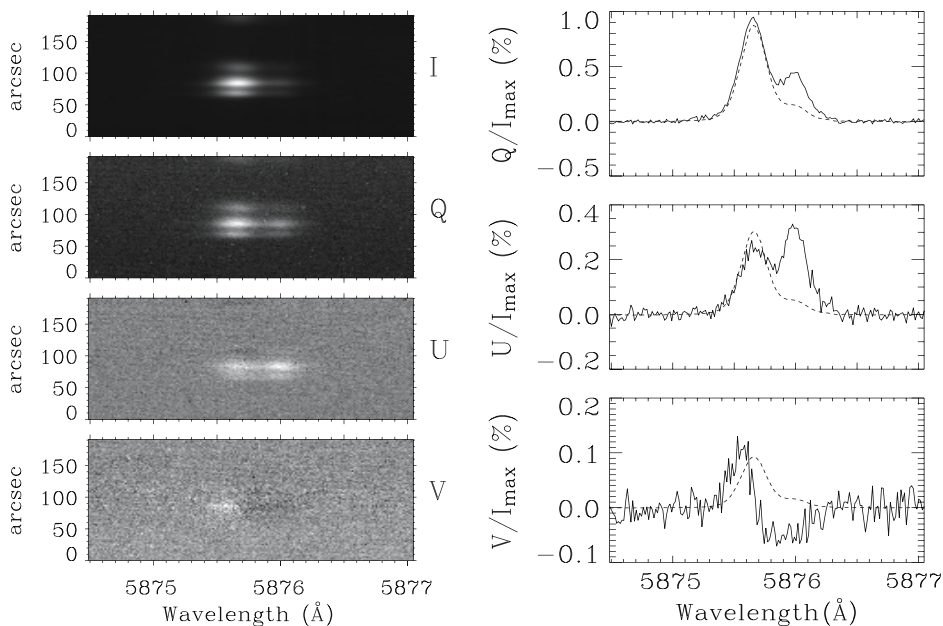
Figure 1.   Left: Example of spectral images of the four Stokes parameters (obtained with the ZIMPOL II system on 23rd May 2003). Right: Polarization profiles obtained from the same images integrating the spatial region where the intensity signal is larger than half the maximum. Stokes Q, U and V divided by the maximum of the intensity profile I_{max} are plotted. The scaled intensity profile is shown by a dashed line.

strong blue component at 5875.6 Å and a faint red component at 5875.97 Å. To analyze the behavior of the two components we average the value of the relative polarization in the intervals 5875.5–5875.7 Å and 5875.9–5876.0 Å, respectively. It is found that usually Q/I is about a factor of two larger in the faint component than in the strong component, as can be seen in the left panel of Fig. 2. In the right panel we show the Hanle diagram for the strong component, where the total linear polarization versus the rotation angle $\alpha = \arctan(U/Q)$ is plotted. The results obtained with the two techniques for different prominences are similar.

4.   Conclusions

The instrumentation at IRSOL and the two techniques used allowed precise measurements of the profiles of all four Stokes components in the HeI-D$_3$ emission line of 35 prominences. Q/I was found to be always positive with values up to 7% in the faint red multiplet component and up to 3% in the blue component. The absolute values of U/I and V/I were generally below 2% and 0.5%, respectively.
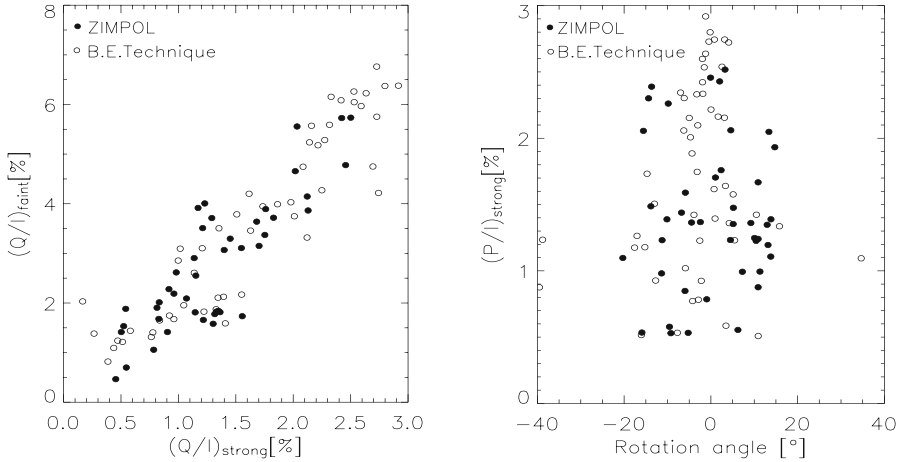
Figure 2. Left: Scatter plot representing Stokes Q/I measured in the faint red component of the D$_3$ multiplet versus Stokes Q/I measured in the strong blue component. Right: Hanle diagram showing the total linear polarization versus the rotation angle $\alpha = \arctan(U/Q)$ for the strong blue component.

Acknowledgements

References

Athay, R.G., Querfeld, C.W., Smartt, R.N., Landi Degl'Innocenti, E., and Bommier, V.: 1983, *Solar Phys.* **89**, 3.
Bianda, M., Solanki, S.K., and Stenflo, J.O.: 1998, *Astron. Astrophys.* **331**, 760.
Gandorfer, A.: 1999, *Opt. Eng.* **38**, 1402.
Gandorfer, A. and Povel, H.P.: 1997, *Astron. Astrophys.* **328**, 381.
Leroy, J.L., Bommier, V., and Sahal.-Bréchot, S.: 1984, *Astron. Astrophys.* **131**, 33.
Paletou, F., López Ariste, A., Bommier, V., and Semel, M.: 2001, *Astron. Astrophys.* **375**, L39.
Povel, H.P.: 1995, *Opt. Eng.* **34**, 1870.
Sanchez Almeida, J., Martínez Pillet, V., and Wittmann A.D.: 1991, *Solar Phys.* **134**, 1.
Semel, M., Donati, J.-F., and Rees, D.E.: 1993, *Astron. Astrophys.* **278**, 231.
Stenflo, J.O., Keller, C.U., and Povel, H.P.: 1992, LEST Foundation Technical Report No. **54**, Univ. Oslo.
Wiehr, E. and Bianda, M.: 2003, *Astron. Astrophys.* **404**, L25.

LINE-OF-SIGHT VELOCITY AND MAGNETIC FIELD IN SUNSPOT PENUMBRAE

D.V. MAKARCHIK and N.I. KOBANOV
Institute of Solar-Terrestrial Physics
Irkutsk, P.O. Box. 4026, Russia

Abstract. As it is well known, sunspots contain both vertical and horizontal strong magnetic fields. We are interested in the line-of-sight velocity structures in sunspots, with emphasis on penumbral motions. There are two types of regular motion of the solar plasma in the sunspot penumbra, namely the Evershed effect and oscillations. We were successful in the identification of a relation between some oscillatory modes of the line-of-sight velocity (8–10, 12–15, 20–30 min) and Evershed flows.

1. Introduction

Shine *et al.* (1994) and Rimmele (1995) found that Evershed flows experience quasi-periodic variations with a period of 12–15 min. Initially we used the differential method to extract the oscillations associated with Evershed flows (Kobanov and Makarchik, 2002b). A comparative analysis made for several tens of time series for the period 1999–2001 showed that photospheric and chromospheric line-of-sight velocity oscillations in the range of Evershed flows have much in common. It is possible to identify three groups of most frequently occurring periods: 20–30, 12–15 and 8–10 min. These are the periods which are the main candidates for the connection with Evershed flows. In 2002 our observations were confirmed and supplemented by data obtained by the modulationless method (Kobanov and Makarchik, 2002a). The chief merit of this method is that both velocity and magnetic field strength can be obtained simultaneously — in one exposure.

2. Observations and results

The observations were carried out at the telescope AST of the Sayan Observatory. We concentrated our attention on a motion pattern at the sunspots penumbrae and, in particular, on the Evershed motions. For this purpose, during the observations the spectrograph slit crossed the sunspots through
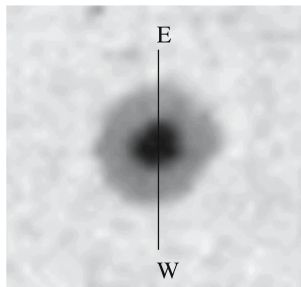
Figure 1.   Continuum image of a sunspot. The dark line shows the orientation of the spectrograph slit.

the umbra center in the line of East-West (Fig. 1). In 2002 two kinds of observations (applying the modulationless method) were obtained: time series in the sunspots (e.g. Fig. 2) and scans through the active regions (e.g. Fig. 3). In that way temporary and spatial distributions of the line-of-sight velocity and longitudinal magnetic field strength were considered. For the photospheric observations the Fe I 6569 Å line with Landé factor 1.375 was used, for the chromospheric observations the Hα line. As a rule, we selected for our observations large regularly shaped sunspots with a well-developed umbra and penumbra.

Despite the rather low spatial resolution of our data $(2-3'')$ we succeeded in detecting temporary variations of the Evershed velocities. A stable phase connection between photospheric and chromospheric oscillations is most frequently identified in the group of periods of 20–35 min. Oscillations from this group of periods have sometimes a totally identical phase at both height levels. We did not detect any instrumental effects that are responsible for the observed oscillations. It can be suggested that these variations are caused by the following factors: directly by changes of the flow velocity value, and by changes of the inclination angle between the flow direction and the line of sight. The latter factor seems preferable in the light of what we know of torsional sunspot vibrations (Gopasyuk, 1984; Pevtsov, 1992).

Furthermore, we investigated the line-of-sight velocity oscillations in the sunspot NOAA 0051 (from July 27 to August 06, 2003). The data obtained in this study provide evidence for the existence of running umbral waves in the chromosphere (Kobanov and Makarchik, 2004). These waves have a period of 2.8 min and propagate from the sunspot center outward with a phase velocity of 45–60 km s^{-1} and a line-of-sight velocity amplitude of about 2 km s^{-1}. In most cases the waves terminate rather abruptly on the umbra boundary and show no direct linkage with running penumbral waves. The spatial coherence of the waves at the umbra center is no more than $2''$. At the photospheric level there are clearly pronounced periodic
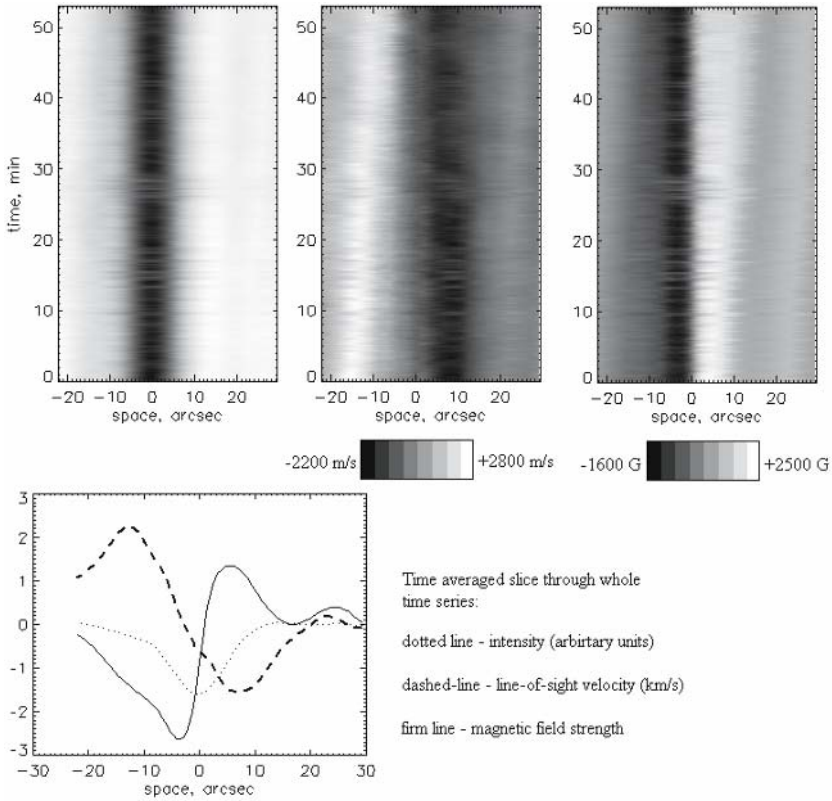
Figure 2.   Example of the time series in AR NOAA 50 at August 3, 2002 (09:10 UT). Top left — continuum near 6569 Å, center — photospheric line-of-sight velocity, right — longitudinal magnetic field strength. Positive and negative velocities correspond to the direction to and from the observer, respectively.

motions (T ∼ 5 min) propagating from the inner penumbral boundary and from the superpenumbra to the lines of maximum Evershed velocity.

3. Conclusions

We believe that the observed wave motions in the sunspot umbra chromosphere are not associated directly with running penumbral waves; but conceivably in some cases where their amplitude becomes sufficiently large (6–8 km s^{-1}), which will be signaled by the occurrence of umbral flashes, oscillations with a period around 300 s will be driven on the umbra-penumbra boundary.

In our opinion, in addition to the 10–12 min periods, a period of 30–35 min is present in the line-of-sight velocity variations of Evershed flows.
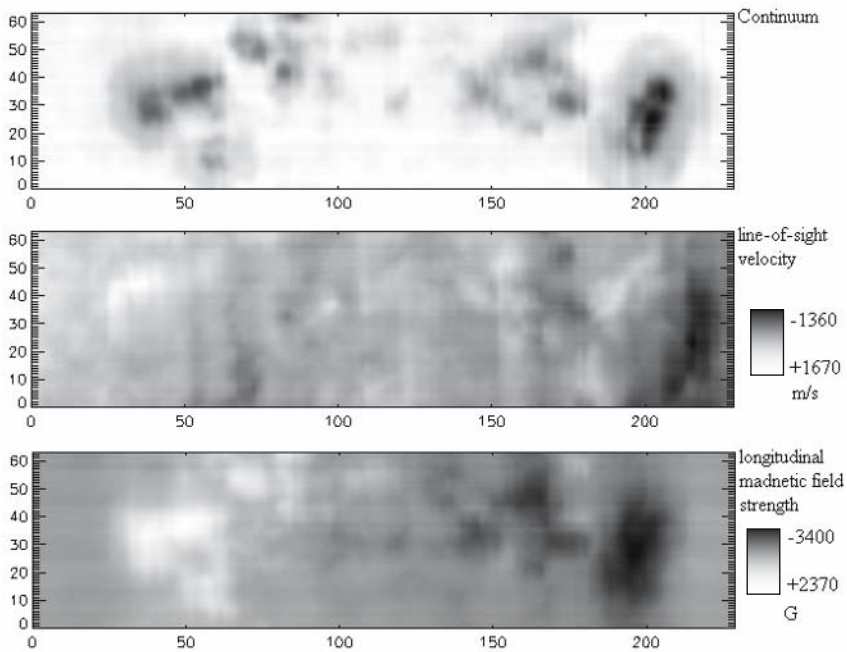
Figure 3. Example of the scan through AR NOAA 50 at July 31 2002 (09:49 UT): continuum near 6569 Å, photospheric line-of-sight velocity, longitudinal magnetic field strength. Positive and negative velocities correspond to the direction to and from the observer, respectively.

We are planning to investigate the possible connection of the 7–8-min oscillations, which we have also observed sometime at two height levels of the sunspot penumbra, with Evershed flows.

Acknowledgements

References

Gopasyuk, S.I.: 1984, *Astron. Rep.* **62**, 157.
Kobanov, N.I. and Makarchik, D.V.: 2002a, *Il Nuovo Cimento* **25 C**, No. 5–6, 609.
Kobanov, N.I. and Makarchik, D.V.: 2002b, *Il Nuovo Cimento* **25 C**, No. 5–6, 695.
Kobanov, N.I. and Makarchik, D.V.: 2004, *Solnechno-Zemnaya Phizika*, in press.
Pevtsov, A.A.: 1992, PhD thesis.
Rimmele, T.R.: 1995, *Astrophys. J.* **445**, 511.
Shine, R.A. *et al.*: 1994, *Astrophys. J.* **430**, 413.

IMPULSIVE X-RAY RADIATION CHARACTERISTICS OF SOLAR FLARE FOOTPOINTS

T. MROZEK and M. TOMCZAK

Astronomical Institute, University of Wrocław
ul. Kopernika 11, PL-51-622 Wrocław, Poland

Abstract. 46 solar flares showing 228 impulsive SXR brightenings have been investigated using Yohkoh data. For 18 flares we made a quantitative comparison between footpoints seen in soft and hard X-rays. We present evidence that in the flare impulsive phase chromospheric evaporation is driven mainly by low-energy non-thermal electrons.

1. Introduction

The Japanese satellite Yohkoh offered the possibility to analyze images acquired in hard X-ray (HXR) and soft X-ray (SXR) emission. Thus, we are able to compare HXR bremsstrahlung from non-thermal electrons stopped in the denser layers of the solar atmosphere with the response of the environmental plasma, seen in SXRs, due to energy deposited by non-thermal electrons. This impulsive SXR response was discovered by Yohkoh and called "impulsive SXR brightening" (Strong *et al.*, 1994).

Tomczak (1999) made a quantitative comparison of the HXR and SXR response due to non-thermal electron beams, and concluded that impulsive SXR brightenings are produced by low-energy non-thermal electrons.

2. Analysis

We chose images, taken with the Al12 filter, covering the whole impulsive phase and searched for pixels with statistically important, impulsive change of brightness. Neighboring pixels were assumed to be part of the same brightening and are denoted as the region of the SXR response. We analyzed light curves of these regions. After subtracting the slowly-varying, gradual component we obtained net light curves describing the pure impulsive SXR signal.

For the quantitative comparison of SXRs and HXRs we selected flares for which it was possible to obtain images in the M2 channel (33–53 keV)
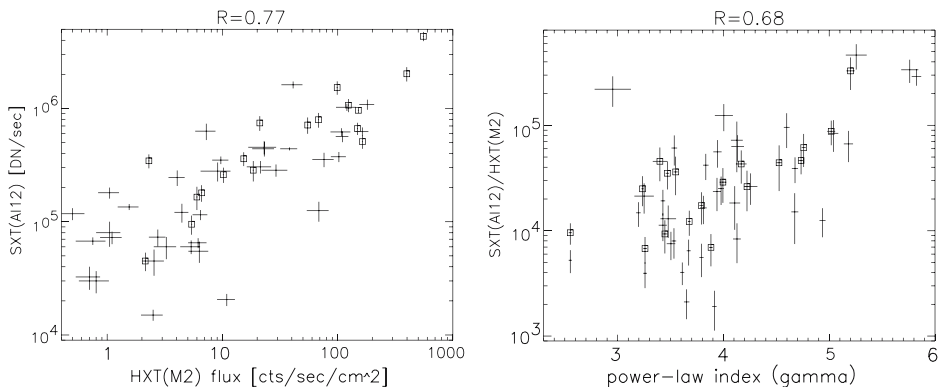
Figure 1. Left panel: relation between two kinds of response to non-thermal electron beams in footpoints observed in HXT (M2 channel) and SXT (Al12 filter). Right panel: productivity of soft X-rays (SXT Al12) relative to hard X-rays (HXT M2) vs. power-law index γ obtained from a single power-law fit. R denotes the correlation coefficient.

which is expected to record mainly non-thermal emission. The HXR photometry was done using images reconstructed with the MEM-Sato method (Sato *et al.*, 1999). For further analysis we chose regions of the SXR response which were spatially correlated to HXR emission sources.

3. Results

A sample of 46 flares was analyzed. Using the net light curve we obtained the observational characteristics for each of the 228 impulsive SXR brightenings. On the basis of these we can describe something like a "typical" impulsive SXR brightening. It has a quasi-symmetrical profile and lasts about 0.5–1 min. Compared to the HXR burst the impulsive SXR brightening shows a delay and lasts several times longer. The FWHM diameter of the region of the SXR response is about 2–8 arcsec. The summed relative brightness of footpoints during the impulsive phase exceeds 20–30% of the total SXR brightness of the flare.

We were able to make a quantitative comparison between the HXR and the SXR responses for 37 events from 18 flares. Figure 1 (left panel) shows the relation between the HXR intensities obtained in the M2 channel and the SXR response recorded in the Al12 filter. The correlation coefficient determined, $R = 0.77$, strongly suggests that both observables are the manifestation of a common physical reason, namely non-thermal electron beams. The scatter in the plot cannot be caused only by observational uncertainties and systematical errors. Data points representing individual footpoints of the same event are often found to be situated along a line
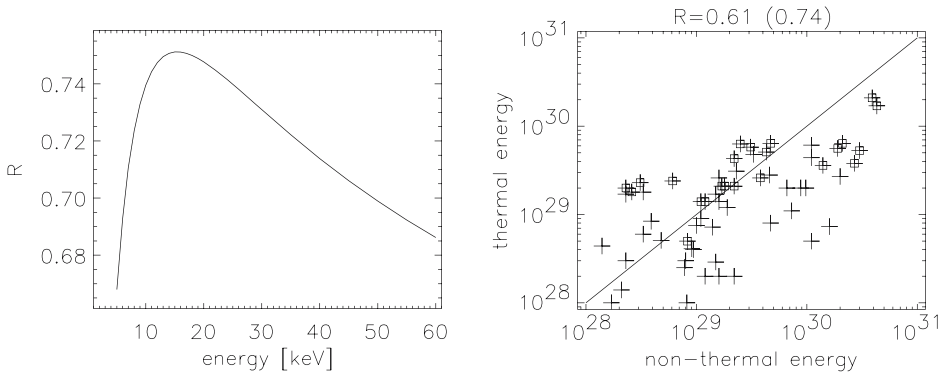
Figure 2.   Left panel: correlation coefficient R between the HXR flux and the SXR response as a function of the photon energy. Right panel: correlation between the maximum thermal energy contained in the plasma and the total, time-integrated energy deposited by non-thermal electrons. Complete events are marked by squares. The straight line gives the location of equality of the two types of energy. The correlation coefficient for all events and for complete events (in parentheses) are given on the top.

that is almost perpendicular to the general trend. An explanation of this behaviour has been given by Tomczak (1999) who compared the power-law index γ (derived from the hardness ratio M2/M1) for events showing comparable SXR responses and different HXR intensities. He found a clear dependence: smaller γ is associated with higher HXR intensity.

Assuming that such a relation is real, there should exist a correlation between the relative productivity of SXRs with regard to HXRs and the power-law index. To verify this we calculated γ from a single power-law fit to the HXR photon flux and plotted it against the mean value of the SXR response divided by the mean value of the HXR emission for each footpoint (Fig. 1, right panel). The correlation ($R = 0.68$) is good enough to conclude that the relative productivity of the SXR signal with regard to the HXR signal increases for larger γ (i.e., softer energy spectrum).

This relation is a function of the energy of HXR photons. Using the parameters obtained from the single power-law fit, we calculated the photon flux for each footpoint for several energy values. For each energy value, we determined the correlation coefficient between the number of HXR photons and the SXR response. This energy-dependent correlation coefficient is presented in Figure 2 (left panel). The highest correlation is found in the range 13–17 keV which suggests that the impulsive SXR brightenings are caused by relatively low-energy electrons. This is in good agreement with other observational results (Farnik *et al.*, 1997; Tomczak, 1999).

Figure 1 (left panel) shows a good correlation between the X-ray emissions but the process of chromospheric evaporation driven by non-thermal

electrons is controlled by the energy balance. We calculated the energy deposited by non-thermal electrons and the maximum thermal energy contained in the plasma heated by this electron population. The obtained values are plotted in Figure 2 (right panel). The smaller correlation coefficient than that in the left panel in Figure 1 can be caused by uncertainties in the estimation of some parameters, especially the low cut-off energy and the volume of the SXR source.

4. Conclusions

We analyzed impulsive SXR brightenings seen in 46 solar flares which show different levels of magnetic complexity, a wide range of released energy and a variety of locations on the solar disk. Nevertheless, the characteristics recorded for impulsive SXR brightenings are relatively uniform which should help to distinguish them from other morphological features. A good spatial and temporal correlation between impulsive SXR brightenings and HXR bursts strongly suggests the same origin – non-thermal electron beams.

Tomczak (1999) showed that a steeper energy spectrum of HXR photons causes a higher SXR productivity. Here we showed for a larger number of events that this correlation is evident.

We found that impulsive SXR brightenings are caused by relatively low-energy electrons. More energetic electrons should reach the denser atmospheric layers (Farnik *et al.*, 1997) and produce an impulsive reaction seen in UV radiation. Such a scenario may be examined by using simultaneous Yohkoh, SOHO/EIT and TRACE images. Moreover, the higher quality of RHESSI X-ray observations makes it possible to obtain a better insight into non-thermal electron precipitation.

5. Acknowledgments

References

Farnik, F., Hudson, H.S., and Watanabe, T.: 1997, *Astron. Astrophys.* **320**, 620.
Sato, J., Kosugi, T., and Makishima, K.: 1999, *Publ. Astron. Soc. Japan* **51**, 127.
Strong, K., Hudson, H., and Dennis, B.: 1994, in Y. Uchida, T. Watanabe, K. Shibata, and H. Hudson (eds.), *X-Ray Solar Physics from Yohkoh*, Universal Academy Press, Tokyo, 65.
Tomczak, M.: 1999, *Astron. Astrophys.* **342**, 583.

VELOCITY FIELDS IN AN IRREGULAR SUNSPOT

J. JURČÁK and M. SOBOTKA
Astronomical Institute AS CR, Ondřejov, Czech Republic

V. MARTÍNEZ-PILLET
Instituto de Astrofísica de Canarias, Spain

Abstract. Line-of-sight velocity fields in an irregular sunspot (NOAA 8990) have been determined from Stokes-I spectra of the line Fe I 630.15 nm, obtained with the La Palma Stokes Polarimeter at the Swedish Vacuum Solar Telescope on May 13, 2000. We show and discuss the resulting velocity maps and asymmetry of the Fe I line.

1. Introduction

A sunspot is a complex structure. High-resolution observations reveal the fine structure of umbra and penumbra. The nomenclature of basic fine structures is summarized in the reviews by Sobotka (1999) and Solanki (2003). We concentrate on velocity fields in light bridges and on the asymmetry of the Fe I line there.

2. Observations and data reduction

On May 13, 2000, we observed an irregular sunspot (NOAA 8990) with the La Palma Stokes Polarimeter at the Swedish Vacuum Solar Telescope. The spot was located at $12°$ N and $17°$ W, μ=0.907. The white light image is shown in Figure 1.

Two fields (marked on Fig. 1) were scanned in the magnetically sensitive line Fe I 630.15 nm. The line originates in the middle and upper photosphere. The areas of the investigated fields are $14.8'' \times 20''$ (185×80 in pixels). This means that we have a spatial resolution of $0.08''$ per pixel on the x-axis (along the spectrograph slit) and $0.242''$ per pixel on the y-axis.

The intensities for every spatial point were measured from the continuum around the Fe I line. The velocity fields were determined from Doppler shifts of this line. Positions of the neighbouring terrestrial O_2 lines are used for zero-velocity reference. The velocities were corrected for the motions of
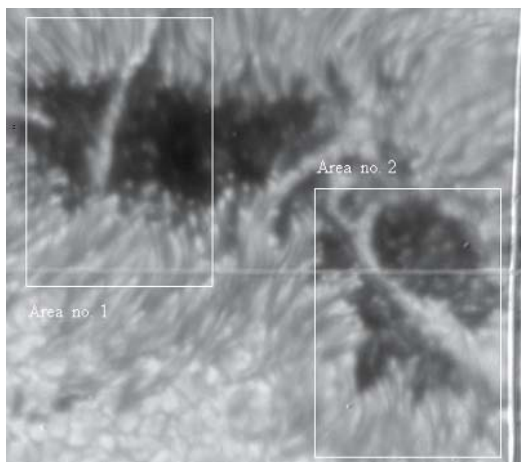
Figure 1.   White-light image of the irregular sunspot NOAA 8990.

the Earth and the rotation of the Sun. These corrections are described by
Howard and Harvey (1970).

The Doppler shifts were measured by the following method. A scan over
the line profile consisted of 52 wavelength points. We interpolated these
points with a spline function consisting of 2000 points and integrate 200
points in each line wing. When the sums of these integrations are equal, the
line-center position is right in the middle between the integrated points.

3. Results

Due to limited space, only the results from area 1 are presented. The result-
ing intensity (left) and velocity (right) images are shown in Figure 2. The
arrows in the velocity map point to the disk centre and the white contours
correspond to zero velocity. We can compare the structures in the velocity
fields with the intensity maps.

The velocity field is as simple as in the case of a regular sunspot. This
means that we observe a blueshift on the centre side and a redshift on the
limb side. In the darkest part of the umbra we observe an area with zero
velocity, which is consistent with many other observations. The velocity
map of the light bridge, which is clearly visible on the intensity map,
is not so simple. On the discward end of the light bridge the blueshift
in the penumbra is amplified by the upflows in the light bridge. On the
limbward end the redshift in the penumbra is diminished by the upflows
in the light bridge and we observe a region with resulting blueshift there.
Both ends of the light bridge, as seen in the velocity map, are located deeply
in the penumbra on the intensity map. Thus, in this case the mechanism
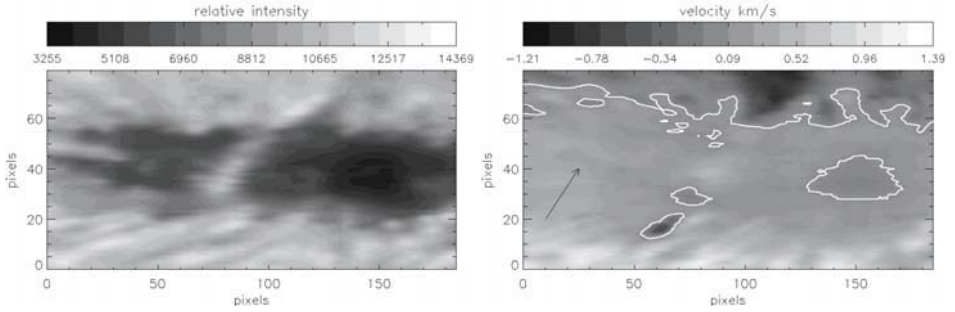
Figure 2.   Resulting intensity field (left) and velocity map (right).

responsible for the formation of the light bridge is not limited only to the umbra.

In Figure 3 we plot the Doppler velocity and relative intensity along the light bridge. The light bridge has a behaviour similar to that described by Rimmele (1997). We observe an anticorrelation between velocity and intensity and the velocities range from -200 m s^{-1} to 500 m s^{-1}, except the ends of the light bridge in the penumbra. In these areas, we observe strong upflows, which reach up to -1000 m s^{-1}. From the anticorrelation we estimate too hot upflows and cold downflows, therefore this light bridge is probably of convective origin.
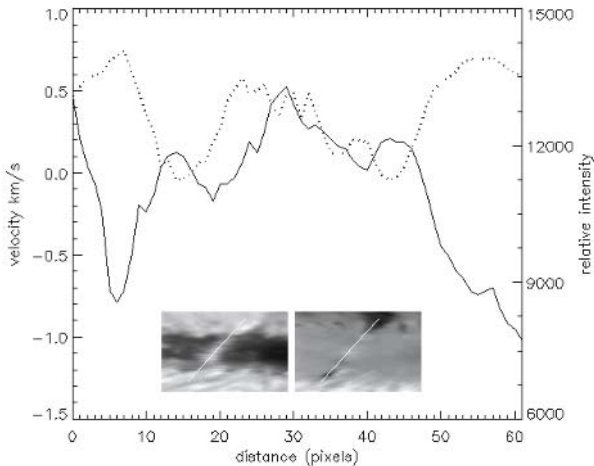
Figure 3.   Doppler velocity (*solid line*) and relative intensity (*dotted line*) along the light bridge. The cuts are marked in the intensity and velocity map (bottom).

Figure 4 (left) shows bisectors from some parts of the umbra and penumbra. From the penumbral bisectors it is apparent that the velocity in the penumbra decreases with photospheric height. The velocity in the umbra
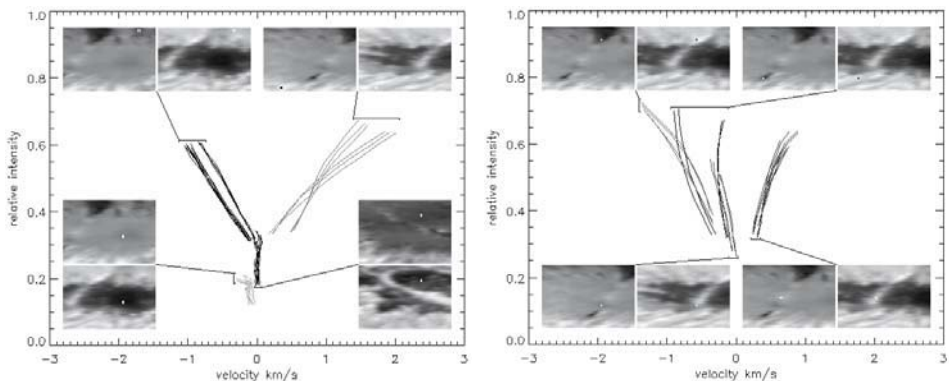
Figure 4.   Some selected bisectors from the umbra and penumbra (left), and bisectors from light bridge (right).

is close to zero at all heights. The lower left bisectors (with the lowest intensity) seem to have some flow at the deepest levels. However, it is a disturbance of line wings blended by weak umbral lines.

In Figure 4 (right) bisectors measured in the light bridge are shown. The flow velocity has almost the same behaviour as in the penumbra, i.e., it decreases with height. A difference is obtained in the asymmetry. The upper left and upper right bisectors are from regions with stronger upflows than the upper left bisectors in the left panel, but they are less inclined, i.e., the asymmetry is smaller. The lower right bisectors are taken from a region with a downflow, and the velocity decreases with height too. This leads us to the same conclusion: the convective origin of the light bridge.

4. Conclusion

The light bridge in active region NOAA 8990 is probably of convective origin. Downflows prevail in this light bridge, but upflows are also present. Strong upflows are observed in the penumbra near the ends of the light bridge. These upflows may result from the interaction of the light bridge velocity and the Evershed flow. This possible interaction, however, has to be proven by further observations.

References

Howard, R. and Harvey, J.: 1970, *Solar Phys.* **12**, 23.
Rimmele, T.R.: 1997, *Astrophys. J.* **490**, 458.
Sobotka, M.: 1999, in A. Hanslmeier and M. Messerotti (eds.), *Motions in the Solar Atmosphere*, Kluwer, Dordrecht, p. 71.
Solanki, S.K.: 2003, *Astron. Astrophys. Rev.* **11**, 153.

ON THE DYNAMIC DISCONNECTION OF RISING Ω-LOOPS

L. TÓTH and O. GERLEI

Heliophysical Observatory of the Hungarian Academy
of Sciences
H-4010 Debrecen, P.O. Box 30, Hungary

Abstract.   We analyzed tilt angles and daily tilt angle changes of bipolar magnetic regions (BMRs). We find that generally regular BMRs grouped by age do not show the phenomenon of toroidal relaxation towards the east-west direction. We interpret this by the disconnection of Ω-loops from the bottom of the convection zone.

1. Introduction

It is assumed that the solar magnetic field originates in the dynamo operating in a stable layer at the base of the convection zone. According to dynamo models (Parker, 1955; Babcock, 1961; Leighton, 1964, 1969) the initial poloidal field turns into toroidal because of differential rotation. The toroidal strands of this subjacent magnetic flux locally may come out of this stable layer and would rise through the convection zone as an Ω-loop. It is one of the possible phenomena that is responsible for the formation of bipolar magnetic regions (BMRs).

The emerged flux tubes show Joy's law which means, in general, that the preceding (p) spots of BMRs are closer to the equator than the following ones (f). Thus the BMRs are inclined to the local latitudinal line by an angle, which increases with latitude (Hale *et al.*, 1919) and is called tilt. One of the explanations for this phenomenon is to take the Coriolis force into account (Schmidt, 1968) that can twist the ascending flux loops so that it finally emerges at the surface with a tilt to the local latitudinal line (Wang and Sheely, 1989, 1991; Howard, 1991, 1996a, 1996b; Sivaraman *et al.*, 1999).

Later on, in the theoretical descriptions (D'Silva and Choudhuri, 1993; Longcope and Choudhuri, 2002) further effects, namely the role of convective turbulence and dynamic disconnection have been taken into account, which influence the rising flux loop. In the present article we investigate observational signatures of the effect of dynamic disconnection.
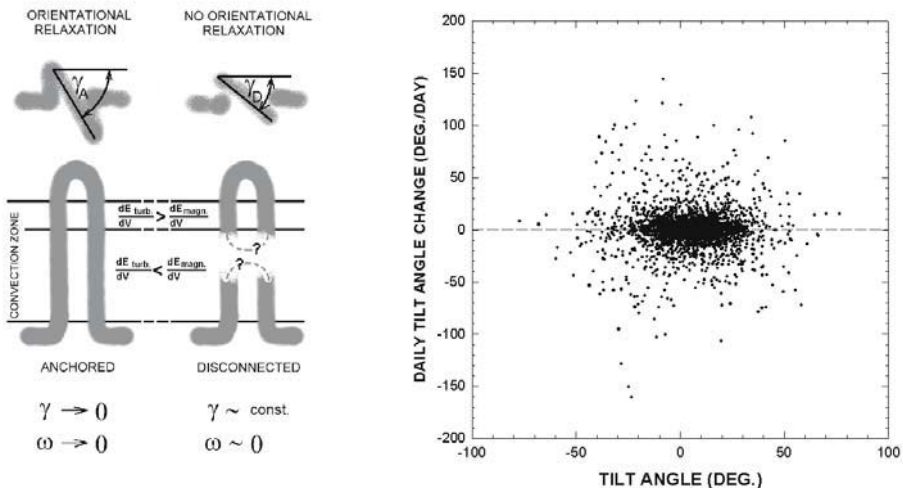
Figure 1. *Left:* Rough sketch of the anchored and the dynamically disconnected Ω-loops (view from above and in profile) and the expected behavior of their tilt and rotation. *Right:* Plot ω versus γ of our selected regular BMRs. The straight line (dashed) indicates the least-squares linear fit to the data.

2. Method of investigation

In our investigations we applied the data of Greenwich Photo-Heliographic Results (GPHR) concerning the 14th solar cycle from 1901 to 1913 from which only those clearly aligned BMRs were taken into account of which longitudinal co-ordinates were not farther from the central meridian than 60 degree. This selection resulted in 3754 BMRs.

The tilt angle, γ, is, by convention, positive for BMRs where p-spots are equatorward and negative if they are poleward of f-spots. Furthermore, this angle was calculated as the bend of a straight line to the local latitudinal line from which the first one was fitted by an area weighted least-squares method to the spots of the given BMR. In accordance with Howard (1991) we applied latitudinal correction as well. Further information is obtainable from the distribution of the daily tilt angle changes of BMRs, which according to Howard (1994) were determined as simple day to day differences, $\omega = \Delta\gamma/\Delta\text{day}$.

3. The role of dynamic disconnection

Howard (1996a) made first a plot of ω against γ that shows a relation between the tilt angle and its change, and fitted a straight line as $\omega = a + b*\gamma$. This fitting (Howard, 1996a) resulted in a slope $b = -0.229\pm0.004$ and

TABLE I.   Our $\gamma_{(\omega=0)}$ [deg] and b [day^{-1}] parameters compared with Longcope and Choudhuri (2002) theoretical results.The explanations of these parameters are given in the text.

	Our work:			Longcope and Choudhuri (2002)		
				anchored		dis-
		life time:		life time:		connec
	all groups	2≤day≤7	7<day	2≤day<7	7≤day	-ted
$\gamma_{(\omega=0)}$	21±30	18±18	9±16	3.3	−0.03	2.12
b	−0.02±0.02	−0.03±0.02	0.07±0.07	−0.302	−0.097	−0.024

the location of the intersection of the γ axis at $\gamma_{(\omega=0)} = 5.65\pm0.32$ degree. This led to the conclusion that the bipoles relax from their orientation toward the angle $\gamma_{(\omega=0)}$ specified by Joy's law. This phenomenon is called orientational relaxation.

On the basis of the work by Howard (1996a), Longcope and Choudhuri (2002) gave an overall theoretical description of this phenomenon. In their theories they took into account the effect of the Coriolis force on the rising flux tube as the origin of Joy's law, and the effect of convective turbulence at the topmost layer of the convection zone as being responsible for the random scatter of tilts around the systemic ones determined by Joy's law. Furthermore, they made calculations for both cases when the rising Ω-loop was connected/not connected to the bottom of the convection zone (Figure 1). The latter case is called dynamic disconnection. Namely, if the flux tube is connected to the strong toroidal magnetic field at the bottom of the convection zone then following the emergence, the magnetic tension with the progress of time may force to align the bipolar magnetic region toward the east-west direction. In this case the above-mentioned slope, b, is negative. Furthermore, this slope b and the intersection $\gamma_{(\omega=0)}$ with the progress of time may keep to zero, that kind of behavior is called toroidal relaxation. However, if the flux tube were dynamically disconnected, this relaxation to zero tilt would stop and $b \approx 0$.

Considering this, Longcope and Choudhuri (2002) calculated artificial ω-γ plots for Ω-loops younger and older than 7 days, in cases when they are connected to or disconnected at 75 Mm below the solar surface from the bottom of the convection zone. The parameters of the straight lines fitted to these artificial plots are listed in Table I.

Based on our selected, clearly aligned BMRs, we have investigated the distributions of the related ω and γ pairs for all and for BMRs of different age-groups as well. The plot of all selected BMRs with the fitted straight line is shown in Figure 1 (right panel). The parameters of the fitted straight

lines, namely the slope b and the intersection $\gamma_{(\omega=0)}$ of all BMRs and of the different age-groups are listed in Table I. The difference between the work of Howard (1996a) (see above) and our's (see Figure 1, Table I) is striking, since our results do not show the phenomena of orientational and toroidal relaxations. However, practically neither the younger than 8-day-old BMRs show these relaxations nor the olders (Table I). On the basis of the work of Longcope and Choudhuri (2002) this may mean that the Ω-loops of the regular BMRs are possibly disconnected (see Figure 1, left panel) from the bottom of the convection zone.

4. Conclusions

The regular, clearly aligned active regions do not show the phenomenon of toroidal relaxation, which presumably means that the Ω-loops are disconnected from the bottom of the convection zone.

Acknowledgements

References

Babcock, H.W.: 1961, *Astrophys. J.* **133**, 572.
D'Silva, S. and Choudhuri, A.R.: 1993, *Astron. Astrophys.* **272**, 621.
Hale, G.E., Ellerman, F., Nicolson, S.B., and Joy, A.H.: 1919, *Astrophys. J.* **49**, 153.
Howard, R.F.: 1991, *Solar Phys.* **132**, 49.
Howard, R.F.: 1994, *Solar Phys.* **149**, 23.
Howard, R.F.: 1996a, *Solar Phys.* **167**, 95.
Howard, R.F.: 1996b, *Solar Phys.* **169**, 213.
Leighton, R.B.: 1964, *Astrophys. J.* **140**, 1547.
Leighton, R.B.: 1969, *Astrophys. J.* **156**, 1.
Longcope, D. and Choudhuri, A.R.: 2002, *Solar Phys.* **205**, 63.
Parker, E.N.: 1955, *Astrophys. J.* **122**, 293.
Schmidt, H.U.: 1968, in K.O. Kiepenheuer (ed.), *Structure and Development of Solar Active Regions*, D. Reider Publ. Comp., p. 95.
Sivaraman, K.R., Gupta, S.S., and Howard, R.F.: 1999, *Solar Phys.* **189**, 69.
Wang, Y.M. and Sheely, N.R.: 1989, *Solar Phys.* **124**, 81.
Wang, Y.M. and Sheely, N.R.: 1991, *Astrophys. J.* **375**, 761.

SEARCHING FOR THE ORIGINS OF THE FAST SOLAR WIND

M.D. POPESCU [1,2] and J.G. DOYLE [1]

[1] *Armagh Observatory*
College Hill, Armagh BT61 9DG, N. Ireland

[2] *Astronomical Institute of the Romanian Academy*
RO-75212 Bucharest 28, Romania

Abstract. Here we present the lowest-in-altitude observed signatures of the fast solar wind streams. They originate from coronal holes (CH) network boundaries, as seen in the low transition region (TR) line O III 703.87 Å ($T_e \approx 8 \times 10^4$ K). Higher in the solar corona, the plasma outflow is seen in the Mg IX 706.02 Å line ($T_e \approx 10^6$ K), as an increased blue-shift inside the CH region. An interesting change in behaviour is observed at the quiet Sun (QS)/CH boundaries, where plasma from the network changes its velocity sign, and, following the closed magnetic structures, falls back to the Sun. This is also the site where signature of magnetic reconnection between the open CH lines and the closed QS loops is seen, in the form of an increased number of bi-directional jets, which represent evidence for the slow solar wind origins.

1. Introduction

Today there is general agreement that the fast solar wind originates mainly from magnetically open regions in the coronal holes (CHs) (Krieger *et al.*, 1973). In order to find more precisely what are the small-scale features responsible for the development and rise of the fast solar wind streams, one needs to correlate the plasma motions with the fine structures inside the CHs, which are only seen from the transition region (TR) downward.

Hassler *et al.* (1999) reported correlations between the plasma outflow as deduced from the coronal Ne VIII 770 Å line (originating at 63×10^4 K) and the chromospheric network as seen in the Si II 1533 Å line (1.3×10^4 K).

The results we present here indicate that we indeed see the fast solar wind streams originating from the magnetic network boundaries, at a temperature as low as $\approx 8 \times 10^4$ K (that means, not far away from the base of the TR). This constitutes the lowest temperature (and height) at which those outflows have ever been observed. Moreover, we also see an increased number of bi-directional jets at the quiet Sun (QS)/CH boundary, which
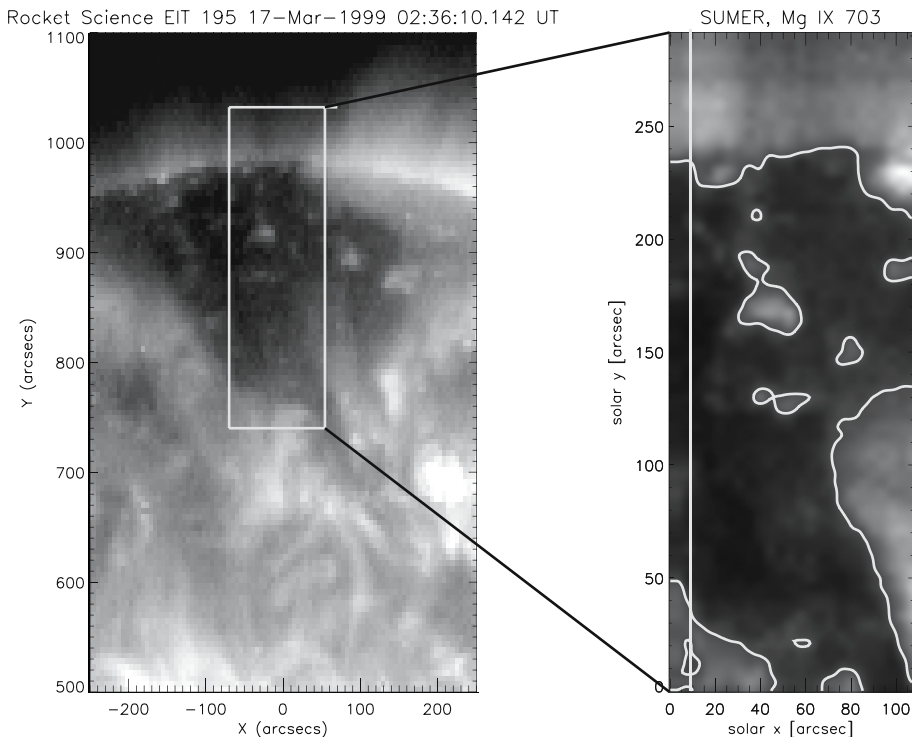
Figure 1. The raster location as seen on the EIT Fe XII 195 Å image (left), together with the raster intensity in the SUMER Mg IX 706 Å line (right). The white contour represents the QS/CH boundary.

represent evidence for the slow solar wind origins, as very recently observed for the first time by Madjarska *et al.* (2004).

2. Data

We analysed a solar on-disk raster taken in a northern polar CH region on 17 March 1999 with detector B from the Solar Ultraviolet Measurements of Emitted Radiation (SUMER) grating spectrograph on SoHO. The final image has a dimension of (108×292) arcsec^2, with a spatial resolution of ≈ 1 arcsec and a spectral resolution of 22.4 mÅ. Each spectrum has an integration time of 150 s. We studied a low TR line, O III 703.87 Å ($\approx 8 \times 10^4$ K), and a coronal line, Mg IX 706.02 Å ($\approx 10^6$ K).

The final aim of our study was to calculate the intensities and the Doppler velocities (LOS velocities) of both lines considered. More details on the calibration procedures applied, as well as on how we extracted the information from the data, are given in Popescu and Doyle (2004).
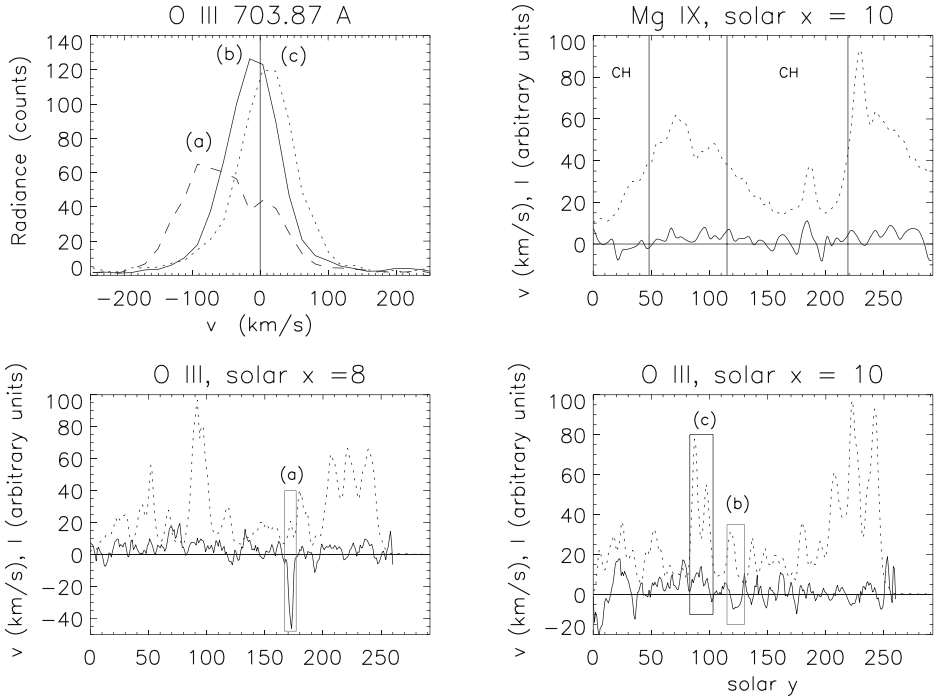
Figure 2. Top left: three example spectra, representing (a) a bi-directional jet, (b) a CH network boundary blue-shift and (c) a QS network boundary red-shift. Top right: intensity (dotted line) and Doppler velocity (continuous line) for the Mg IX line at *solar x* = 10. The vertical lines mark the QS/CH boundary. Bottom: intensity and Doppler velocity for the O III line, where the selected examples are again marked.

The location of the raster on the Sun, as seen in the EIT Fe XII 195 Å image, is indicated in Figure 1 (left). To the right of the figure, we plot the Mg IX 706 Å intensity, as derived from our data.

3. Results

In the coronal line, the CH is seen as a reduction in the intensity, surrounded by the brighter QS, and very well correlated with negative Doppler velocities (outflows) of about -4 km s^{-1}.

In order to see the correlation between the Doppler velocity and the intensity for the O III line, we made a one dimensional cut at *solar x* = 10 (see the vertical line in Figure 1, right).

We selected as examples three types of phenomena, where the O III intensity has high values, but the plasma moves differently (see features (a),

(b) and (c) on Figure 2, bottom). On the top left panel in Figure 2, we also present the spectra of the selected features.

In the bi-directional jet (a), plasma undergoes rapid movements, both up and down. The spectrum shows a double peak structure, and when fitted with a double Gaussian, the derived outflow velocities are about -100 km s^{-1}.

In the CH network boundaries (b), plasma is blue-shifted. In the chosen example, the highest outflow is -15 km s^{-1}. This blue-shift represents the plasma upward motion seen originating from the CH network boundaries, representing evidence of the fast solar wind origins. In the CH, one can see that every time there is an increase in the intensity, it corresponds to a decrease in the velocity, which generally becomes blue-shifted.

In the QS network boundaries (c), the plasma behaviour is completely changed. The spectrum of this feature is red-shifted up to 13 km s^{-1}. Also, here signature of magnetic reconnection between the open CH lines and the closed QS loops is seen, in the form of an increased number of bi-directional jets, which represent evidence for the slow solar wind origins.

4. Conclusions

Our results (see also Popescu and Doyle, 2004) constitute the first precise indication of fast wind streams seen originating from the CH network boundaries at such a low height in the TR. We have derived this conclusion from direct correlation between the O III 703 Å Doppler velocity and the intensity of the same ion.

Acknowledgements

References

Krieger, A.S., Timothy, A.F., and Roelof, E.C.: 1973, *Solar Phys.* **29**, 505.
Hassler, D.M., Dammasch, I.E., Lemaire, P., *et al.*: 1999, *Science* **283**, 810.
Madjarska, S.M., Doyle, J.G., and van Driel-Gesztelyi, L.: 2004, *Astrophys. J.* **603**, L57.
Popescu, M.D. and Doyle, J.G.: 2004, *Astron. Astrophys.*, accepted.

DETECTABILITY OF HIGH FREQUENCY ACOUSTIC WAVES WITH TRACE

A. FOSSUM and M. CARLSSON

Institute of Theoretical Astrophysics
P.O. Box 1029 Blindern, N-0315 Oslo, Norway

Abstract. High frequency acoustic waves have been proposed as a mechanism to heat the solar chromosphere in internetwork regions. Such waves are difficult to detect using ground based observations because of seeing. Space based solar observatories like SOHO and TRACE are not hampered by such high frequency disturbances caused by the Earth's atmosphere. We have used detailed NLTE radiation hydrodynamic simulations to investigate the detectability of high frequency acoustic waves with TRACE. A broad spectrum of acoustic waves are fed into the computational domain at the lower boundary of the model atmosphere and TRACE UV continuum intensities are calculated by folding the derived intensities with the TRACE filter functions for the 1600 and 1700 Å filters. Power spectra, phase diagrams and intensity response functions are calculated and intensity formation heights are derived. The simulations show that the width of the TRACE intensity response functions sets an upper frequency limit of 40 mHz for the detection of high frequency waves even in the absence of instrumental noise.

1. Introduction

High frequency acoustic waves are often assumed to play an important part in the energy balance of the Sun's chromosphere. Testing this hypothesis is difficult because the signal we get from high frequency waves is weakened by the width of the response function. In addition, the seeing blurs the ground based observations and makes these waves hard to observe.

Krijger *et al.* (2001) tried to detect high frequency acoustic waves using image sequences from TRACE in three ultraviolet passbands (1700, 1600 and 1550 Å) which sample the upper solar photosphere and low chromosphere. They did not diagnose any high frequency waves above 15 mHz, a fact attributed by the authors to be due to the non-simultaneity of the imaging in the different passbands.

In this article we have looked at the possibility of detecting high frequency waves if we *know* that they are present using TRACE, assuming a regularity in the sampling. To achieve this we use numerical simulations of
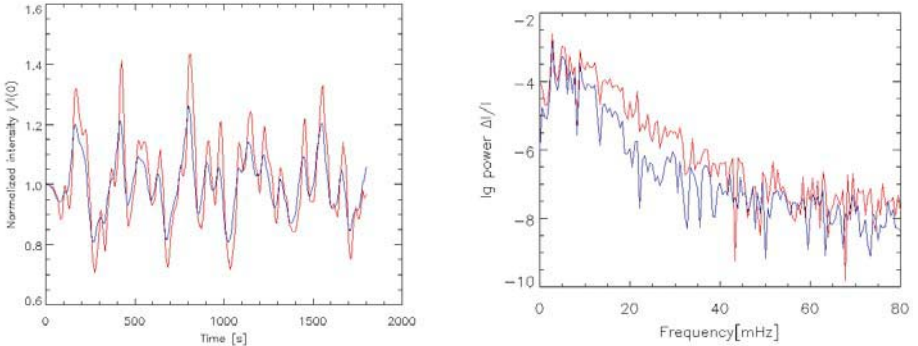
Figure 1.   a) Normalized intensities from the simulations folded with the TRACE 1600 Å (grey) and 1700 Å (black) passbands and integrated over the wavelengths. The fact that I_{1700} is leading I_{1600} implies that there are phase differences in the data. b) Log power spectra of $\frac{\Delta I}{I}$ as a function of frequency. Grey line is for I_{1600}, black line is for I_{1700}.

the propagation of acoustic waves to make artificial observations, and these are then analyzed in the same way as real observations.

2. Numerical simulations

The numerical simulations used to study the detection of high frequency waves were made with the radiation hydrodynamics code used by Carlsson and Stein (e.g. 1990, 1992, 1994, 1995, 1997, 2002). The code includes most essential physical processes in a one dimensional model without magnetic fields, including a self-consistent treatment of the radiation field and matter, a detailed treatment of the non-LTE thermodynamics and accurate fluid treatments of shocks.

The initial atmosphere is in radiative equilibrium with a sound speed of about 7 km/s and a cut-off frequency of 5 mHz. The upper boundary is a corona at 10^6 K at 10^4 km with a transmitting boundary condition. Incident radiation from the corona taken from observations (Tobiska, 1991) is included. Waves are driven through the atmosphere by a piston located at the bottom of the computational domain. The piston velocity is taken from Ulmschneider's (private communication) theoretical model for wave excitation and has significant power up to 50 mHz.

3. Results

The intensities that result from our numerical simulations are folded with the TRACE 1600 Å and 1700 Å passbands. We then integrate the intensities over the wavelengths and obtain the intensities I_{1700} and I_{1600} in Fig. 1a
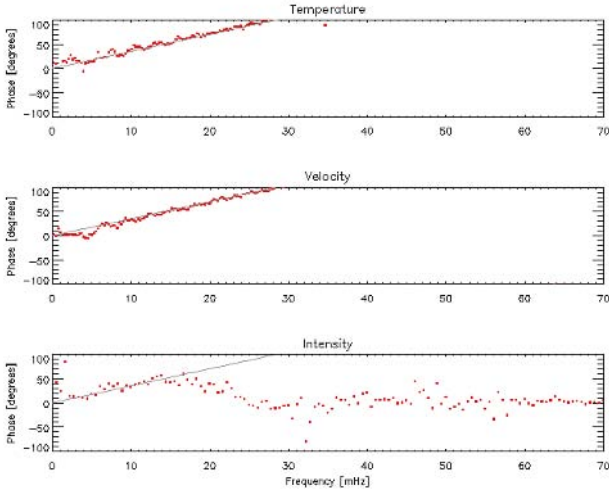
Figure 2.   Top and middle panel: Phase differences of temperatures and velocities from the simulations taken at heights 360 km and 430 km as a function of frequency. Bottom panel: Phase difference of I_{1600} and I_{1700} as a function of frequency. In all three graphs, the grey line is the line that acoustic waves would propagate along with a constant velocity of about 7 km/s and a height difference of 70 km.

as a function of time. I_{1600} is produced higher up in the atmosphere where the temperature is larger. This is enhanced by a non-linear Planck function and explains why the amplitude of the I_{1600} wave in Fig. 1b has more high frequent power than the I_{1700} amplitude. We also see that the I_{1600} amplitude is larger compared to I_{1700}. The figure shows that we retain power much longer in I_{1600} than in I_{1700}, when we reach about 40 mHz in I_{1600} and 30 mHz in I_{1700} we have so little power that it is impossible to distinguish this from noise.

Fig. 2 shows the phase differences as a function of frequency. The phase differences of the temperature and velocities in the upper two graphs follow nicely the grey line that acoustic waves would propagate along with a constant velocity of 7 km/s and a height difference of 70 km. The phase difference of the intensities in the lower graph follows the grey line up to about 15 mHz where it then declines towards zero again. This is a consequence of the width of the response function. In the observations of Krijger *et al.* (2001) we find the same shape of the phase difference plots.

Fig. 3 shows the response function, $R_{I,T}(x)$, of $\frac{\Delta I}{I}$ given a perturbation in the temperature. This function is derived numerically from the simulations. We saw from the power plots that I_{1600} retains power much longer than I_{1700}, and the explanation lies in the width of the response functions. More high frequent waves will pass through $R_{I1600,T}$ and still have significant power than through the much broader $R_{I1700,T}$.
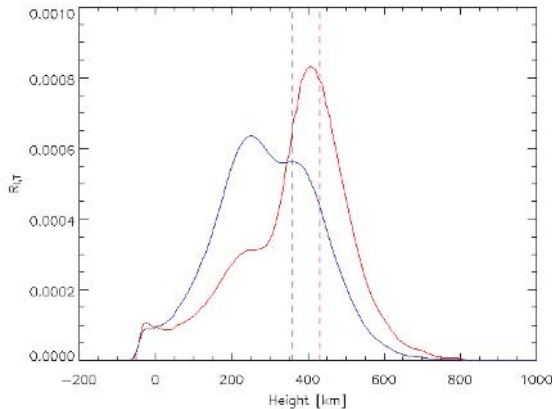
Figure 3. Response function of $\frac{\Delta I}{I}$ given a perturbation in the temperature (grey line for I_{1600}, black line for I_{1700}). The dashed lines show the heights of the best correlation of the intensities with the local temperature using scatter plots. This implies that the formation height of I_{1600} is at 360 km and I_{1700} is at 430 km. This is only a mean since the filters are so broad that the response functions have FWHM of 185 km and 325 km for the 1600 and 1700 Å filters, respectively. Before integration we need to multiply the response function by $\frac{\Delta T}{T}$, which increases with height. It is important to bear in mind that the response functions depend on the background atmosphere. Here we are simulating a quiet area of the Sun, and the background atmosphere has no temperature rise in the lower chromosphere.

4. Conclusions

We conclude that we can not detect waves above 40 mHz with TRACE in the absence of noise. This is due to the very broad response function caused by the wide band filters of TRACE. It might be worth trying to combine the two filters to narrow the response function and then be able to see more of the high frequent waves.

References

Carlsson, M. and Stein, R.F., 1990, in P. Maltby (ed.), *Proc. Mini-Workshop on Physical Processes in the Solar Transition-region and Corona*, 177.
Carlsson, M. and Stein, R.F.: 1992, *Astrophys. J.* **397**, L59.
Carlsson, M. and Stein, R.F.: 1994, in M. Carlsson (ed.), *Proc. Mini-Workshop on Chromospheric Dynamics*, 47.
Carlsson, M. and Stein, R.F.: 1995, *Astrophys. J.* **440**, L29.
Carlsson, M. and Stein, R.F.: 1997, *Astrophys. J.* **481**, 500.
Carlsson, M. and Stein, R.F.: 2002, in H. Sawaya-Lacoste (ed.), *Proc. Magnetic Coupling of the Solar Atmosphere Euroconference and IAU Colloquium 188*, ESA SP-505, 293.
Krijger, J.M., Rutten, R.J., Lites, B.W., *et al.*: 2001, *Astron. Astrophys.* **379**, 1052.
Tobiska, W.K.: 1991, *J. Atm. Terr. Phys.* **53**, 1005.

LINKING CORONAL TO INTERPLANETARY MAGNETIC HELICITY

M.L. LUONI, S. DASSO and C.H. MANDRINI
Instituto de Astronomía y Física del Espacio, IAFE
CC. 67 Suc. 28, 1428 Buenos Aires, Argentina

L. VAN DRIEL-GESZTELYI
Observatoire de Paris, LESIA, F-92195, Meudon, France
Mullard Space Science Laboratory, Univ. College London, UK
Konkoly Obs., H-1525 Budapest, P.O. Box 67, Hungary

P. DÉMOULIN
Observatoire de Paris, LESIA, F-92195, Meudon, France

Abstract. Magnetic helicity (MH) has been recognized as a useful tool to study the link between active regions (ARs) and magnetic clouds (MCs). In this work, we compare the MH and flux of the MC of October 18–19, 1995, and its associated AR. We compute both quantities and we find that the AR flux is one order of magnitude larger than in the MC, while the coronal MH is lower after an ejection linked to a long duration event and comparable to the MC helicity. We conclude that the MH in the interplanetary flux rope comes from the coronal one.

1. Introduction

The magnetic cloud (MC) that reached the Earth by Oct. 18–19, 1995, produced an intense geomagnetic storm. This MC was observed by the Magnetic Field Instrument (MFI) on board the WIND spacecraft (Lepping *et al.*, 1997).

The solar source of this phenomenon was located in AR NOAA 7912 (van Driel-Gesztelyi *et al.*, 2000). On October 14, 1995, highly twisted magnetic loops with an S-shape were observed. A C1.6 long duration event (LDE) started by loop brightenings in the central part of the AR on that day. The duration of this event is estimated in 15 h between 5:00 UT and 20:00 UT reaching maximum at 9:21 UT, according to Solar-Geophysical Data. This AR wasn't prolific in flares, but some sigmoidal loops appeared in the Soft X-Ray Telescope (SXT/Yohkoh) in expansion.
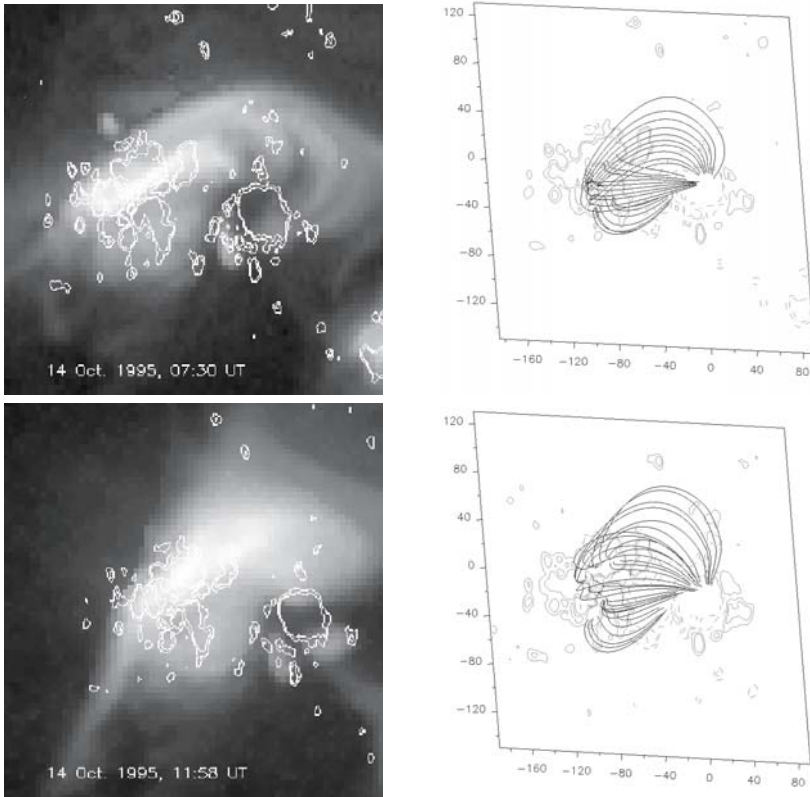
Figure 1. SXT images with longitudinal magnetograms overlaid (left) and coronal linear force-free model (right) of AR 7912. Iso-contours (±70, ±140 G) have been drawn with cont./dashed lines for positive/negative magnetic field values (left).

Several studies have suggested that the magnetic helicity (MH) in clouds comes from the one transported by coronal mass ejections (CMEs). The MH is a good indicator of topological complexity because it measures the twisting and linking of fields (Berger and Field, 1984). It is also one of the few global quantities that is preserved in the absence or near absence of resistivity, so it is a very useful tool to compare phenomena occurring in very different physical regimes. In this paper we compute the flux and MH for the October 18–19 MC and AR 7912, using different assumptions, and compare their values.

2. Coronal helicity

We extrapolated the photospheric line of sight magnetogram, obtained at Kitt Peak Solar Observatory on October 14, using a linear force-free
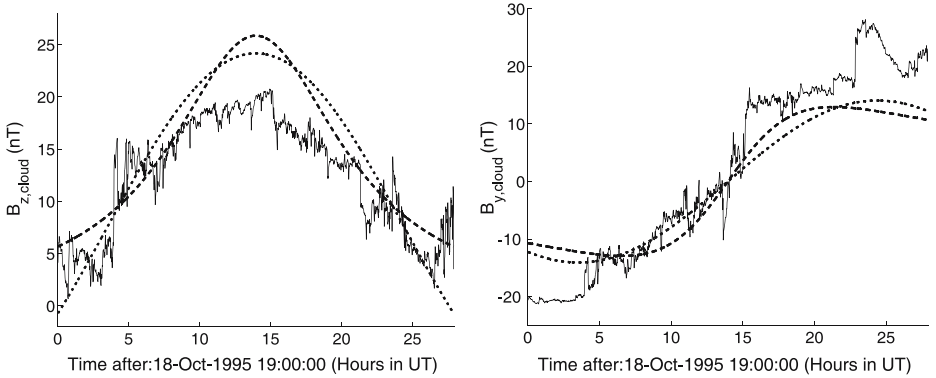
Figure 2. Interplanetary WIND magnetic field data and models. The thin solid line displays the observed field, while the dotted and dashed curves display the field components for Lundquist and Gold-Hoyle models, respectively.

approach (see Figure 1). Then, we found the best α parameter to fit SXT loops at 7:30 UT and 11:58 UT. The value of α is not unique for a given time, but it turns out to be in average higher at 7:30 than at 11:58 UT, in agreement with the observed coronal loops that seem more relaxed at the later time (after the ejection). Using the expression given by Berger (1985), we compute the coronal relative helicity (Hr_{cor}) for both times. The results are summarized in Table I.

3. Interplanetary helicity

The MC associated to AR 7912 was observed from 19:00 UT on Oct. 18 to 23:00 UT on Oct. 19, 1995. We analyze the WIND magnetic data with a one minute resolution (`http://cdaweb.gsfc.nasa.gov/cdaweb/istp-public/`).

The magnetic structure of MCs is usually modeled by a cylindrical helix. To determine its orientation, we apply the minimum variance (MV) method to the data (e.g. Bothmer and Schwenn, 1998). Then, we obtain the components of the field in a cartesian system associated to the cloud, such that: (a) $B_{z,cloud}$ is the axial component, being its value positive at the center, (b) $B_{y,cloud}$ is the poloidal component once the spacecraft crossed its axis, and (c) $B_{x,cloud}$ is the radial component, also after leaving the MC's center.

Several MC physical models have been used; however, it is not clear yet what is the best to describe their magnetic structure. We model the cloud field using two force-free field (FFF) configurations: (1) a linear FFF (Lundquist's model), and (2) a non-linear FFF with uniform twist (Gold-Hoyle's model). Using the MV coordinates we compare the observations with the results for the two models. The physical parameters that best fit

TABLE I.   The left block of columns gives the time, the α range and Hr_{cor}. The right block lists the model name, the computed MC flux (F_{MC}) and helicity Hr_{MC}, for a length of 2.4 AU.

Solar Corona				Interplanetary Medium		
TIME (UT)	α (10^{-2} Mm^{-1})	Hr_{cor} (10^{42} Mx^2)		Model	F_{MC} (10^{21} Mx)	Hr_{MC} (10^{42} Mx^2)
07:30	0.15–0.31	8.0–16.0		Lundquist	1.1	+9.4
11:58	0.15–0.18	8.0–10.0		Gold-Hoyle	1.2	+8.4

the observations are computed following the method described in Dasso *et al.* (2003). Figure 2 shows $B_{z,cloud}$ and $B_{y,cloud}$.

4.   Conclusions

From Table I (left) it can be seen that the variation of Hr_{cor} before and after the ejection is between zero, which is unlikely since the field relaxes, and 8×10^{42} Mx^2. Table I (right) shows the MC flux (F_{MC}) and helicity (Hr_{MC}), assuming a length of 2.4 AU (Larson *et al.*, 1997). The two MC models give similar values for the global quantities, being both similar to the mean values in MCs (Green *et al.*, 2002). The range of the obtained coronal and interplanetary MH are in a very good agreement, while the MC flux is 10% of the AR flux ($\approx 1.5 \times 10^{22}$ Mx).

Acknowledgements

References

Berger, M.A.: 1985, *Astrophys. J. Suppl. Ser.* **59**, 433.
Berger, M.A. and Field, G.B.: 1984, *J. Fluid Mech.* **147**, 133.
Bothmer, V. and Schwenn, R.: 1998, *Annales Geophysicae* **16**, 1.
Dasso, S., *et al.*: 2003, *J. Geophys. Res.* **108**, 1362.
Green, L.M., *et al.*: 2002, *Solar Phys.* **208**, 43.
Larson, D.E., *et al.*: 1997, *Geophys. Res. Lett.* **24**, 1911.
Lepping, R.P., *et al.*: 1997, *J. Geophys. Res.* **102**, 14049.
van Driel-Gesztelyi, L., *et al.*: 2000, *J. Atmosph. Solar Terrestrial Phys.* **62**, 1437.

DEBRECEN PHOTOHELIOGRAPHIC DATA AND ITS COMPARISON WITH OTHER SUNSPOT DATABASES

G. MEZŐ, T. BARANYI and L. GYŐRI

Heliophysical Observatory of the Hungarian Acad. of Sciences
Debrecen, P.O. Box 30, H-4010, Hungary

Abstract. We compared the corrected sunspot area data of the Debrecen Photoheliographic Data (DPD) with the data of the Solar Optical Observing Network (SOON) and with the data of Rome and of Catania for the year 1988. The results of comparison were similar to the previous results of the years of 1986 and 1987. To facilitate the identification of the spot groups we made a new HTML presentation of DPD. We investigate the possibility of making a composite sunspot area database.

1. Introduction

Sunspot area measurements play an important role in the studies of sunspot groups and variations in solar irradiance. However, the measured areas may be burdened with systematic and random errors, which may affect the results in these fields. Mainly the total solar irradiance models can be improved by using more precise area data. In order to choose the most appropriate area data for a given study or create a homogeneous composite area database, there is a need to compare the sunspot areas provided by different observatories. While determining the sunspot area one has to cope with many difficulties which result in random and systematic errors (Győri, 1998; Baranyi *et al.*, 2001). These errors may affect the results of the study in which they are used. The random errors only cause scatter in the related data but the systematic errors can distort the main results. The systematic errors may vary in time because of the variation of the observing and measuring facilities, variation of the seeing on the site of the observatory, and so on. Therefore, the comparison of the data of different observatories has to be repeated from time to time.

2. Observational data

The Debrecen Photoheliographic Data (DPD) catalogue (Győri *et al.*, 2001, 2003) contains daily data for the whole group as well as each spot in it.

These data are measured on daily white-light full-disk photographic plates as it was carried out in Greenwich. DPD achieves full yearly coverage with the help of several cooperating observatories.

The catalogue of the Rome Observatory is also based on photographic plates. It contains the area of the whole group but in some cases some groups are omitted from the area measurements. Its coverage is limited by the local weather.

The SOON is a worldwide network of solar observatories, namely Boulder, Holloman, Learmonth, Palehua, Ramey, and San Vito. Culgoora also provides data for this network. The SOON makes 24-hour synoptic solar patrol and operates in a real time mode. Sunspot drawings are made daily, and the observing telescopes and measurement procedures are the same at all of these sites. It is the only sunspot catalogue that gives relatively complete (80%) daily coverage.

In the Catania Astrophysical Observatory sunspot drawings are also made on a daily basis. The yearly coverage is very good but limited by the local weather.

DPD data can be downloaded from `http://fenyi.solarobs.unideb.hu`, the other data are available from `http://www.ngdc.noaa.gov/stp`.

3. HTML presentation of DPD

Parallel to the measurements we created a user friendly web-presentation of DPD. The aim is to create a site which facilitates to survey the daily full-disc observations as well as the group and sunspot data. With the help of this presentation one can browse among the data in the DPD graphically. After choosing the date one can find the computer drawing of the solar disk. The spots are plotted as ellipses with the same areas as the spots have. The NOAA sunspot group number of the sunspot groups on these drawings are clickable and after clicking it the digitalized photographic image of the sunspot group appears with its numerical data of the DPD. It can be used via internet (`http://fenyi.solarobs.unideb.hu/DPD/index.html`) or in off-line mode after retrieving the files from this site.

4. Comparison of databases

At first a relational database has been made from the catalogues. Then, by using the Structured Query Language, the sunspot groups from each catalogue corresponding to those contained by the DPD have been selected for each day with the help of their position data. The groups close to the limb were omitted from the selection. In the problematic cases of the selection we checked this mutual correspondence by means of the HTML

TABLE I.   *Results of the linear regression for the area of the whole group.*

Database	Number of cases in 1988	a	b	Std. Error of the Estimate
Boulder	1321	-1.56	0.628	87.81
Catania	1630	-0.5	0.865	66.07
Culgoora	1542	-6.02	0.563	71.78
Holloman	1870	-4.23	0.725	74.94
Learmonth	1937	9.9	0.631	73.64
Palehua	1628	2.8	0.696	74.46
Ramey	1725	5.14	0.756	65.04
Rome	661	12.3	0.990	91.51
San Vito	1581	-1.49	0.739	91.31

presentation of DPD. Sometimes a given group of one of the catalogues was separated into two groups in the other catalogue. In these cases the areas of the separated groups have to be added. Finally we obtained tables in which there were data pairs. One member of the data pair was the sunspot group area measured in Debrecen and the other member of it was the area of the corresponding group measured in the other sites on the same day.

We made a linear regression analysis for these data sets in the form: dependent $= a + b *$ independent. The independent variable was the area U+P published in DPD. The dependent variables were the areas of the areas published in the other catalogues (see Table 1).

The results of Table 1 are similar to those which were published earlier by Baranyi *et al.* (2001) for 1986–87. This is an important result because the measuring method of DPD was different before and after July 1987.

5.   Composite sunspot area database

If the different databases are compared and the results of the linear regression is known, one can create a composite database. Because there is no systematic difference between the photographic databases ($b \sim 1$), it is plausible to accept the DPD as a standard for the graphical databases by dividing all the area data with the related b value. This procedure allows the homogenization of different databases giving an internal consistency after screening for outliers or errors. This method also allows the increase of the time resolution of the area data. By using the set of daily data, one can obtain hourly area data. Figure 1 shows an example for the area evolution of a sunspot group on the basis of a composite database.
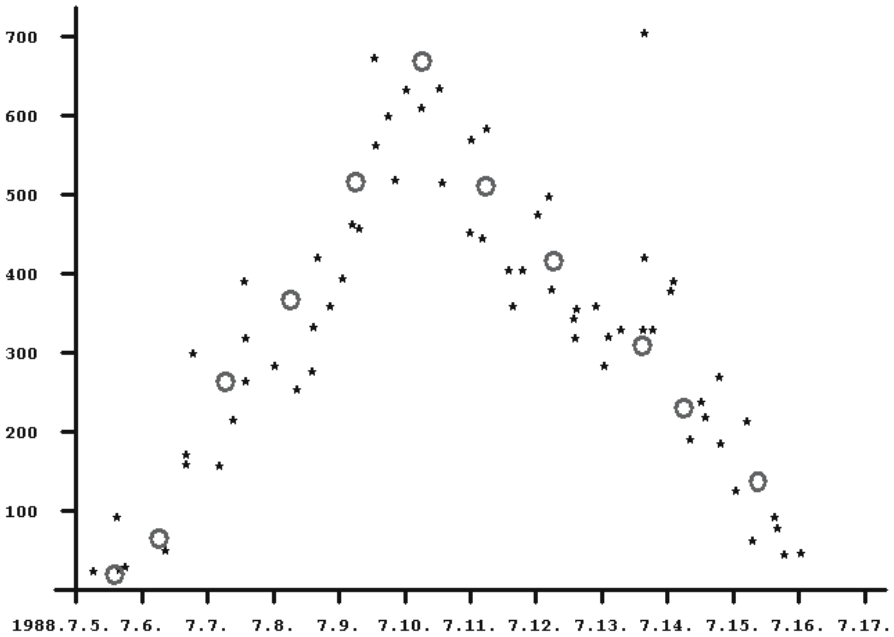
Figure 1.   Development of the whole area of group NOAA 5069 on the basis of DPD (circle) and recalibrated SOON data (stars).

Acknowledgements

References

Baranyi, T., Győri, L., Ludmány, A., and Coffey, H.E.: 2001, *Mon. Not. R. Astron. Soc.* **323**, 223.
Győri, L.: 1998, *Solar Phys.* **180**, 109.
Győri, L., Baranyi, T., Ludmány, A., Gerlei, O., and Csepura, G.: 2001, *Publ. Debrecen Obs. Heliographic Series* **12**, 1.
Győri, L., Baranyi, T., Ludmány, A., and Mező, G.: 2003, in A. Wilson (ed.), *Proc. ISCS 2003: Solar Variability as an Input to the Earth's Environment*, ESA SP-535, 707.

PROPERTIES OF A SMALL ACTIVE REGION IN THE SOLAR PHOTOSPHERE

S. STANGL and J. HIRZBERGER
Institute for Geophysics, Astrophysics, and Meteorology
University of Graz
Universitätsplatz 5, A-8010 Graz, Austria

Abstract. A small pore and its surroundings were tested for small bright points using 2D spectro-polarimetric data from the German VTT (Tenerife, Spain) using the Göttingen Fabry-Perot Interferometer. The Stokes $I \pm V$ profiles of the Fe I 6302 Å line were used for the computation of the line-of-sight Doppler velocity, v_{LOS}, and magnetic field maps, B_{LOS}. We present scatter plots of the line core intensity vs. these physical quantities.

1. Observations and data reduction

Two dimensional spectro-polarimetric scans were produced by scanning three spectral lines, two solar (Fe I 6301.5 Å and Fe I 6302.5 Å) and one telluric (O$_2$ 6302.8 Å), resulting in wavelength profiles of intensities proportional to $(I_\lambda \pm V_\lambda)$. These profiles were reconstructed following mostly the method described in Janßen (2003). The Stokes I and V profiles were computed by summation and subtraction of the restored profiles, respectively. Furthermore, the center-of-gravity method (Semel, 1967) was applied to the wavelength profiles to obtain the line-of-sight (hereafter: LOS) component of the magnetic field strength after

$$B_{\mathrm{LOS}} = \frac{\lambda_+ - \lambda_-}{2} \frac{4\pi mc}{eg_{\mathrm{L}}\lambda_0^2},$$

and additionally the LOS Doppler velocity maps according to

$$v_{\mathrm{LOS}} = \frac{\lambda_+ + \lambda_-}{2} \frac{c}{\lambda_0}.$$

The centroids of the right- and left-hand-circularly polarized profiles are denoted by $\lambda_\pm$, m and e are the electron's mass and charge, respectively, g_{L} is the effective Landé factor, λ_0 is the laboratory wavelength, and c the speed of light.
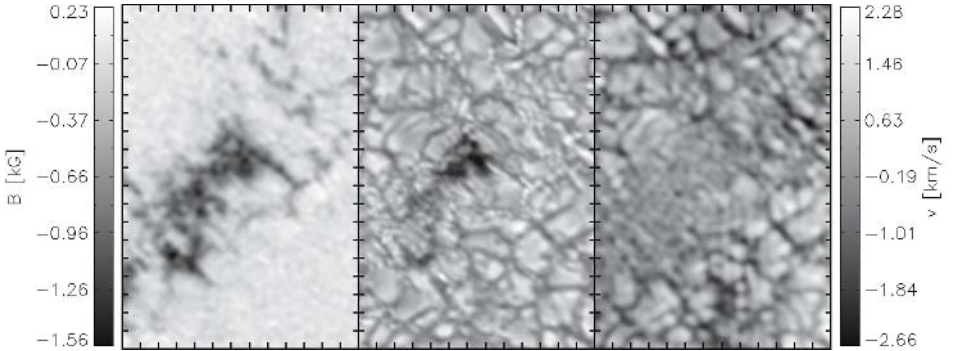
Figure 1.   Maps of the best scan of the analyzed time series. Left: magnetic map, middle: speckle image, right: velocity map. The resolution in all maps is approximately 0.''3. Tick marks are at 1'' distance.

Uitenbroek (2003) tested this method for reliability and accuracy and stated this procedure as an adequate method for high spatial resolution observations.

2. Results

Figure 1 exhibits the magnetic field map, the speckle reconstructed image, and the velocity map for the best scan of the time series obtained from the Fe I 6301.5 Å line. The resolution in the speckle image is 0.''3, in the two maps it is slightly higher than 0.''3. In the magnetic map the extension of the field beyond the visible dark features is obvious. Several small bright points are related to these strong fields.

Close investigation of the bright points in the speckle image compared with according line core images reveals that not every detected bright point in the speckle image is necessarily bright in the line core image and therefore – since the bright line core points are connected to B_{LOS} – not strong magnetic (some hundreds of Gauss) as usually assumed. This is in contradiction to the result of Muller *et al.* (2000). In contrast, bright points in the line core images are not always related to bright analogues in the speckle image.

This fact can be seen from the scatter plots of the best two images in Figure 2, where the line core intensity is displayed as a function of v_{LOS} for four different field strength intervals. The line core intensity is normalized to the continuum intensity (set to 1). The upper left plot in Figure 2 shows the pixels with the strongest magnetic field belonging to areas within the pore (lower half of cloud, i.e. dark in the line core) and the proto-pore (bright in the line core; cf. the speckle image in Figure 1). Intermediate strong fields (-1 kG $< B_{\mathrm{LOS}} < -0.6$ kG) are exhibited in the top right
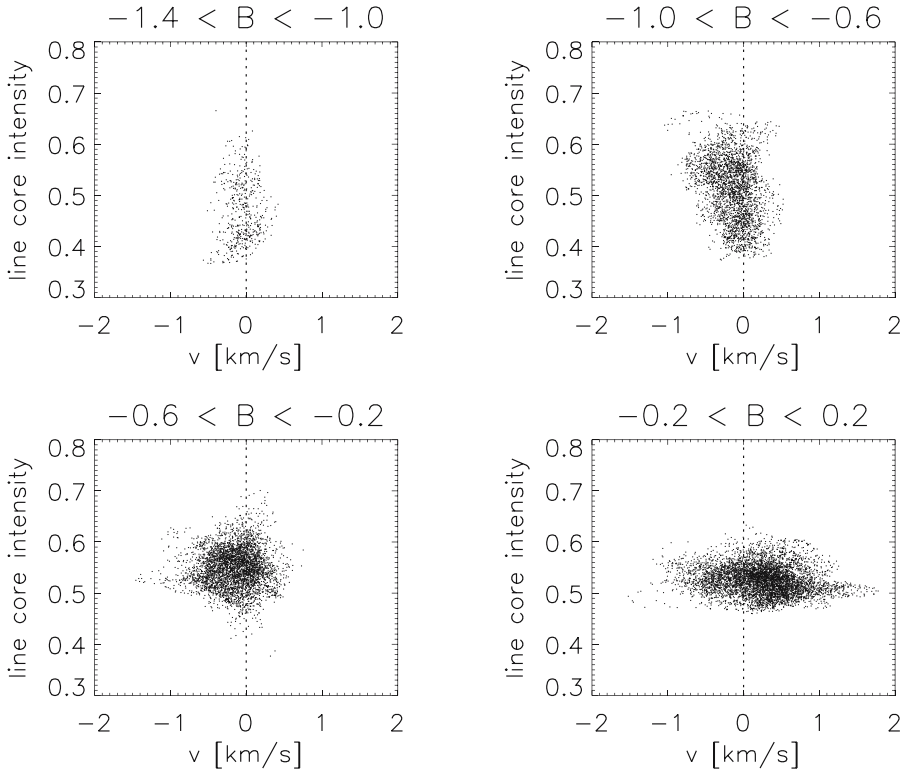
Figure 2.   Scatter plots of the line core intensity as a function of the line-of-sight velocity for four field strength ranges (in kG). The scatter changes shape from a vertical to a horizontal distribution as the field strength increases.

scatter plot, which mainly represents the pixels of the pore bordering area. The weaker the magnetic field (bottom left) the less dark are the pixels in line core intensity and the more the convective motion of the plasma becomes visible (bottom right).

In Figure 3 the scatter of the magnetic field strength is shown vs. the line core intensity. The majority of the pixels is located in a relative dense cloud between ±0.2 kG. This is predominantly the region of the granulation and the appendant intergranular lanes with line core intensities between 0.47 and 0.62. In the stronger magnetic regions the plot is more scattered than in the weak magnetic areas. The reason is that the pore is dark in the line center, however, there exist several magnetic features not yet dark in the higher atmosphere. These structures are small and change from bright to dark in the line core when they exceed some 300 km (Keller, 1992).

In general, on the one hand there exists a large variety of bright pixels in line core intensity lower than 0.6 with high field strength ($-1.4\,\mathrm{kG} < B_{\mathrm{LOS}} < -0.6\,\mathrm{kG}$) and negligible Doppler velocity and on the other hand
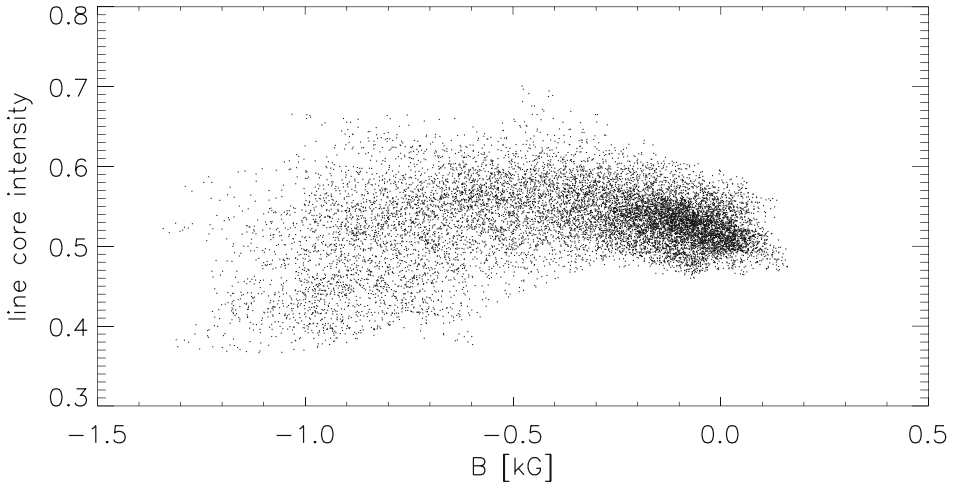
Figure 3.   Relation of the line core intensity to the line-of-sight magnetic field strength. The distribution is the more scattered the stronger the field.

there are points with the same line core intensity exhibiting only a few hundred Gauss field strength and higher v_{LOS}.

3.   Conclusions

We analyze the properties of a small pore and its surroundings, especially the relation of the line core intensity, the magnetic field strength B_{LOS}, and the Doppler velocity v_{LOS}. Bright points in the speckle image are not necessarily bright in the line core, formed in higher atmospheric layers than the continuum, and vice versa. This leads to the result that some bright points have small B_{LOS} and are not always co-spatial in the continuum and line center images.

References

Janßen, K.: 2003, PhD thesis, University of Göttingen.
Keller, C.U.: 1992, *Nature* **359**, 307.
Muller, R., Dollfus, A., Montagne, M., Moity, J., and Vigneau, J.: 2000, *Astron. Astrophys.* **359**, 373.
Semel, M.: 1967, *Annales d'Astrophysique* **30**, 513.
Uitenbroek, H.: 2003, *Astrophys. J.* **592**, 1225.

SMALL SCALE EVENTS SEEN IN SXT OBSERVATIONS

S. GBUREK and J. SYLWESTER
Space Research Center, Solar Physics Division
Polish Academy of Sciences
Wroclaw, Kopernika 11, Poland

Abstract. We analyze properties of small scale events observed by the Soft X-ray Telescope (SXT) aboard the *Yohkoh* satellite. The analysis focuses on a sequence of highest resolution SXT images of the quiet Sun. Non-standard methods were used in order to correct images for dark current and hot pixels. Basic properties of weak X-ray events found in the data are discussed.

1. Introduction

The Soft X-ray Telescope (SXT) was a grazing-incidence mirror instrument aboard the *Yohkoh* satellite. During the *Yohkoh* mission 1991–2001, the SXT recorded millions of solar soft X-ray images in the energy range 0.25–4.0 keV. The different SXT X-ray analysis filters allowed for recording solar radiation in slightly different energy bands for the purpose of plasma conditions diagnostic. A detailed description of SXT, its capabilities and operational performance can be found in Tsuneta *et al.* (1991).

For the purposes of the present study, full resolution SXT data (with a pixel size of 2.45 arcsec, i.e. ∼1800 km on the Sun) are particularly useful since weak soft X-ray sources are often small in size. In 2002, we performed an extensive search in the SXT data archive in order to find images of weak, well localized, compact events (Gburek, 2002a) and to determine their distribution on the Sun in solar cycle 23 (Gburek, 2002b).

Here we analyze a sequence of SXT data found during this search in which small-scale solar X-ray events are seen. This sequence consists of 177 images taken in the Al.1 and AlMg SXT analysis filters. These filters are used for quiet Sun observations in the lowest SXT energy ranges. All images are exactly of the same size (128×64 pixels) and are from the same region of the CCD. Each image was taken with a relatively long exposure (15.2 s) which is an advantage for observing faint solar features. However, due to the long exposure time all images are affected by high dark current levels
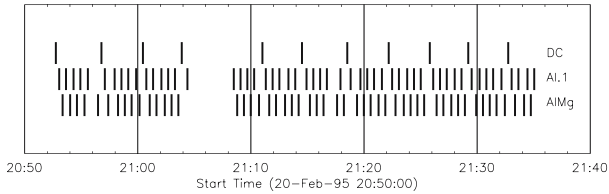
Figure 1.   Data coverage and cadence for the selected SXT observation period.
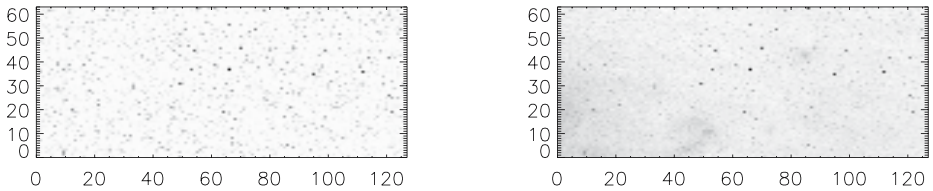
Figure 2.   Left: dark current SXT image taken on 20 February 1995 at 21:03:53 UT. Right: SXT X-ray image taken in the Al.1 filter on 20 February 1995 at 20:54:55 UT. The darker the gray intensity the stronger the image signal.

and hot pixel defects. Therefore, non-standard data reduction methods are necessary. Fortunately, SXT dark current images (of the same size, exposure time and resolution) were regularly recorded and sandwiched in between the X-ray images during the selected observation sequence. These dark current frames allow for almost perfect dark current subtraction and reduction of hot pixel effects in the X-ray data.

2. Data selection and reduction

The data cube selected for analysis consists of 52 images in the AlMg filter, 54 images in the Al.1 filter and 11 dark current frames. The image sequence starts with a dark current image recorded on 20 February 1995 at 20:52:45 UT and ends with an Al.1 image taken at 21:35:03 UT the same day. The data coverage and cadence in this data set is shown in Figure 1.

All selected images are of the same size (128×64 pixels), equal exposure time and were taken from the same CCD region centered at the CCD pixel (735, 591). Figure 2 shows an example of the SXT dark current and X-ray image from the analyzed data cube.

From each X-ray SXT image we subtracted the dark current image closest in time. This gave us much better results than the use of the standard SXT dark current reduction method. In order to reduce effects of optical leak which significantly disturb the X-ray intensities (particularly in Al.1 filter images), we subtracted also the leak images from the X-ray data.

The inspection of the signal in the dark current image from Figure 2 shows many pixels with exceedingly high signal value. At these hot pixel
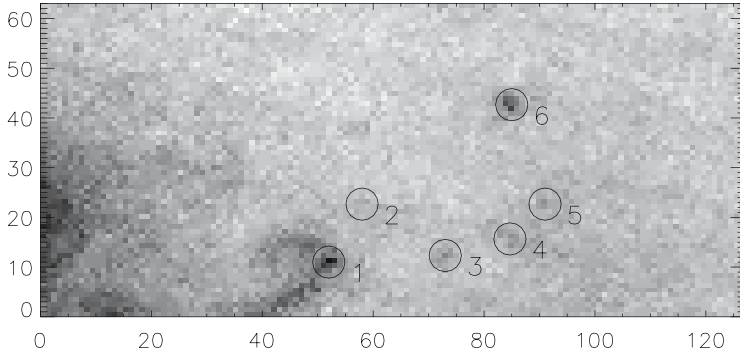
Figure 3.   SXT X-ray image after reduction (the raw image is shown on the right hand side of Figure 2). Encircled and labeled are location of six sources of weak soft X-ray emission.

positions, also in the X-ray data substantial deviations from the signal value in comparison to the neighbor pixels occur. Therefore we applied an additional correction for hot pixels. First, we checked that still many pixels in the dark current frames have regular signal values. The histograms of the dark current images show a sharp peak at the signal value of about 16 data numbers (DN) which is an acceptable dark current generation rate for the chosen data set. We found only about 230 pixels (3% of all pixels in each image) with a signal above 16 DN plus three times the r.m.s. error of the dark images. These pixels are considered as hot pixels. We identified the positions of all hot pixels found in the dark current frames and corrected the signal value in the X-ray images at these positions. The signal value at hot pixel positions was replaced by the average signal from neighboring, not hot pixels. All the X-ray images were processed in the way described above. An example of a reduced, clean image is shown in Figure 3 in which we also marked the location of six sources of weak soft X-ray emission which are studied in more detail in the next section.

3. Properties of small X-ray events

The analysis of the X-ray data sequence for the events encircled in Figure 3 shows that they brighten up and fade nearly simultaneously in their 10-min life-time interval. Events 2 to 5 are located along the edges of an oval in which no significant emission rise above the background level is seen. The diameter of the oval estimated from the distance between sources 3 and 5 in Figure 3 is about 56400 km.

To estimate the physical properties of our event sample we performed a more detail study of event 5, which is the average scale event in the entire set. From the SXT X-ray image pairs taken in the Al.1 and AlMg filter

we determined that the source kernel temperature was about 1.3×10^6 K and the emission measure 5.4×10^{44} cm^{-3} near the time of the maximum intensity. Assuming that the volume of the event kernel was comparable to the volume of small observed X-ray loops ($\sim 2.0 \times 10^{25}$ cm^3), we calculated that the thermal energy at the maximum was only $\sim 5.6 \times 10^{25}$ erg – a value below the thermal energy content estimated from RHESSI observations of microflares (Benz and Grigis, 2002). Inspecting the light curve of event 5, we note that it has a similar time evolution as solar flares. The emission rises suddenly at about 21:10 UT, reaches maximum at about 21:17 UT and then again drops to the background level which is slightly higher than at the beginning of the event.

4. Conclusions

We have performed an analysis of SXT X-ray observations of the quiet Sun. The chosen data sequence was reduced using non-standard methods for dark current subtraction and corrected for hot pixel effects. We found that such corrections necessary in order to obtain acceptable data quality for the investigation of small X-ray events in SXT measurements. We found that five of the identified events are located along the edges of an oval (with a diameter of ~ 56400 km) in which no significant emission is observed. A closer analysis of the physical properties of one of the selected events shows that the thermal energy released near maximum intensity time is below the level reported for microflares. The light curve of this event revealed a temporal evolution similar to that of solar flares.

References

Benz, A. and Grigis, P.: 2002, *Solar Phys.* **206**, 431.
Gburek, S. and Sylwester, J.: 2002a, *Solar Phys.* **206**, 273.
Gburek, S. and Sylwester, J.: 2002b, in A. Wilson (ed.), *Solar Variability: From Core to Outer Frontiers*, ESA SP-506, 359.
Tsuneta, T. *et al.*: 1991, *Solar Phys.* **136**, 37.

PROPERTIES OF TYPE IV RADIO BURSTS WITH PERIODICAL FINE STRUCTURES

J. MAGDALENIĆ and B. VRŠNAK
Hvar Observatory, Faculty of Geodesy
Kačićeva 26, HR-10000 Zagreb, Croatia

P. ZLOBEC and M. MESSEROTTI
INAF – Osservatorio Astronomico di Trieste
Via G.B. Tiepolo 11, I-34131 Trieste, Italy

M. TEMMER
IGAM, University of Graz
Universitätsplatz 5, A-8010 Graz, Austria

Abstract. Properties of solar type IV radio emission consisting of a continuum and superposed fine structures are investigated. We analyze a large data set of single frequency time profiles recorded in the dm–m band by the INAF-OAT radiotelescope. It is shown that the maximum peak is proportional to the average value of the background continuum. This relationship is similar at all observing frequencies, whereas the relationship between the average background level and the burst duration seems to be frequency dependent. The existence of short type IV-like events that consist of only one "train" of periodical structures is reported.

1. Introduction

The broadband type IV background continuum can be explained by gyro-synchrotron emission of accelerated electrons. On the other hand, if the superimposed fine structures are considered, coherent plasma emission mechanisms seems to be more appropriate (Aurass *et al.*, 2003). Therefore, further analyses of type IV bursts are required. This paper is a continuation of the analysis of type IV events comprising fine structures in the dm–m range (Magdalenić *et al.*, 2002, 2003), focusing on type IV continua "hosting" fine structures (FSs) and periodical fine structures (PFSs).
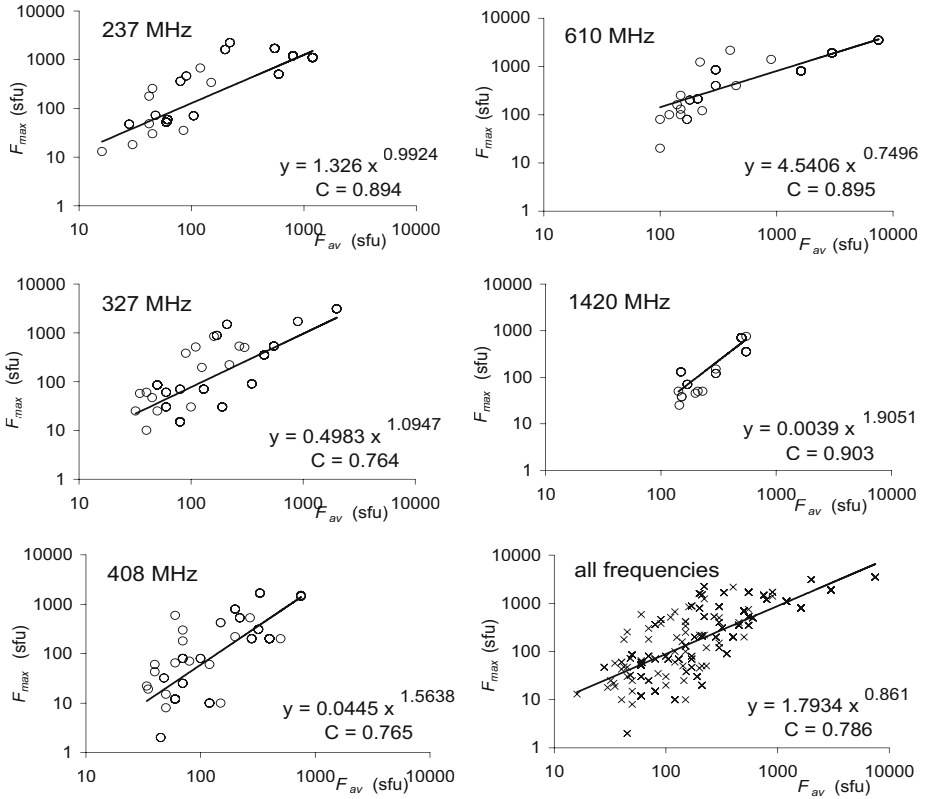
Figure 1.   Maximum intensity of the type IV burst, F_{max}, as a function of the average background intensity, F_{av}. The results are presented for each observing frequency separately as well as for the whole data set. The exponents of the power law fit are close to 1, thus indicating a proportionality $F_{max} \propto F_{av}$.

2. Data set and results

We analyzed single frequency time profiles (at 237, 327, 408, 610, and 1420 MHz) recorded by the Trieste Solar Radio System at INAF-Trieste Astronomical Observatory (TSRS-OAT). The data set is limited to observations carried out between October 1997 and August 2000.

Fine structures are found superposed on type IV continua in 101 events, and 55% of these contain PFSs. For this subsample we estimated:

- the duration of the type IV burst, T (minutes);
- the average value of the background continuum measured near the type IV burst maximum, F_{av} (solar flux units, sfu);
- the maximum peak of the type IV burst, F_{max} (solar flux units, sfu);
- the number of individual PFS-"trains" in each type IV burst, N;
- the duration of individual PFS-trains, t (seconds).
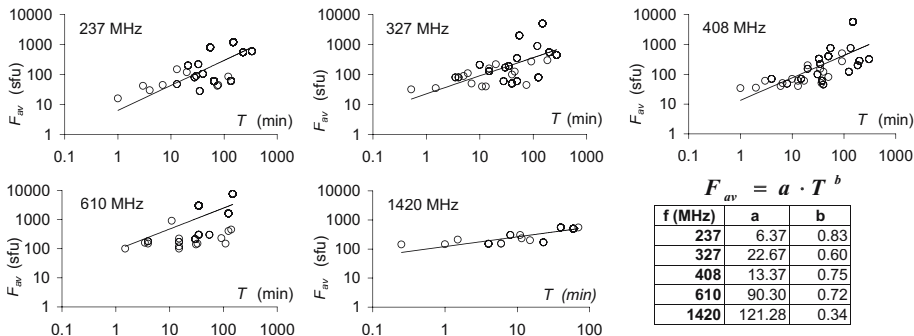
Figure 2.   Relationship between the average value of the background continuum, F_{av}, and the duration of type IV burst, T, for each observing frequency. The parameters of the power law fit are shown in the enclosed table. The correlation coefficients are in the range $C = 0.56$ to 0.84.

Inspecting the properties of the selected type IV bursts, we first analyzed the dependence of the maximum peak on the average value of the type IV continuum, $F_{max}(F_{av})$. Figure 1 reveals an almost-linear relationship between these two parameters. Note that, at higher frequencies, the range of F_{max} values decreases. It is reduced from almost four orders of magnitude at metric wavelengths to one order of magnitude at decimetric wavelengths.[1] This result is consistent with the observational fact that microwave continua are smoother, with lower FSs and PFSs occurrence rate, compared to decimetric events. A narrower range of intensities at higher observing frequencies is not surprising since at high frequencies the radio waves are more attenuated by collisional damping than at lower frequencies. Therefore, statistically, higher intensities are required for the escape at higher frequencies (Aschwanden *et al.*, 1985).

In Figure 2 the dependence of the average background intensity, F_{av}, on the duration of type IV bursts, T, is shown. The duration (in minutes) is spread over three orders of magnitude at all observing frequencies. Most of the considered type IV bursts could be classified as "ordinary" type IV bursts ($T > 5$ min) covering a broad-band frequency range ($\Delta f > 100$ MHz). However, we found also very weak bursts (few sfu) lasting only some tens of seconds. In this "type IV-like" events almost the whole burst is consisting practically of just fine structures.

The considered type IV continua host a variable number of distinct individual short lived elements – PFS-trains. Sometimes there are only a few trains and sometimes a large number of them is found. Statistically,

---

[1] We emphasize that the pre-burst background (not substracted) does not depend much on the observing frequency (typically from 10 sfu at 237 MHz to 50 sfu at 1420 MHz), and it does not seriously affect the results.
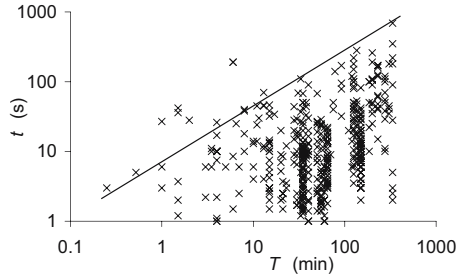
Figure 3.   Duration t of individual PFS-trains as a function of the duration T of the type IV burst. The depicted line indicates well defined upper limit of t. Most of the events above the line are short "type IV-like" events.

the durations of individual PFS-trains, t, can be longer in a longer duration type IV continuum (see Figure 3): longer lasting type VI bursts "allow" a rather wide palette of duration of PFS-trains. The scatter of t at a single observing frequency is up to one order of magnitude.

3. Conclusions

The analysis of type IV bursts hosting fine structures provided the following results: 1) There is a distinct proportionality between the maximum intensity peak of type IV bursts and the average background intensity, $F_{max} \propto F_{av}$. Values of F_{max} are reduced by three orders of magnitude from metric to decimetric wavelengths; 2) the duration of type IV bursts, T, is not frequency dependent; 3) longer lasting type IV bursts "allow" longer durations of PFS-trains, the upper limit of the $t(T)$ dependence is rather well defined.

Acknowledgements

References

Aschwanden, M.J., Wiehl, H.J., and Benz, A.O.: 1985, *Solar Phys.* **97**, 159.
Aurass, H., Klein, K.-L., Zlotnik, E.Ya., and Zaitsev, V.V.: 2003, *Astron. Astrophys.* **410**, 1001.
Magdalenić J., Zlobec P., Messerotti M., and Vršnak B.: 2002, in A. Wilson (ed.), *Solar Variability: From Core to Outer Frontiers*, ESA SP-506, 331.
Magdalenić, J., Zlobec, P., Vršnak, B., Messerotti, M., Aurass, H., and Veronig, A.: 2003, *Hvar Obs. Bull.* **27**, 131.

TESTING THE NEUPERT EFFECT

A.M. VERONIG
Institute for Geophysics, Astrophysics and Meteorology
University of Graz, A-8010 Graz, Austria

J.C. BROWN
Astrophysics Group, Department of Physics and Astronomy
University of Glasgow, Glasgow G12 8QQ, U.K.

B.R. DENNIS, R.A. SCHWARTZ, L. SUI
and A.K. TOLBERT
Laboratory for Astronomy and Solar Physics, Code 682
NASA/Goddard Space Flight Center, Greenbelt, MD 20771

Abstract. The Neupert effect is commonly interpreted as evidence that the energetic electrons causing the hard X-ray flare emission are the main source of heating and mass supply of the soft X-ray emitting hot coronal loop plasma. RHESSI and GOES data are used to test the Neupert effect by comparing the beam power supply inferred from hard X-ray spectra and the actual power required to explain the observed soft X-ray emission.

1. Introduction

The Neupert effect is the observed temporal correlation of the flare microwave or hard X-ray (HXR) flux with the time derivative of the soft X-ray (SXR) flux (Neupert, 1968; Dennis and Zarro, 1993). This is often taken to mean that the energetic electrons responsible for the HXR emission by thick-target collisional bremsstrahlung are the main source of heating and mass supply (via chromospheric evaporation) of the hot coronal plasma seen in SXRs. We test these physical implications by comparing the beam power supply inferred from RHESSI HXR spectra and the actual power required to explain the GOES SXR flux and spectrum, allowing for variations in both emission measure EM and temperature T and also for cooling losses.

2. Empirical Neupert effect model

Based on a simple model of the flare energy budget, we use flare SXR and HXR observations to compare the total rate of change of the SXR plasma

263
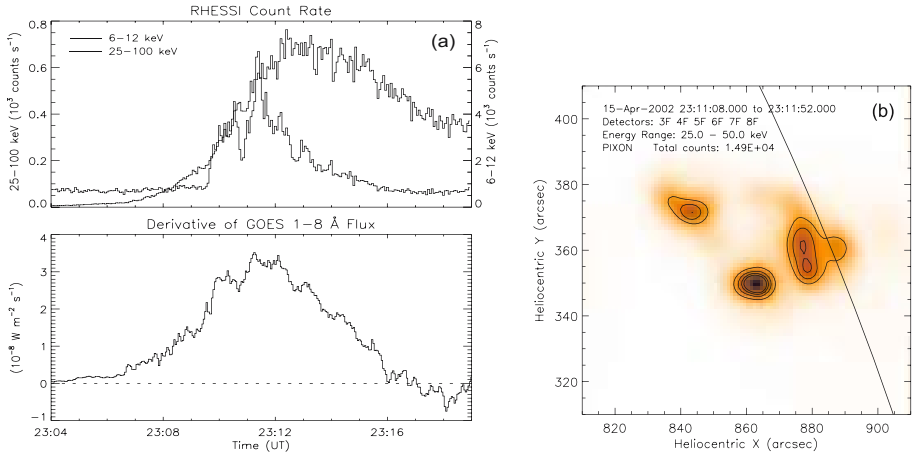
Figure 1. a) RHESSI count rates in the 6–12 keV and 25–100 keV energy bands (top panel), and time derivative of the GOES 1–8 Å flux smoothed with a 30-s box-car average (bottom panel). b) RHESSI 25–50 keV image reconstructed with PIXON using front detector segments 3 to 8 (giving an angular resolution of $\sim 7''$).

energy content with the electron beam power that goes into the hot part of the loop. The model is described in detail in Veronig *et al.* (2004).

Heating, e. g. by an electron beam with power $P_{\text{in}}(t)$, has not only to provide at each instant of time t the observed increase of the SXR plasma energy content, $\dot{U}_S(t)$, but it also has to offset cooling losses by radiation, $L_{\text{rad}}(t)$, and by conduction, $L_{\text{cond}}(t)$, i. e.

$$P_{\text{in}}(t) = \dot{U}_S(t) + L_{\text{rad}}(t) + L_{\text{cond}}(t) \ (\text{erg s}^{-1}) . \tag{1}$$

Taking into account its mass, thermal, kinetic and gravitational energies, the observed SXR plasma energy content is estimated to lie within the extreme range $(3\text{--}10)\cdot kT(t)\,(EM(t)V)^{1/2}$ where k denotes Boltzmann's constant, T the temperature, EM the emission measure and V the loop volume. Conductive and radiative losses are approximated by $L_{\text{cond}}(t) \approx (4A/l)\kappa_0 T(t)^{7/2}$ and $L_{\text{rad}}(t) \approx EM(t) \cdot 6 \cdot 10^{-22}(T(t)/10^5)^{-1/2}$ where κ_0 is the Spitzer conductivity and l the loop length.

From RHESSI HXR spectra we derive the electron beam power injected above energy E_1, $P_1(t)$, assuming a collisional thick-target model (Brown, 1971). We only want the part of the beam power that goes into the hot loop (i. e. above the transition zone), given as

$$P_{\text{beam}}(t) = P_1(t) \cdot \left[1 - \frac{(\delta(t) - 2)}{2} B\left(\frac{\delta(t)}{2} - \frac{1}{2}, \frac{3}{2}\right) \left(\frac{3KN(t)}{E_1}\right)^{-\delta(t)+2}\right] \tag{2}$$

with $B(a, b)$ the complete beta function, K the collisional stopping parameter, δ the electron spectral index and N the loop column density.
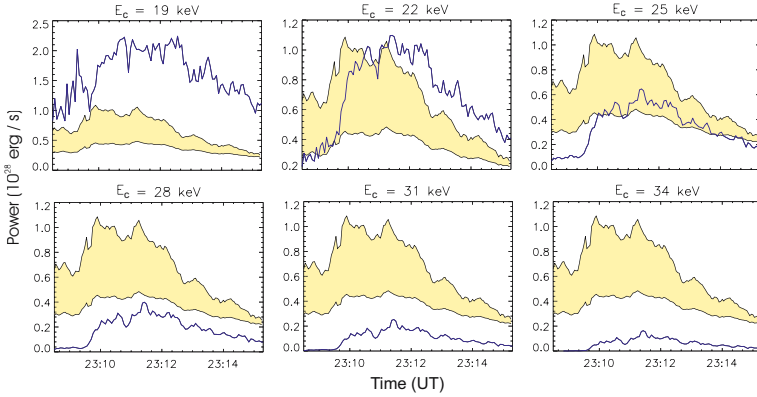
Figure 2. Comparison of the actual power $P_{in}(t)$ required to explain the observed SXR flux (min/max range: shaded area) and the electron beam power $P_{beam}(t)$ that goes into the hot part of the loop (thick line) calculated for different low cut-off energies E_c.

3. Observations and results

Here we test the Neupert effect by comparing $P_{in}(t)$ and $P_{beam}(t)$ derived from RHESSI and GOES observations for the M1.2 flare that occurred on 15 April 2002, 23:05 UT near the solar limb (N20 W72). The RHESSI instrument is designed to investigate high-energy emission from solar flares from 3 keV to 17 MeV with high spectral and spatial resolution (Lin *et al.*, 2002). During the flare the RHESSI thin attenuators (Smith *et al.*, 2002) were in the field of view, limiting the X-ray observations to $\gtrsim$6 keV.

In Figure 1a the evolution of RHESSI 6–12 and 25–100 keV count rates (4-s integration) together with the derivative of the GOES 1–8 Å flux (3-s data) are plotted, revealing some observational Neupert effect. Figure 1b shows a 25–50 keV RHESSI image reconstructed with the PIXON method (Hurford *et al.*, 2002). The source of the HXR emission is concentrated in two footpoints and the loop top.

RHESSI images are used to obtain footpoint area $A \simeq 21.5 \cdot 10^{16} \, cm^2$, loop length $l \simeq 77.3 \cdot 10^8 \, cm$, and volume $V \simeq 16.7 \cdot 10^{26} \, cm^3$ (assuming a cylindrical geometry). GOES 0.4–5 and 1–8 Å observations give a peak emission measure $EM_p \simeq 1.3 \cdot 10^{49} \, cm^{-3}$ and peak temperature $T_p \simeq 17.0 \, MK$. From l and EM we obtain a peak column density $N_p \simeq 3.5 \cdot 10^{20} \, cm^{-2}$. RHESSI spectroscopy reveals steep HXR spectra ($\delta \lesssim 5.9$) and a peak beam power in electrons above 25 keV, $P_{25,p} \simeq 6.7 \cdot 10^{27} \, erg \, s^{-1}$.

In Figure 2 we plot the extreme range of power required to explain the SXR flux, $P_{in}(t)$, together with the beam power that goes into the loop above the transition zone, $P_{beam}(t)$, for different values of the low cut-off energy E_c of the accelerated electron spectrum (E_c is basically unknown). To match the total energy in the hot SXR emitting plasma and in the electron
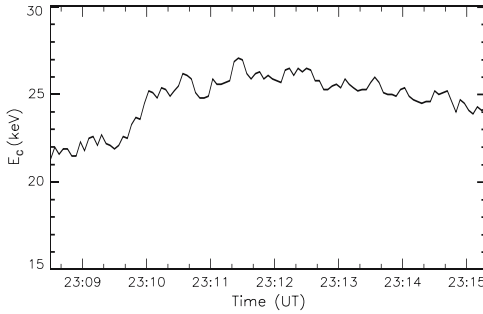
Figure 3. Evolution of the low cut-off energy E_c derived from the demand that at each instant of time $P_{\text{in}}(t) = P_{\text{beam}}(t)$.

beam, i. e. the cumulative integrals of the plotted curves, E_c should be $\sim$25 keV. For this E_c, $P_{\text{in}}(t)$ and $P_{\text{beam}}(t)$ do show a reasonable agreement but strong deviations occur during the first $\sim$100 s where $P_{\text{beam}}(t)$ is too low and does not lie within the estimated min/max range of $P_{\text{in}}(t)$ (see Fig. 2). However, if we allow E_c to vary in time, then only small changes are necessary to yield a perfect match between $P_{\text{beam}}(t)$ and $P_{\text{in}}(t)$ (Fig. 3).

4. Conclusions

If the beam low cut-off energy E_c is taken as constant, the correlation of $P_{\text{beam}}(t), P_{\text{in}}(t)$ is not better than that of the HXR flux and the time derivative of the SXR flux (i. e. the Neupert light curve effect). This result means either that fast electrons are *not* the main source of SXR plasma supply and heating or that E_c varies with time. Because $P_{\text{beam}}(t)$ depends strongly on E_c for the typically steep HXR spectra, only small variations in $E_c(t)$ need be invoked to get a perfect correlation of $P_{\text{beam}}(t), P_{\text{in}}(t)$.

Acknowledgements

References

Brown, J.C.: 1971, *Solar Phys.* **18**, 489.
Dennis, B.R. and Zarro, D.M.: 1993, *Solar Phys.* **146**, 177.
Hurford, G.J., Schmahl, E.J., Schwartz, R.A. *et al.*: 2002, *Solar Phys.* **210**, 61.
Lin, R.P., Dennis, B.R., Hurford, G.H. *et al.*: 2002, *Solar Phys.* **210**, 3.
Neupert, W.M.: 1968, *Astrophys. J.* **153**, L59.
Smith, D.M., Lin, R.P., Turin, P. *et al.*: 2002, *Solar Phys.* **210**, 33.
Veronig, A.M., Brown, J.C., Dennis, B.R. *et al.*: 2004, *Astrophys. J.*, submitted.

THE FAINT YOUNG SUN PROBLEM

A. HANSLMEIER

Institute for Geophysics, Astrophysics and Meteorology
University of Graz, A-8010 Graz, Austria

Abstract. In this contribution we give a review on the faint young Sun problem. It will be demonstrated that new results on climate studies of Mars, Venus and Earth can give hints and constraints on the early evolution of the Sun.

1. Introduction

The total solar irradiance which is the integral over the spectral irradiance over all wavelengths is about 1366 W m^{-2}. In the visible and IR part of the spectrum it can be very well fitted by a black body radiation curve of a temperature of 5770 K and at present, the variation caused by different fluxes during solar maximum and solar minimum in these wavelengths is very low ($\sim 10^{-3}$). At a wavelength of about 200 nm the variation increases by a factor of 10, in the EUV this variation is more than 100! Short wavelength radiation has important influences on planetary atmospheres such as ionization, photolysis, warming and density variations.

The penetration of different parts of the solar irradiance into the Earth's atmosphere decreases with shorter wavelengths. The mid UV penetrates to 50 km, the far UV to 100 km, the EUV to 150 km in the Earth's atmosphere.

From simple theoretical arguments it follows that the early Sun produced 70% of its today luminosity. The gas pressure P is proportional to $\sqrt{\Re T/\mu}$, where $\Re$ is the gas constant, T the temperature and μ the mean molecular weight. The early Sun had a much lower primordial He content ($\sim 23\%$) than today and therefore μ was smaller implying a lower temperature T to produce the pressure to balance gravity and thus lower luminosity.

$E = \sigma T^4$ denotes the energy received from the Sun and since the energy was only 0.7 of today's value, the resulting temperature was $T_{\text{early}} \sim 0.97\ T_{\text{now}}$. The present globally averaged value on the Earth's surface

is 283 K. The lower solar luminosity means a global average temperature on Earth of 258 K.

Under present atmospheric conditions such a low temperature would imply global glaciation on Earth, however we have no geological evidence of world wide glaciations during the last 2.8×10^9 years.

Let us consider Mars. At a distance of 1.52 AU it receives only 43% of S_{Earth}, where $S_{\text{Earth}} = 1366$ W m^{-2}. Today, its mean surface temperature is 218 K, the atmospheric pressure 6.5 mbar. During the young Sun phase, the temperature would have been lowered to 196 K, its present CO_2 content in the atmosphere would have frozen out and the atmospheric pressure would have been reduced to 1 mbar. Yet we see erosion networks and channels on Mars that appear to have been caused by flowing liquids that are impossible under the present atmospheric conditions (too low pressure and temperature).

2. Influence on planetary atmospheres

We can learn much about the evolution of the Sun by comparing it with other stars that are similar to it. Since the mass is the most critical parameter for stellar evolution, stars with masses in the range of $1\, M_\odot \pm 0.1\%$ can be classified as solar like. Now there exists a list of solar like stars that are in different evolutionary states. There exists a relation between stellar rotation rates and their variability. Younger stars, rotating faster than older ones, are strongly variable, especially in the short wavelengths.

From the theory of stellar evolution we know that the Sun passed through a T Tauri phase before reaching the main sequence at an age of 100 Myr at a time when planetary atmospheres formed. T Tauri stars are young pre main sequence stars still contracting. T Tauri stars were detected in 1945, and besides optical variability, strong chromospheric lines, and X-ray activity which is 1000 times the present Sun was detected. Some of them show molecular outflows, stellar winds (strong) and half of them have disks (near IR and sub mm excess emission). Also the UV radiation was a factor of 100 higher than today. Huge spots can cover up to 50% of the hemisphere (present Sun max. 1–2%). Luminosity variations are up to 50%, therefore the early planets were exposed to strong irradiance variations.

The early planets were strongly affected by the active early Sun:

- Chemical purification of the atmosphere, H, He evaporate, heavier components left (N_2, CH_4 and NH_3).
- Solar wind: strong stellar wind could cause a strip away of the atmosphere if the planet does not have a strong magnetic field.

- Dissociation: on the early Earth, there was no protective ozone layer, energetic X-ray and UV emission from the active Sun caused a dissociation of molecules.
- Evolution of life on Earth: Deeper in the atmosphere, the radiation caused by the star's higher magnetic activity induces reactions in the mixture of N, CH_4, H_2O, NH_3 and residual hydrogen. Out of that form amino acids, sugars, purines and pyrimidines (that combine with sugar and phosphate to make the nucleotides). The reactions driven by the solar energetic radiation may have outweighed those induced by Earth's own processes like lightning by a factor of up to 30.

3. Solutions for the faint young Sun problem

The geological records show that there was liquid water on Earth even in the first billion years of its existence. Yet, the young Sun should have been some 30% fainter than the current mature Sun according to stellar-evolution models. This should have resulted in a much cooler Earth, covered in ice. Why this did not occur remains a mystery. The greenhouse effect as a result of the high concentration of carbon dioxide may have compensated the lower energy input from the young Sun. Alternatively, the Sun may have been significantly more massive, and therefore brighter, early in its life; if there has been substantial mass loss in a strong wind in the first billion years, this paradox would be resolved.

There seems to be an upper limit for pCO_2 of 30 PAL (Present Atmospheric Level). This would be an order of magnitude below to what is needed to induce a strong enough greenhouse effect to obtain a warm earth (Rye *et al.*, 1995). pCO_2 cycling and climate impacts were discussed by Zahnle and Sleep (1999). Schatten and Endal (1982) suggested that volcanic influences could allow a passage from the frozen branch into the unfrozen branch of climate models. A broad equatorial belt of volcanic ash is one scenario which would allow a transfer from the frozen earth state into the unfrozen one.

Shaviv (2003) found that the faint young sun problem can be partially resolved by considering the cooling effect that cosmic rays are suspected to have on the global climate and by considering that the younger Sun must have had a stronger solar wind such that it was more effective at stopping cosmic rays from reaching Earth. The paradox can then be completely resolved with the further contribution of modest greenhouse gas warming. When adding the cosmic ray flux modulation by a variable star formation rate in the Galaxy, the long-term glacial activity on Earth can also be recovered. As to the future, we find that the average global temperature will increase by typically 10 K in the coming 2 Gyr.

The early climate on Mars was studied by Bullock *et al.* (2001) where further references can be found. It is stressed that two factors can be used to explain a warm period of ancient Mars: CO_2 clouds and a dense CO_2 and H_2O atmosphere and intense vulcanism in the Tharsis region. The volcanic magma probably contained substantial quantities of H_2O, CO_2, and sulfur gases that would have been released, providing input of gases to the atmosphere and possibly contributing to an early, thicker atmosphere and cloud formation.

Thus there is no definite solution of the faint young Sun problem. It is clear that a combination of planetary data, solar analogue stars, solar evolution models can bring new insights and rule out some theories.

Acknowledgements

References

Bullock, M.A., Grinspoon, D.H., and Phillips, R.J.: American Geophysical Union, Fall Meeting 2001, abstract P31B-03.
Rye, R., Kuo, P.H., and Holland, H.D.: 1995, *Nature* **378**, 603.
Schatten, K.H. and Endal, A.S.: 1982, *Geophys. Res. Lett.* **9**, no. 12, 1309.
Shaviv, N.J.: 2003, *J. Geophys. Res.* **108**, Issue A12, SSH 3-1.
Zahnle, K.J. and Sleep, N.H.: 1999, in *Proc. Ninth Annual V. M. Goldschmidt Conference*, Cambridge, Massachusetts, 7607.

CCD SPECTROSCOPY OF SOLAR ROTATION

S. JEJČIČ and A. ČADEŽ

University of Ljubljana, Department of Physics
Jadranska 19, SLO-1000 Ljubljana, Slovenia

Abstract. Velocity measurements in the solar photosphere were obtained by the double monochromator DFS-12 on September 10, 13 and 14, 1999 at Ljubljana observatory. The parameters are determined from Doppler shift measurements of the Fraunhofer sodium D_2 line at 5891.583 Å. Five telluric water lines in the interval between 5888.847 Å and 5899.788 Å were used for wavelength calibration. The results were fitted to the rotation model yielding the solar rotation (sidereal) coefficients and gravitational redshift velocity. The rotation coefficients for these three successive days are compared with the coefficients derived by Howard and Harvey (1970) and Wittmann (1996).

1. Introduction

The solar rotation measurements with sunspot motion started by Carrington in the middle of the 19th century, who first noticed the differential rotation of the Sun. Since then, solar rotation has been measured by many observers. The four different methods that are used – Doppler shift measurements, Doppler feature tracking, magnetic feature tracking and p mode splitting (Beck, 2000) – obtain variable rotation rates. Observers notice that solar rotation rates, determined by the Doppler shift method depend both on the time of observation and the line chosen for Doppler shift tracking. The solar rotation rates from those measurements are generally slightly lower (by about $\sim 2\%$) than rates determined by Doppler feature tracking (Snodgrass and Ulrich, 1990).

We measured the solar rotation with the Doppler shift method. The advantage of this method is that it gives a measure of the plasma motion at the solar surface and is not limited by the visibility of the tracking feature. However, one must be careful about problems due to instrumental and atmospheric scattered light (Scherrer *et al.*, 1980), interference fringes in the spectrograph and instrumental polarization (Howard *et al.*, 1980). Large-scale background velocity fields such as limb redshift, meridional flow and torsional oscillations may introduce systematic errors that require thorough analysis.
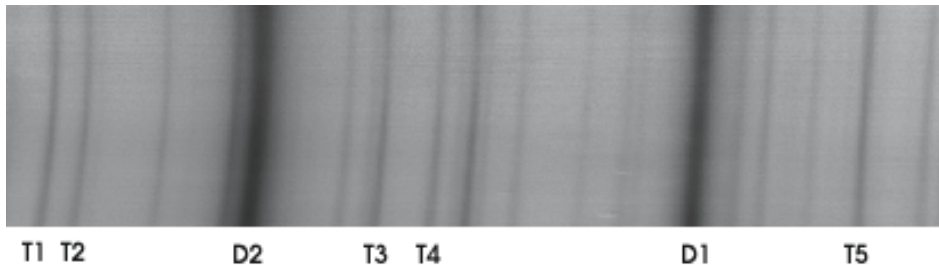
Figure 1.   Solar spectrum between 5888.192 Å and 5900.522 Å. D_2 and D_1 are sodium lines with wavelengths $\lambda_{D_2} = 5891.583$ Å and $\lambda_{D_1} = 5897.557$ Å, respectively. The telluric water lines (which serve for wavelength calibration) are marked by T_1, T_2, T_3, T_4, and T_5. Their wavelengths are $\lambda_{T_1} = 5888.847$ Å, $\lambda_{T_2} = 5889.286$ Å, $\lambda_{T_3} = 5893.284$ Å, $\lambda_{T_4} = 5894.022$ Å, and $\lambda_{T_5} = 5899.788$ Å.

2. Measurements

Our observations were taken with the double monochromator DFS-12 (Jejčič and Čadež, 2002) on September 10, 13 and 14, 1999 at the Ljubljana observatory. The spatial-sampling interval was $0.83''$/pixel and the wavelength-sampling interval was 0.01249 Å/pixel or 636 m s^{-1}/pixel.

Our image of the Sun has a diameter of 16 mm and is scanned during its movement across the input slit of the spectroscope with an exposure time of 1 s (Jejčič and Čadež, 2003). The whole data set consists of a scan of the solar disk along four strips equally spaced with respect to the solar center. Each strip is subdivided into 10 or 14 observational points, so that the velocity of the solar disk has effectively been measured at 48 regions. Each region is represented by one spectrum. A complete run took about one hour. A typical spectrum is shown in Figure 1. The curvature of the lines is due to the optical construction of the spectrograph. Figure 2 shows a typical spectrum averaged over 10 rows.

3. Analysis

The wavelength calibration is based on telluric water lines marked by the letter T in Figure 1 and is estimated to be accurate to about 20 m/s. The Doppler shifts due to the Earth's rotation and orbital motion were removed. According to Wittmann (1996), the magnetic influence on Doppler results is negligible for sodium lines.

The standard deviation of the absolute radial velocity scatter for the sodium D_2 line was estimated to 100 m/s on September 10, 200 m/s on September 13 and 150 m/s on September 14. No detailed template fitting was performed in determining the line centers. We estimate that the systematic error in absolute velocity due to this omission is <200 m/s.
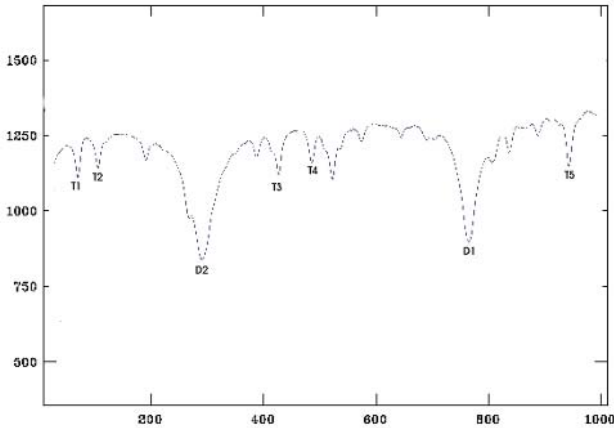
Figure 2.   Absorption line profiles averaged over row 140 to 150. The wavelength along the x-axis is given in pixels, while the y-axis shows intensity.

4. Results

Radial velocity data were fitted to the rotation model:

$$v_R = \omega(\varphi) \ R \ \sin \Psi + d,$$

where $\omega(\varphi)$ is the angular velocity, φ the heliographic latitude, R the solar radius, Ψ the heliographic longitude starting from the sub-earth point and d the gravitational redshift velocity. The angular velocity is most often expressed in the form

$$\omega(\varphi) = a + b \ \sin^2 \varphi + c \ \sin^4 \varphi,$$

where the coefficient a is the rotation rate at the solar equator and the coefficients b and c parameterize the differential rotation rate.

The solar rotation coefficients and the gravitational redshift velocity for the sodium D_2 line were determined separately for each observation day. The results are tabulated in Table 1 together with Wittmann's (1996) – who used the same sodium D_2 line – and Howard and Harvey's (1970) coefficients, which are very often cited and used in the analysis.

The measured rotation rates are plotted in Figure 3. The uncertainty obviously becomes larger at higher latitudes. The standard deviation of measured values with respect to the smooth theoretical curves are of the order of 200 m/s, consistent with the error bars. However, our rotation rate at the equator is by about 10% lower than the value usually found. This is due to the fact that we did not take into account all telluric spectral lines on the observed interval as mentioned above.

TABLE I. Observed spectroscopic rotation rate measurements.

Reference	a [deg/day]	b [deg/day]	c [deg/day]	d [km s^{-1}]
10 September 1999, Na D$_2$	12.90 ± 0.77	-2.78 ± 9.66	-2.65 ± 2.38	0.67 ± 0.05
13 September 1999, Na D$_2$	12.60 ± 0.33	2.87 ± 1.50	-9.26 ± 3.79	0.46 ± 0.02
14 September 1999, Na D$_2$	13.14 ± 0.77	1.95 ± 3.45	-7.63 ± 8.70	0.42 ± 0.05
Wittmann (1996), Na D$_2$	14.75 ± 0.45	-1.6 ± 4.1	-4.3 ± 4.3	/
Howard and Harvey (1970)	13.76 ± 0.12	-1.74 ± 0.08	-2.19 ± 0.13	/
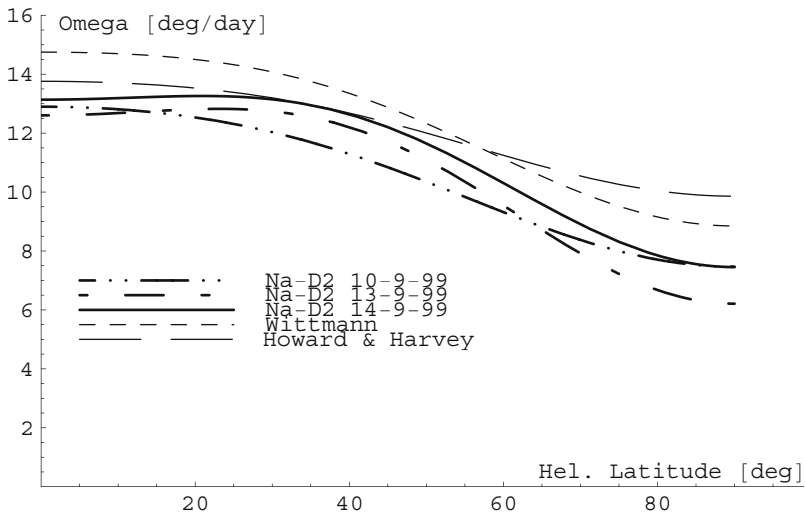
Figure 3. Comparison of measured rotation rates together with the results of Howard and Harvey (1970) and Wittman (1996).

References

Beck, J. G.: 2000, *Solar Phys.* **191**, 47.

Howard, R. and Harvey, J.: 1970, *Solar Phys.* **12**, 23.

Howard, R., Boyden, J.E., and LaBonte, B.J.: 1980, *Solar Phys.* **66**, 167.

Jejčič, S. and Čadež, A.: 2002, in A. Wilson (ed.), *Solar Variability: From Core to Outer Frontiers*, Proc. 10th European Solar Physics Meeting, ESA SP-506, 959.

Jejčič, S. and Čadež, A.: 2003, *Hvar Obs. Bull.* **27**, 197.

Scherrer, P.H., Wilcox, J.M., and Svalgaard, L.: 1980, *Astrophys. J.* **241**, 811.

Snodgrass, H.B. and Ulrich, R.K.: 1990, *Astrophys. J.* **351**, 309.

Wittmann, A.D.: 1996, *Solar Phys.* **167**, 441.

THE OBSERVING PROGRAMS AT KANZELHÖHE SOLAR OBSERVATORY

W. OTRUBA

Kanzelhöhe Solar Observatory, University of Graz
A–9521 Treffen, Austria

Abstract. Kanzelhöhe Solar Observatory is the experimental executive of the Institute for Geophysics, Astrophysics and Meteorology, University of Graz, Austria. The observing program is mainly related to science objectives of the solar physics division but additional observations are carried out in order to support satellite missions as well as international programs like Max Millenium. The program comprises full disk observations in several optical bands with a high temporal resolution for surveillance purposes. Independent projects deal with improvement of instruments, observing techniques and data archiving.

1. Introduction

Kanzelhöhe Solar Observatory (KSO), located on a mountain at 1500 m, carries out observations mainly but not exclusively for the solar physics division of the Institute for Geophysics, Astrophysics and Meteorology, University of Graz, Austria. Motivation for the work is derived from science objectives of this division and from collaborations with international partners. KSO supports several international projects and satellite missions like SOHO and RHESSI with ground based observations. The solar physics division studies the dynamics of the solar atmosphere and solar activity. Science objectives of recent projects are statistical properties of solar activity features, pre-flare mechanisms, heating and energy transport processes as well as propagation of disturbances in the solar atmosphere (wave phenomena) and solar drivers of space weather like CMEs. Further projects deal with large scale dynamics of the photosphere and irradiance variations.

2. Instrumentation

High quality observations need specialized instruments for the fields of scientific research. Instrument design and science objectives of the solar physics division at the main site were a common evolution. Derived from the interest to study the dynamics of the solar atmosphere and solar activity features like flares and sunspots our instrumentation is designed for a multi-band observation of the solar atmosphere in the optical spectral range in order to observe several atmospheric layers. We execute full-disk observations in continuum, Hα and Na-D but with high temporal resolution. Observing with a Magneto-Optical Filter operated in the Na-D lines allows also to obtain Doppler- and magnetograms of the solar photosphere. The observing program is complemented by independent projects with technical background related to the observations like event and solar activity triggered observation control, automatic real-time flare recognition and the development of an on-line archives system.

3. Observations

The standard solar surveillance program is carried out on a daily basis yielding about 2000 hours of observations on 300 days per year. The so-called Patrol Instrument is a 4-telescope system on a common mounting for white-light, Na-D and Hα observations.

3.1. CONTINUUM OBSERVATIONS ("WHITE-LIGHT")

A refractor $d/f = 110/1650$ with a projection lens system is used for the daily sunspot drawings (disk diameter 25 cm) which continue a long tradition of more than 50 years. Mainly intended for the derivation of the sunspot relative number they provide also a quick preview about solar activity without extra means. Positions of spots can be obtained precise enough for statistic investigations of sunspot motions. Since 1989 a set of three photoheliograms per day is taken on special film plates for a very accurate determination of sunspot positions and areas using an extra, larger refractor ($d/f = 130/1950$). This data set supports the Debrecen Photoheliographic Results (Pettauer, 1990).

3.2. Hα OBSERVATIONS

Full-disk Hα observations with high temporal resolution enable to follow the evolution of rapid changing phenomena like flares and propagating waves. Kanzelhöhe Solar Observatory is one of three base stations of the

Global Hα Network (Steinegger *et al.*, 2000). The solar disk is imaged by a $d/f = 100/2000$ lens. A filter tuning unit rotates the polarizers of the 0.7 Å Lyot filter to shift its passing band. Behind the filter the light is splitted by a beam-splitter cube and lenses adapt the image size and focus the solar images to two CCD cameras: a fast $1k \times 1k \times 8$ bit Pulnix and a slower $2k \times 2k \times 14$ bit Apogee. The digital image acquisition system for Hα was introduced in 1997 and is operated since 2000 on a regular basis. The $1k \times 1k \times 8$ bit Pulnix system was described in Otruba (1999). The high resolution camera for the Global Hα Network was implemented in 2000. Recent improvements (Otruba and Pötzi, 2003) comprise frame selection, automatic exposure time control, increased image acquisition rate and a Hα filter tuning unit to observe optional in the line wings of the Hα spectral line which is particularly useful in observing the hot plasma in flare kernels and allows further to obtain Doppler images. The high-speed $1k \times 1k$ 8-bit CCD camera delivers up to 15 frames/sec which are grabbed by the PC-based instrument controller and undergo a simple frame selection process. The maximum image acquisition rate is 1 image per 2 sec, with optional line-wing observations in a script mode it is limited to 1 image per 5 sec. The exposure time is automatically adjusted according to the sky transparency to exploit the dynamic range. The image acquisition rate and optional wing images can be triggered by external signals, currently we use the 1 min GOES X-ray flux. The low-speed CCD camera of the Global Hα Network has a high resolution of $2k \times 2k$ and 14-bit but the disadvantage of a slow read-out of 5 sec per frame which is the limiting parameter and inhibits a frame selection mode. An upgrade from the fast 8-bit camera to a 10-bit model is in progress.

3.3. NA-D OBSERVATIONS

Since 1997 a Magneto-Optical Filter with Sodium vapour cells has been operated at Kanzelhöhe Solar Observatory and was subsequently improved for stable operation on a daily basis. Full-disk simultaneous spectrograms, Dopplergrams and longitudinal magnetograms are obtained with a cadence of 1 set per min and a spatial resolution of 4.3 arcsec. The instrument is described in Cacciani *et al.* (2000).

4. Data archiving

Observational data obtained directly in digital form pass a local primary quality check and are transferred to the archives system via the LAN after end of observation. The archives system manages the data stream and reformatting to standard formats like FITS and JPEG and swapping of

older data to archives media. Due to the huge amount of Hα images per day we archive a standard time-series of 1 image per min but keep the full temporal resolution for periods of higher solar activity. A data-base which provides an online catalogue of the archived data is automatically updated and logs all operations. Web-based forms assist the observer in entering ancillary data and provide an interface to tabular data. Recent observations still in analog form like sunspot drawings are scanned and added to the digital archives. Older data will be digitized according to the available resources and on request. The archives system generates also monthly reports.

Acknowledgements

References

Cacciani, A., Moretti, P.F., Messerotti, M., Hanslmeier, A., Otruba, W., and Pettauer, T.V.: 2000, in A. Hanslmeier and M. Messerotti (eds.), *Motions in the Solar Atmosphere*, Kluwer, London, 271.

Otruba, W.: 1999, in B. Schmieder, A. Hofmann and J. Staude (eds.), *Third Advances in Solar Physics Euroconference: Magnetic Fields and Oscillations*, ASP Conference Series, San Francisco, 314.

Otruba, W. and Pötzi W.: 2003, *Hvar Obs. Bull.* **27**, 189.

Pettauer, T.: 1990, in L. Deszö (ed.), *The Dynamic Sun*, Publ. Debrecen Heliophysical Observatory, Debrecen, 62.

Steinegger, M., Hanslmeier, A., Otruba, W., Freislich, H., Denker, C., Goode, P.R., Marquette, W.M., Varied, J., Wang, H., Luo, G., Chen, D., and Zhang, Q.: 2000, *Hvar Obs. Bull.* **24**, 179.

THEORETICAL MODELING OF POTENTIAL MAGNETIC FIELD DISTRIBUTION IN THE CORONA ABOVE AXIALLY SYMMETRIC PHOTOSPHERIC ACTIVE REGIONS IN A UNIFORM MAGNETIC FIELD

V.M. ČADEŽ
Belgian Institute for Space Aeronomy
Ringlaan 3, B-1070 Brussels, Belgium

A. DEBOSSCHER
K. U. Leuven-CPA
Celestijnenlaan 200B B-3001 Heverlee, Belgium

M. MESSEROTTI, P. ZLOBEC, M. IURCEV and A. SANTIN
INAF-Trieste Astronomical Observatory
Via G.B. Tiepolo 11, I-34131 Trieste, Italy

Abstract. Low plasma β magnetic structures are modeled by force-free magnetic field topologies. In particular, we limit our treatment to axially symmetric potential magnetic fields with suitably prescribed boundary conditions that simulate active regions on the surface of the photosphere. Analytical solutions are obtained and plotted for magnetic fields emerging from some typical examples of active regions in presence of a global uniform magnetic field. The results show how complex magnetic structures can develop from combinations of such fields.

1. Introduction and basic equations

Numerous authors (Aly and Seehafer, 1993; Sakurai, 1995; Yan and Wang, 1995) have treated the coronal magnetic field by various numerical methods.

In this paper, we apply the analytical approach of solving the magneto-hydrostatic equation as done in our previous work (Čadež *et al.*, 2001). We consider some typical axially symmetric magnetic field topologies in a static low β plasma of the solar corona which arise above photospheric active regions in presence of a global uniform magnetic field. As magnetic forces dominate in low β plasmas, static magnetic field configurations are

those in which these forces are mutually balanced:

$$\mu_0 \vec{j} \times \vec{B} \equiv \vec{B} \cdot \nabla \vec{B} - \nabla B^2 / 2 = 0. \tag{1}$$

A subclass of such force-free fields are the current-free or potential magnetic fields characterized by $\mu_0 \vec{j} = \nabla \times \vec{B} = 0$. In this case, an axially symmetric, i.e. a $\phi-$invariant magnetic field can be written as $\vec{B} = \nabla \vec{A}$ which reduces to $\vec{B} = \nabla \mathcal{A} \times \hat{e}_\phi / r$ in cylindrical coordinates. Here: $\mathcal{A} = A/r$, $\vec{A} = A(r, z)\hat{e}_\phi$, and $\vec{B} = (B_r(r, z), 0, B_z(r, z))$. Consequently, $\vec{B} \cdot \nabla \mathcal{A} = 0$, i.e. $\mathcal{A}$ is constant along a magnetic field line. Thus the $\phi-$invariant magnetic field topology is given by the set of curves (Čadež, 1996; Oliver $et~al.$, 1998):

$$\mathcal{A} = const, \qquad \text{where } \mathcal{A} \text{ satisfies:} \qquad \nabla^2 \mathcal{A} - \frac{2}{r}\frac{\partial \mathcal{A}}{\partial r} = 0. \tag{2}$$

Once the solution for $\mathcal{A}$ is obtained, the magnetic field components follows as: $B_r = -\delta_z \mathcal{A}/r$, $B_\phi = 0$, and $B_z = \delta_r \mathcal{A}/r$.

2. Solution and boundary conditions

Eq. 2 has an analytical solution of the following type:

$$\mathcal{A} = \int_0^\infty dr' \mathcal{A}_0(r') \int_0^\infty dp\, J_1(r'p) J_1(rp) rp\, e^{-zp}, \tag{3}$$

where $\mathcal{A}(r, 0) = \mathcal{A}_0(r)$ is the boundary condition imposed on $\mathcal{A}$ at $z = 0$. The details of the derivations are described in Čadež $et~al.$ (2001).

To model a magnetic active region on the photosphere ($z = 0$) it is necessary to prescribe a suitable profile for $\mathcal{A}_0(r)$ that yields realistic distributions for magnetic field components at $z = 0$. Thus:

– If $\mathcal{A}_0(r)$ is a monotonous function of r, then its $r-$derivative, i.e. $B_z(r, 0)$, has the same sign for all r. Magnetic field lines are then everywhere either emerging from the photosphere or sinking into it, depending on the sign of the derivative.

– If $\mathcal{A}_0(r)$ is not a monotonous function of r, then its $r-$derivative, i.e. $B_z(r, 0)$, changes sign. In that case there are regions where magnetic field lines emerge/sink from/into the photosphere depending on the sign of the derivative.

– Regions with steeper profiles of $\mathcal{A}_0(r)$ correspond to regions with stronger $B_z(r, 0)$ and vice versa. These domains with enhanced magnetic field may further be related to observed active regions on the photosphere.

– A vertical uniform magnetic field $\vec{B}_u = B_0 \hat{e}_z$, $B_0 = const$, can be considered as axially symmetric with a potential $\mathcal{A}_u(r, z) = \mathcal{A}_{0u}(r) = B_0 r^2 / 2$.
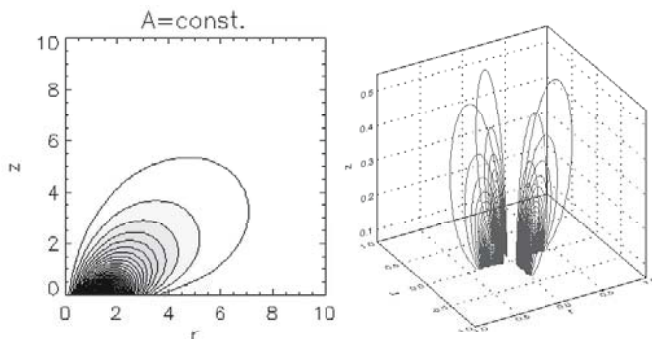
Figure 1. A single active region ($A = 40$, $a = 1$).
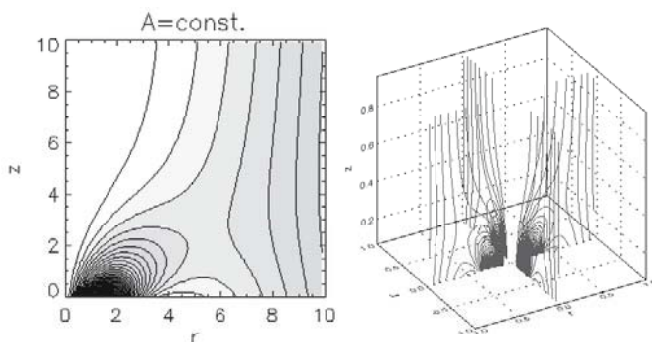
Figure 2. A single active region as in Figure 1 in a uniform magnetic field ($b_{0z} = 0.1$).

– It is possible to apply also a linear combination of several types of profiles in Eq. 3 to model complex magnetic structures with combinations of various sinks and sources at the photosphere: $\mathcal{A}_0 = \sum_n \mathcal{A}_{0n}$.

3. Examples and results

The choice of profiles $\mathcal{A}_0(r)$ depends on the example that is going to be considered. In what follows, we shall model a case of two active regions embedded into a uniform magnetic field by using the following boundary function:

$$\mathcal{A}_0(r, 0) = A_1 \frac{r^2}{a_1} e^{-r^2/a_1} + A_2 \frac{r^2}{a_2} e^{-r^2/a_2} + B_0 \frac{r^2}{2}, \tag{4}$$

which when substituted into Eq. 3 yields magnetic field topologies $\mathcal{A}(r, z) = const$ as shown in Figures 1–4 for the indicated values of the parameters.

As can be seen, suitable combinations of a global uniform magnetic field and magnetic fields from localized active regions can result into structures with magnetic dips (as typical for regions with prominences), with neutral
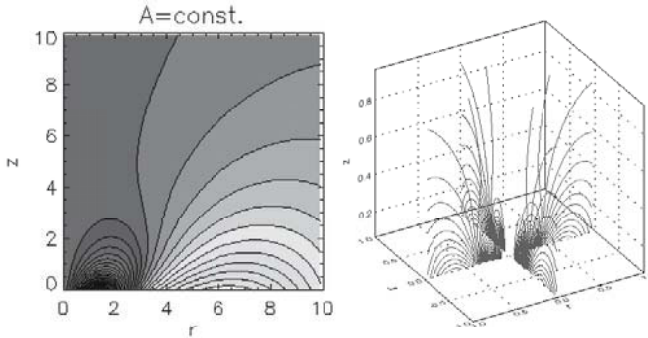
Figure 3.   A set of two active regions ($A_1 = 40$, $a_1 = 1$, $A_2 = -20$, $a_2 = 20$).
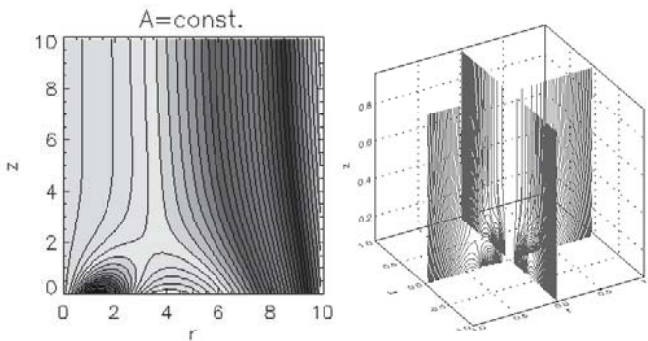
Figure 4.   Two active regions as in Figure 3 in a uniform magnetic field ($b_{0z} = 0.5$).

points (typical for domains where magnetic reconnection may occur), and with open magnetic field lines (streamers and coronal holes).

Acknowledgements

References

Aly, J.J. and Seehafer, N.: 1993, *Solar Phys.* **144**, 243.
Čadež, V.M.: 1996, *Hvar Obs. Bull.* **20**, 1.
Čadež, V.M., Debosscher, A., Messerotti, M., and Zlobec, P..: 2001, in A. Hanslmeier, M. Messerotti and A. Veronig (eds.), *The Dynamic Sun*, Kluwer Academic Publishers, Astrophysics and Space Science Library 259, 231.
Oliver, R., Čadež, V.M., and Ballester, J.L.: 1998, *Astrophys. Space Sci.* **254**, 67.
Sakurai, T.: 1995, *Space Sci. Rev.* **51**, 11.
Yan, Y. and Wang, J.: 1995, *Astron. Astrophys.* **298**, 277.

Author Index

Astrophysics and Space Science Library

Volume 316: *Civic Astronomy - Albany's Dudley Observatory, 1852-2002,* by
G. Wise
Hardbound ISBN 1-4020-2677-3, October 2004

Volume 315: *How does the Galaxy Work - A Galactic Tertulia with Don Cox
and Ron Reynolds,* edited by E. J. Alfaro, E. Pérez, J. Franco
Hardbound ISBN 1-4020-2619-6, September 2004

Volume 314: *Solar and Space Weather Radiophysics - Current Status and
Future Developments,* edited by D.E. Gary and C.U. Keller
Hardbound ISBN 1-4020-2813-X, August 2004

Volume 313: *Adventures in Order and Chaos — A Scientific Autobiography,* by
G. Contopoulos
Hardbound ISBN 1-4020-3039-8, December 2004

Volume 312: *High-Velocity Clouds,* edited by H. van Woerden, U. Schwarz, B.
Wakker
Hardbound ISBN 1-4020-2813-X, September 2004

Volume 311: *The New ROSETTA Targets- Observations, Simulations and
Instrument Performances*, edited by L. Colangeli, E. Mazzotta Epifani, P.
Palumbo
Hardbound ISBN 1-4020-2572-6, September 2004

Volume 310: *Organizations and Strategies in Astronomy 5,* edited by A. Heck
Hardbound ISBN 1-4020-2570-X, September 2004

Volume 309: *Soft X-ray Emission from Clusters of Galaxies and Related
Phenomena*, edited by R. Lieu and J. Mittaz
Hardbound ISBN 1-4020-2563-7, September 2004

Volume 308: *Supermassive Black Holes in the Distant Universe,* edited by
A.J. Barger
Hardbound ISBN 1-4020-2470-3, August 2004

Volume 307: *Polarization in Spectral Lines*, by E. Landi Degl'Innocenti and
M. Landolfi
Hardbound ISBN 1-4020-2414-2, August 2004

Volume 306: *Polytropes – Applications in Astrophysics and Related Fields,* by
G.P. Horedt
Hardbound ISBN 1-4020-2350-2, September 2004

Volume 305: *Astrobiology: Future Perspectives,* edited by P. Ehrenfreund,
W.M. Irvine, T. Owen, L. Becker, J. Blank, J.R. Brucato, L. Colangeli, S.
Derenne, A. Dutrey, D. Despois, A. Lazcano, F. Robert
Hardbound ISBN 1-4020-2304-9, July 2004
Paperback ISBN 1-4020-2587-4, July 2004

Volume 304: *Cosmic Gammy-ray Sources,* edited by K.S. Cheng and G.E.
Romero
Hardbound ISBN 1-4020-2255-7, September 2004

Volume 303: *Cosmic rays in the Earth's Atmosphere and Underground*, by
L.I, Dorman
Hardbound ISBN 1-4020-2071-6, August 2004

Volume 302:*Stellar Collapse,* edited by Chris L. Fryer
Hardbound, ISBN 1-4020-1992-0, April 2004

Volume 301: *Multiwavelength Cosmology*, edited by Manolis Plionis
Hardbound, ISBN 1-4020-1971-8, March 2004

Volume 300:*Scientific Detectors for Astronomy*, edited by Paola Amico, James
W. Beletic, Jenna E. Beletic
Hardbound, ISBN 1-4020-1788-X, February 2004

Volume 299: *Open Issues in Local Star Fomation,* edited by Jacques Lépine,
Jane Gregorio-Hetem
Hardbound, ISBN 1-4020-1755-3, December 2003

Volume 298: *Stellar Astrophysics - A Tribute to Helmut A. Abt,* edited by
K.S. Cheng, Kam Ching Leung, T.P. Li
Hardbound, ISBN 1-4020-1683-2, November 2003

Volume 297: *Radiation Hazard in Space*, by Leonty I. Miroshnichenko
Hardbound, ISBN 1-4020-1538-0, September 2003

Volume 296: *Organizations and Strategies in Astronomy, volume 4,* edited by
André Heck
Hardbound, ISBN 1-4020-1526-7, October 2003

Volume 282: *Radio Recombination Lines,* by M.A. Gordon, R.L. Sorochenko
Hardbound, ISBN 1-4020-1016-8, November 2002

Volume 281: *The IGM/Galaxy Connection,* edited by Jessica L. Rosenberg,
Mary E. Putman
Hardbound, ISBN 1-4020-1289-6, April 2003

Volume 280: *Organizations and Strategies in Astronomy III,* edited by André
Heck
Hardbound, ISBN 1-4020-0812-0, September 2002

Volume 279: *Plasma Astrophysics , Second Edition,* by Arnold O. Benz
Hardbound, ISBN 1-4020-0695-0, July 2002

Volume 278: *Exploring the Secrets of the Aurora,* by Syun-Ichi Akasofu
Hardbound, ISBN 1-4020-0685-3, August 2002

Volume 277: *The Sun and Space Weather,* by Arnold Hanslmeier
Hardbound, ISBN 1-4020-0684-5, July 2002

Volume 276: *Modern Theoretical and Observational Cosmology,* edited by
Manolis Plionis, Spiros Cotsakis
Hardbound, ISBN 1-4020-0808-2, September 2002

Volume 275: *History of Oriental Astronomy,* edited by S.M. Razaullah Ansari
Hardbound, ISBN 1-4020-0657-8, December 2002

Volume 274: *New Quests in Stellar Astrophysics: The Link Between Stars
and Cosmology,* edited by Miguel Chávez, Alessandro Bressan, Alberto
Buzzoni,Divakara Mayya
Hardbound, ISBN 1-4020-0644-6, June 2002

Volume 273: *Lunar Gravimetry,* by Rune Floberghagen
Hardbound, ISBN 1-4020-0544-X, May 2002

Volume 272:*Merging Processes in Galaxy Clusters,* edited by L. Feretti, I.M.
Gioia, G. Giovannini
Hardbound, ISBN 1-4020-0531-8, May 2002

Volume 271: *Astronomy-inspired Atomic and Molecular Physics,* by A.R.P.
Rau
Hardbound, ISBN 1-4020-0467-2, March 2002

Volume 270: *Dayside and Polar Cap Aurora*, by Per Even Sandholt, Herbert C. Carlson, Alv Egeland
Hardbound, ISBN 1-4020-0447-8, July 2002

Volume 269: *Mechanics of Turbulence of Multicomponent Gases*, by Mikhail Ya. Marov, Aleksander V. Kolesnichenko
Hardbound, ISBN 1-4020-0103-7, December 2001

Volume 268: *Multielement System Design in Astronomy and Radio Science*, by Lazarus E. Kopilovich, Leonid G. Sodin
Hardbound, ISBN 1-4020-0069-3, November 2001

Volume 267: *The Nature of Unidentified Galactic High-Energy Gamma-Ray Sources,* edited by Alberto Carramiñana, Olaf Reimer, David J. Thompson
Hardbound, ISBN 1-4020-0010-3, October 2001

Volume 266: *Organizations and Strategies in Astronomy II,* edited by André Heck
Hardbound, ISBN 0-7923-7172-0, October 2001

Volume 265: *Post-AGB Objects as a Phase of Stellar Evolution,* edited by R. Szczerba, S.K. Górny
Hardbound, ISBN 0-7923-7145-3, July 2001

Volume 264: *The Influence of Binaries on Stellar Population Studies*, edited by Dany Vanbeveren
Hardbound, ISBN 0-7923-7104-6, July 2001

Volume 262: *Whistler Phenomena - Short Impulse Propagation,* by Csaba Ferencz, Orsolya E. Ferencz, Dániel Hamar, János Lichtenberger
Hardbound, ISBN 0-7923-6995-5, June 2001

Volume 261: *Collisional Processes in the Solar System,* edited by Mikhail Ya. Marov, Hans Rickman
Hardbound, ISBN 0-7923-6946-7, May 2001

Volume 260: *Solar Cosmic Rays,* by Leonty I. Miroshnichenko
Hardbound, ISBN 0-7923-6928-9, May 2001

Volume 259: *The Dynamic Sun,* edited by Arnold Hanslmeier, Mauro Messerotti, Astrid Veronig
Hardbound, ISBN 0-7923-6915-7, May 2001

Volume 246: *The Legacy of J.C. Kapteyn*, edited by Piet C. van der Kruit, Klaas van Berkel
Paperback, ISBN 1-4020-0374-9, November 2001
Hardbound, ISBN 0-7923-6393-0, August 2000

Volume 245: *Waves in Dusty Space Plasmas,* by Frank Verheest
Paperback, ISBN 1-4020-0373-0, November 2001
Hardbound, ISBN 0-7923-6232-2, April 2000

Volume 244: *The Universe*, edited by Naresh Dadhich, Ajit Kembhavi
Hardbound, ISBN 0-7923-6210-1, August 2000

Volume 243: *Solar Polarization*, edited by K.N. Nagendra, Jan Olof Stenflo
Hardbound, ISBN 0-7923-5814-7, July 1999

Volume 242: *Cosmic Perspectives in Space Physics*, by Sukumar Biswas
Hardbound, ISBN 0-7923-5813-9, June 2000

Volume 241: *Millimeter-Wave Astronomy: Molecular Chemistry & Physics in Space,* edited by W.F. Wall, Alberto Carramiñana, Luis Carrasco, P.F. Goldsmith
Hardbound, ISBN 0-7923-5581-4, May 1999

Volume 240: *Numerical Astrophysics,* edited by Shoken M. Miyama, Kohji Tomisaka,Tomoyuki Hanawa
Hardbound, ISBN 0-7923-5566-0, March 1999

Volume 239: *Motions in the Solar Atmosphere,* edited by Arnold Hanslmeier, Mauro Messerotti
Hardbound, ISBN 0-7923-5507-5, February 1999

Volume 238: *Substorms-4,* edited by S. Kokubun, Y. Kamide
Hardbound, ISBN 0-7923-5465-6, March 1999

For further information about this book series we refer you to the following web site:
www.springeronline.com

To contact the Publishing Editor for new book proposals:
Dr. Harry (J.J.) Blom: harry.blom@springer-sbm.com